Title
A Numeric Predictive Failure Model for Percussive Excavation

Author
Green, Alex Nicholas

Publication Date
2011

Peer reviewed|Thesis/dissertation

A Numeric Predictive Failure Model for Percussive Excavation

By

Alex Nicholas Green

A dissertation submitted in partial satisfaction of the

requirements for the degree of

Doctor of Philosophy

in

Engineering - Mechanical Engineering

in the

Graduate Division

of the

The University of California, Berkeley

Committee in charge:

Professor Dennis K. Lieu, Chair
Professor C.K. Hari Dharan
Professor Juan M. Pestana-Nacimento

Fall 2011

Abstract

A Numeric Predictive Failure Model for Percussive Excavation

by

Alex Nicholas Green

Doctor of Philosophy in Engineering - Mechanical Engineering

University of California, Berkeley

Professor Dennis Lieu, Chair

NASA is currently developing technology for future human space exploration missions. One of these technologies is percussive excavation. The presented research examines how percussion affects soil behavior during the excavation process.

The purpose of this research was to develop a numeric code for the prediction of reaction forces associated with soil failure during percussive excavation. In order to achieve this objective a variety of different excavation variables were tested. Those variables include: percussive frequency, percussive impact energy, excavation speed, excavation attack angle, excavation depth, and soil relative density.

The results of the experimental testing showed that through percussion the effects of dilatancy along a soil's failure boundary layer were mitigated. This result was seen both in the reduction of the soil draft force as well as the soil's ability to continuously create shear planes during excavation. In relation to the draft force, the effects of percussion resulted in an exponential decay in the soil's internal friction angle.

Within this report a numeric code is proposed and tested which predicts an excavation draft force given input parameters of: percussive frequency, excavation speed, percussive impact energy, geometric dimensions of a flat-backed excavation implement, excavation attack angle, gravitational constant, and in situ soil internal friction angle.

The theoretical basis of the numeric code is the upper limit analysis method which uses virtual work to back-calculate an unknown applied traction force at incipient soil failure. In order to use the upper limit analysis approach the soil is idealized as perfectly plastic, stable, and obeying the flow rule.

To incorporate the effects of percussion into the theoretical model the upper limit analysis is used, but changes are made to the defining control volume geometry of the failure volume based on percussive, soil, and speed parameters. Those changes are implemented through the internal friction angle. The internal friction angle is characterized as having an exponentially decaying relationship in terms of applied percussive energy. The exponential decay factor is

given as a function of the in situ internal friction angle of the soil, and the applied excavation velocity.

Results from the theoretical model show agreement between predicted and experimentally measured excavation reaction forces. Results are provided using a wide array of different input values from the following variables: percussive frequency, percussive impact energy, excavation speed, excavation attack angle, excavation depth, and soil relative density.

In addition, the theoretical model is used to predict percussive excavation forces when gravity is changed to 1/6 the magnitude of earth's gravitational force. By comparing those results with ones taken using earth's gravity, it is found that the asymptotic limit of the internal friction angle is achieved through lower percussive frequencies and lower power requirements in lunar gravity than in earth gravity. Furthermore, it is shown that the reduction in excavation force between a lunar gravity environment and an earth gravity environment is not a constant, rather a value dependent on applied percussion and excavation parameters.

It is concluded that this work provides an adequate first generation numeric model which can be used for approximating percussive excavation reaction forces in terms of a wide array of different input variables. It is recommended that future work be done to continue refinement and calibration of the code, as well as further validation.

This dissertation is dedicated to my parents and to my wonderful wife. Their love and encouragement have continuously helped me achieve my personal goals and aspirations.

Table of Contents

List of Symbols

ϕ_o-In situ internal friction angle of the soil

ϕ_μ-The Coulomb-friction component of the internal friction angle

ϕ_v-The dilatancy component of the internal friction angle

ϕ_{min}-Minimum internal friction angle. Asymptotic limit of soil degradation

τ-Applied shear force

σ-Applied normal force

σ_n-Normal force in the direction of "n". N references principle stress axes 1,2, and 3 as well as the vertical, horizontal and mean stresses v,h, and m.

G-The shear Modulus of the soil

β-Angle of inclination of soil above horizontal

α-Attack angle of excavation implement

ϱ-Angle of mixed zone in soil deformation which is subject to soil-tool interface effects

ψ-Angle of transition zone in soil deformation

θ-Angle of discrete elements within the transition zone during soil deformation

γ-Angle of applied surcharge force

ξ- Coefficient for determining the effect of vibrations for soil type

δ-Angle of friction between the excavation implement and soil

P_{pe}-Applied traction force to induce soil failure

D_n-Dissipation energy term where "n" represents a velocity discontinuity along a boundary of the control volume

W_n-Work energy term where "n" references a specific traction or body force applied to the control volume

DR-The soil's relative density

c-Soil cohesion

c_a-Soil adhesion

H-The axial length of excavation implement inserted into the soil

m-Mass of failure volume

e-Void ratio

e_n-Void ratio where “n” represents either the minimum or maximum

OCR-Over consolidation ratio

g-Gravitational force constant

η-Normalized acceleration ratio from applied percussion

ω-Angular frequency

ρ-Soil density

ρ_n-Soil density where “n” represents either the minimum or maximum

V_o-Excavation implement velocity

V_n-Velocity term where “n” represents the geometric location of velocity discontinuity

q-Surcharge force

Acknowledgements

This research was supported by the NASA Graduate Student Researchers Program. Experimental work was done in collaboration with Honeybee Robotics Spacecraft Mechanisms Corporation. Honeybee Robotics Spacecraft Mechanisms received funding for the experimental hardware from the National Lunar Science Institute and the NASA Small Business Innovative Research Grant.

1 Introduction

1.1 Purpose of Research:

Starting with the space race of the 1960's, NASA has always been a beacon of innovation and exploration. Although the aim and the specific mission statements of the different directorates have changed over the past 50 years, a common thread has always been to further man's understanding of our universe [Wilson 2011]. A critical piece in the development of future exploration missions to neighboring planets, moons, and asteroids is the ability to utilize the resources available on their surfaces. This is a component of the Vision for Space Exploration Program, as outlined by the Science & Mission Systems Office and is referred to as In Situ Resource Utilization (ISRU). Some of the possibilities of ISRU are: extraction of consumables (O2, H2O, N2, He, etc.), human life-support system replenishment, source materials for In Situ Fabrication and Repair technologies, and source materials for radiation shielding and shelters [McLemore 2011].

In order to excavate and mobilize the necessary resources to facilitate ISRU different hardware designs are being developed. The design of ISRU hardware for the extraction and mobilization of lunar resources presents a persistent obstacle: how to overcome the reaction forces partnered with excavation in a low-gravity environment. Terrestrial earth-moving machines rely on high body forces to break up and excavate soil. The simple and consistent solution whenever high shear strength soils are encountered is to build bigger and heavier excavators with stronger hydraulics. Unfortunately such a one-dimensional approach is not feasible when considering excavation on space bodies. The prohibitive nature of increasing the weight of an excavator for higher body forces is twofold: first, any increase in weight is coupled with a dramatic increase in launch cost; second, any increase in weight will need to be scaled appropriately for reduced gravity forces.

Although reduced gravity forces will influence both the shearing resistance of the soil as well as the weight of an excavator the relative effect is not equal. A study given in [Kobayashi 2005], based on plasticity theory, predicts that excavation forces exerted on a vertical blade in an 1/6 g environment will be 70-80% of the magnitude of those in a normal gravity environment, whereas the body forces of an excavator will be less than 20% of their original magnitude.

The solution then comes at the other end of the problem, the reaction forces. If the body forces cannot be increased then the reaction forces in the soil must be decreased. This can be accomplished through percussive excavation. Percussive excavation, in its most basic definition, is the periodic application of impact energy to a preloaded excavation implement.

1.2 Background:

As early as the 1930's the effects of vibration on soil strength were explored [Pokrovskiy 1934]. Barkan used Pokrovskiy's work as a stepping stone and took his investigation into vibration and soil strength even farther [Barkan 1962]. The work done in these early years was focused on how vibration influences foundation engineering. The motivating factor was to understand how a vibrating piece of machinery interacts with a foundation of dry cohesionless sand. In this effort, Barkan laid some of the ground work for an analytical relationship between vibration and internal friction angle. It was he and others, [Balyshkin 1966] [Ermolaev (1968)], who showed that the defining mechanical properties of sand change as a soil acceleration threshold is exceeded.

Although Barkan's work gave great insight into the dynamics of foundation engineering, it did not explore the possibility of vibration as a tool for decreasing reaction forces during excavation. That idea came later and has been explored by several different scientists [Zhu 2008][Trapp 1974][Klosky 1996][Szabo 1998][Sulatisky 1972]. Through their work, and others like them, it was shown that vibrating a plow blade as it translates through soil produces a dramatic reduction in reaction forces. Sazbo in [1998] reported draft force reductions as high as 90%. The cause of reduction was cited as being a result of vibration inducing soil failure in both the passive and active sense. However the actual soil particle interactions and the associated soil-mechanical properties leading to those reductions were not discussed. Instead different factors such as moisture content and particle size were listed as contributors to the effectiveness of draft force reduction, but no numeric correlation was derived.

The result of these different researchers was compelling, but frustrating. The engineers in charge of designing the excavation equipment that is to be used for ISRU recognized the possibilities that could come through vibratory excavation, but had no criteria or constraints upon which they could base their design. In addition, since the actual physical change taking place within the soil during vibratory excavation was not completely understood, they were not sure how a low gravity environment would influence their desired outcome. Unlike most laboratory research, the design engineers did not have the ability to perform trial and error field tests.

In 2008 the research to which this paper pertains was proposed. That being, the development of a first generation numeric code which can provide an approximate excavation reaction force given certain soil and excavation parameters. The purpose of the numeric is to have a simple and easy-to-use tool through which quick and reasonable approximations can be calculated. Based on those calculated approximations, an initial prototype design can be suggested, which can then pass through a more rigorous, numerically convoluted and time-intensive finite element code. In essence, the proposed purpose of the numeric code is to provide a filter for prototype designs prior to the use of costly finite element analysis code.

To facilitate the necessary hardware and work-space needed for experimental testing this research was done in collaboration with Honeybee Robotics Spacecraft Mechanisms, a Small

Business Innovative Research (SBIR) company funded by NASA. At the onset of this project, it was determined that the numeric model would be used to predict reaction forces based on percussive excavation rather than vibratory excavation. Initial research, done by Honeybee Robotics, prior to this project, showed that vibratory excavation was only effective in loose to medium relative density soils. In high relative density soils the vibratory actuation was not able to achieve the desired range of motion without a dramatic increase to the system's power requirements. To combat this issue Honeybee performed investigative work with percussive excavation and showed that through the use of low-energy shock impact similar force reductions could be achieved [Craft 2009] [Zacny 2009b].

1.3 Research Objective and Goals

NASA is currently planning future missions to low gravity environments which will require surface soil excavation and mobilization. A reaction-force-reducing technology under consideration is percussive excavation. To properly incorporate percussive excavation into their future hardware NASA design engineers are in need of a simple numeric calculation tool which can approximate expected reaction forces. The objective of this research is to provide a first generation version of that numeric code. The requirements, as outlined by NASA, for this first generation code are: its implementation is simple, its calculation time is fast, the underlying code is not too esoteric, and the underlying theory allows for further refinement and development. To accomplish this objective a test stand apparatus was built which was able to test different values of specific excavation variables; an analysis of test data was performed to understand soil interactions induced through percussive excavation; an analysis of empirical test data was coupled with a failure model theory; a calibration of the proposed numeric code was undertaken based on experimental test data.

2 Hardware

2.1 Introduction:

The first and most critical step into developing a numeric code was obtaining good and consistent experimental test data. To this end, extensive work went into the design and development of the test stand apparatus used in this research. This apparatus was built to enable both static and percussive excavation tests. Static test data were used as a benchmark by which the percussive test data were compared.

To investigate how percussion interacts with soil properties, the test stand was built to allow user control of the following variables: relative soil density, frequency of percussion, impact energy of percussion, speed of excavation, excavation angle of attack, and depth of excavation. The following chapter discusses how these variables were measured and controlled.

2.2 Design of the Test Stand

2.2.1 Overall structure of the test stand

The test stand was designed onsite at Honeybee Robotics Space Mechanisms Corporation located in New York City, New York. The design was done by the author, and a Honeybee design engineer, Arthur Ashby. Our objective was to design and build a robust and sturdy structure, provide user control of a variety of different parameters, and acquire specific data measurements pertaining to soil characterization and excavation reaction forces. The structure needed to be able to sustain forces accompanied with excavation as well as those introduced with percussion.

Figure 2-1 provides a graphical representation of the geometry, actuation, and measurement components of the test stand. Figure 2-2, shows a picture of the physical apparatus used for all the testing done in this work.

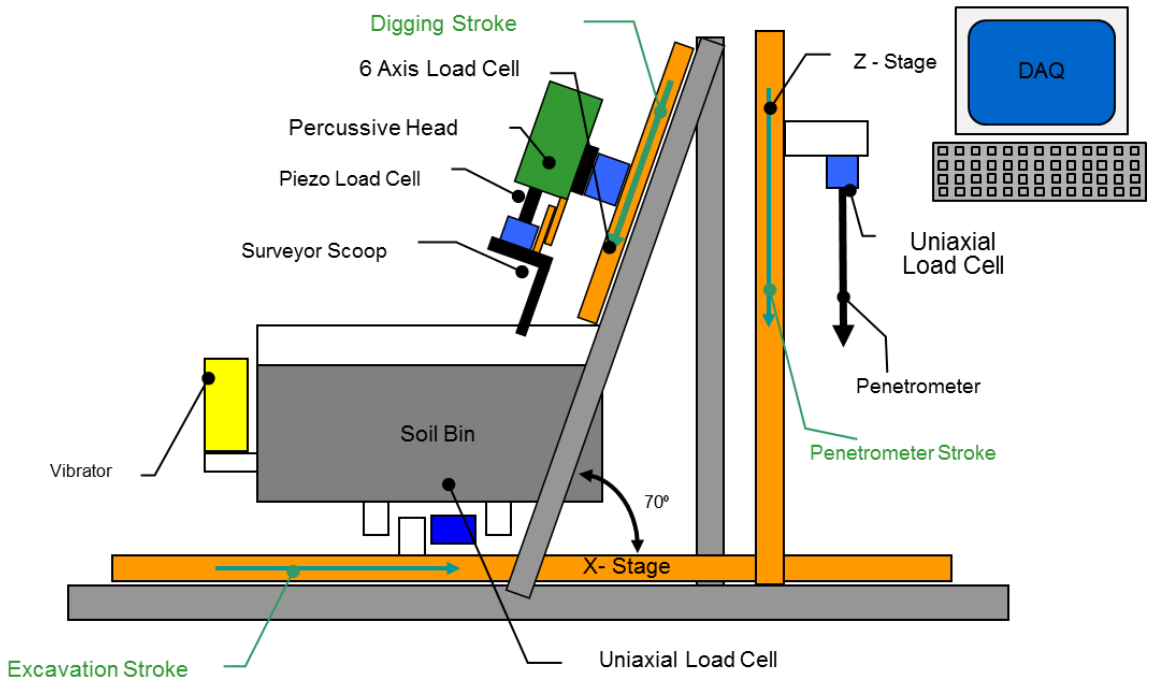

Figure 2-1: The proposed component layout for test stand.

Figure 2-2: Actual test stand apparatus and data acquisition system set up.

2.2.1.1 Surveyor Scoop

The purpose of this research was to provide NASA with a first generation numeric code which could be used to develop percussively-driven excavation equipment. Given its application, a

replica of the Surveyor SMSS (Soil Mechanics Surface Sampler) was selected as the excavation implement. Although atmospheric and gravitational conditions were different, the selection of the SMSS as the excavation implement allowed for the experimental results from this work to be viewed in the context of observations provided by the astronauts from the Surveyor missions.

The scoop had very thin walls and measured 2 inches across or approximately 50 mm. The back plate of the scoop was flat from the edge to about 80 mm in height, at which point it curved inward. All tests were performed at a depth of 70 mm or less, thus restricting the implement geometry to only interface the virgin soil with a flat surface. This restriction allowed for the development of a more simplistic geometry in the theoretical model.

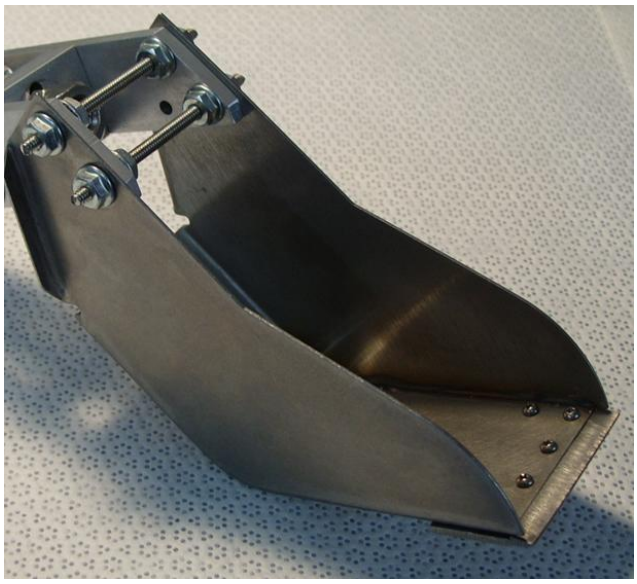

Figure 2-3: Surveyor SMSS replica.

2.2.1.2 Soil Bin

A critical dimensional criterion for the test stand was that it be no wider or taller than 3 feet. The reason being, future testing will take place where the entire apparatus will be placed inside of a vacuum chamber. Those tests will determine the effects that atmospheric moisture and pressure have on soil behavior.

To comply with the dimensional constraints of the apparatus, the size of the soil bin was also restricted. However, its permissible volume was maximized in order to reduce near wall effects. The final dimensions were 75 cm x 50 cm x 30 cm.

The soil bin was made out of acrylic. This material enabled the user to see how the soil behaved along the side walls below the surface, as well as visually determine the height of the soil from outside the container.

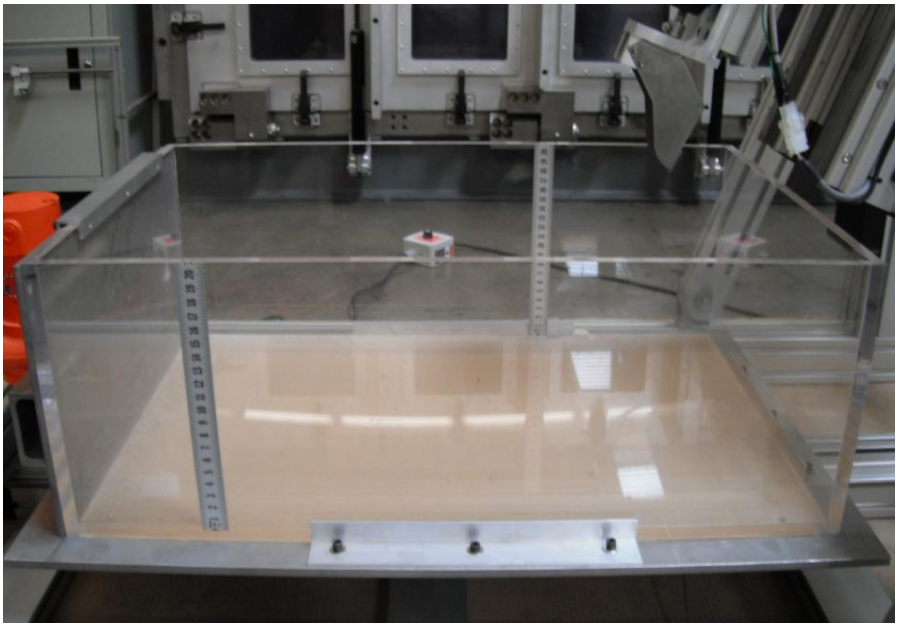

Figure 2-4: Acrylic bin used for housing during testing. Side wall ruler is given in 1/2" increments.

2.2.1.3 Soil Selection-JSC 1a

JSC 1a is a lunar regolith simulant and was used for all of the experimental tests. More details regarding JSC 1a soil properties and how they relate to those pertaining to lunar regolith can be found in Section 4.5.3.

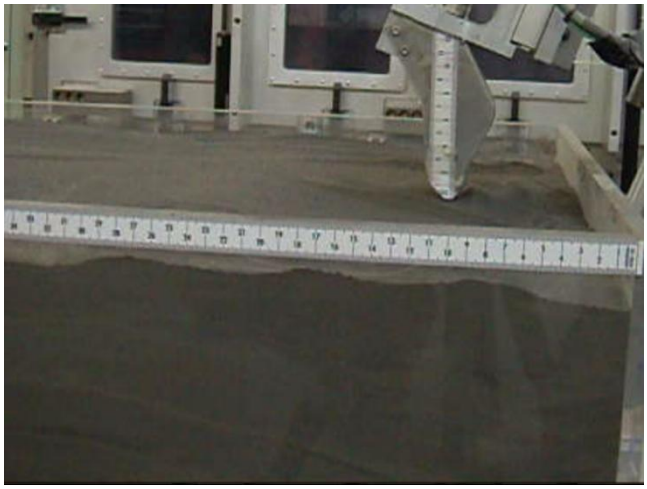

Figure 2-5: JSC 1a is a soil simulant of lunar regolith and was the test material for all experiments.

2.2.1.4 Soil Bin Platform

Critical to the process of excavation was the relative motion between the soil and the scoop. To accomplish this motion the soil bin was moved from left to right across the fixed scoop. This motion was provided by a moving platform underneath the soil bin. The soil bin was fully constrained to the platform along the horizontal plane by four brackets and along the vertical plane by gravity. The platform was rigidly mounted to the test stand on the bottom side by three separate roller carriages. These were the "follower" carriages. A fourth carriage, not fixed to the platform, acted as the "driver". All four carriages were attached to the same rail. The driver carriage was connected to a ball-screw-driven motor. When the driver carriage was actuated through the motor it would make contact with an adjacent supporting carriage and "push" the soil bin. Figure 2-1 shows this concept and Figure 2-6 through Figure 2-8 show a progression of the hardware setup. The purpose of this arrangement was to allow for a load cell to be placed along the excavation axis which measured the horizontal resistance of the scoop against the soil. This force measurement was used as a crosscheck mechanism to validate the summation of the horizontal force components measured by the six axis load cell. Further discussion regarding load cells is given in Section 2.2.1.7.

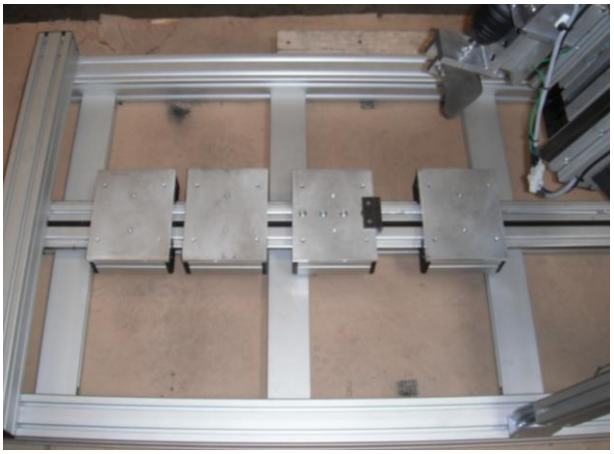

Figure 2-6: Roller carriages support the soil bin and carriage plate. From left to right carriages #1, #2 and #4 are fixed to the carriage plate, and #3 is the actuated "driver" carriage. The bracket on #3 interacts with the excavation load cell shown in Figure 2-13.

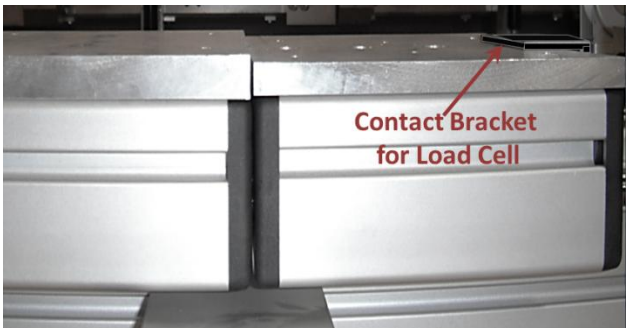

Figure 2-7: The difference in height between carriage #2 and #3; the follower carriage and the driver carriage. Load cell interaction bracket shown on driver carriage.

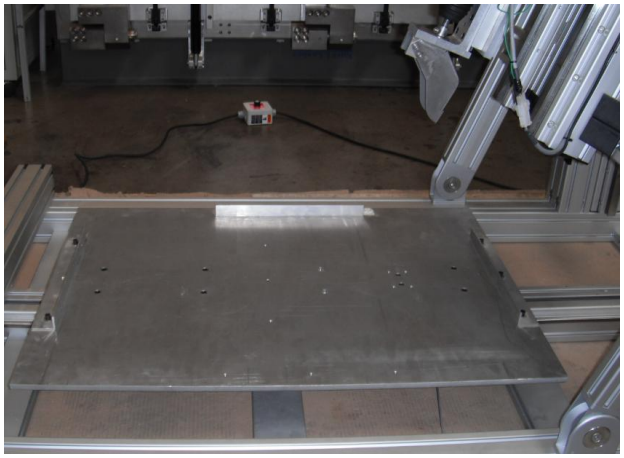

Figure 2-8: Mounted carriage plate is fixed to follower carriages: #1, #2, and #4. The plate is moved by the driver carriage, #3, pushing the adjacent follower carriages, #2 or #4.

2.2.1.5 Soil Compaction Vibrator

During the Apollo missions it was observed that lunar soil was very “fluffy” on the surface, but below the top 15 cm the soil became incredibly dense and stiff [Heiken 1991][Mitchell 1972]. Given the wide breadth of possible soil behavior, a focus of this research was to understand how percussive excavation forces vary in relation to different relative soil densities. To achieve testing of different relative densities, a compaction process was employed utilizing an external vibrator fastened to the soil bin. The vibrator was a Vibco SCR-200, and was mounted to a strip of channel iron clamped to the soil bin. This setup allowed the vibrator to agitate the walls of the soil bin, which, in turn, propagated transverse waves through the soil particles causing them to reconstitute themselves and settle into more compact states.

Prior to each test, soil simulant was added to the soil bin through a controlled pouring process. By adding soil to the bin in a controlled manner it was normally consolidated and in its loosest possible state. Starting at this initial state, the soil could be tested as a very loose soil, or the vibrator could be turned on, for a prescribed amount of time, and cause the soil to reach a desired more compaction state. After the applied vibration, the soil’s relative density would be tested to determine if it fell in the appropriate range. If the soil was still too loose, then the vibrator would be turned on and allowed to agitate the soil particles further. If the soil was too dense, then it would be removed from the soil bin and the process would be repeated. More details regarding this testing procedure are given in Section 2.4.

Figure 2-9: External vibrator used for soil compaction.

2.2.1.6 Transmissions and Motor Drives

In order to achieve a desired amount of torque and speed along the three different axes of translation (excavation, digging, and penetrometer) each ball-screw driver was equipped with a

MAXON motor, gearhead, and encoder. Each motor used a 3:4 or 4:3 transmission. The digging and penetrometer axes used a 4:3 reduction to accommodate more torque and the excavation axis used a 3:4 increase to enable higher trenching speeds. The data sheet outlining the calculated specifications of the motors and transmissions is found in the appendix, Section 9.1.1.

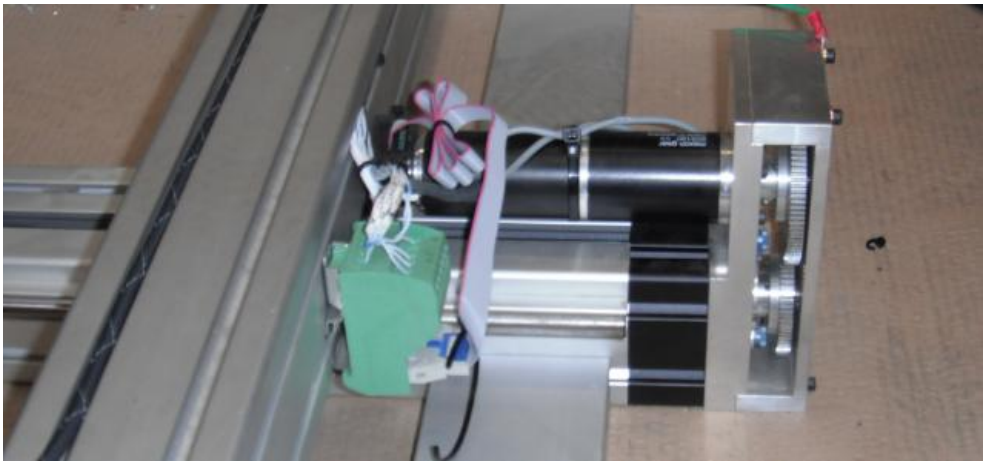

Figure 2-10: Motor and transmission for soil bin actuation.

2.2.1.7 Load Cells

In order to measure and record the pertinent forces involved in this research, the test stand was equipped with 4 different load cells: a six axis load cell, a uniaxial excavation load cell, a piezo load cell, and a uniaxial penetrometer load cell.

2.2.1.7.1 Six Axis Load Cell

The data analyzed to evaluate differences in excavation force on account of different test variables were taken from the six axis load cell. Rigidly mounted between the support plate of the excavation scoop head and the test stand fixture, the six axis load cell provided the most realistic force measurements for soil excavation. The 3-axes measurement capability of the load cell allowed the data to be broken down into vertical, horizontal, and total excavation force components. A free body diagram illustrating the forces encountered by the six axis load cell is given in Figure 2-11.

As the definition of percussive excavation dictates, an external and repeated impact force was applied to the tool interfacing with the soil. Given the nature of that percussive application, extraneous input force measurements were logged by the six axis load cell along the axis-of-impact. These impact forces disrupted the desired force data, the excavation reaction force. To filter out any undesired percussive impact noise a simple moving average routine was used. The

filter averaged data over a span of .16 seconds which was enough to remove the sudden and dramatic impact and dynamic recoil forces, while still maintaining integrity of the actual reaction force. More regarding this procedure and an example data set can be found in Section 3.2.2.

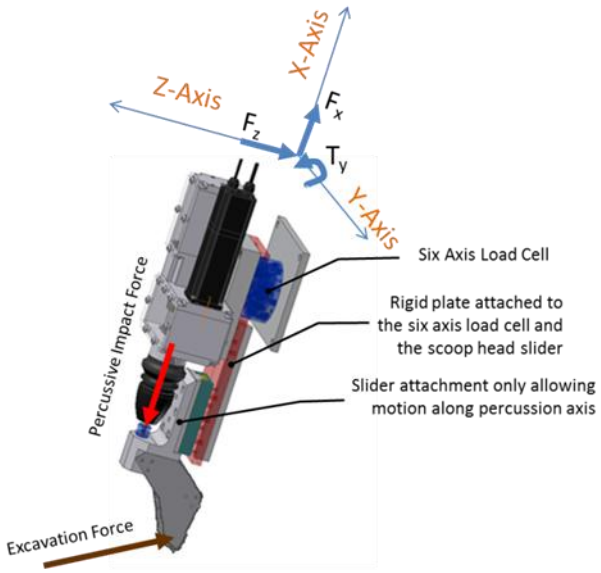

Figure 2-11: Six axis load cell orientation and forces measured by the six axis load cell.

Figure 2-12: ATI Mini 85 Six Axis Force and Torque Load Cell rigidly fixed to the digging axis bearing rail and the percussive mechanism.

2.2.1.7.2 Uniaxial Excavation Load Cell

For measured force validation purposes, a uniaxial load cell was placed between the actuated "driver" carriage and a "follower" plate-fixed carriage. The forces measured from this load cell were compared against the summation of the horizontal force components from the X and Z axes of the six axis load cell, Figure 2-11. The button style load cell shown in Figure 2-13 interacted with the black bracket shown in Figure 2-6 and Figure 2-7.

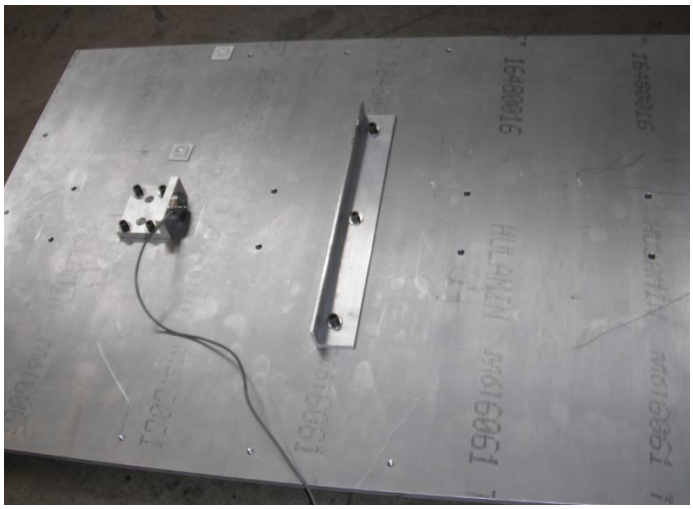

Figure 2-13: Omega 500 lb. button style excavation load cell. The load cell is mounted on the bottom side of the soil bin plate and contacts the driver carriage, reference Figure 2-6.

2.2.1.7.3 Piezo Load Cell

The actual percussive force applied to the scoop during excavation was a function of applied impact energy and soil stiffness. The piezo load cell was used to capture and record the dynamic response of the soil due to applied impact energy. Owing to the high sampling rate required to properly read the piezo load cell signal, the data acquisition was performed with an oscilloscope.

The actual measured impact force wasn't able to be perfectly controlled due to variability in soil stiffness. Consequently, the magnitude of the percussive impact energy rather than percussive force was used as the user–defined variable.

Figure 2-14: Piezo load cell mounted between the excavation scoop and the impact rod.

2.2.1.7.4 Uniaxial Penetrometer Load Cell

The purpose of the uniaxial penetrometer load cell was to evaluate the pressure index of the soil. This was evaluated by dividing the measured pressure from the cone penetrometers cross sectional area by depth below the soil surface. More details regarding this procedure are given in Section 2.4.1.

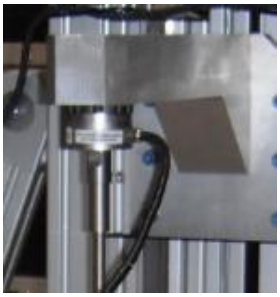

Figure 2-15: Penetrometer load cell (Omega 300 lb. Uniaxial Load Cell).

2.2.1.8 Brief description of the Penetrometer

A cone penetrometer is a common in situ measurement tool used for geotechnical study. It measures the insertion resistance of soil as a cone tip is driven vertically through the soil at a constant rate. By measuring the force resistance and the cross sectional area of the cone the user is able to obtain an idea of the amount of pressure that the soil exerts upon the cone face as the cone is inserted deeper and deeper. This measurement is called the pressure index. The pressure index is used to determine the compaction of the soil by using a reference chart. This process was used in this research to determine the relative density of every soil sample prior to each excavation test. More details are given in Section 2.4.

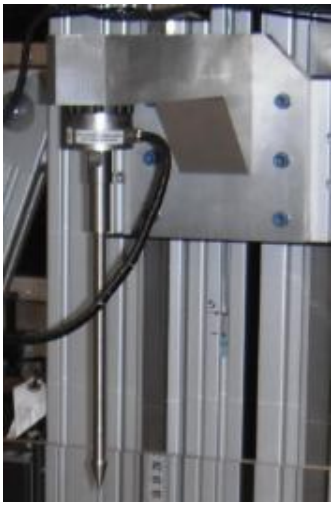

Figure 2-16: Cone Penetrometer (30 degree angle and 12.3 mm cone diameter).

2.2.1.9 Data Acquisition System

A data acquisition and control module were used to convert and record the different analog signals from the load cells, as well as control the actuation of the different motors. The motors and uniaxial load sensors communicated to the computer through a C++ code written by Honeybee Robotics. To accommodate a higher sampling rate, the six axes load cell and piezo load cell communicated with the computer through separate digital signals provided by ATI software and an oscilloscope, respectively. Details regarding the graphical user interface and user controls can be found in the Appendix, Section 9.1.2.

Figure 2-17: Data acquisition system: Honeybee Robotics control module, ATI data acquisition software, and oscilloscope.

2.3 The Percussive Mechanism

The most critical part of percussive excavation experimentation was the percussive mechanism itself. The percussive mechanism was a standalone device designed and fabricated at Honeybee Robotics. The mechanism is a complete and separate unit which is rigidly fixed to the digging axis carriage. Figure 2-11 and Figure 2-12 show this arrangement.

2.3.1 The Actuation of the Percussive Mechanism

The purpose of the percussive mechanism was to deliver periodic impact energy to the excavation scoop. The periodicity of this applied energy was accomplished through a cam-spring mechanism. An externally-mounted motor attached to the percussive unit spun an internal gear train which drove the cam. The profile on the cam was a spiral winding from the bottom of the cam up to the top of the cam. The spiral wrapped completely around the circumference traversing the vertical axis from bottom to top. At the top of the cam there was a discontinuity in the profile which caused the follower to temporarily disengage. The follower, which would build up spring and gravitational potential energy as it was displaced by the cam, would convert its potential energy into kinetic energy and deliver an impact to the impact rod connected to the scoop. After the energy was transferred the cam would engage the follower once again to repeat the process. Given the discontinuity in the cams profile it was labeled a ski-jump cam. The frequency of the applied impact was determined by the supplied current to the drive motor. The magnitude of the impact energy was determined by the mechanical spring stiffness. The design of the mechanism allowed the user to easily switch the internal spring. A diagram of the mechanism is provided in Figure 2-18.

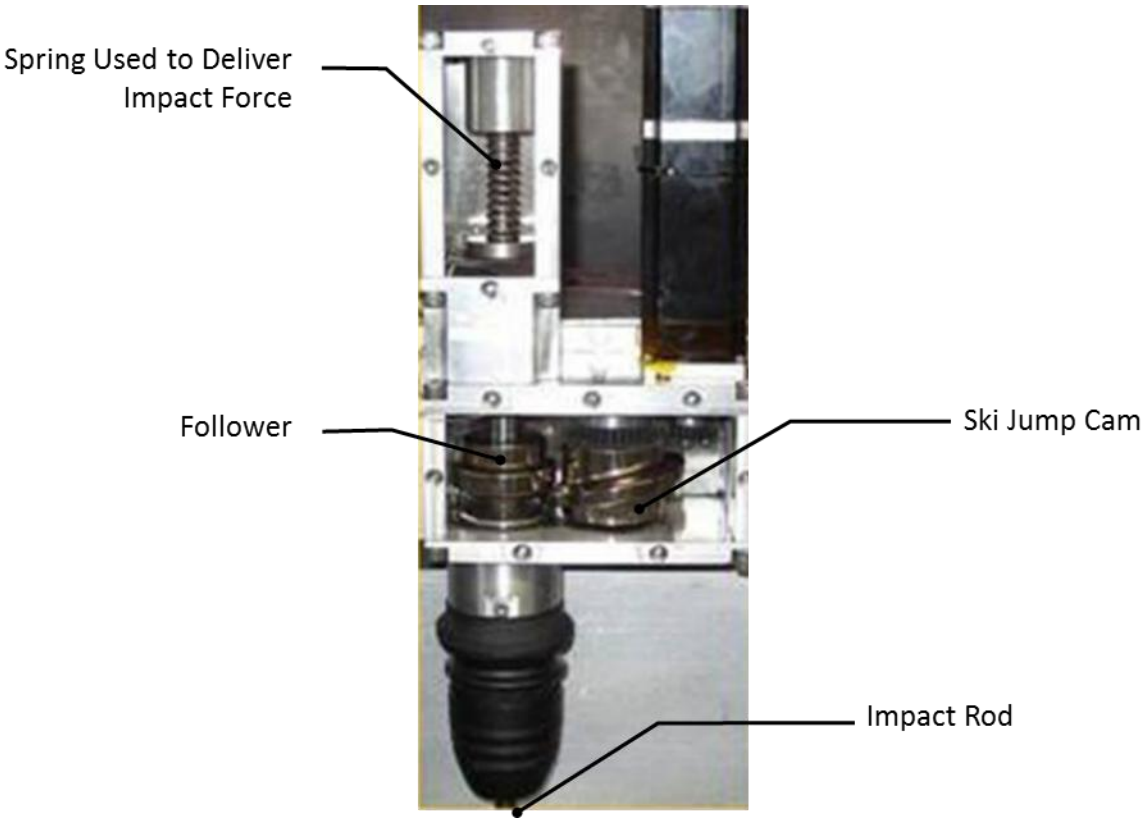

Figure 2-18: Drive mechanism of the percussive unit.

The impact rod was attached to the follower on the bottom side and was constrained to only move axially. The piezo load cell was fixed to the top of the excavation scoop and was the interface through which the impact was delivered to the scoop. To effectively deliver the impact energy to the soil the excavation scoop was mounted to the percussive unit through a slider joint. The impact rod would only interact with the scoop if the soil provided a preload force. The preload was accomplished by driving the scoop into the soil. A stop was used to prevent the scoop from sliding off the slider joint. Figure 2-19 and Figure 2-20 provide a graphic representation of the scoop when it's been preloaded and just after the impact energy has been delivered to the scoop.

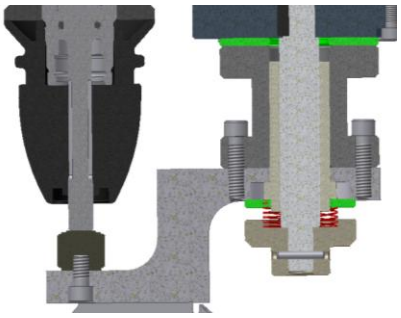

Figure 2-19: Scoop in pre-loaded state.

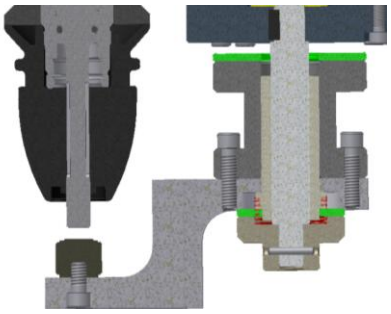

Figure 2-20: Scoop in full extension after applied percussive impact.

2.4 Testing Procedure

2.4.1 Penetrometer

Soil is a complex aggregate of particles which might be homogenous or inhomogeneous, anywhere in a spectrum of saturated to dry, and can be compacted in several different arrangements. The permutations that exist for simply defining a soil state are almost limitless. Fortunately, in this work two of those variables were fixed. The soil in this research was assumed to be homogeneous throughout and all tests were run in atmospheric dry conditions. What remained as a deterministic variable was the soil's compaction.

In order to evaluate the density of each prepared soil sample a cone penetrometer test was used. Each cone penetrometer test provided a measured resistance in terms of soil penetration. This resistance to penetration gradient was equated to a state of relative density through a distinct and unique calibration curve.

2.4.1.1 Density Relationship to Pressure Gradient

To establish a unique calibration curve for JSC 1a a series of different cone penetrometer tests were conducted in a variety of different soil compaction states. For each test a prescribed amount of soil mass was added to the soil bin in a controlled manner. The soil bin was then vibrated, by means of the external vibrator, until the soil level achieved a desired volume. Following, a penetrometer test was run at 1 cm/s. This test returned a pressure/depth gradient value known as the pressure index. The pressure index value was then plotted on a graph with its associated soil density value. The density was calculated by the measured mass and volume of the soil in the soil bin. After a series of similar tests a theoretical regression curve was plotted defining a relationship between the density of JCS 1a and pressure index. An example of a cone penetrometer test for loose soil is shown in Figure 2-21. A graph providing the tested pressure index point along with the regression curve is given in Figure 2-22.

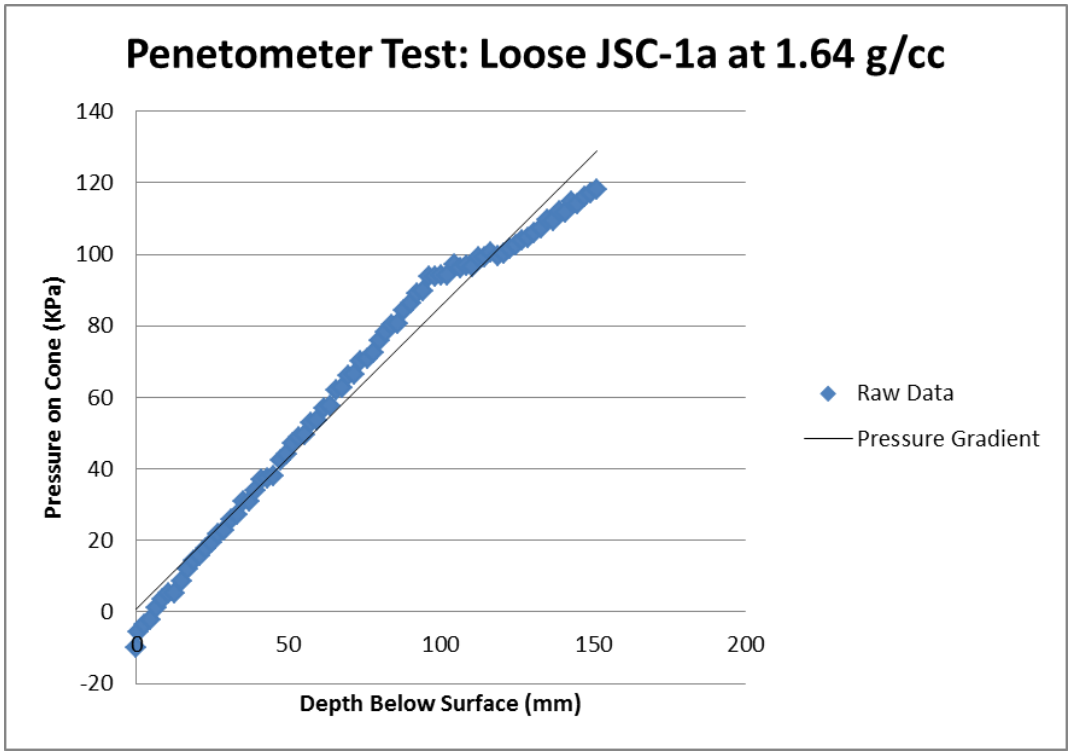

Figure 2-21: Penetrometer test for loose soil.

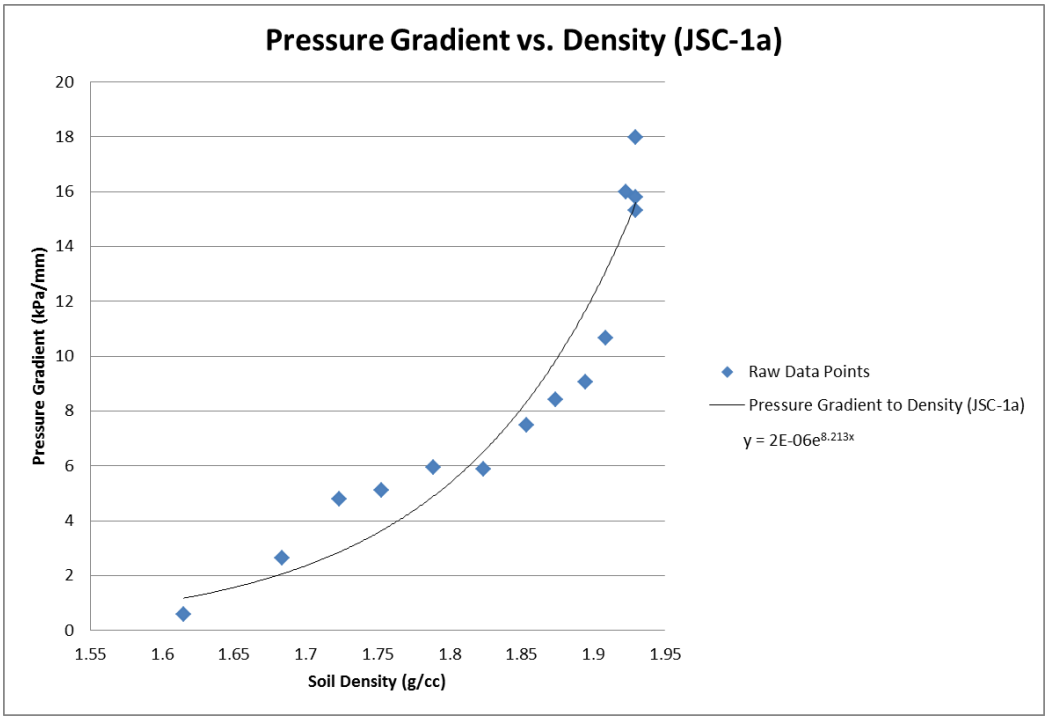

Figure 2-22: Test data from penetrometer tests showing relation of pressure gradient to soil density for JSC 1a.

2.4.1.1.1 Relative Destiny

Every soil is made up of different particle sizes and has a different grain size distribution. Because of this, the measured density of a soil doesn't provide perspective on its actual state of compaction. It is often common to see soil compaction referred to as a relative density value. The relative density is a value from 0% to 100 % which signifies how close the particular soil is to its minimum possible density, 0 %, and to its maximum possible density, 100 %. Following the nomenclature from the Lunar Sourcebook [Carrier 1991] the relative density in this paper is referred to as DR. The values used for the minimum and maximum possible density of JSC 1a were taken from [Alshibli 2009] and were 1.556 g/cc and 2.016 g/cc respectively. Figure 2-23 was constructed to show the same relationship as in Figure 2-22 but in terms of relative density.

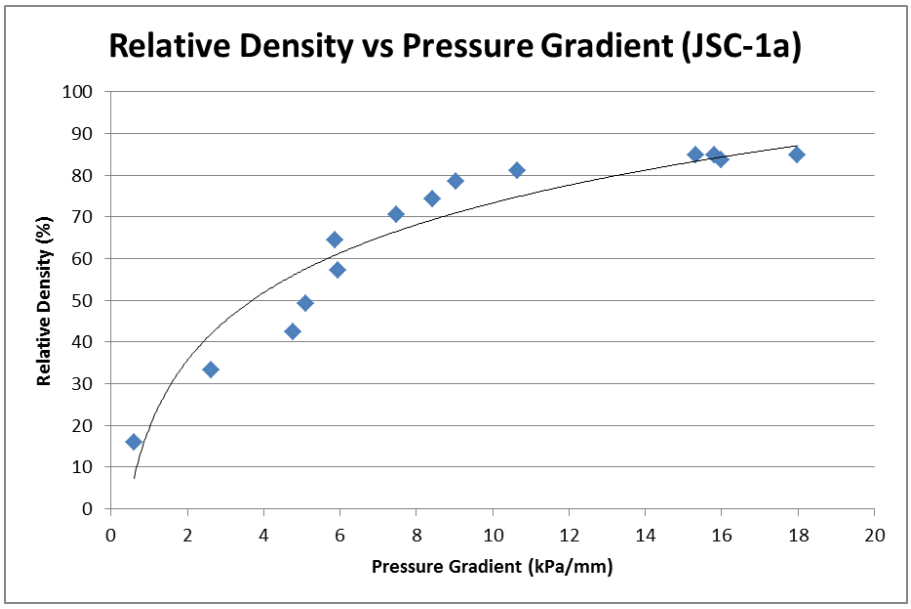

Figure 2-23: Relative Density verses Pressure Gradient for JSC-1a.

Given that a penetrometer test can only give an approximation of a soil's true relative density, oftentimes a range of relative density percentages constitute a descriptive soil compaction state. In the Lunar Sourcebook [Carrier 1991], 5 different soil sates are described based on different ranges of measured relative densities.

Relative Density (%)	Description
0 – 15	Very loose
15 – 35	Loose
35 – 65	Medium
65 – 85	Dense
85 – 100	Very dense

Figure 2-24: Soil compaction states with respect to measured relative density.

For this work only three different states were considered: Low Relative Density (Low DR), Medium Relative Density (Medium DR), and High Relative Density (High DR). These states were determined based on whether the measured relative density from a penetrometer test fell within a specific range. If the measured relative density did not fall in the appropriate range the soil was either removed, replaced, and re-vibrated or was left in its measured state and vibrated for a longer time.

Relative Density (%)	Description
5-20%	Low DR
45-60%	Medium DR
85-99%	High DR

Figure 2-25: Description of soil states tested in this research based on relative density.

2.4.2 Testing Methodology

A series of different tests were run in this work. The tests and the results are given in Chapter 3. Details about how specific tests were run in terms of the graphical user-interface can be found in the appendix, Section 9.1.3. Here, a brief outline is given representing the general procedure that was used, were specific tasks are only referred to as steps.

- Power on all instruments
- Home all axes
- Add soil to soil bin
- Vibrate the soil bin for a specific time to reach desired state of soil compaction
- Test soil using a penetrometer test
    - If soil is too loose vibrate again for a desired amount of time
    - If soil is too compact remove from soil bin, replace soil in soil bin in loosest state, vibrate soil for a shorter period of time

- Once penetrometer test confirms desired relative density move soil bin underneath excavation scoop
- Set the desired excavation variables and run an excavation test
- Record and analyze data

3 Empirical Testing

3.1 Introduction:

The basis of this research comes from past work in which researchers discovered that disrupting a soil with vibrations caused a reduction in its inherent strength [Sulatisky 1972]][Szabo 1998][Ermolaev 1968][Balyshkin 1966][Barkan 1962][Craft 2009][Zacny 2009b]. Such an observation has profound implications. Soil integrity and strength are critical factors in the engineering design process. When those values become altered, even in an advantageous way, it is important to understand the cause and nature of that alteration.

By taking a closer look at the factors dealing with percussive excavation greater insight can be garnered as to what mechanisms enable this reduction of soil strength. With this objective in mind a series of empirical tests were undertaken.

125 tests, in total, were conducted. Within each of those tests 6 different variables were monitored and controlled. The selection of those variables was based upon environmental factors, as well as those factors which are generally under an operator's control when performing a percussive excavation task. Those 6 variables include: frequency of percussion, percussive impact energy, the attack angle of excavation, excavation speed, excavation depth, and soil relative density.

3.2 Methodology

3.2.1 Force Data Collection

The measured forces from the six axis load cell were used to determine how each variable altered the soil's shear strength. The six axis load cell was mounted between the support plate of the excavation scoop head and the test stand's rigid fixture. Figure 3-1 and Figure 3-2 show the location of the load cell as well as a simplistic free body diagram outlining the forces measured by the load cell.

Figure 3-1: Six axis load cell used to collect excavation forces for data analysis.

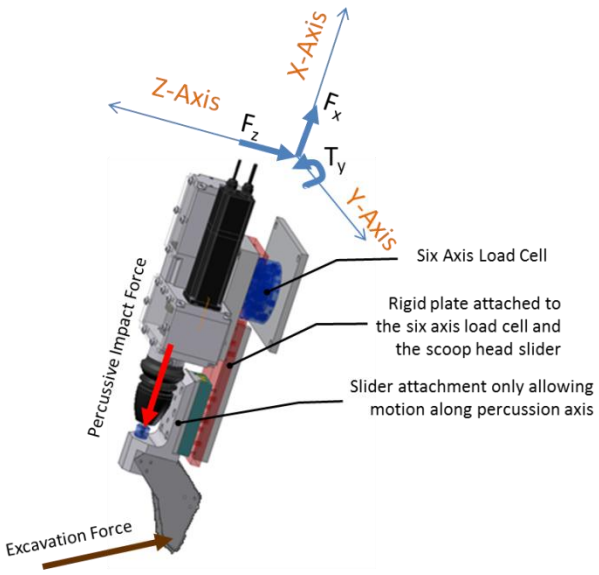

Figure 3-2: Free body diagram of percussive head.

3.2.2 Data Filtering

The very definition of percussive excavation involves periodic and dramatic force impacts. On account of these impacts, the data collected by the six axis load cell needed to be "cleaned". The load cell sampled at a rate of 62 Hz. The percussive periodic impacts ranged from 4.16 Hz to 29.16 Hz (250 BPM – 1750 BPM). In order to eliminate noise associated with impact blows the data points were filtered using a moving average. Each point collected was averaged with the 10 subsequent data points. The effect of this moving average is seen in Figure 3-3 and Figure 3-4.

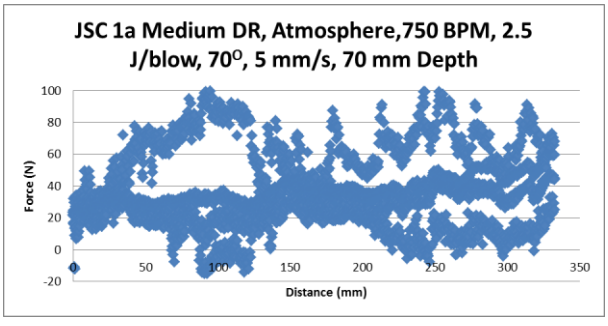

Figure 3-3: Original data collected from the six axis load cell along the Z-axis.

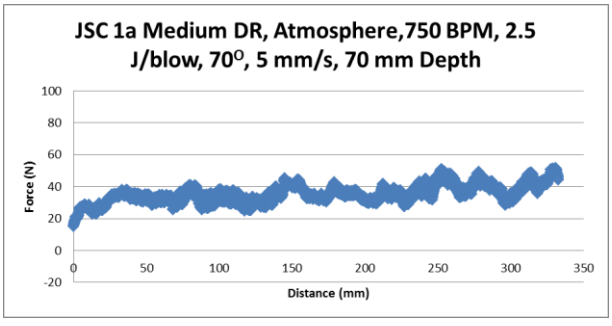

Figure 3-4: Cleaned data from the six axis load cell along the Z-axis.

After the moving average was applied there was still residual noise, but to a much less severe degree. Further filtering, or a larger moving average, wasn't applied in order to preserve the

integrity of the data and maintain acute soil behavior. Discussed in Section 3.4.1, a broader moving average regime was employed as part of a statistical analysis.

3.2.3 Composite Force Data

A vector summation was used to measure the magnitude of the total excavation force. Referencing Figure 3-2, the square root of the summation of the squares of measured forces along the X and Z axes yielded the total force magnitude. This force constituted the system's output response and represented the total excavation reaction force.

To best analyze the data, the data products were given in terms of excavation distance. Each excavation test lasted between 300-350 mm unless the load cell saturated due to extreme forces.

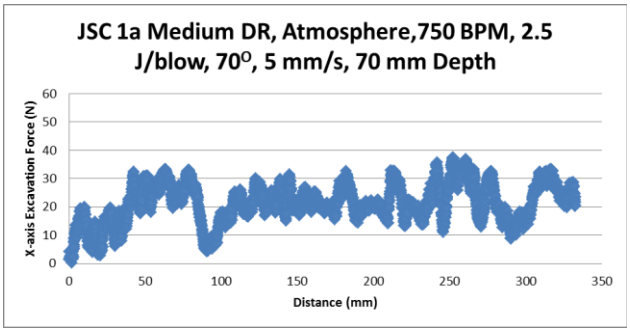

Figure 3-5: X-Axis force component measured by six-axis load cell.

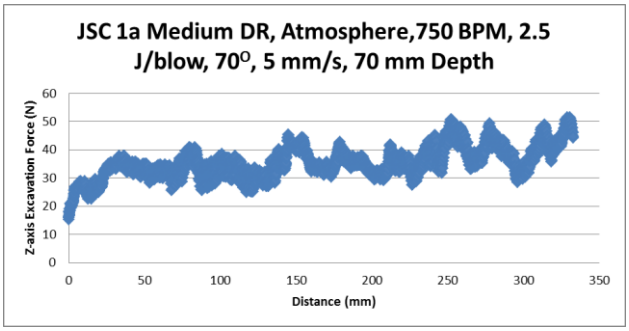

Figure 3-6: Z-Axis force component measured by six axis load cell.

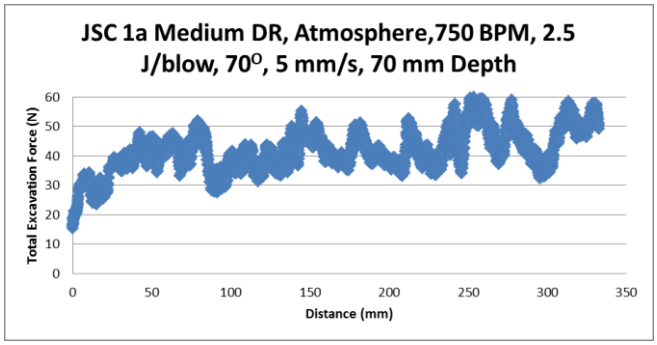

Figure 3-7: The total measured excavation force measured by the six axis load cell based on X and Z axis components.

3.2.4 Relative Density

Three different soil states were tested. Those three states were characterized by the pressure gradient as measured from a cone penetrometer test. Referencing Figure 3-8, a soil was

classified as either low, medium, or high relative density based on the criteria given in Table 1. More details regarding the formation of Figure 3-8, Table 1 and the penetrometer test can be found in Section 2.4.

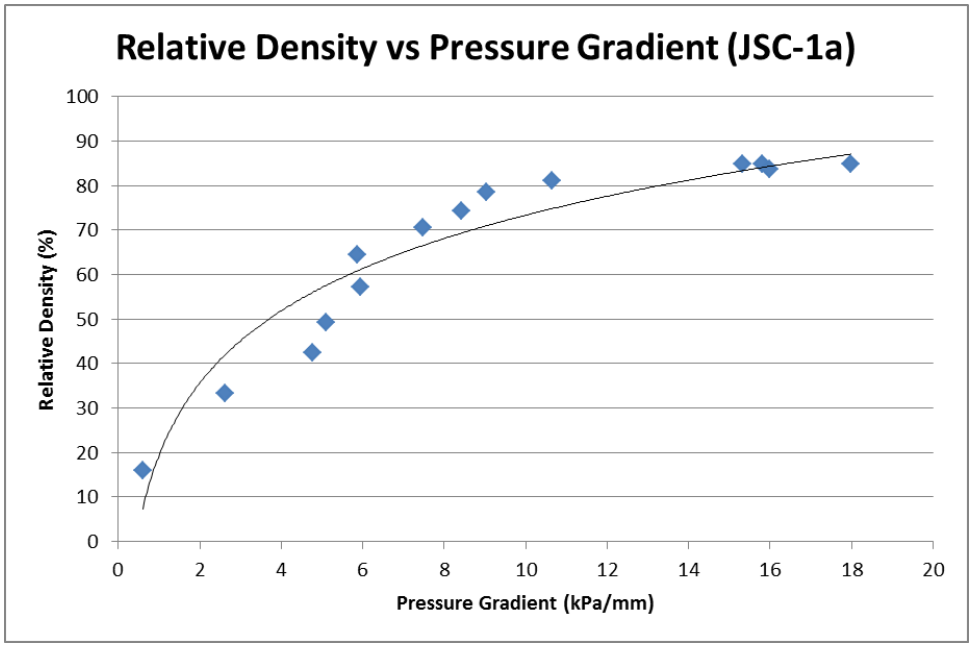

Figure 3-8: Relative Density verses Pressure Gradient for JSC-1a.

Relative Density (%)	Description
5-20%	Low DR
45-60%	Medium DR
85-99%	High DR

Table 1: Classification of Low, Medium, and High relative density soil used for testing

3.2.5 Near Wall Effects

A critical part of acquiring research data is making sure that the experimental data that one gathers specifically relates to the variables that are in question. In other words, consideration was taken to minimize any extraneous force factors.

This research is meant to be extrapolated for excavation in an infinite boundary environment. In order to best replicate such an environment, while still satisfying the dimensional constraints of the vacuum chamber, near wall effects were addressed. The effects of each of the walls outlined in Figure 3-9 were taken into account.

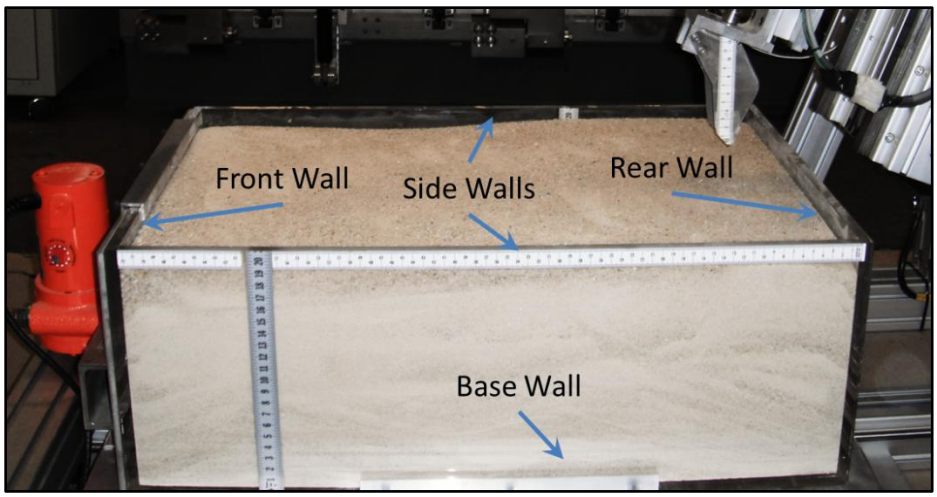

Figure 3-9: Nomenclature for soil bin walls.

3.2.5.1 Side Walls

To account for any interaction from sidewall-effects the excavation scoop was inserted into the middle of the soil bin, relative to the side walls. In addition, the soil bin was constructed so that the distance between the side walls and the excavation scoop was approximately 10 times the width of the scoop. More specifically, the width of the scoop measured 50 mm, while the width of the soil bin was 500 mm.

3.2.5.2 Base Wall

The soil bin was filled to a height of approximately 270 mm with soil (The vertical ruler on Figure 3-9 is in increments of ½ inches). The maximum depth the excavation scoop achieved during testing was 70 mm along the X-axis (Reference Figure 3-2: Free body diagram of percussive head. for the orientation of the X-axis). A depth of 70 mm along the X-axis translated to a vertical depth of 66 mm. A cone penetrometer test was performed prior to each excavation test. Those penetrometer tests were used to evaluate the soil's relative density. Each of those tests was done to a depth of 150 mm below the soil surface, over twice the depth that the excavation scoop was inserted. Each of those tests demonstrated a linear relationship between cone pressure and depth. From this observation it was inferred that the base wall had minimal to zero wall-effect. This conclusion was irrespective of the soil state. Figure 3-10 to Figure 3-12 show examples of penetrometer tests for low, medium, and high relative density soils, each of which manifests a constant linear relationship.

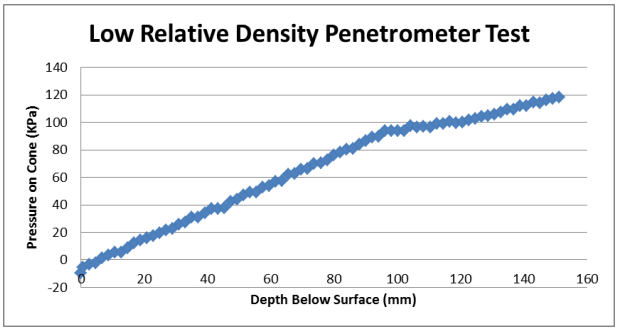

Figure 3-10: Penetrometer test showing the linear force gradient for low relative density, JSC-1a.

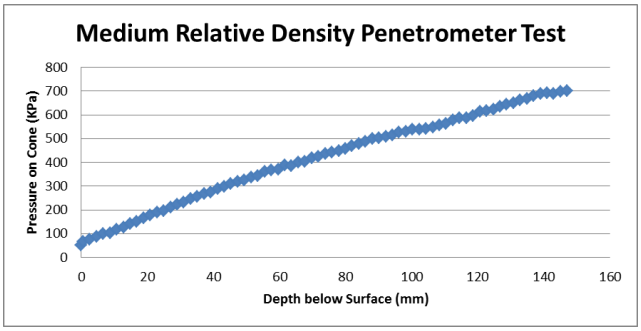

Figure 3-11: Penetrometer test showing the linear force gradient for medium relative density, JSC-1a.

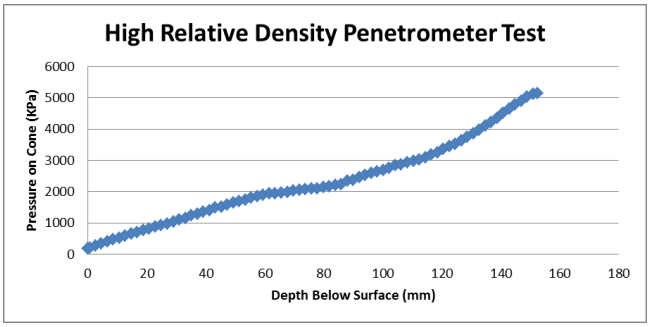

Figure 3-12: Penetrometer test showing the linear force gradient for high relative density, JSC-1a.

3.2.5.3 Front and Rear Wall

The soil bin measured approximately 750 mm from the front wall to the back wall. In an effort to negate any wall-effects from the front and rear wall the total excavation trench length for all the tests was between 300 to 350 mm. Every excavation test began with the scoop being introduced into the soil at a distance of 150 mm in front of the rear wall. Accordingly, all the excavation tests were stopped at least 250 mm behind the front wall. Although the soil was assumed to be homogeneous throughout the bin, it was concluded that the influence of the external vibrator was more strongly felt near the font wall and consequently created a slight gradient in soil density. In order to adjust for this incongruity, the excavation trench was shifted away from the exact middle of the soil bin towards the rear wall. The data that was obtained shows that, in general, for both static and percussive tests the wall effects associated with the front and rear wall were minimal.

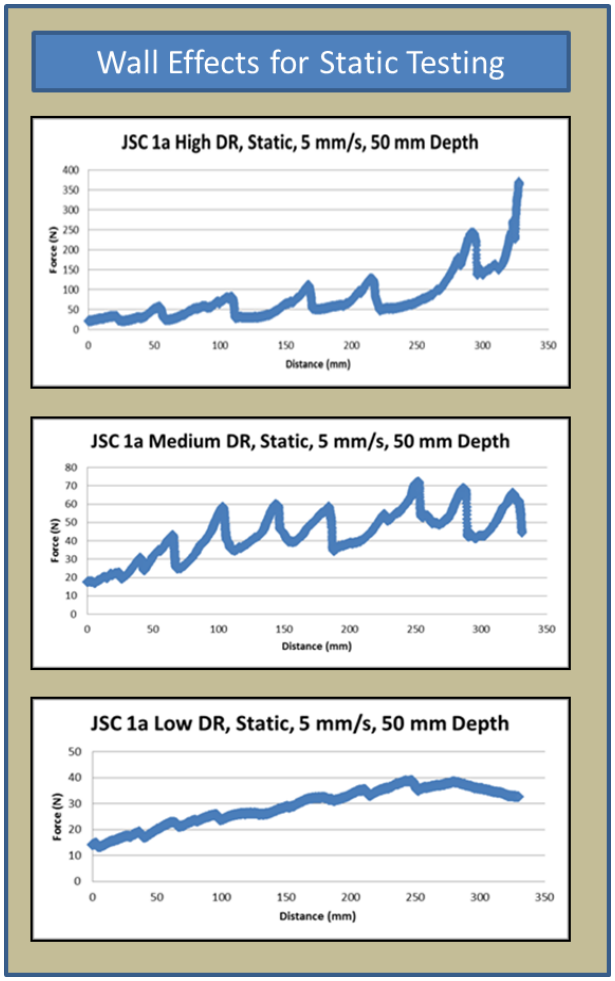

Figure 3-13: Tests conducted to determine near wall effects for static excavation in different soil densities.

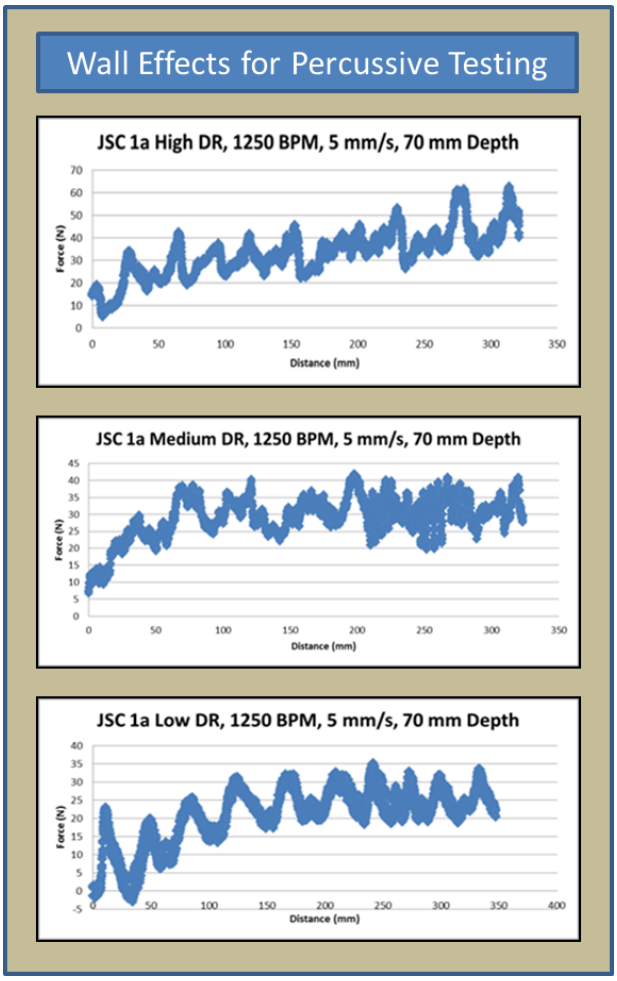

Figure 3-14: Tests conducted to determine near wall effects for percussive excavation in different soil densities.

In the case of static high relative density testing, there was an exponential increase in the excavation forces after the scoop had passed the 275 mm mark. Consequently the data pertaining to static tests in high relative density soils was truncated, and only the data points reflecting excavation from 0-275 mm were used.

3.2.5.4 Graphical representation reflecting near wall effects

To conclude Section 3.2.5, Figure 3-15 was created to illustrate the excavation volume with respect to the total volume of the soil bin.

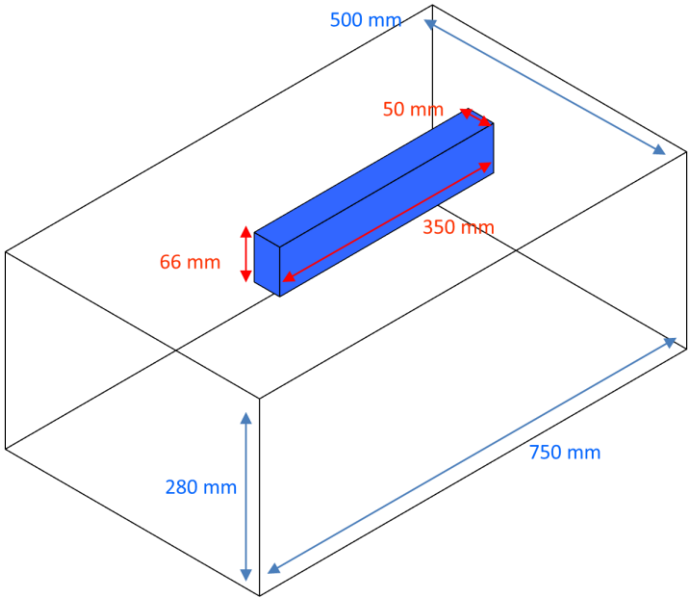

Figure 3-15: Graphical representation comparing the soil volume excavated (blue) to the volume of soil within the soil bin (clear).

3.3 Shear Planes: Cause and Effect

After looking at the all the data products, from the 125 different excavation tests, it was determined that there were two main force effects that took place during excavation. The first was a baseline draft force which remained more or less constant during excavation. The second were random force spikes which had exponential growths and sudden collapses. Although the specific time of their appearance during a particular test was unpredictable, there were key factors which lead to a higher probability of force spike formation. Figure 3-16 provides a good example of the two different force effects.

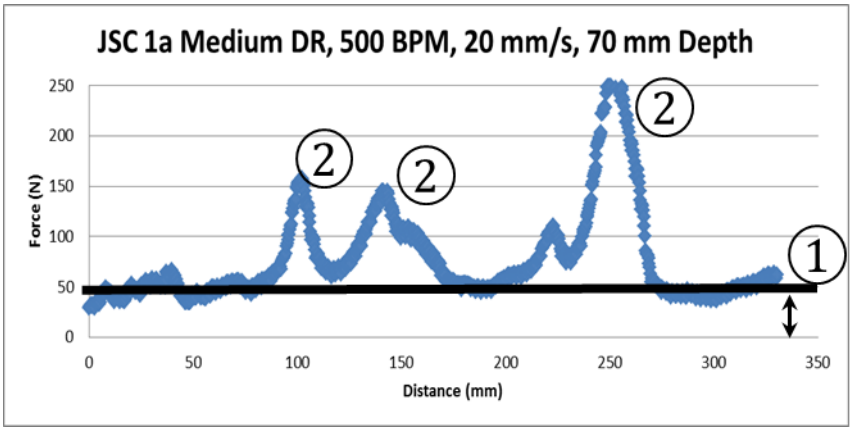

Figure 3-16: Test data showing 2 different force effects: 1 is the baseline draft force; 2 are random force spikes.

To better understand the cause and effect of each of these force contributions they were examined separately. First, in this section, the appearance of these random and periodic force spikes is discussed. Section 3.4 analyzes the magnitude of the baseline reaction force in the context of test variables by using results from an analysis of variance.

The force spikes were examined first in the context of different variables in static excavation; and second, in the context of those same variables in percussive excavation. It will be shown that the force spikes were physical manifestations of the soil's inability to continuously create shear failure planes on account of soil dilatancy.

3.3.1 Shear Failure Planes in Static Excavation

When an excavation scoop is introduced to soil, and then asked to move, the geometry of the scoop, the matrix arrangement of the soil particles, and the rate of displacement dictate how the soil will fail and develop shear planes. Shear planes are physical representations of soil failure and particle disengagement. They are formed by creating a boundary between displaced soil and fixed in situ soil.

When an excavation scoop is moved through the soil it continuously asks the soil particles in front of the scoop to disengage from the surrounding soil by creating a shear plane, and then move along the contour of the scoop. However, if the original set of particles in front of the scoop does not move or free itself then a different failure boundary has to be formed by creating a new shear plane geometry. The construction of a new shear plane geometry causes buildup of compression within the soil particles. This compression can be considered strain hardening in the soil. It is only after the potential energy has sufficiently developed and is high enough to overcome the interlocking forces that a new shear plane is formed. The buildup of this type of potential energy was the cause of the exponential force spikes in the experimental data.

During experiments, when a shear plane was formed the built up potential energy was released and the induced forces felt by the scoop dramatically dropped. Figure 3-17 and Figure 3-18 are still shots taken at the end of 2 different static excavation tests depicting the formation of periodic shear failure planes.

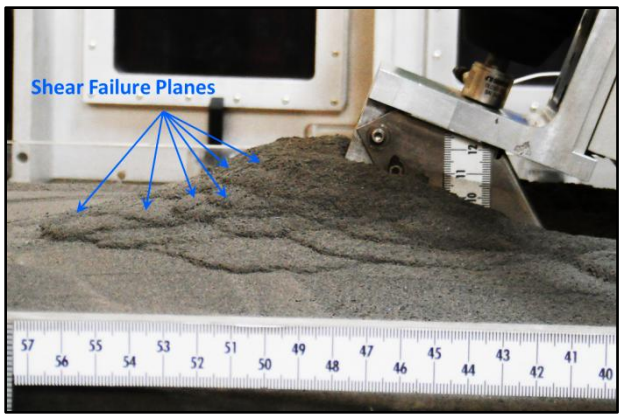

Figure 3-17: Side profile shot of discontinuous shear failure planes.

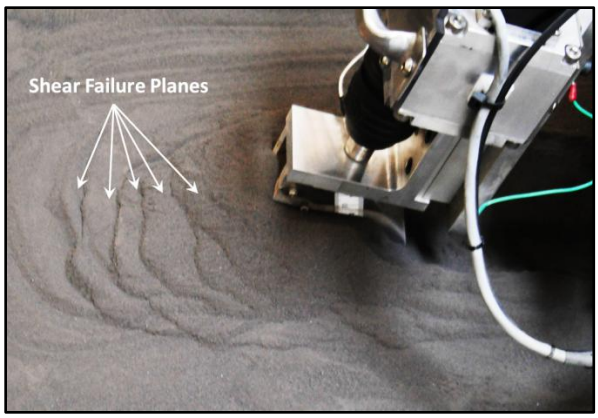

Figure 3-18: Top view of discontinuous shear failure planes formed while statically excavating in JSC-1a.

Given that a continuous formation of shear failure planes is desirable, the factors which opposed their formation were examined. Those factors were considered to be anything which inhibited the relative movement of soil particles between one another. The three main impeding factors were: an increase in relative density, a change in scoop geometry that required more soil to be displaced, and an increase in speed of excavation.

3.3.1.1 Shear Failure Planes and Relative Density

An increase in volume due to horizontal displacement is called soil dilatancy. Dilatancy is caused by forcing once particle over another. Figure 3-19: Physical model of soil dilatancy. The spheres represent soil particles in a compact, dense arrangement. As the force Pt is applied, the soil particles are required to move at an angle of θ [Chen 1975]. provides a graphic representation of a change in volume due to horizontal displacement.

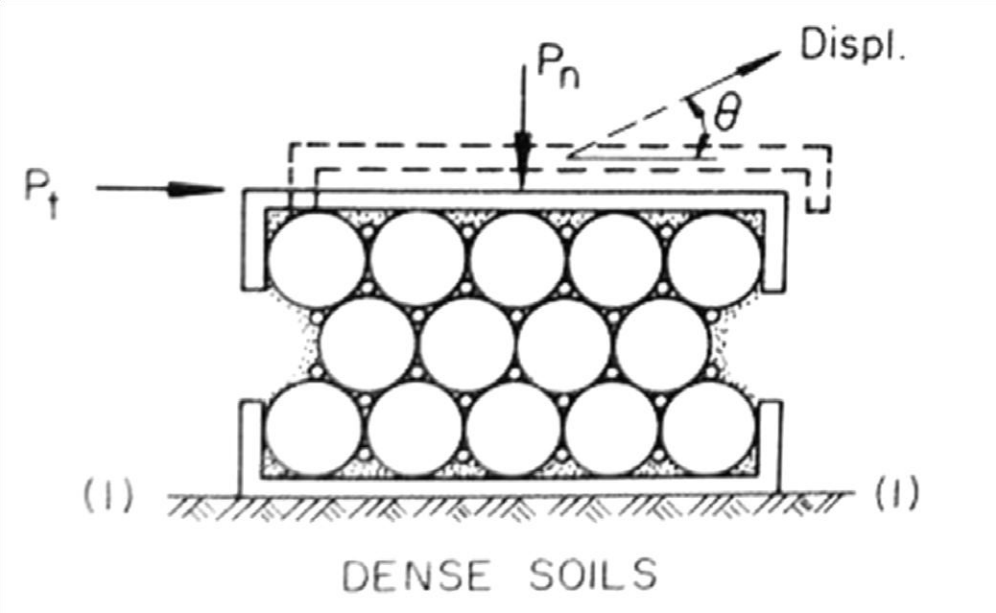

Figure 3-19: Physical model of soil dilatancy. The spheres represent soil particles in a compact, dense arrangement. As the force P_t is applied, the soil particles are required to move at an angle of θ [Chen 1975].

By changing a soil's relative density one is changing its intrinsic dilatancy, and the degree of particle-to-particle interaction within a volumetric area. An increase in dilatancy causes the protruding shape of a failure plane to be directed farther in front of an excavation implement. Figure 3-20 shows how the shape of a shear plane changes as a function of dilatancy.

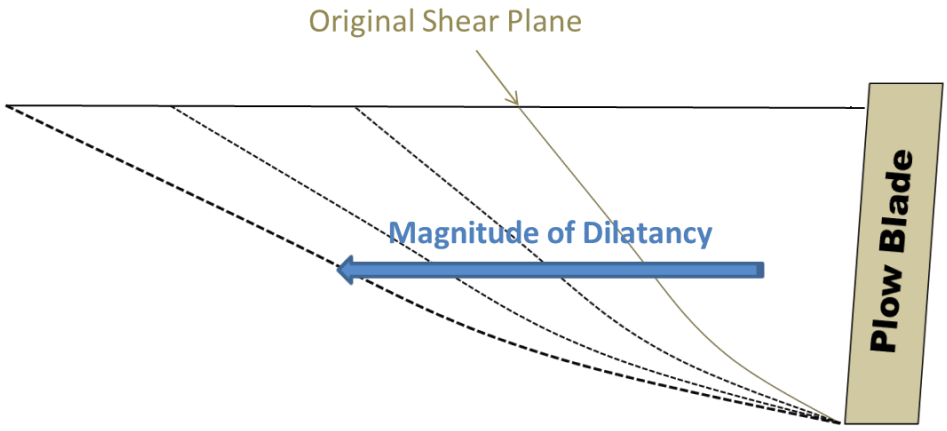

Figure 3-20: Change in shape of shear plane as a function of relative density, dilantacy.

Forcing the scoop to move a higher volume of soil and to overcome a larger number of particle-to-particle interactions impedes the development of shear planes during excavation. The result

is a higher frequency and increased magnitude of force spikes. This is easily seen by comparing the experimental results from three different soil types Low DR, Medium DR, and High DR.

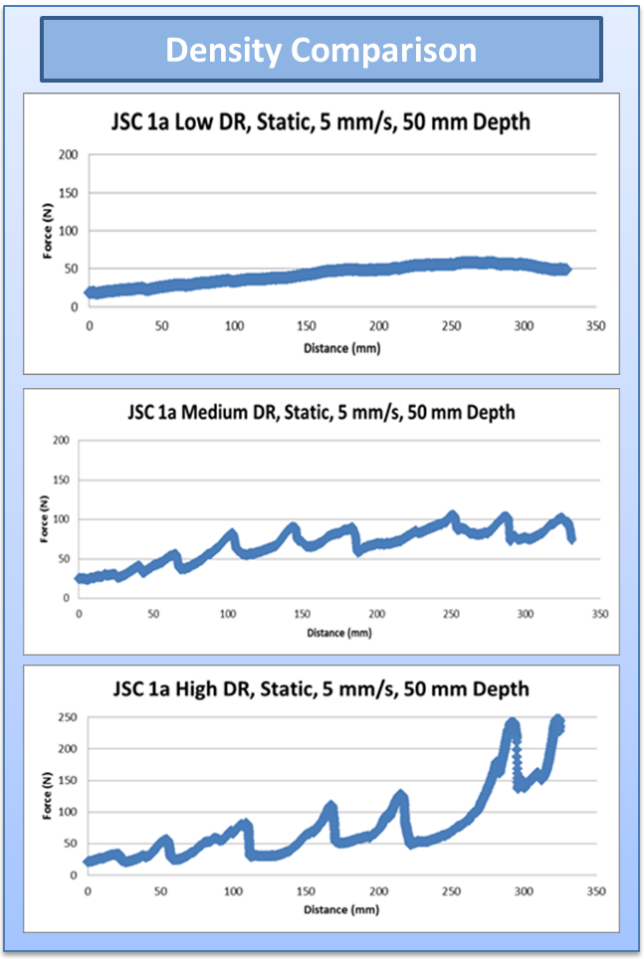

Figure 3-21: Comparison of progressive shear plane formation dependent on relative density of the soil.

3.3.1.2 Shear Failure Planes and Scoop Geometry.

Although changing the geometry of the excavation scoop doesn't change the volumetric density of particle-to-particle interactions, it does change the required shape of a shear plane. Simply by inserting the scoop deeper into the soil or changing the attack angle the associated shape of the boundary layer increases or decreases in surface area. Figure 3-22 depicts this change in boundary layer geometry. Figure 3-23 shows how a change in the development of the shear plane shape affected the creation of force spikes.

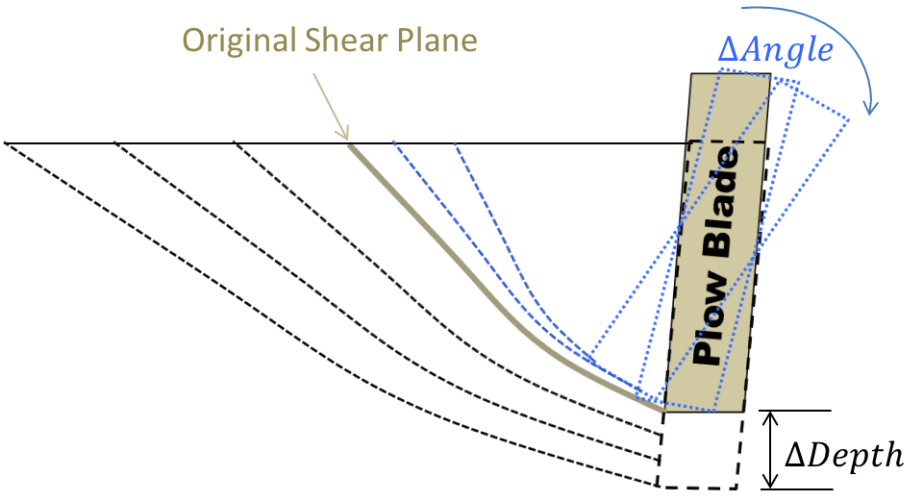

Figure 3-22: The change in shape of a shear plane due to geometry.

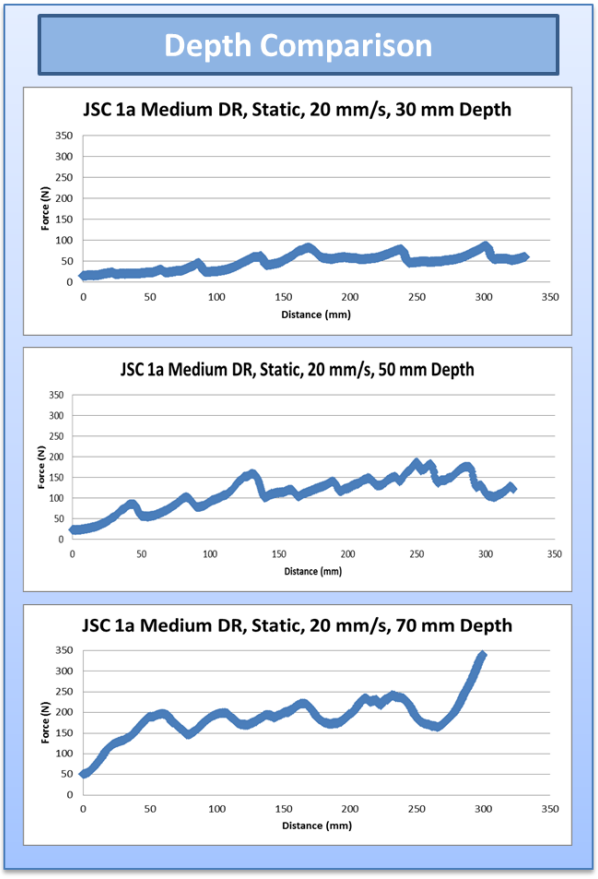

Figure 3-23: Comparison of progressive shear plane formation dependent on depth of the excavation scoop.

3.3.1.3 Shear Failure Planes and Excavation Speed

Although a change in excavation speed doesn't cause the intrinsic formation of a shear plane to change in shape it does require the particles to move relative to one another at a higher rate. Given that there is time dependency in the relative movement of particles, sometimes a boundary layer can't develop fast enough to create a shear failure plane. In essence, when one increases the excavation speed of an implement the volumetric rate of particle interaction is increased. The resulting geometric consequence in shear plane development is similar to increasing soil dilatancy, refer to Figure 3-20. Figure 3-24 demonstrates the experimental relationship found in shear plane development due to speed.

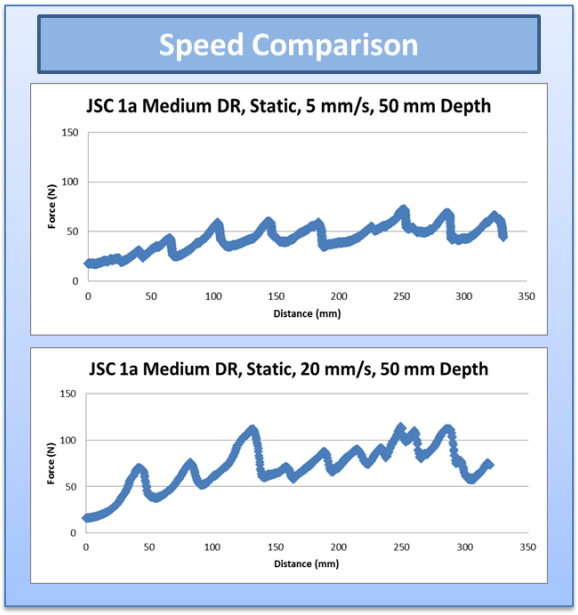

Figure 3-24: Comparison of shear plane formation dependent on the speed of the excavation scoop.

3.3.2 Shear Failure Planes and Percussion

The formation of shear failure planes is an interesting phenomenon. Their absence is a deleterious effect with respect to the minimization of excavation forces. Ideally, a soil would continuously create new shear failure planes as the scoop moved through it; similar to what is seen in the low relative density case of Figure 3-21.

When percussion was introduced into the excavation system the appearance of force spikes was removed as a function of impact frequency. Once an appropriate frequency was reached, for a specific set of excavation and soil parameters, the soil continuously failed in front of the scoop removing force effects coupled to dilatancy.

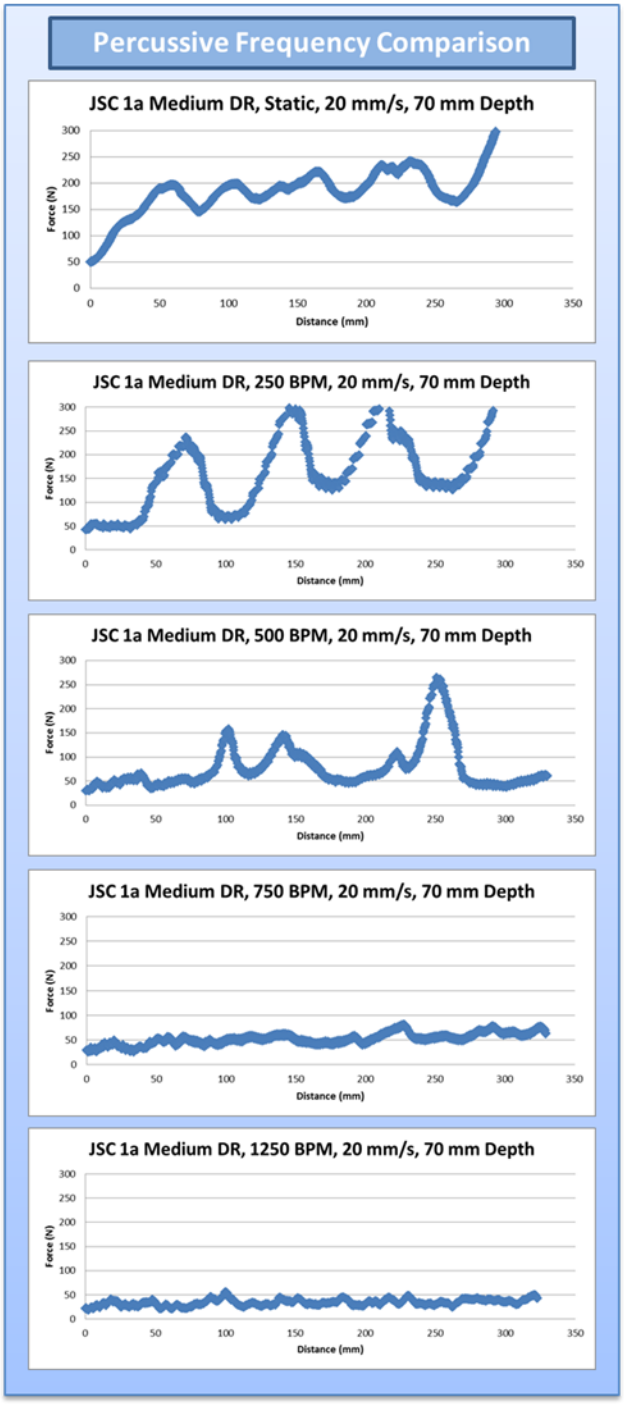

Figure 3-25: Progressive elimination of shear failure planes based on percussive frequency.

The elimination of the dilatancy effects along the shear plane was attributed to the dynamic response of the individual soil particles. Each applied percussive impact introduced an external source of mechanical energy to the control volume. This energy was dissipated within the failure volume and, more importantly, along the shear plane boundary layer. The energy was dissipated by causing relative movement and rearrangement of the soil particles. Given enough time between impact blows, the soil particles were able to settle, reconstitute, and create new dilatancy forces. However, as the time between each blow decreased, the individual particles were no longer able to dissipate all of the applied energy and reorganize themselves before a subsequent impact was applied. The result was that the soil particles along the shear plane found themselves in a continuously disorganized and uncompact state. Once an adequate frequency was achieved for a particular set of soil and excavation parameters, any increase in percussive frequency was superfluous. Starting from a static case, up to this "adequate frequency", there was a spectrum of dilatancy effects which progressively decreased as the frequency increased.

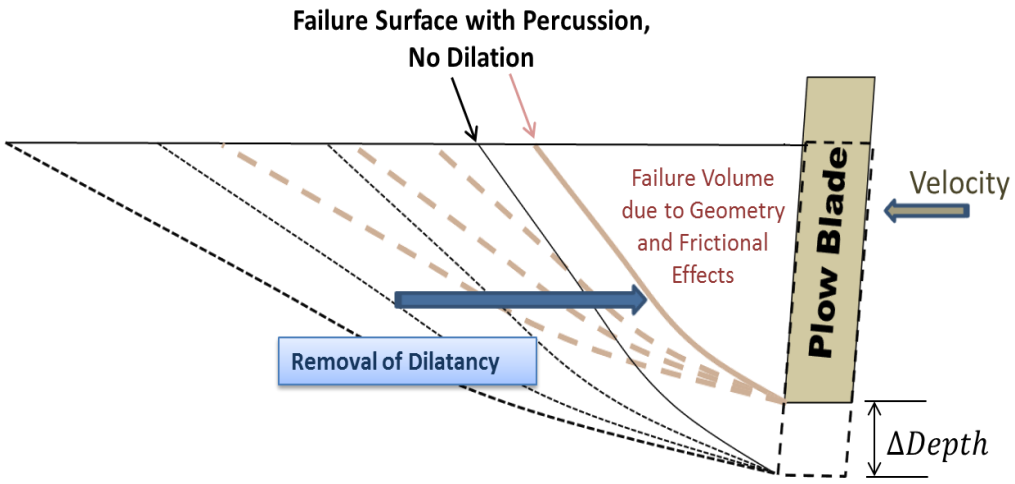

Figure 3-26: Shear failure plane formation through removal of dilatancy on account of percussion.

The appropriate frequency to achieve this free-flow state was not a constant; rather it was dependent on several factors. As was the case in static excavation, the effects of percussive excavation were closely tied to speed, depth, and relative density. Understanding the micro-environment that is produced along the failure boundary layer gives insight into how and why those factors played a role in the development of shear failure planes during percussion.

3.3.2.1 The Effect of Speed on Shear Failure Plane Formation in Percussion

The effectiveness of percussive excavation is contingent on excavation velocity because it determines the relative time for the soil particles to reconstitute themselves along the boundary layer between percussive impacts. At higher excavation speeds, and following a

percussion impact, the soil particles are forced into neighboring fixed particles in a shorter time then at lower excavation speeds. This decrease in time during the settling phase increases the probability of particle interlock and subsequent force spike formation. In order to combat this decrease in time, the duration of time between successive impacts has to be decreased by increasing the percussive frequency.

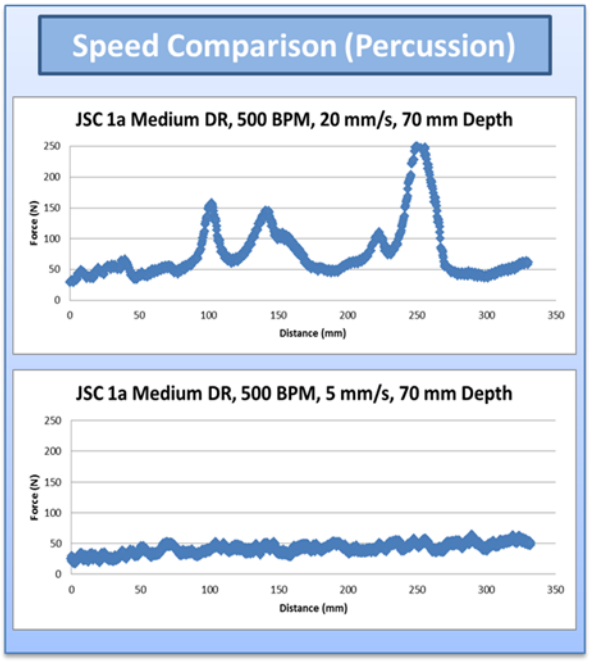

Figure 3-27: The dependence of shear plane formation based on speed. Speeds of 20 mm/s and 5 mm/s are compared with all other variables equal.

3.3.2.2 The Effect of Excavation Depth on Shear Failure Plane Formation in Percussion

The relevance of depth to shear plane formation is attributed to the direct dependence of boundary layer length to the depth of the excavation scoop. Shear plane development initiates at the tip of the excavation scoop and creates a log spiral type shape directed toward the soil surface. The exponential growth factor describing the shape of the log spiral curve is dependent upon the soil dilatnacy, but the starting point of that boundary layer is determined by the depth of the scoop.

A longer boundary layer results in 2 coinciding consequences which influence the effectiveness of percussion. Frist, the larger surface area translates into more particle interlocking. Second, the larger surface area decreases the percussive energy density along the boundary layer. The result, the percussive impact energy frequency has to be increased to apply a sufficient level of percussive power for particle disengagement over a larger area. This is physically shown in

Figure 3-28 which shows the same soil excavated at the same speed and percussed at the same frequency but with a change in depth.

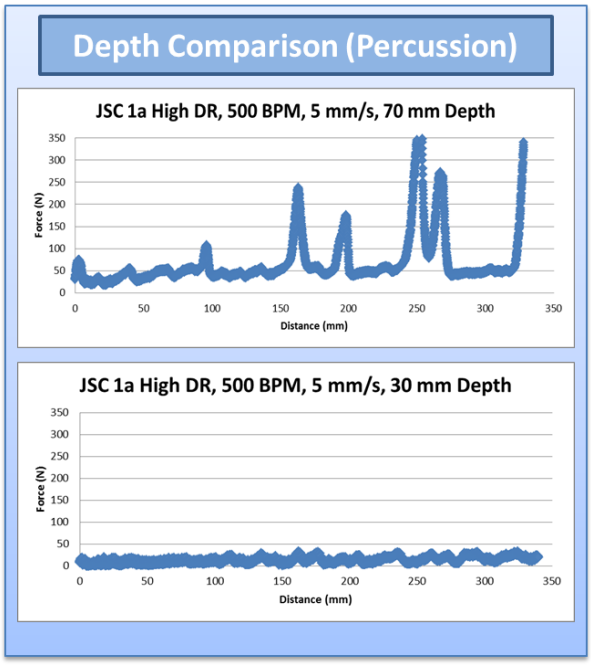

Figure 3-28: The dependence of shear plane formation based on depth for percussive excavation. Depths of 30 mm and 70 mm are compared with all other variables equal.

3.3.2.3 The Effect of Relative Soil Density on Shear Failure Plane Formation in Percussion

Percussion is able to remove the effects of dilatancy by disrupting particle interlocking forces. Given that an increase in relative density directly increases the magnitude of dilatancy forces, more percussive power is required to overcome the higher dilatancy forces in more compact soils. Figure 3-29 shows how the same frequency used to remove force spikes for low and medium relative density soils is not sufficient for a high relative density soil.

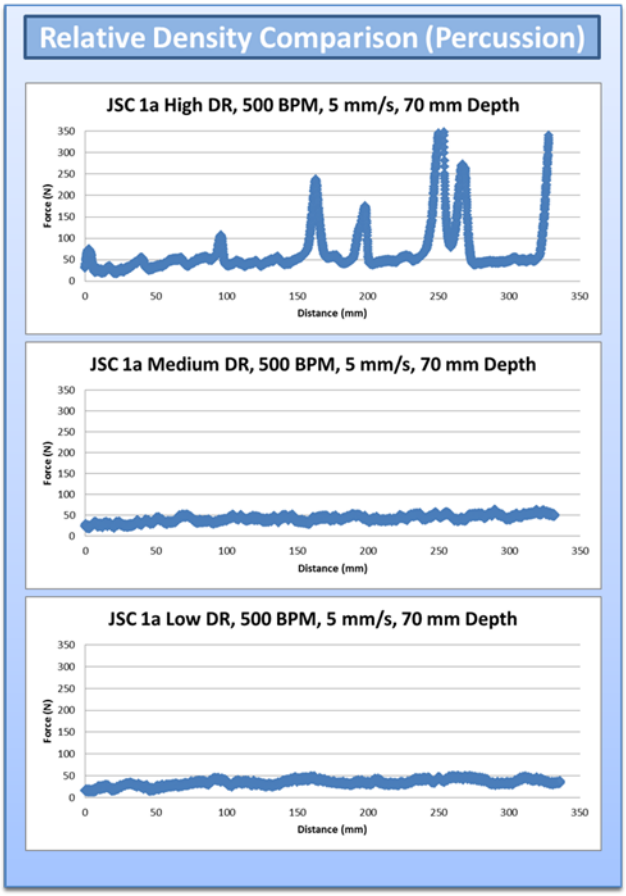

Figure 3-29: The dependence of shear plane formation based on relative soil density during 500 BPM percussive excavation.

3.3.3 Physical Depiction of Shear Failure Plane Dependency on Excavation Variables

Changes in the soil particle interactions along the boundary layer were not only shown in the excavation force data, but could be physically seen as well. Still shots of the excavation scoop profile taken during testing show the development and change in shape of the boundary layer due to the factors just discussed: percussive frequency, excavation speed, depth, and relative density. Based upon the shape that the displaced soil created on the soil surface an extrapolation can be made regarding the size and shape of the boundary layer underneath the soil surface.

The shape and the exponential growth of the log spiral failure plane underneath the soil is directly tied to the soil properties. In this work this change is taken into account by adjusting the internal friction angle. More details regarding the internal friction anlge and its correlation to percussion are discussed in the theoretical model in Chapter 4.

The following figures not only show a change in length along the failure surface in front of the excavation scoop, but in addition, they show a change in the continuous formation of shear

planes and the removal of force spikes. These changes are based on the smoothness of the displaced soil profile.

All the still shoots in the following figures were taken when the excavation scoop hit the 320 mm mark along the side of the soil bin. At approximately 170 mm into the trenching test. Unfortunately the development of shear planes was not directly proportional to the excavation distance. Consequently, at the time of the snapshot the shear planes might have been in the process of being formed and were not fully manifested on the soil surface. The tic marks on the scoop as well as the soil bin were in centimeter units. The perspective of each picture was adjusted to be close to equal, but for a more precise measurement a comparison of the tic marks should be used.

Figure 3-30: Graphical display of the geometric change in shape of displaced soil during excavation. An extrapolation can be made pertaining to the boundary layer shape beneath the surface.

Demonstrated in Figure 3-30 is the visual relationship between the displaced soil profile and both impact frequency and relative density.

In the vertical direction, as frequency is increased, the boundary layer shape changes and decreases in size. The leading edge of the boundary layer moves closer to the excavation scoop.

In addition, the continuous formation of shear failure planes increases dramatically between a static test and one at 500 BPM and similarly one at 1750 BPM.

Along the horizontal direction of Figure 3-30, where the relative density of the soil is increased, the projected length of the failure plane also increases. This is due to increased soil dilatancy. The continuous formation of shear planes is also contingent on dilatancy and requires higher frequencies in more compact soils.

Figure 3-31 and Figure 3-32 give a physical representation to the data presented in Figure 3-27 and Figure 3-28 pertaining to shear failure plane formation based on speed and depth.

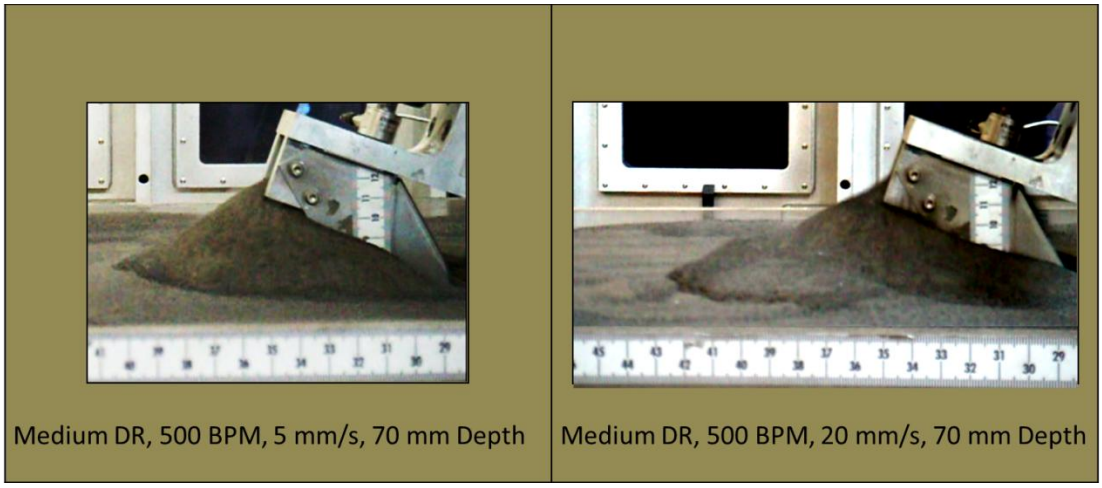

Figure 3-31: Physical display of the change in boundary layer based on the speed of percussive excavation.

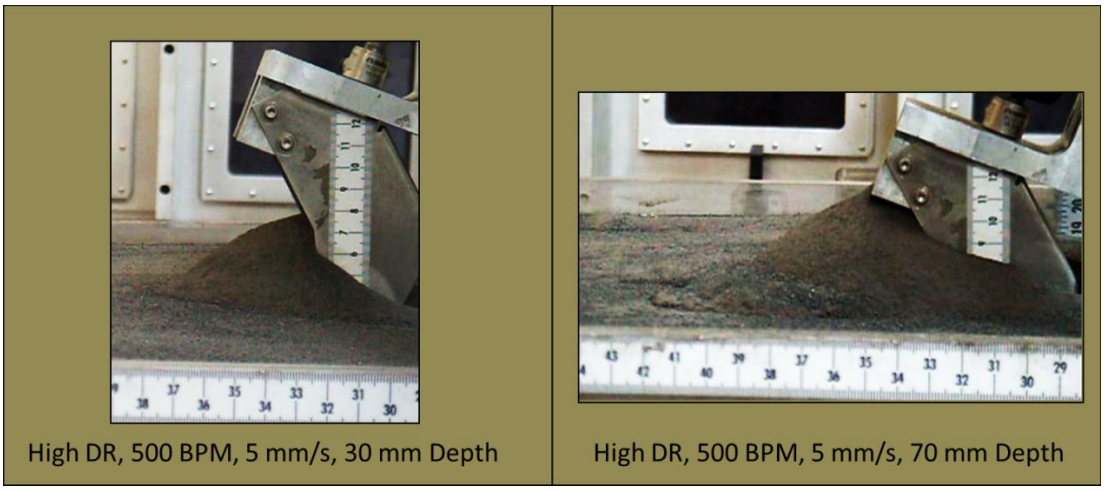

Figure 3-32: Physical display of the change in boundary layer based on the depth of percussive excavation.

3.4 Baseline Draft Force: Cause and Effect

Aside from force spikes due to the absence of shear plane formation, there is also an underlying baseline draft force associated with excavation. To better understanding how this force relates to different excavation variables the test data was filtered and then analyzed with an analysis of variance statistical test.

3.4.1 Formatting the Test Data

Due to the appearance of force spikes in the excavation test data it was difficult to analyze the baseline draft force. If a statistical analysis were to be run on the data sets in their original state, the results would be too greatly skewed by any appearance of a force spike. In order to properly analyze how different excavation variables affect the baseline force, a similar averaging regime to that discussed in Section 3.2.2 was used but with a much larger moving average data set. The moving average data set encompassed the data over a span of 80 mm (number of points varied depending on the speed of excavation). It was determined that this range allowed for the acute force spike effects to be averaged out while still maintaining as much data integrity as possible.

The effects of that moving average are shown in Figure 3-33 and Figure 3-34. Because each point was an average, representing a set of data points covering a distance of 80 mm, the formatted data graphs were truncated by 80 mm.

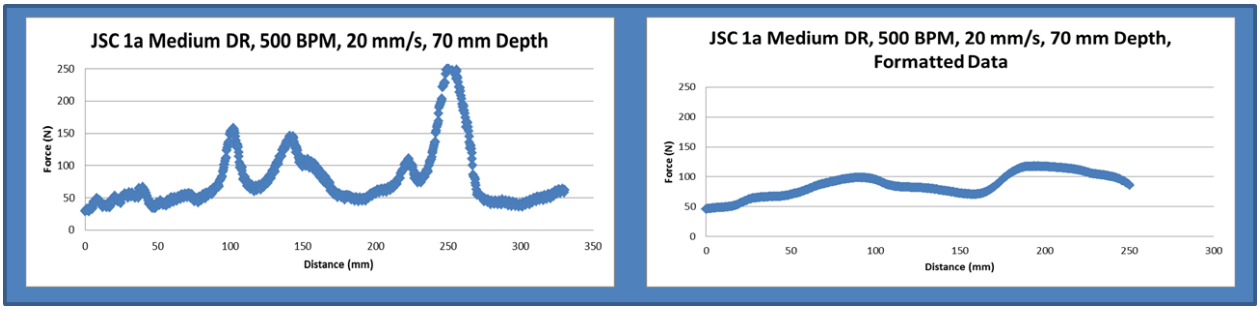

Figure 3-33: Data comparison showing the filtering effects of moving average. Data to the right is used for baseline force analysis.

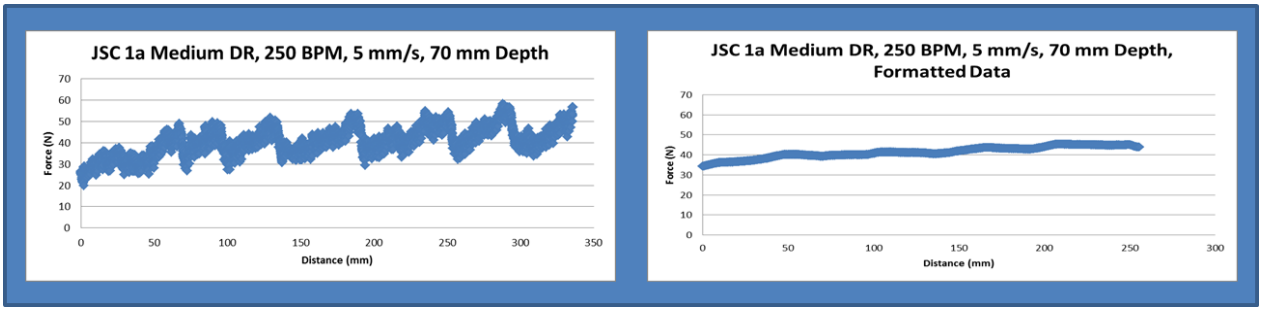

Figure 3-34: Data comparison showing the filtering effects of moving average. Data to the right is used for baseline force analysis.

3.4.2 Analysis of Variance Statistical Setup

In order to understand how each of the excavation variables influenced the overall excavation baseline force an analysis of variance was performed. The response variable was the maximum force value from the formatted data set. The selection of this response variable was meant to include the effects of surcharge while still mitigating the overall effects of the force spikes.

The variables tested and analyzed were: the percussive frequency, the percussive impact energy; the translational speed of excavation; the depth of excavation; the attack angle of excavation; the soil relative density; and the environmental pressure. The different values tested for each variable are given in Table 2. The respective values for the Low, Medium, and High Density were given in Table 1 but are provided again for the reader's convenience.

Excavation Variables	Units	Values Tested
Frequency of Percussion	Blows / Minute (BPM)	0, 250, 500, 750, 1000, 1250, 1750
Impact Energy of Percussion	Joules / Blow (J/Blow)	2.25, 2.5, 4.5
Attack Angle	Degrees (°)	70,90
Speed of Excavation	mm/s	5, 20
Depth of Excavation	mm	30, 70
Relative Soil Density	See Table 1	Low, Medium, High

Table 2: List of the excavation variables as well as the test values

Relative Density (%)	Description
5-20%	Low DR
45-60%	Medium DR
85-99%	High DR

Table 1: Classification of Low, Medium, and High relative density used in testing

Because of the wide breadth of variables tested, a complete and rigorous data set, inclusive of all possible permutations, was not conducted. Instead, the results from the 125 different tests were broken down into subsets of data. Each subset of data pertained to a specific excavation variable. Within each subset the test variable was assed at the values listed in Table 2 for different combinations of the remaining 5 variables. A complete breakdown of the different subsets of data and the response variable values for each test are given in the Appendix. This approach did not test all possibilities or provide a complete analysis. It did, however, create an initial framework upon which conclusions can be drawn.

In addition to analyzing the individual effects that each variable had on the excavation force, an analysis was also untaken to look at interaction effects. For those interaction tests the response term remained the same, the maximum force from the formatted data set. Since not all possible permutations of the different test variable sets were able to be tested some variable interactions were not able to be examined. It should be noted that the interactions which are given are only representative of the data sets shown in the Appendix.

3.4.3 Findings from the Analysis of Variance

To illustrate the influence of each of these variables the results from the analysis of variance test are given in the context of the total excavation force. The data points presented in the subsequent figures represent the mean value of the response variable for all tests within a data set which pertain to a specific test variable value. For example, in the case of Figure 3-35, each point represents the average response of 9 different tests within the frequency data set which pertain to a specific frequency value on the horizontal axis. Since the data points represent mean values over a wide variety of test permutations, and not specific test values, the graphs are simply meant to represent general trends.

One of the test variables considered in this study was spring energy. This was the impact energy that was delivered at each impact blow of the precursor. Aside from a select set of tests which examined the effects of a 2.25 J/blow and a 4.5 J/blow spring, all testing was done statically or with a 2.5 J/blow spring. Consequently, when looking at the interaction plot of different variables, the spring force only plots two values, 0 J/blow and 2.5 J/blow. Although this doesn't give specific insight into the relevance of the impact energy level to the different test variables, it does show something very interesting and important to this work: the general difference between static tests and percussive tests. The 2.5 J/blow data point represents the mean of all the percussive tests (aside from the frequency interaction plot in which all frequencies are plotted), regardless of frequency, and the 0 J/blow represents the mean of all the static tests. Because the 2.5 J/blow data point is an average of all the percussive tests is doesn't show the full possible reduction in force which is accomplished at the higher frequencies. However, it still shows there is a sizable force reduction and gives insight into how the other test variables might be more or less affected, based on percussion.

3.4.3.1 Excavation Variable effects on Total Excavation Force

3.4.3.1.1 Frequency verses Total Excavation Force

The most important variable for percussive excavation is frequency. [Craft 2009] and [Zacny 2009b] both report dramatic reductions in shear strength through percussive exaction; [Craft 2009] citing reductions of up to 80%. Unfortunately a correlation between frequency and force reduction was not provided in their research. Figure 3-35 shows that, indeed, such dramatic reductions are found in this work, once an appropriate frequency was applied. The relationship between excavation draft force and applied frequency is one of exponential decay. Table 3 shows the percent reduction in total excavation force, compared to the static excavation, for each tested frequency. It is inferred that there is an asymptotic limit to the force reduction. The value of that asymptotic limit is assumed to be dependent on residual particle-to-particle Coulomb surface friction.

By examining Figure 3-36 other interesting observations are made. Because percussion is able to remove the force effects of soil dilatancy by agitating the interlocking forces along the boundary layer the state of compaction almost becomes irrelative. This is easily seen through the continual digression of gradient magnitude between relative density and excavation force as the frequency is increased. By the time 1750 BPM is reached, there is little to no detectable difference in the average total force between low and high relative density soil. At these high frequencies particles no longer have to force themselves over one another but instead are free to have relative movement and are only hampered by the surface friction between them. Given that higher relative density soils have a higher density of particle surface interactions the residual asymptotic value that can be achieved in very loose soils is always slightly lower than that of initially very compact soils. This concept is explored further in Chapter 5, where the numeric model is constructed.

In comparing the “spring” term, which can be considered a comparison of all static tests verses all percussive tests, no new insight is gained. This comparison simply demonstrates the same relationship given in Figure 3-35, namely that through a progressive increase in applied frequency the total excavation force is reduced.

By referencing Figure 3-26 the comparison of depth and excavation force in terms of percussive frequency makes perfect sense. As the applied frequency is increased the developing shear plane is moved closer to the scoop and the amount of displaced mass is reduced. Because a change in geometry leads to an increase in boundary layer length there is an increase in excavation force as the scoop is inserted deeper into the soil. However, the application of percussion dramatically reduces the degree to which that change increases the excavation force.

The interaction between speed and frequency is an interesting one. The slope of change between the two different speeds suggests that speed influences the effectiveness of low-medium range percussive frequencies more than it does static and high frequencies. The reason for this change in slope is attributed to particle settlement time. In the static case the particles are asked to be forcibly moved relative to one another by a rigid blade. If asked to be displaced

at a faster rate the binding forces increase, but the possibility of completely removing those binding forces isn't contingent on the rate at which particles are forcibly moved. In percussion, however, impact energy acts on particles in such a way that they are momentarily disengaged from one another, removing those binding forces for a brief period of time. If those particles are asked to move during that period of disengagement, then those binding forces are removed. On the other hand, if the particles are given sufficient time to dissipate the impact energy and settle, those binding forces, although decreased, will reappear. Consequently the effectiveness of percussion is tied much more to speed then is the effectiveness of static excavation.

Figure 3-37 gives insight into the design process for the utilization of percussive excavation. Due to the linear relationship between power and percussive frequency, and the exponential relationship between resistive force and frequency, an optimized frequency can be achieved with the highest ratio of force reduction to power required. This frequency will vary between soil types and testing conditions, but can be determined through a closed-loop feedback control system.

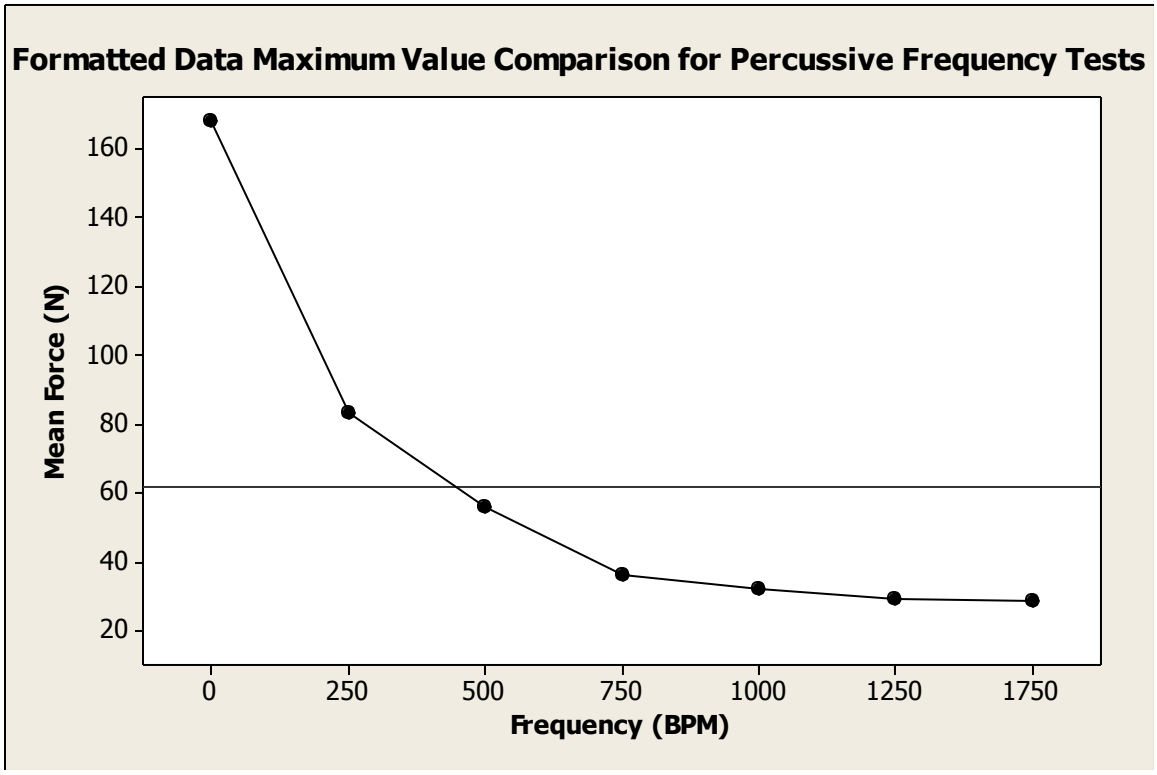

Figure 3-35: Relationship between the total excavation force and the applied percussive frequency for all test data. Refer to the appendix for the data set test values.

Percussive Frequency (BPM)	Percent Reduction in Total Excavation Force
250	51%
500	67%
750	78%
1000	81%
1250	83%
1750	84%

Table 3: A breakdown of the total excavation force reduction as a function of percussive frequency (All percentage reduction values are based on the static excavation force value)

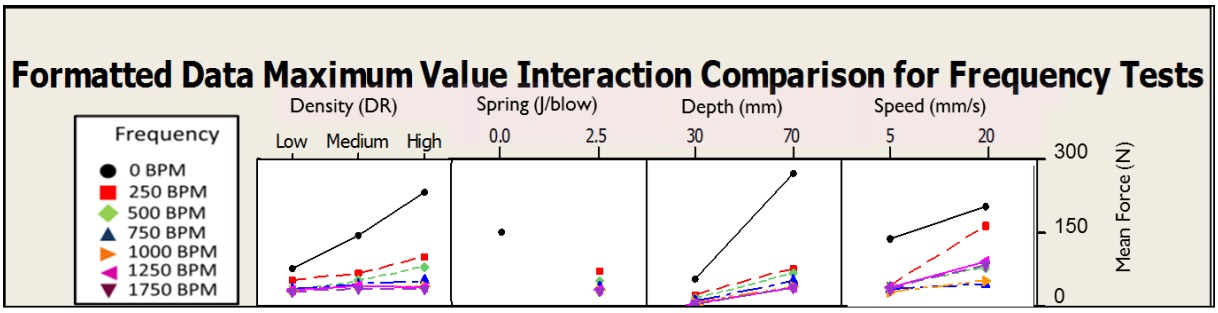

Figure 3-36: Relationship between frequency and other test variables. Refer to the appendix for the data set test values.

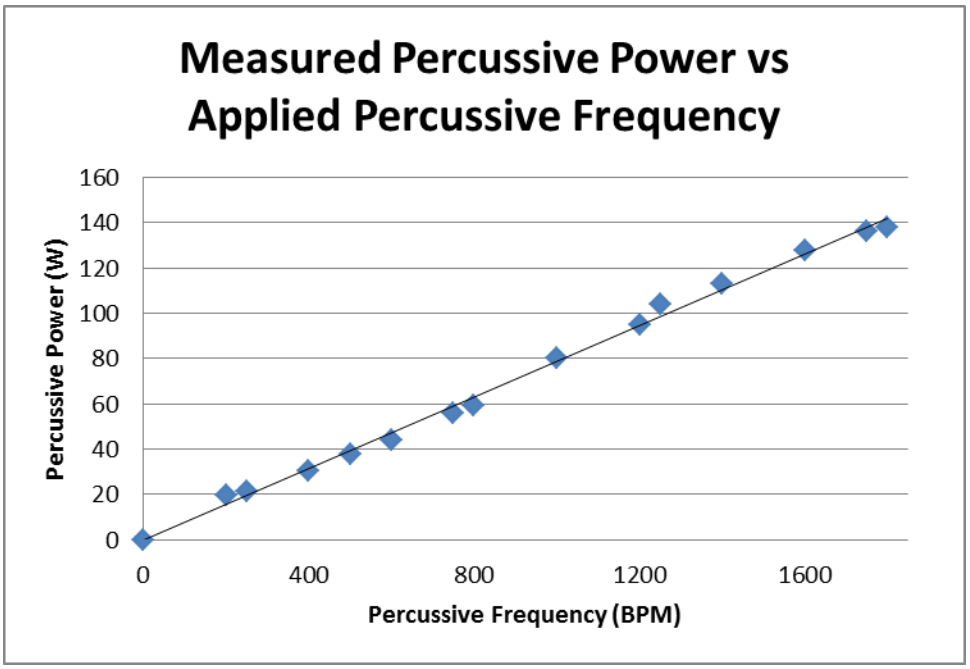

Figure 3-37: Comparison between percussive frequency and required power. All data points are measured values taken during testing.

3.4.3.1.2 Impact Energy verses Total Excavation Force

The default impact energy used for the majority of testing was 2.5 Joules. However, for a series of tests the impact energy was varied across three different frequencies (500 BPM, 1250 BPM, 1750 BPM) and three different densities (Low, Medium, High), making 9 tests for 2 differing values of impact energy. It was observed that the range of impact energy values tested had a minor influence on the effectiveness of percussion.

Although this result would seem to have little significance, it still showed something interesting. That is: after an appropriate impact energy level is reached any increase in impact energy is superfluous. In other words, if the conditions for force reduction are already present for a prescribed test, meaning the speed, frequency, density, depth, and angle then any increase in the percussive impact energy will not alter the outcome. This has ramifications in the design of future excavation hardware where any excess in applied impact energy results in wasted power.

It is also interesting to note that a change in impact energy did not aggressively affect the formation of shear planes; refer to Section 3.3 for a discussion on shear plane formation. This means that although more energy was applied to the boundary layer it was the time duration between impacts that determined the success rate of shear plane formation. That said, the impact energy had to be sufficiently high before its relevance was diminished. If the impact energy was too low, then the boundary layer soil particles would not be disrupted and regardless of the applied frequency, speed, depth, or density the particles would never have disengaged from one another.

It is suggested that in future work lower impact energies be tested at lower frequencies and higher excavation speeds to better understand the relevance of spring energy.

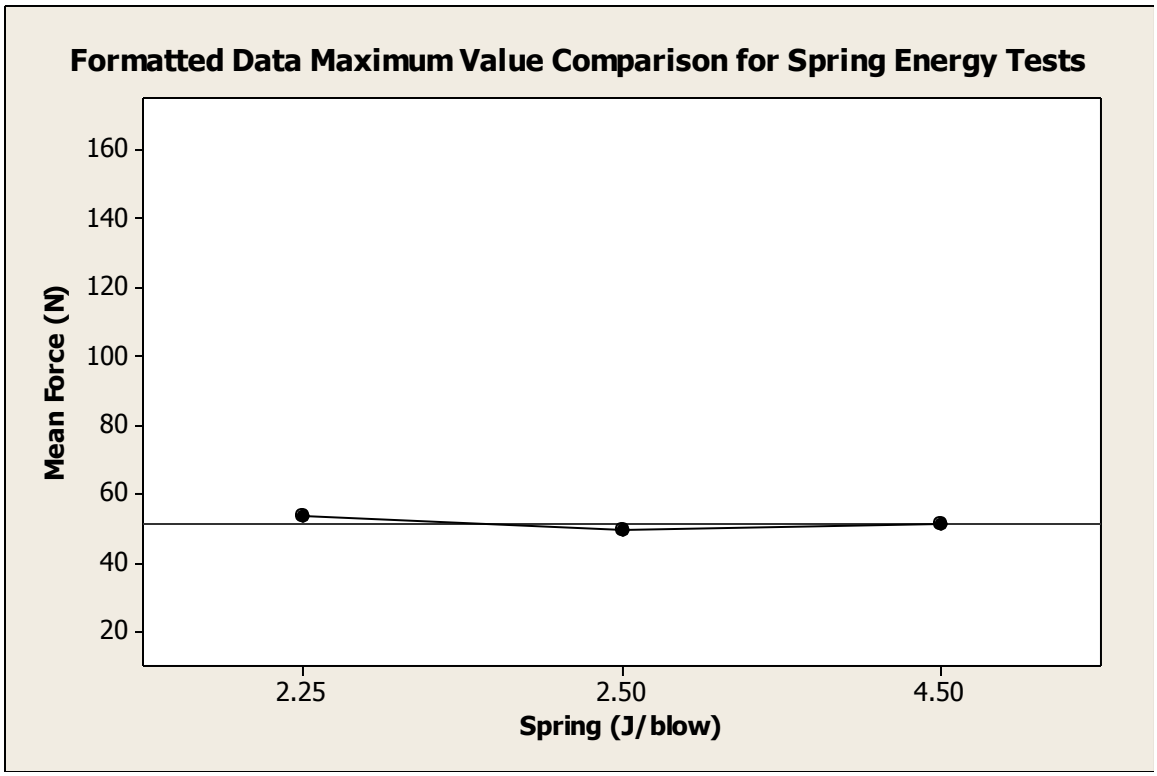

Figure 3-38: Relationship between the total excavation force and impact energy. Refer to the appendix for the data set test values.

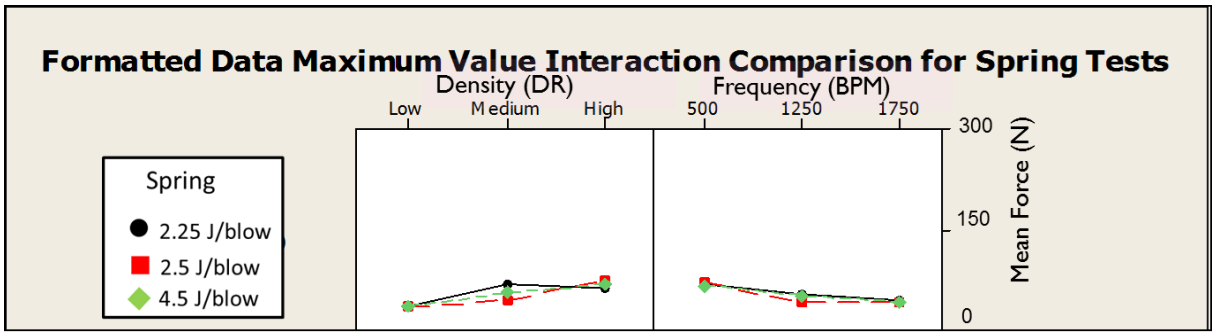

Figure 3-39: Relationship between the impact energy and other test variables. Refer to the appendix for the data set test values.

3.4.3.1.3 Excavation Angle Verses Total Excavation Force

To normalize the effects of excavation angle relevant to the depth of excavation, the scoop depth below the surface was held constant. This means that the scoop was inserted 70 mm axially into the soil when at 70 degrees, but only inserted 66 mm during 90 degree tests.

Figure 3-40 shows that by changing the angle from 90 degrees to 70 degrees, the force was reduced by 21 percent. However, Figure 3-41 shows that that reduction was based more on an advantageous rake angle rather than on a percussive interaction.

The angle of excavation and angle of percussion were the same variable because of the hardware design of the percussive mechanism. As can be seen in Chapter 2 the applied percussive impact and scoop displacement were directly in line with the orientation of the scoop. In [Sulatisky 1972], it states that the most advantageous angle of percussion is at 45 degrees in relation to a plow blade oriented at 90 degrees. Unfortunately this test was not able to be replicated in this work. However, the relationship between frequency and angle at 1750 BPM suggests that there is an ideal frequency range in relation to scoop orientation. This comparison shows that in the case of a 90 degree rake angle a frequency of 500 BPM proved to be more advantageous than at 1750 BPM. The reasoning for this effect is not known but it is suggested that the interaction lies in the dynamic response of the soil being farther away from the resonant frequency of excitation. This effect was only made manifest in the case of the 90 degree orientation because the directional component of percussion acting along the boundary layer was reduced in comparison to the 70 degree orientation. Future work must be done in terms of relating percussive orientation to excavation implement orientation; as well as percussive orientation in reference to direction of travel.

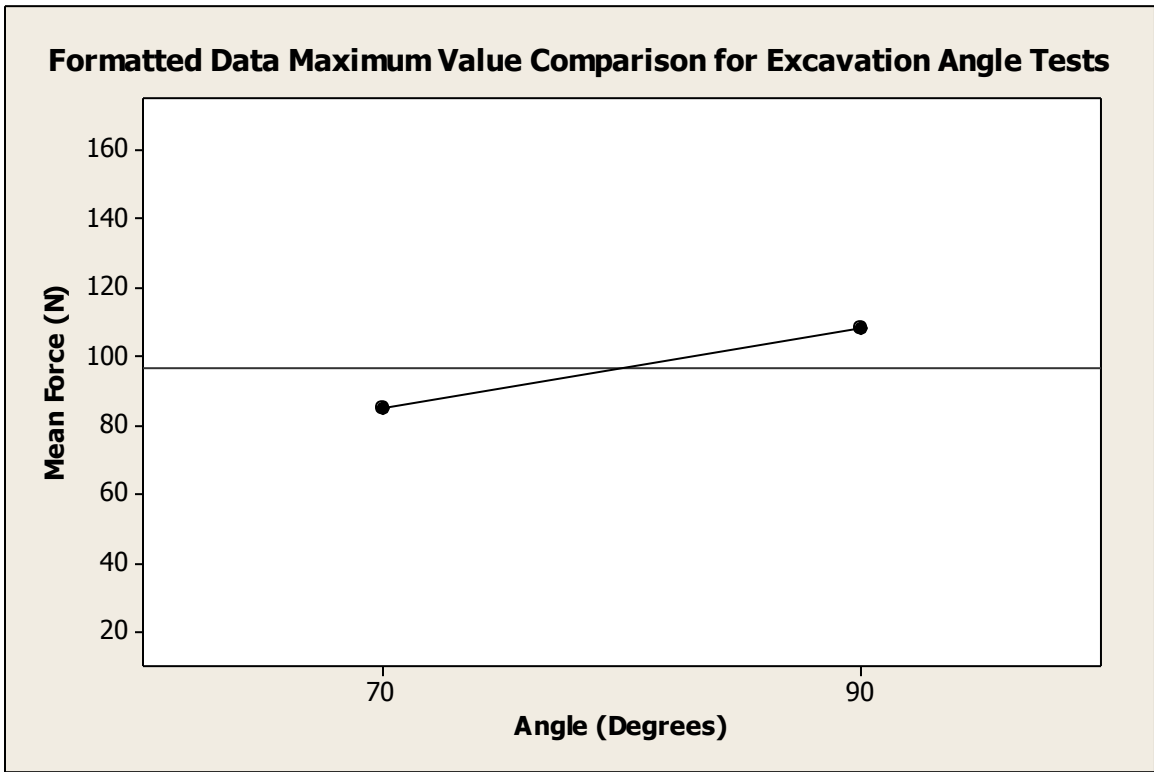

Figure 3-40: Relationship between the total excavation force and excavation angle. Refer to the appendix for the data set test values.

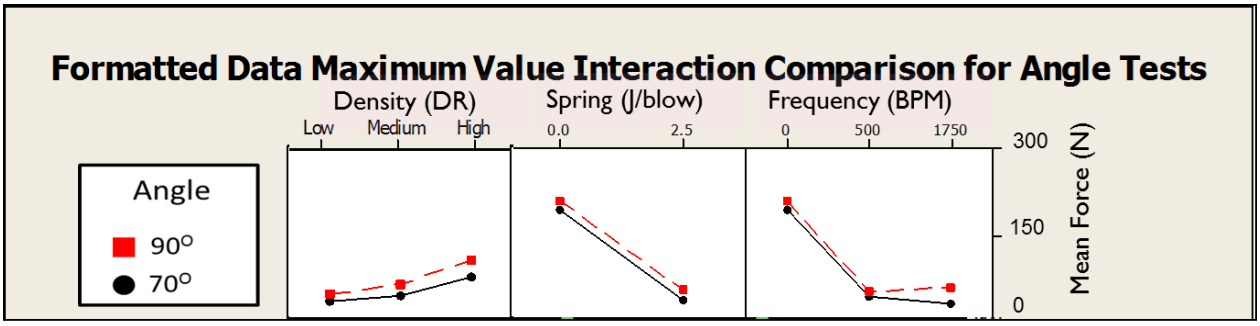

Figure 3-41: Relationship between the angle of excavation and other test variables. Refer to the appendix for the data set test values.

3.4.3.1.4 Excavation Speed verses Total Excavation Force

It was shown earlier that speed of excavation had a strong influence on the development of shear planes. Speed also affects the baseline draft force. Figure 3-42 shows a reduction of 38 percent between 20 $^{mm}/_{s}$ and 5 $^{mm}/_{s}$.

Although Figure 3-42 does show a reduction in force relative to speed it is important to point out that the graph depicts all tests conducted at 5 $^{mm}/_{s}$ as well as 20 $^{mm}/_{s}$, regardless of percussion being applied to the system. By breaking down the data set into two separate graphs, one depicting the effect of speed in static excavation and the other depicting speed in percussive excavation it is easy to see that there was a much stronger dependency in the percussive case. This dependency is derived from the soil particles ability to remain in a state of disengagement.

The effect of speed on other excavation variables can be directly tied to the inter-particle movement along the boundary layer. In the case of relative density, the change in speed had minimal effect in low relative density because the particles were already in a loose state. As the state of compaction was increased the effect of those inter-particle forces became more prominent. Consequently the relative difference between the two speeds exponentially increased with an increase in soil density.

The plot to the farthest right in Figure 3-44 is very interesting. It shows that the degradation curve of excavation force relative to impact frequency is dependent on excavation speed. Higher frequencies have to be applied to achieve the same reduction in shear strength if the scoop is moved at a higher velocity. In addition, this plot shows that the value of the asymptotic limit of the degradation curve increases with excavation speed. Particles have to be allowed sufficient time to properly reach a “floating” point prior to being excavated if optimum force reduction is to be achieved. This can only happen if the frequency, relative to the displacement rate, is sufficiently high. A velocity ratio is introduced in Chapter 4 which is a non-dimensionalized term relating frequency to excavation speed. In Chapter 5 this term is used to characterize the shape and limiting value of the degradation curve in the theoretical model.

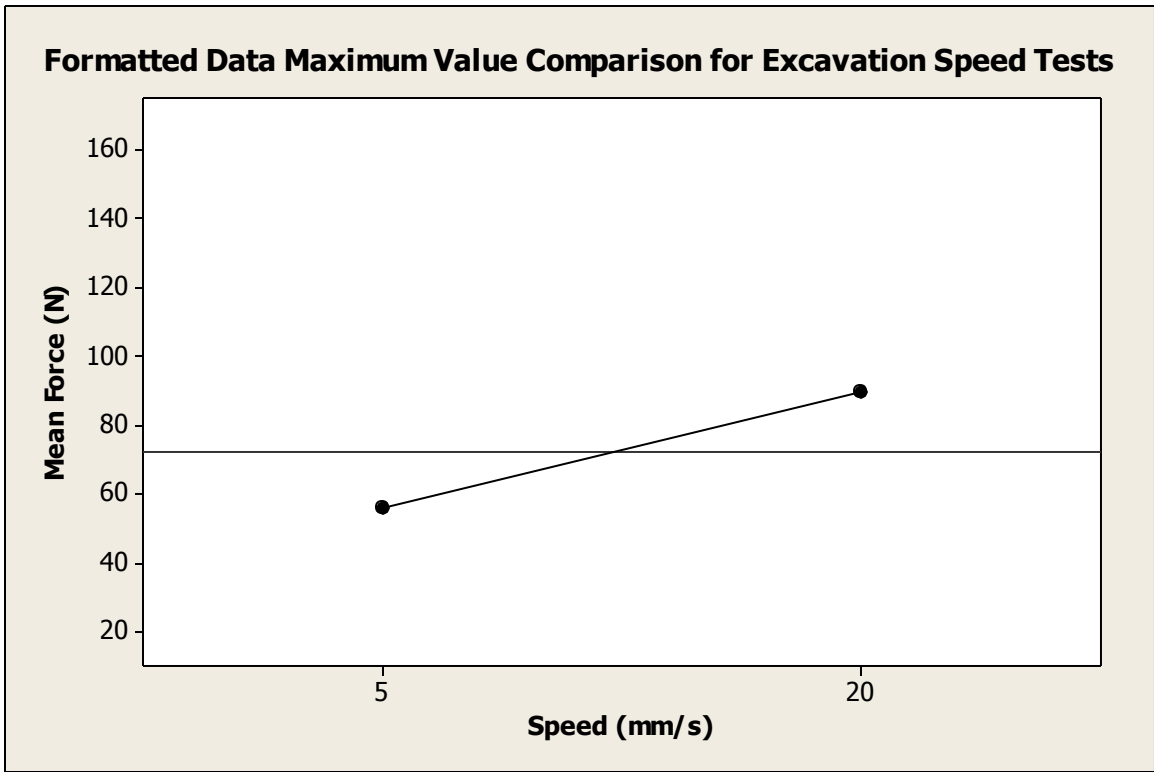

Figure 3-42: Relationship between the total excavation force and excavation speed for all tests, percussive and static. Refer to the appendix for the data set test values.

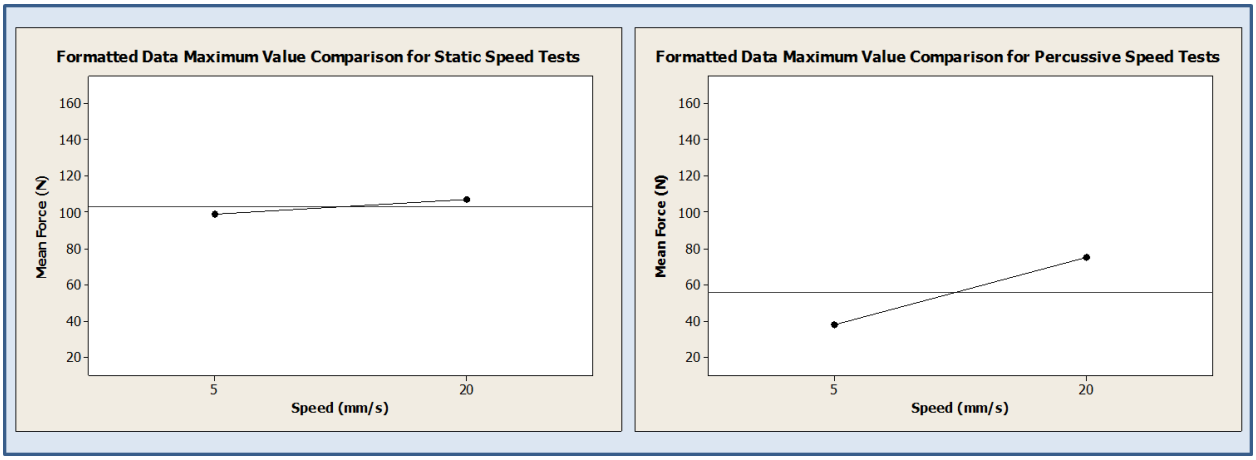

Figure 3-43: Effect of speed on static and on percussive tests. The slope of change demonstrates higher dependence of speed for percussive excavation.

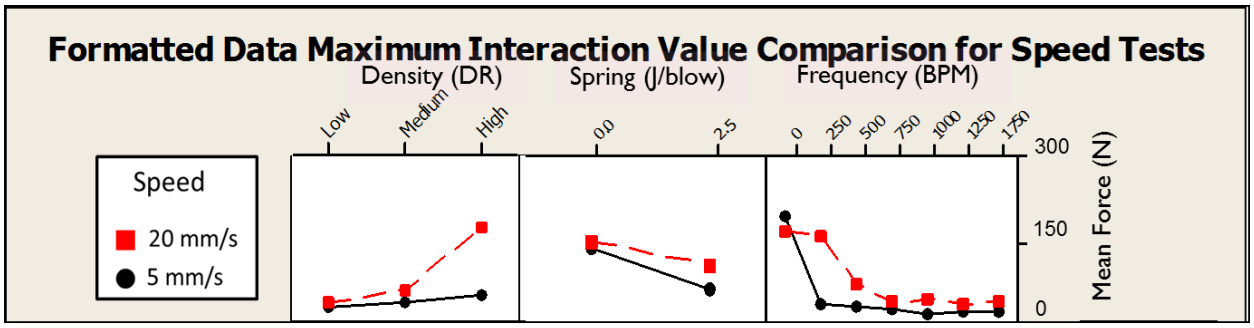

Figure 3-44: Relationship between the speed of excavation and other test variables. Refer to the appendix for the data set test values.

3.4.3.1.5 Excavation Depth verses Total Excavation Force

A 78 percent reduction in excavation force was found, on average, between 30 mm and 70 mm (Figure 2-11). Based on a smaller dataset sample, inclusive of tests taken at 50 mm, a linear force trend was shown relative to depth.

Figure 3-47 provides a different perspective to what was shown in Figure 3-36 where the relationship between depth and frequency was given in the context of frequency. In Figure 3-47 it can be seen that deeper depths require higher frequencies to reach an asymptotic state, and that the limiting value of that asymptotic state is a function of depth.

The interaction between depth and relative density becomes more significant at deeper depths. As the scoop is inserted deeper, into more compact soils, the change in boundary layer shape exponentially increases. Figure 3-48 provides a simplistic representation of the development of boundary layer dependent on depth and relative density.

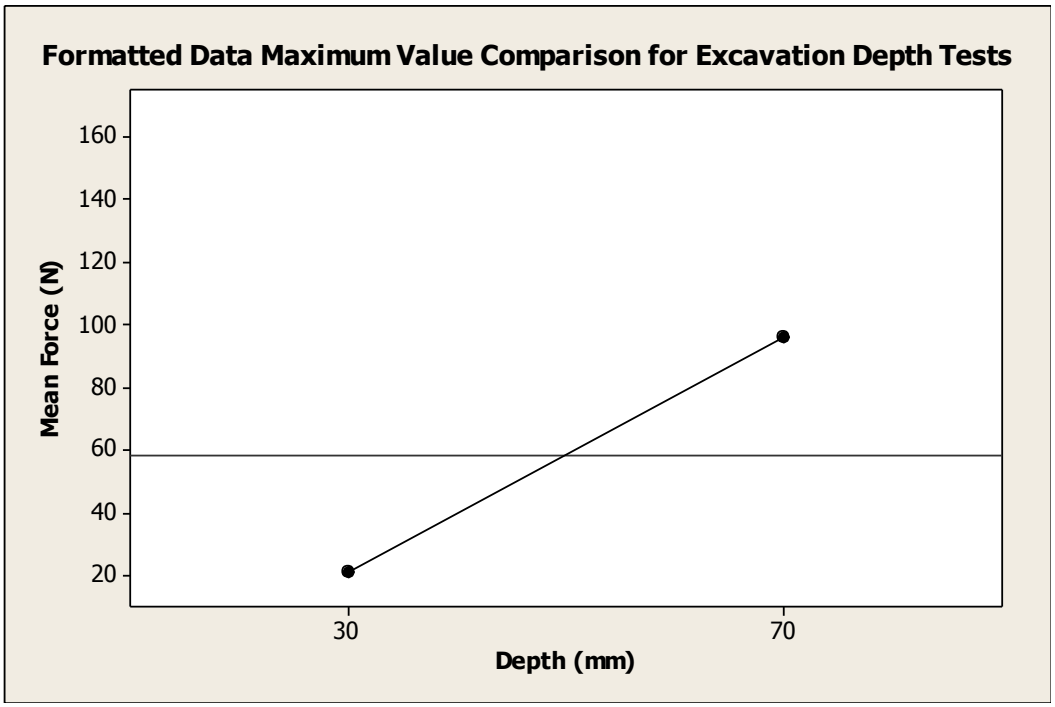

Figure 3-45: Relationship between the total excavation force and excavation depth. Refer to the appendix for the data set test values.

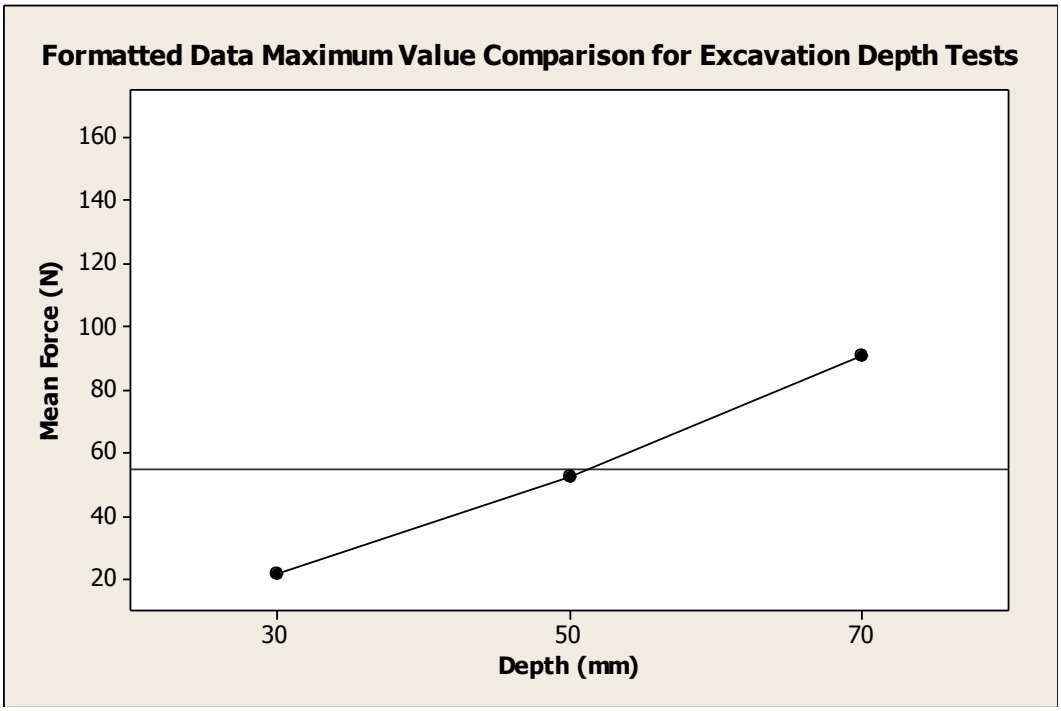

Figure 3-46: Supplemental graph to Figure 3-45 showing the results from a smaller data set which further demonstrate a linear increase in excavation force in relation to scoop depth.

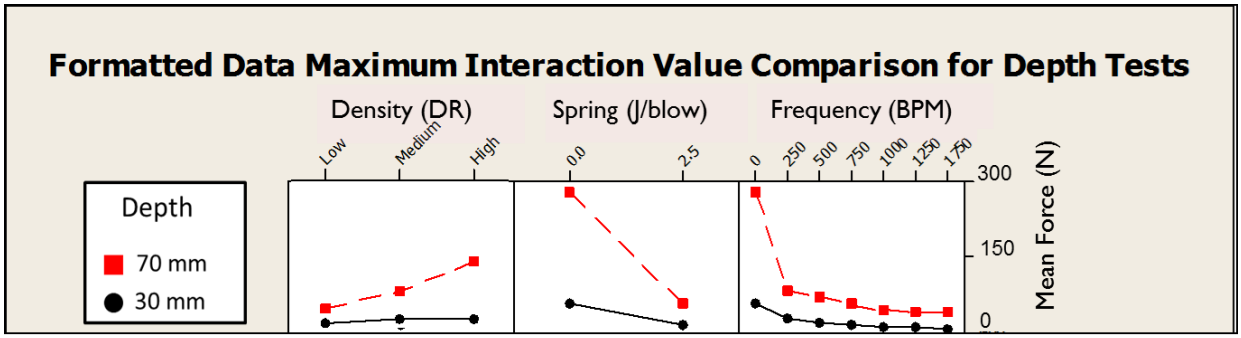

Figure 3-47: Relationship between the depth of excavation and other test variables. Refer to the appendix for the data set test values.

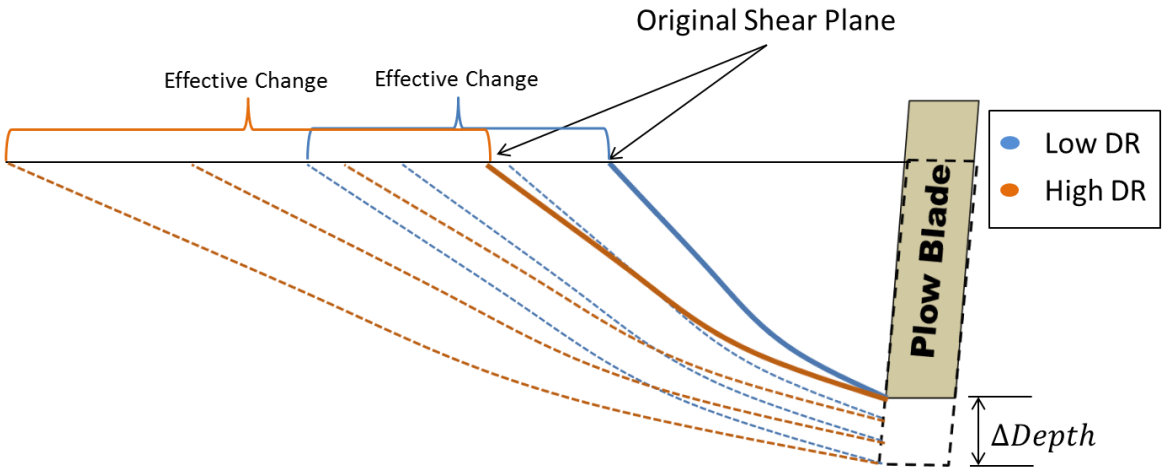

Figure 3-48: Graphic showing the change in shear plane shape as a function of depth and relative density.

3.4.3.1.6 Relative Soil Density verses Total Excavation Force

Relative density is directly related to soil dilatancy. Given that percussion is able to remove the effects of dilatancy the in situ relative density of a soil gradually becomes inconsequential as percussive power is increased. Because Figure 3-49 is inclusive of all tests, both static and percussive, the gradient does not represent how relative density truly affects excavation force. Figure 3-50 provides a more clear distinction. Based on the interaction plot, the diminishing relevance of the in situ density can easily be inferred. That said, it is important to note that relative density does affect the shape of the shear strength degradation curve and its corresponding asymptotic limit. This is due to energy density requirements for particle separation. This association is also integrated into the theoretical model found in Chapter 5.

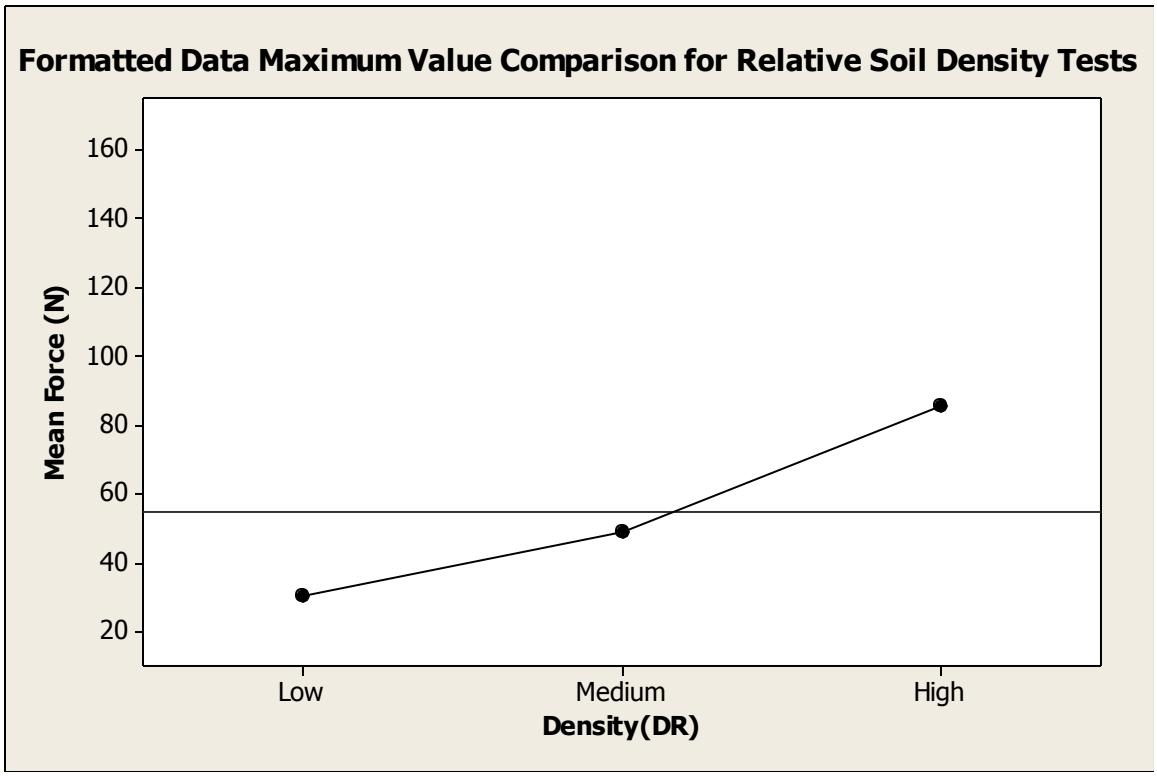

Figure 3-49: Relationship between the total excavation force and relative soil density. Refer to the appendix for the data set test values.

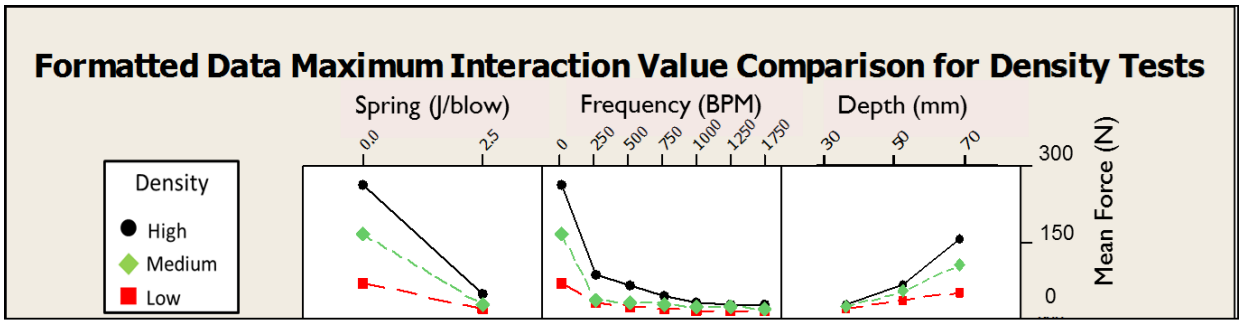

Figure 3-50: Relationship between the relative soil density and other test variables. Refer to the appendix for the data set test values.

4 Theoretical Model

4.1 Introduction:

The purpose of this chapter is to provide the reader with the necessary insight to understand how the theoretical model was developed, and the underlying theory upon which it is based. One of the primary goals of this research, as stated in Section 1.3, was to create a first generation numeric code which can approximate the reaction force for percussive shear failure given specific soil and percussion properties. The governing criteria for this code was that it be simple and easy-to-use, the underlying theory not be too esoteric, and that the structure enables further refinement and development. With these guidelines, the following numeric code was developed and is meant to predict the baseline reaction force. Due to soil assumptions and the random nature of the force spikes associated with soil strain hardening, this code only deals with prediction of the baseline draft force.

The following chapter will include: information regarding the characteristics of the soil used, JSC-1a; the simplifying assumptions that were made to the soil characteristics; the limit theory, its derivation and application; percussion, the degradation of shear strength with respect to percussion; and the integration of percussion into the numeric limit theory model.

4.2 Soil Characteristics

4.2.1 Soil Selection: JSC-1a and Sand

Critical to creating a numeric model is having real data to analyze and research. Given that the purpose of this work was to create a theoretical model which simulates excavation forces on the surface of moons, asteroids and other planets, experimental data was scarce. The data collected during the Apollo missions was available [Carrier 1991], but insufficient for this effort.

JSC 1a is a man-made simulant used to replicate the mechanical properties of lunar regolith for testing purposes [Alshibli 2009]. All tests within this work were done using JSC-1a. Accordingly, the following numeric code is based upon the soil properties of JSC-1a.

Although JSC-1a has been well published as a good substitute for the mechanical properties of lunar regolith, there has been very limited data published with respect to its dynamic properties. Consequently, published data pertaining to the dynamic behavior of dry cohesionless sand were used as a starting point in predicting the dynamic behavior of JSC-1a. Cohesionless sands lack a critical mechanical component found in JSC-1a, cohesion. With that

said, the gran size distribution and the dynamic particle-to-particle interaction of dry sand gave great insight into possible JSC-1a dynamic behavior.

Recent finding from LCROSS show ice in the polar caps of the moon [Chang 2009]. It is suggested for future research that experimental work be undertaken to explore how moisture content affects percussion and shear strength degradation. It is well documented that the dynamic properties in sand are adversely affected by moisture content [Balyshkin 1966] [Ermolaov 1968] [Barkan 1962].

4.2.2 Nonlinear behavior approximated as perfectly plastic

Soil, like all material, has a distinct relationship between applied stress and induced strain. The relationship between the two depends on several factors, such as grain size distribution, saturation level, void ratio, and others. At low stress levels, relative to the material, the relationship between the applied stress and resultant strain is considered linear. The proportionality of strain to stress changes once stress levels are increased to a material's yield point. At which point, unrecoverable work is done to the system and relative displacement takes place between individual soil particles. If the applied stresses were to be removed the soil would no longer return to its virgin state as it would prior to yielding, but rather would remain in a state of dislocation. Prior to the yield point the soil is said to be in its elastic range. Once the stresses begin to produce unrecoverable work the soil is in its plastic range.

After the soil has reached the plastic range it no longer has the same predictable linear behavior that it does during elastic deformation. Instead the soil can exhibit a variety of different stress-strain relationships. Some soils continue to increase in strain without any increase in applied stress; others require an increase in stress but the proportionality between stress and strain is now higher or lower than during elastic deformation; still others depend on the rate of the applied stress in addition to the magnitude. Due to the complexity of a soil's non-linear behavior during plastic deformation a common practice is to idealize the stress-strain behavior to something that is mathematically simpler. Johnson in [1983] provides a graphical representation of some idealized stress-strain models.

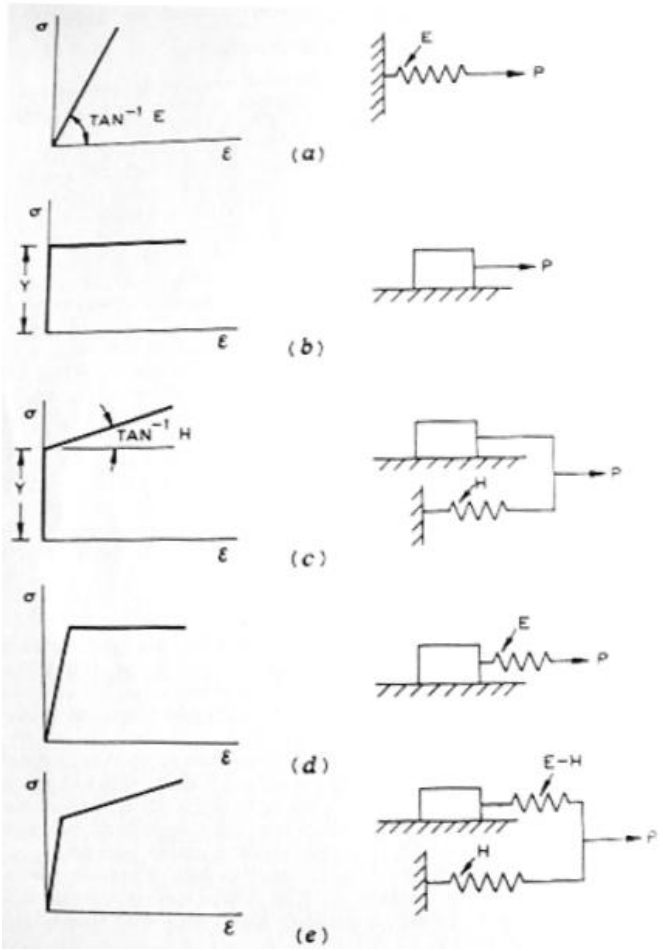

Figure 4-1: Idealized stress-strain diagrams and dynamic models of mechanical loading behavior [Johnson 1983].

The pictures to the right of the stress-strain diagrams are meant to provide the reader with a more physical understanding of how the system is being idealized. A spring is representative of elastic recoverable work. A sliding block on the ground is a representation of inelastic unrecoverable work. Accordingly (a) represents a perfectly elastic model in which all applied stresses are coupled to a linear recoverable strain; (b) is a perfectly plastic model where there is no soil deformation at any stress magnitude below a specific state. Once the stresses reach that state the material is free flowing; (c) is a linear plastic model where the applied stresses have no effect until they reach a critical value. Beyond that value point the plastic unrecoverable work is assumed to have a linear relationship between stress and strain; (d) is elastic-perfectly plastic, where the material behaves linearly and elastically until a critical state at which point free plastic flow takes place without any increase in applied stress; and finally (e) is representative of a simplified linear model of both elastic and plastic soil deformation, where the distinction between the two is a change in slope.

This work focused on shear failure, and the stress magnitude to reach that failure. It was of no importance what recoverable work was done prior to failure. As part of the proposed

theoretical model the strain rate must be known. This requirement is satisfied through the flow rule which is discussed in Section 4.2.6. Given these conditions the soil was approximated as perfectly plastic. In relation to Figure 4-1, given that the elastic of the soil is irrelevant, the soil was idealized as either (b) or (d).

4.2.2.1 Defining the Soil Frame of Reference

In addition to the simplifying assumption of perfectly plastic stress-strain behavior at yield, the problem was further streamlined through characterizing the proper frame of reference of the soil. Soil is a material which is composed of several different particles, each with their own shape and size. Thus to define the constituency of the soil depends heavily on the frame of reference one takes.

The dimensions of particles for a soil skeleton can vary and range between 5 mm (gravelly soils) to several microns (clay). Accordingly soils may be considered homogeneous only in volume elements that have dimensions which are large in comparison with the dimensions of the soil particles. For this work the volume element under examination was considered to be sufficiently large to justifiably assume that the soil was homogeneous.

4.2.3 Strain Hardening Rule

To properly define the stress at which material begins to plastically deform, a yield surface must be defined. A yield surface is a 5-dimensional surface within a 6 dimensional stress state that characterizes the material through normal and shear stresses [σ_x σ_y σ_z τ_{xy} τ_{yz} τ_{xz}]. The surface is a representation of the material modulus, stress state and stress history. At the origin, all applied stresses are zero. As different stresses are applied to the material, in different directions and magnitudes, they are represented as vectors mapped into a 6 dimensional stress space. As long as those vectors don't reach the yield surface within the stress space of the material then no unrecoverable work is done. At the point that a stress state vector does reach the yield surface, then the material's yield criterion is reached and there is incipient failure. Depending on the material, and the stress-strain relationship, the yield surface will change in shape and orientation. For an isotropic hardening material the yield surface will expand radially outward, maintaining its orientation, until the new yield surface corresponds to the current stress state. In kinematic hardening the yield surface changes orientation to accommodate the expanding stress state vector but the shape of the yield surface does not change. Other models exist which combine these two hardening effects [Johnson 1983]. Since the soil behavior at failure in this model was represented as perfectly plastic there was no work hardening, or softening, associated with material failure. The material was idealized and expected to behave as shown in Figure 4-2.

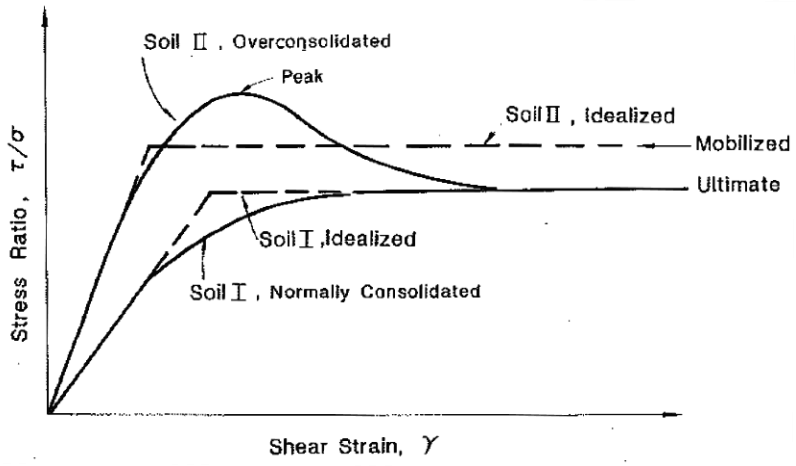

Figure 4-2: Typical stress strain curves and perfectly plastic idealizations [Chen 1991].

4.2.4 Yield Surface and Flow Rule

When considering perfectly plastic material, the recoverable deformation prior to the critical yield stress is inconsequential. For failure theory the only important behavior is after the yield surface is reached. Because the material is idealized and not confined by any strain-hardening or strain-softening rules the flow is unconstrained for as long as the stress is continuously applied. Given that the soil's plastic flow is unconstrained, strain values cannot properly characterize the material behavior. Instead, the strain rate value is used, $\dot{\varepsilon}_{ij}^{\,p}$.

Since the soil for this work was assumed to be isotropic, the principal strain rate axes coincided with the principal stress axes. In other words, if a rectangular element of this isotropic material were to undergo simple compression then any plastic deformation would be expected to behave such that all the sides remained mutually perpendicular[Chen 1975].

On account of the isotopic assumption, a flow rule was used to characterize the soil strain rate behavior. A flow rule is based upon the hypothesis that there exists a plastic potential in a material and that that potential is a scalar function of the applied stress, $g(\sigma_{ij})$. The strain rate is solved for by partially differentiating $g(\sigma_{ij})$ with respect to σ_{ij} and multiplying it by a scalar proportionality factor, λ [Johnson 1983][Lubliner 1990][Chen 1975].

$$\dot{\varepsilon}_{ij}^{p} = \lambda \frac{\partial g(\sigma_{ij})}{\partial \sigma_{ij}}$$

Equation 4-1

In this work λ was not explicitly solved for, but Equation 4-1 was still used as a fundamental building block for understanding perfectly plastic soil behavior at failure. See Section 4.2.6.

4.2.4.1 Yield Surface Definition

In order to utilize the flow rule the yield surface function, $g(\sigma_{ij})$, had to be defined. For soils it is generally assumed that plastic flow occurs when the shear stress, τ, reaches a critical value dependent upon the cohesion of the soil, c, and the normal stress, σ. The proportionality between the shear stress τ, and the normal stress σ, is not one to one, but instead related through the internal friction angle, ϕ. In 1773, Coulomb proposed the following equation to represent this relationship.

$$\tau = c + \sigma tan\phi$$

Equation 4-2

To understand how this equation was derived a Mohr's circle is used. Mohr's circle is a representation of the 6 dimensional stress space using only the principal stresses.

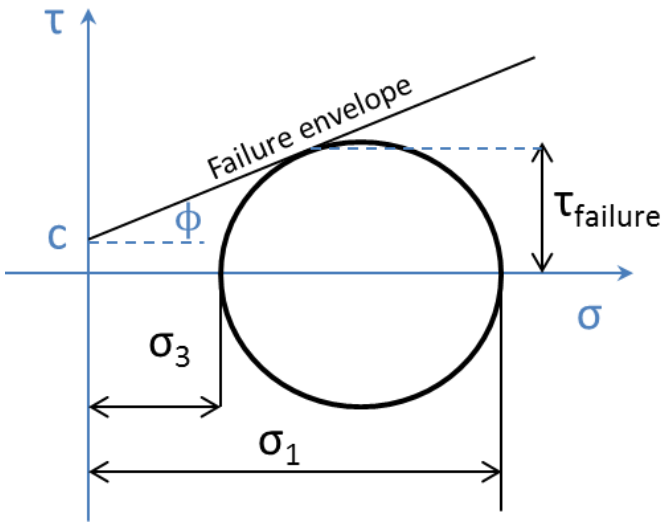

Figure 4-3: Mohr's Circle for a soil. Stress values are taken as positive in compression.

Figure 4-3 shows the stress state of soil with an applied shear τ, and normal stress σ. The values for the shear and normal stresses are taken as positive in compression. A line is constructed to represent the soil strength and is dependent on the soil cohesion and internal friction angle. This line is a called the failure envelope, because any stress state between this line and a symmetric one below the x-axis represents a safe and stable soil. If applied shear and

normal stresses are such that the corresponding Mohr's circle becomes tangent to the failure envelop then soil failure occurs.

4.2.5 Drucker's Postulate

A critical part to approximating a failure material as perfectly plastic is to understand Drucker's postulate and its significance to the direction of plastic flow of a material after failure. The following derivation of Drucker's Postulate is based on work given in [Chen 1990] for a stable material and Figure 4-4 is referenced within the derivation.

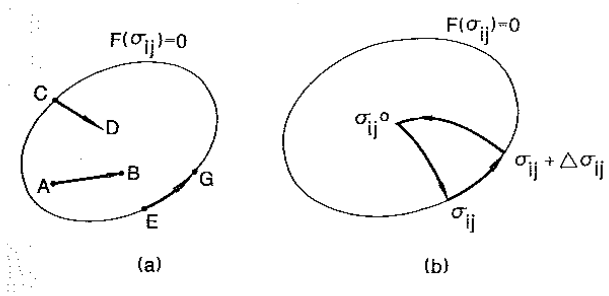

Figure 4-4: Different stress states inside stress space [Chen 1990].

Assume that at time t=0, σ_{ij}^{o} are any set of stresses, in equilibrium with the traction forces as well as the body forces. Now apply additional external forces to the body at time t=t to such a degree that the stress state reaches the yield surface and becomes σ_{ij}. After reaching the yield surface the stress state travels along the yield curve and at time t=t+Δt the stress state is σ_{ij}+ $\Delta\sigma_{ij}$. Now remove the external forces at time=t^{*} and allow the stress state to return to σ_{ij} again. The work associated with the steps just outlined is shown mathematically:

$$\Delta W = \int_{0}^{t} \sigma_{ij}\dot{\varepsilon}_{ij}dt + \int_{t}^{t+\Delta t} \sigma_{ij}\dot{\varepsilon}_{ij}dt + \int_{t+\Delta t}^{t^{*}} \sigma_{ij}\dot{\varepsilon}_{ij}dt$$

Equation 4-3

Decomposing the strain rate into its elastic and plastic parts changes Equation 4-3 to the form:

$$\Delta W = \int_{0}^{t} \sigma_{ij}\dot{\varepsilon}_{ij}^{e}dt + \int_{t}^{t+\Delta t} \sigma_{ij}\left(\dot{\varepsilon}_{ij}^{e} + \dot{\varepsilon}_{ij}^{p}\right)dt + \int_{t+\Delta t}^{t^*} \sigma_{ij}\dot{\varepsilon}_{ij}^{e}dt$$

Equation 4-4

Summing all the elastic work done over the time integral produces a closed loop which can be set equal to zero. Thus the total work done from the initial stress state σ_{ij} to the stress state $\sigma_{ij}+\Delta\sigma_{ij}$ and then back to the original state σ_{ij} is equal to:

$$\Delta W = \oint \sigma_{ij}\dot{\varepsilon}_{ij}^{e}\,dt + \int_{t}^{t+\Delta t} \sigma_{ij}\dot{\varepsilon}_{ij}^{p}dt = \int_{t}^{t+\Delta t} \sigma_{ij}\dot{\varepsilon}_{ij}^{p}dt$$

Equation 4-5

Note however that in order to first arrive at the initial state of stress σ_{ij}^{o} work was done to the system. Therefore to have an accurate representation of the work done just over the load cycle the initial work done to the system must be subtracted from the current work performed to the system.

$$\Delta W - \Delta W_{o=} \int_{t}^{t+\Delta t} \left(\sigma_{ij} - \sigma_{ij}^{o}\right)\dot{\varepsilon}_{ij}^{p}dt$$

Equation 4-6

As the limit of Δt goes to zero then the following inequality is left

$$\left(\sigma_{ij} - \sigma_{ij}^{o}\right)\dot{\varepsilon}_{ij}^{p} \geq 0$$

Equation 4-7

[Chen 1990][Johnson and Mellor 1983][Lubliner 1990][Drucker 1953]

This inequality is Drucker's postulate. Equation 4-7 prescribes the direction of plastic flow in relation to the yield surface. As stated by the inequality, the relative direction between the

stress vector and the strain rate vector must have an angle less than or equal to 90 degrees. This is shown as the angle between $\overline{AB}$ and $\overline{BC}$ in Figure 4-5. Figure 4-5 represents a yield surface in stress space. Since the direction of any hypothetical stress vector arriving at the yield surface, point B, is not prescribed then the only way that Equation 4-7 can always hold true for any $\overline{AB}$ is to require that the yield surface be convex and that the direction of plastic flow, $\overline{BC}$, always be normal to the yield surface. The idea of the surface normal uniquely describing the plastic flow is also often referred to as the principle of maximum work dissipation [Lubliner 1990][Johnson and Mellor 1980][Drucker 1953].

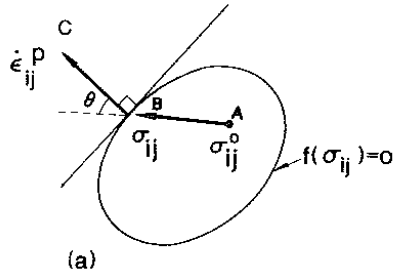

Figure 4-5: Convex yield surface and surface normal strain rate for stable materials [Chen 1990].

4.2.6 Flow rule and Dilatancy

In Chapter 3 it was briefly stated that the soil friction angle is influenced by two major factors: the Coulomb frictional resistance between particles and the resistance to expansion due to particle interlocking. The internal friction angle in real soils can then be expressed as $\phi=\phi_\mu+\phi_v$, where ϕ_μ represents sliding friction and ϕ_v the effect of dilatancy. Dilatancy is a direct effect of soil compaction; the higher the relative density the more dramatic the effect of dilatancy. When a soil's internal friction changes, the change is only made to the angle of dilatancy, ϕ_v. ϕ_μ is a soil characteristic and a constant [Das 1983].

When a soil is assumed to fail in a perfectly plastic manner it means that frictional effects are ignored and $\phi=\phi_v$. This would seem to render the perfectly plastic assumption unusable in this work given that dilatancy is removed through percussion. However, as will be discussed in the following section, the nature of the upper limit analysis approach enables the perfectly plastic assumption to be used while still providing a conservative approximation for frictional soils. The mathematical ramifications of the perfectly plastic assumption are now presented:

If the principle stresses are used to define the soil yield function then Equation 4-2 is given as:

$$g(\sigma_{ij}) = \sigma_1(1-sin\phi) - \sigma_3(1+sin\phi) - 2c*cos\phi = 0$$

Equation 4-8

Equation 4-8 is helpful because it can be used to obtain a relationship between the maximum and minimum strain rate through a manipulation of Equation 4-1.

$$\frac{\dot{\varepsilon}^p_{max}}{\dot{\varepsilon}^p_{min}} = \frac{{\partial g}/{\partial \sigma_{max}}}{{\partial g}/{\partial \sigma_{min}}}$$

Equation 4-9

If $\dot{\varepsilon}^p_{max}$ is solved for, with *g* denoting the yield criteria given in Equation 4-8, then the following relationship represents the minimum strain rate.

$$\dot{\varepsilon}^p_{max} = -\dot{\varepsilon}^p_{min}\frac{1-sin\phi}{1+sin\phi} = -\dot{\varepsilon}^p_{min} * tan^2\left(45 - \frac{1}{2}\phi\right) \text{ [Chen 1975]}$$

Equation 4-10

Equation 4-10 shows that for a deformed perfectly plastically Coulomb material, any friction angle greater than zero causes the minimum strain rate to be greater than the maximum strain rate. In other words, volume expansion must take place. This is the mathematical definition of soil dilatancy: particles must move around one another and increase the geometric volume of the control volume. When particles are acted upon by an applied shear force the particles on the top are forced to move not only in the direction of the applied force but vertically as well. The ramifications of this prescribed motion become more apparent in the following section where the upper limit analysis is presented along with the soil's kinematically admissible velocity field.

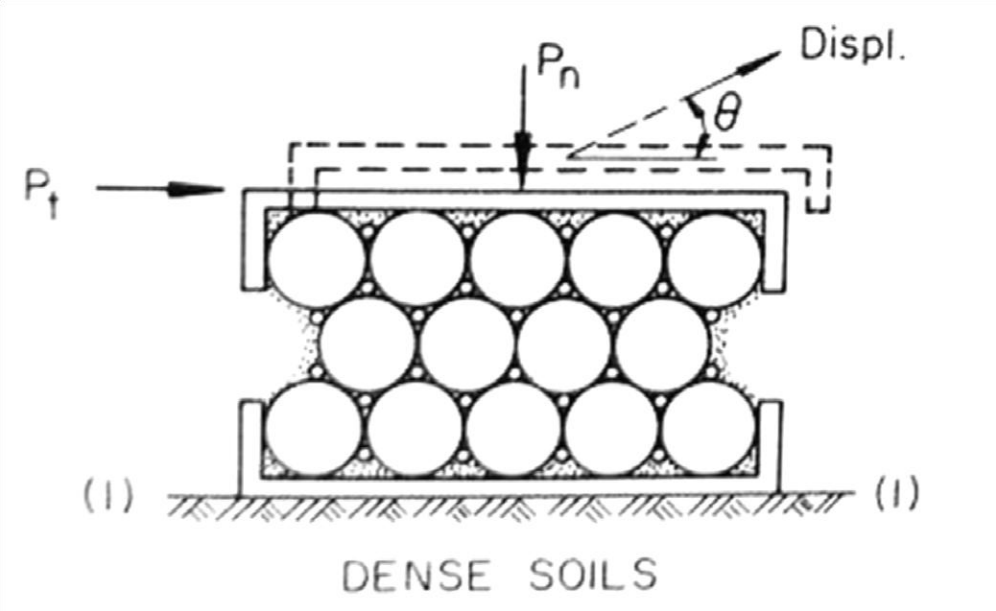

Figure 4-6: Simple physical model of dilatancy [Chen 1975].

4.3 Soil Failure Models

4.3.1 Introduction

Within the discussion of soil mechanics, like other fields dealing with continuums, there are two general types of problems, those concerned with elastic behavior and small deformation and those concerned with failure and unconstrained deformation. The first type deals specifically with stresses at points in the soil under a footing, behind a retaining wall, and settlements. The principle motivation in evaluating elastic behavior is to understand how the soil undergoes recoverable deformation. Small strains are considered important evaluation criteria.

The second type of problem focuses on ultimate failure. In these problems the engineer doesn't care about small strains or any elastic deformation, rather the load at which unconstrained plastic deformation begins to take place. Examples of this type of problem include earth pressure, bearing capacity, and slope stability. As mentioned earlier in this paper, the focus of this work was to deal with catastrophic failure and the plastic flow of material during the excavation process. Consequently, this research fell under the second category.

Several different models exist for evaluating the failure state of soil. Three different approaches are reviewed: the slip line method, the limit equilibrium method, and the limit analysis method.

It is the last, the limit analysis method, which was used as the analytical mechanism for this work.

In addition to these methods there is the finite element approach. This approach, however, is not discussed because of its inherent time constraints. One of the main design criteria for the proposed numeric algorithm was that it be capable of delivering a solution in a quick and timely manner. That said, it has been noted that the selected limit analysis approach has demonstrated numeric results close to those found with the finite element method in prior static failure analyses [Hong 2001].

4.3.2 The Slip-line Method

At the instant of impending plastic flow within a soil both the equilibrium and the yield conditions must be satisfied. Combining the Coulomb criterion with the equations of equilibrium yields a set of equations that describe plastic equilibrium. In the slip-line method these equations are transformed into curvilinear coordinates defining slip lines. A slip-line network represents an acceptable solution to the yield and equilibrium conditions and defines the failed boundary layer in the soil. This approach, however, is only for problems which are statically determinate. In the non-statically determinate problems the solution can only be found by considering both the stresses and the velocities simultaneously.

In both statically determinate and statically indeterminate problems partial differential equations are used to define the curvilinear coordinate system. Although these partial differential equations do successfully define slip lines, the slip lines created are not unique. In fact, a major feature of the slip line theory concerns the manner in which the engineer arrives at the solution. The process is usually a result of experience and intuition [Johnson 1983][Chen 1975].

Due to the esoteric approach inherent with the slip line method further work with this methodology was not undertaken. A driving factor of the design for the numeric code was that the methodology to determine the failure criteria of the soil be one that doesn't involve a steep learning curve. The slip line method does not lend itself easily to someone inexperienced in the approach and does not deliver an upper load limit in a timely fashion.

4.3.3 The Limit Equilibrium Method

The limit equilibrium method assumes plain strain and a predefined failure surface. This failure surface is generally composed of several simple shapes such as planes, circles or logspirals. These simple shapes approximate the real slip-line network. With assumed slip-line shapes, the limit equilibrium method proceeds to find the most critical geometric orientation while satisfying static equilibrium. A critical part of the limit equilibrium method is making assumptions regarding the stress distribution along slip line surfaces. The basic building blocks of the approach entail: assuming a failure surface, statically solving the problem with an admissible stress field, evaluating the problem, and then reconstructing the failure surface with

a new statically admissible stress field to determine if a more critical stress field can be created. These steps are repeated until the most critical stress field is generated, which is the assumed failure stress state [Chen 1975].

4.3.4 The Upper Limit Analysis Method

The limit analysis method is similar to the limit equilibrium method in many aspects, but contains a significant characteristic lacking in the limit equilibrium method; it takes soil kinematics into consideration. As in the case of the limit equilibrium method, the limit analysis method presupposes a failure surface and assumes deformation under plain strain. The limit analysis can solve for two different solutions, an upper limit and a lower limit. Given that this numeric tool will be used as a design instrument for hardware development, only the more conservative upper limit solution is considered.

The basic underlying principle of the upper limit analysis approach is the conservation of energy: the amount of energy being supplied to the control volume must be dissipated by the control volume. Energy conservation is accomplished by using the virtual work approach. The input force vectors and the dissipation vectors are multiplied by a kinematically admissible velocity field and then set equal to one another. Since the applied traction force is an unknown it can be solved for by determining the residual energy in the system after the body and dissipation forces have been taken into account. Because the failure volume geometry must be an assumed slip-line network, the resultant solution is not unique. Instead an optimization scheme must be employed to determine the minimum possible traction force with its corresponding failure geometry.

4.3.4.1 Advantages and Disadvantages of the Upper Limit Analysis Approach

Inherent with the upper limit approach are several strategic advantages to solving soil collapse problems. Due to the approximate nature of the approach there are no restrictions on the shape and complexity of the failure volume. The problem can always obtain a realistic value for the collapse load. The approach is relatively simple to apply. The methodology provides engineers will a clear and intuitive picture of the mode of failure. Many of the solutions have been substantiated. Work done in [Hong 2001] shows that after several different numerical methods were applied to the same problem, and contrasted with the results obtained from a rigorous finite element solution, that the upper limit analysis method provided the closest approximate solution across the widest array of mechanical-soil properties. This finding is of special importance to this work because mechanical-soil properties dynamically change when percussive excitation is applied.

The main drawback to the upper limit analysis approach is that it is hinged upon the assumption that the soil is perfectly plastic and follows Drucker's postulate with its associated flow rule. This assumption is not valid for any granular soil, making it invalid for the JSC 1a used in this work. However work done by Davis in [1968] shows that the upper limit analysis can still provide a valid solution.

The argument made by Davis states that given the boundary conditions are not too restrictive, the assumed perfectly plastic material, $\phi = \phi_v$, serves as a upper bound to any soil that has $\phi_v < \phi$. The reasoning is that any real soil with $\phi_v < \phi$ will fail in a statically admissible field. Given that $\phi = \phi_v$, by definition, requires the highest possible statically admissible collapse for a soil; a real frictional soil must be bounded by the upper limit solution.

Although the upper limit analysis approach has been substantiated for the use of real soils, [Chen 1990] [Chen 1969], it is noted that because the ultimate failure load for real soils is higher than the yield point it is possible that ultimate failure be greater than the collapse load for an ideal plastic material. However, as shown in Chapter 5, the proposed perfectly plastic model, with its associated upper limit analysis approach, does reasonably predict real failure loads.

4.3.4.2 Mathematical derivation of the limit analysis theorem.

The actual concept behind limit analysis begins with the derivation of virtual work. The derivation deals with two separate and unrelated sets: the equilibrium set and the compatibility set. Each set, although independent of the other, is brought together to formulate the equation of virtual work:

The equation for the equilibrium set:

$$\int_A T_i dA + \int_V F_i dV = \int_V \sigma_{ij} dV$$

Equation 4-11

The equation for the compatibility set:

$$\int_A \dot{u}_i dA + \int_V \dot{u}_i dV = \int_V \dot{\varepsilon}_{ij} dV$$

Equation 4-12

The equation for virtual work:

$$\int_A T_i \dot{u}_i dA + \int_V F_i \dot{u}_i V = \int_V \sigma_{ij} \dot{\varepsilon}_{ij} dV$$

Equation 4-13

In the equation of virtual work the integrals are summed over the area and volume. T_i and F_i are traction and body forces and the state of stresses is given as σ_{ij}. $\dot{\varepsilon}_{ij}$ represents any set of strains or deformation compatible with the real or imagined displacement rate $\dot{u}_i$.

The equation of virtual work is in essence stating that there must be conservation of energy within the deformed body. The work being applied to the system must be equaled to the work being dissipated by the system. On the left hand side of the equation the traction and body forces multiplied by their respective rate of displacement represent the work that is being put into the system. The right hand side describes the amount of energy that is being dissipated by the system.

It is important to point out another critical assumption, when using the equation of virtual work the values are taken at the impending plastic collapse or incipient plastic flow. This means that any prior deformation to the system on the same order of magnitude as elastic deformation and the associated changes in geometry are neglected [Lubliner 1990]. To be stated another way, if equilibrium equations are established for the original state of the problem; it will be assumed that the overall dimensions at the brink of collapse will alter by only negligible amounts, so that the same equations can be used to describe the deformed state of the problem [Chen 1975].

Based upon these definitions and assumptions the upper bound limit analysis theorem is given as:

If a compatible mechanism of plastic deformation $\dot{\varepsilon}_{ij}^p$, $\dot{u}_i^p$ is assumed, which satisfies the condition $\dot{u}_i^p = 0$ on the displacement boundary A_u; then the loads T_i and F_i determined by equating the rate at which the external forces do work:

$$\int_{AT} \boldsymbol{T_i \dot{u}_i^p dA} + \int_V \boldsymbol{F_i \dot{u}_i^p dV}$$

to the rate of internal dissipation

$$\int_V \boldsymbol{D\left(\dot{\varepsilon}_{ij}^p\right) dV} = \int_V \boldsymbol{\sigma_{ij}^p \dot{\varepsilon}_{ij}^p dV}$$

will either be higher or equal to the actual limit load [Chen 1990].

As noted in the theorem, A_u, the displacement boundary is omitted because it must be fixed and rigid. If $\dot{u}_i^p \neq 0$ on the boundary layer, then an undeterministic amount of energy could be dissipated by the boundary and the unknown solution to the applied force could not be solved.

Based upon the assumptions made in this problem, the above theorem states that a conservative estimation for the critical loads at plastic failure can be approximated by knowing the failure geometry, a kinematically admissible velocity field, and the amount of dissipated energy based upon the flow rule.

4.3.4.3 Application of the Theorem

With the theorem stated, it becomes relevant to discusses its application and define the energy inputs as well the energy dissipation mechanism of the system. To more easily define the energy terms a graphical representation of the failure geometry is provided. The reader is encouraged to remember that, like the limit equilibrium method, the limit analysis method presupposes failure geometry. Through an optimization scheme the dimensions of the presupposed volume are adjusted to render a critical geometric state while minimizing the necessary applied forces.

For the numeric code derived in this research the geometry causing the soil failure was assumed to be a flat plow blade. The plow blade is a simplistic representation of the excavation scoop. This alteration in geometry is justifiable because the scoop, as shown in Chapter 2, had a flat back plate with very thin side walls. Given that the numeric model is a proposed procedural approach to solving a percussive excavation problem, the same methodology can be employed for other excavation implement geometries as long as an appropriate kinematically admissible velocity field is used.

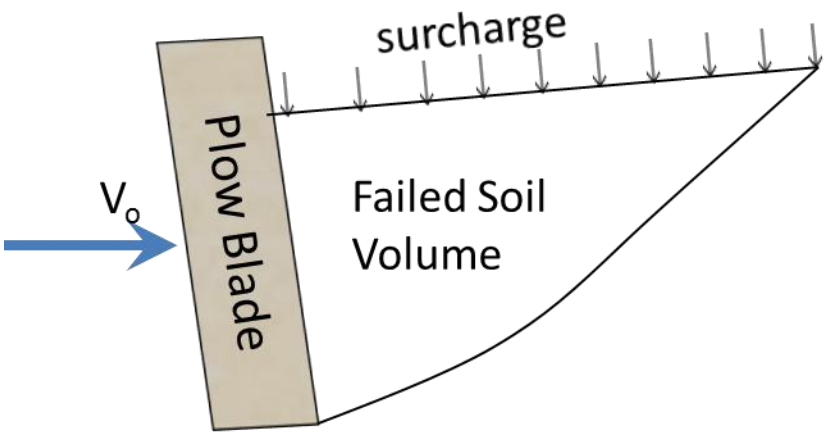

Figure 4-7: Graphic representation of failed soil volume.

As the plow blade moves through the soil at a prescribed velocity, V_o, the soil in front will fail in a shape similar to that shown in Figure 4-7. The surcharge is the compressive stress atop the failure volume which can be due to any number of factors, but most commonly is just the weight of the displaced soil which has built up during excavation.

When using the limit analysis approach to construct the failure geometry there are two types of deformation fields. The first is a family consisting of concurrent straight lines and concentric circles. The second consists of concurrent straight lines and logarithmic spirals. In the case of Mohr Coulomb soils, involving both cohesion and internal friction, the second type of deformation field is more representative of soil behavior [Chen 1975].

The failed soil volume is assumed to have three distinct regions: the first, region OAB, is a mixed zone which is subjected to the influence of the interface between the blade and the soil, this shape is triangular [Hettiaratchi 1975]. The second, region OBC, is a transition zone which is best approximated with a log spiral slip line failure surface [Chen 1973]. The final region, OCD, is the Rankine zone which, like the first, is represented by a triangular shape [Chen 1990].

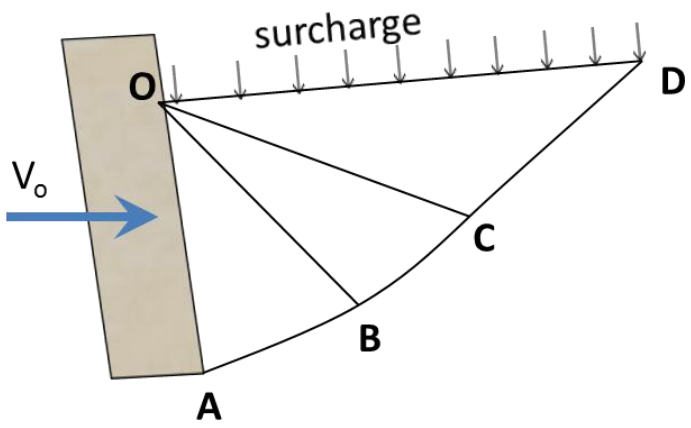

Figure 4-8: Failed soil volume broken down into its slip-line deformation fields: triangle OAB, logsprial OBC, and triangle OCD.

These three regions are defined by the geometric terms given in Figure 4-9. The log spiral curve has an exponential growth factor equal to $\theta\tan\phi$. θ is defined below, and ϕ is the internal friction angle of the soil.

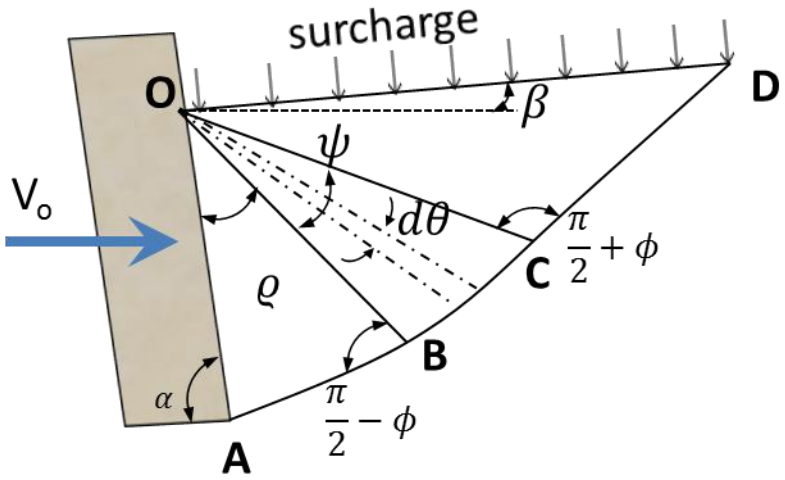

Figure 4-9: Geometric variable definitions of soil failure volume.

The energy input into the system, as well as the energy dissipated by the system, is defined according to the geometry and symbols just presented. For ease of discussion, only the energy involved in static failure will at present be discussed. After the limit analysis is established for static failure the effects of percussion will be examined and a new dynamic failure model is presented in Section 4.6.

4.3.4.4 Static Energy Failure

The perfectly plastic idealization of the Coulomb yield criterion implies that any deformation is plastic and must be accompanied by an increase in volume. This increase in volume also means that the discontinuity velocity along the slip line must carry with it a separation velocity component. This idea is modeled in Figure 4-11.

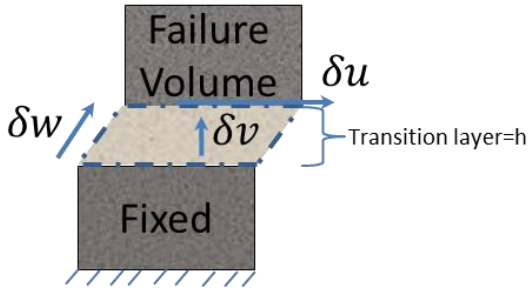

Figure 4-10: Mode of deformation in a transition layer of a perfectly plastic material.

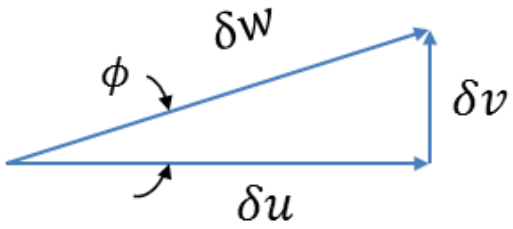

Figure 4-11: Slip line velocity profile.

$$dv = du * tan\phi$$

Equation 4-14

The associated flow rule requires that the tangential velocity *du*, be supplemented by a separation velocity *dv*. This separation velocity is defined as *dv=du*tanϕ.* The implication of this separation velocity is that the relative velocity change *dw* in a narrow transition zone bounded by two parallel planes must form an angle ϕ. This is shown in Figure 4-12.

In addition to the separation velocities along the boundary layer, another velocity is defined in Figure 4-12, $V_{o\text{-}AO}$. $V_{o\text{-}AO}$ is the velocity of separation at the interface between the soil and the tool blade. Different approaches are used to address the direction of this velocity. For this work it was assumed that the wall only behaved frictionally and hence there is no separation velocity.

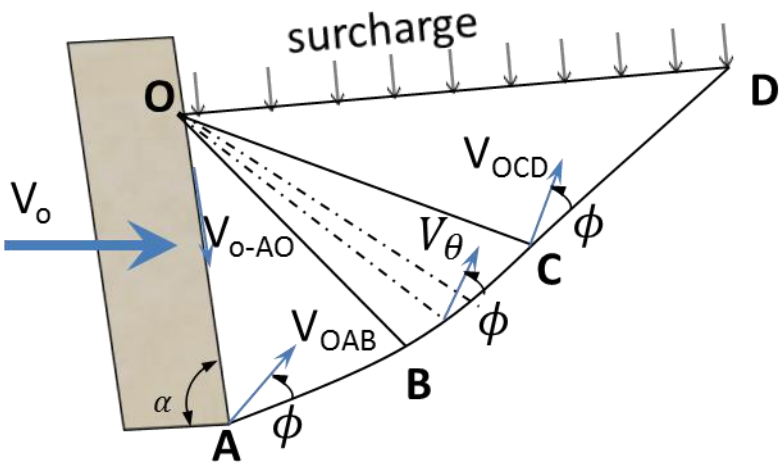

Figure 4-12: Kinematically admissible velocity field of failure volume.

Referring back to the equation of virtual work, Equation 4-13, the energy being applied to the system is a function of the body and traction forces multiplied by the velocity projected in the direction of the applied force. Due to the simple nature of the problem examined in this work, only one traction force was considered, the plow blade pressure force represented as P_{pe} in Figure 4-13. P_{pe} can be broken down into its normal and tangential components for geometric calculation simplicity. The direction of P_{pe} is dependent on δ, which is the angle of the soil-wall interface friction. It is often assumed that this angle is some proportional factor of the internal friction angle of the soil. For this work it was assumed that δ was equivalent to the frictional component of the internal friction angle, ϕ_μ. The body forces of a failure volume are equal to

the mass of each region multiplied by the environmental gravity constant. Gravity was left as an adjustable parameter in this work to allow for force calculations for low-gravity planetary surfaces. The surcharge force is commonly assumed to be uniform across OD and is simply added to the body force calculations of region OCD.

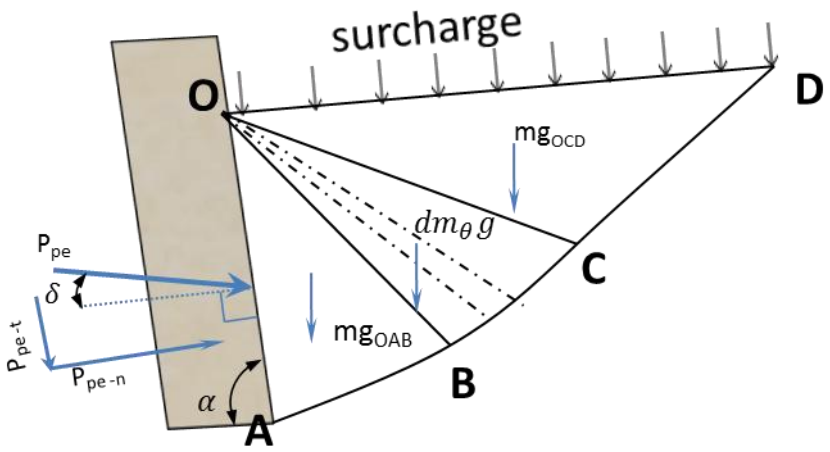

Figure 4-13: Forces acting on the soil failure volume.

In order to understand the energy that is being applied to a failure volume both the forces and the velocities need to be understood. Figure 4-13 shows the forces involved in the system and Figure 4-14 shows the velocity components within the system along the direction of the different applied forces. The velocities presented in Figure 4-14 are all components of the applied velocity of the plow blade, V_o.

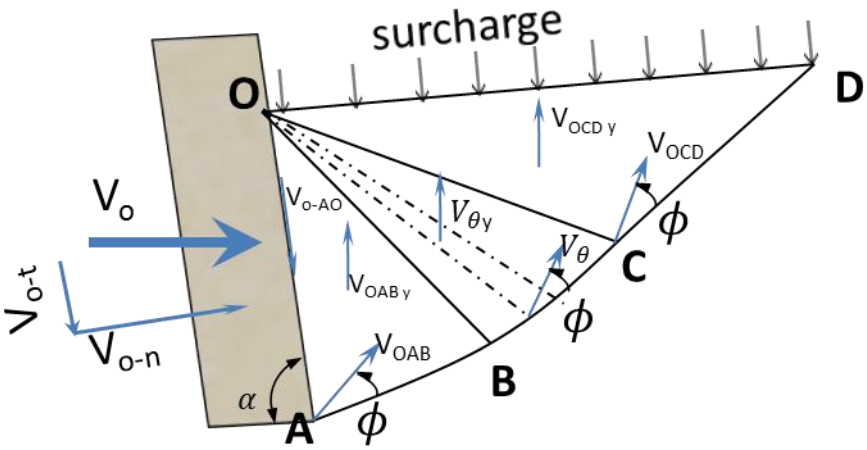

Figure 4-14: Projected velocity components in direction of applied forces.

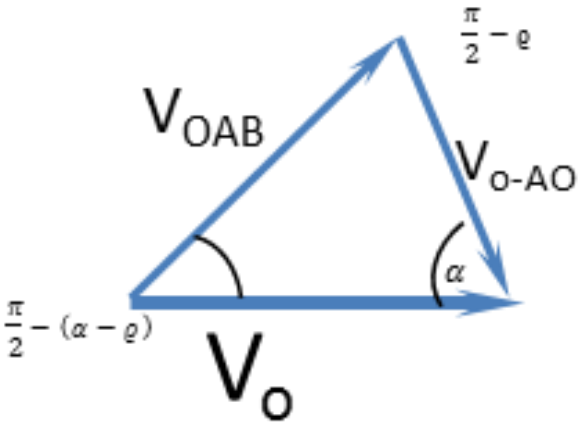

Figure 4-15: Velocity triangle relating V_O, V_{OAB}, and $V_{o\text{-}AO}$.

$$\bar{V}_{OAB} = V_o \left(\frac{\sin(\alpha)}{\cos(\varrho)} \right)$$

Equation 4-15

$$\bar{V}_{o\text{-}AO} = V_o \left(\frac{\cos(\alpha - \varrho)}{\cos(\varrho)} \right)$$

Equation 4-16

$$\vec{V}_\theta = \vec{V}_{OAB} e^{\theta \tan(\phi)}$$

Equation 4-17

$$\vec{V}_{OCD} = \vec{V}_{OAB} e^{\psi \tan(\phi)}$$

Equation 4-18

Referencing Figure 4-9, for geometrical definitions; Figure 4-14, for velocity definitions; and Figure 4-13, for force definitions the following energy input terms, per unit width, can be defined:

$$Work_{OAB} = mgV_{OAB_y}$$

Equation 4-19

$$Work_{OBC} = \int_V \gamma \, V_{\theta_y} dV$$

Equation 4-20

$$Work_{OCD} = mg_{OCD}V_{OCD_y}$$

Equation 4-21

$$Work_{Ppe} = Ppe_n V_{o_n} + Ppe_t V_{o_t} = Ppe(cos\delta)V_o(sin\alpha) + Ppe(sin\delta)V_o(cos\alpha)$$
$$= PpeV_o(cos\delta sin\alpha + sin\delta cos\alpha) = PpeV_o sin(\alpha + \delta)$$

Equation 4-22

These terms are defined in their most general sense. Once the complete derivation is presented for the percussive upper limit analysis approach in Section 4.6 these terms will be explicitly defined using only the applied velocity.

4.3.4.4.1 Section OBC

Before the energy dissipation of the system is presented, the failure geometry of zone OBC must be discussed. As stated previously, the slip lines of the failure volume break the soil into simple triangles and a logarithmic spiral. The triangular sections OAB and OCD are assumed to behave as rigid blocks. The log spiral section, however, does not move as a uniform rigid body but rather as a deformable body. Graphically it can be represented as shown in Figure 4-16 where the entire region is made up of an infinite number of discrete triangles.

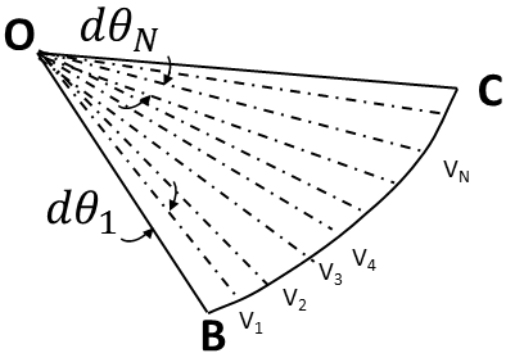

Figure 4-16: Velocity profile for logarithmic deformation section OBC.

Each incremental dθ is its own rigid body moving at its own velocity. In [Chen 1990] Chen derived the incremental displacement velocity at any location θ along the spiral to be:

$$V_i = V_{\theta'=}V_{OB}e^{\theta_i tan\phi}$$

Equation 4-23

4.3.4.5 Energy Dissipation

In the upper bound limit analysis theorem the dissipation of energy is defined as:

$$\int_V \boldsymbol{D}\left(\dot{\boldsymbol{\varepsilon}}_{\boldsymbol{ij}}^{\boldsymbol{p}}\right)\boldsymbol{dV} = \int_V \boldsymbol{\sigma}_{\boldsymbol{ij}}^{\boldsymbol{p}}\dot{\boldsymbol{\varepsilon}}_{\boldsymbol{ij}}^{\boldsymbol{p}}\boldsymbol{dV}$$

Equation 4-24

To apply this definition the mode of deformation in a transition layer is reviewed. The transition layer is where the velocity discontinuities and energy dissipation manifest themselves. Figure 4-10 and Figure 4-11 are given once more to represent perfectly plastic failure. Figure 4-17 provides a simple graphic of the applied forces for a discrete volume element.

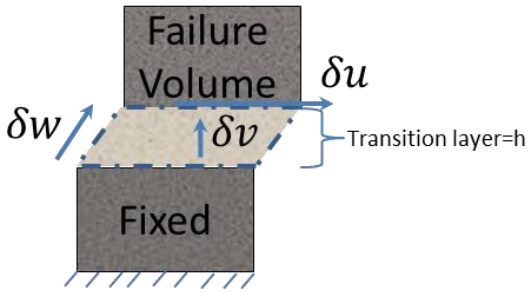

Figure 4-10: Mode of deformation in a transition layer of a perfectly plastic material.

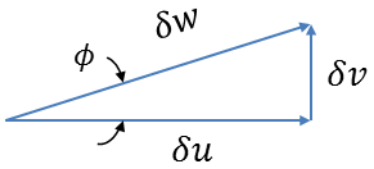

Figure 4-11: Slip line velocity profile.

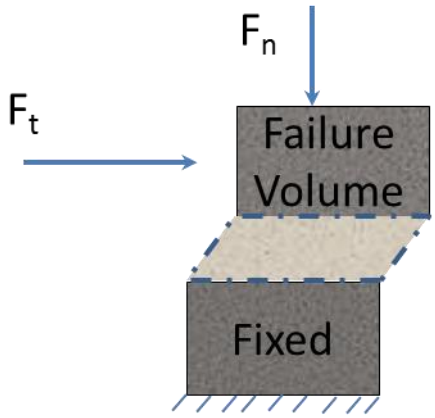

Figure 4-17: Applied forces for a discrete volume element along the failure boundary layer.

The applied force is broken down to its components and the resulting dissipative work done by the system is given as:

$$D = F_t * du - F_n * dv$$

If the vertical velocity component is put in terms of the horizontal velocity through the flow rule then:

$$D = F_t * du - F_n * du * tan\phi$$

Putting this in terms of shear strain gives:

$$D = F_t h * \dot{\gamma} - F_n h * \dot{\gamma} tan\phi$$

To determine the energy dissipation per unit volume all terms are divided by the height, h, length, l, and width, b of the transition layer:

$$\frac{D}{b * h * l} = \frac{F_t}{bl} * \dot{\gamma} - \frac{F_n}{bl} * \dot{\gamma} tan\phi$$

Simplifying the equality and putting it in terms of stresses yields:

$$D_V = \dot{\gamma}(\tau - \sigma tan\phi)$$

Based on the Mohr Coulomb criteria this states that the dissipative energy per unit volume is equal to the shear strain rate multiplied by the soil cohesion. The shear strain can further be simplified, for application in limit analysis, by equating it to the velocity discontinuity at the boundary surface multiplied by cosϕ.

$$D_V = \dot{\gamma} c = \Delta V cos\phi * c$$

Equation 4-25

The following equations represent work dissipated by a failure volume moving across fixed soil, per unit width.

$$Energy\ Dissipation\ on\ AB = c * (\overline{AB}) * V_{OAB} * cos\phi$$

Equation 4-26

$$Energy\ Dissipation\ on\ BC = \int_{Arc\ Length\ of\ BC} (c * V_{\theta'} * cos\phi) dL$$

Equation 4-27

$$Energy\ Dissipation\ on\ CD = c * (\overline{CD}) * V_{OCD} * cos\phi$$

Equation 4-28

[Chen 1975] states that the energy dissipated due to deformation within OBC is equivalent to the energy dissipated along the velocity discontinuity surface BC. Therefore:

$$Energy\ Dissipation\ within\ OBC = \int_{Arc\ Length\ of\ BC} (c * V_{\theta'} * cos\phi) dL$$

Equation 4-29

The velocity discontinuity pertaining to the line OA contributes to two different forms of energy dissipation. The first deals with the losses associated with the soil/tool interface friction, the second with the adhesive force of the soil to the plow blade.

Just as the soil particles have cohesive forces amongst themselves they too have a similar adhesive force, c_a, toward the tool surface. Logically the maximum value that c_a can have is equal to the cohesive force of the soil, c. For reasons of simplicity, it was assumed in this work that c_a=c. The numeric value for both c and c_a will be discussed in Section 4.5.3.2.

$$Soil/Tool\ Interface\ Frictional\ Loses\ on\ OA = Ppe_n * tan\delta * V_{o-AO}$$

Equation 4-30

$tan\delta$ represents the coefficient of friction that exists between the soil and the tool blade. V_{o-AO} is the component of the velocity which is collinear to the frictional force on the interface.

$$Adhesion\ Plow\ Blade\ Losses\ on\ OA = c_a * (\overline{OA}) * V_{o-AO}$$

Equation 4-31

After applying geometric simplifications and adding Equation 4-30 to Equation 4-31 the total energy dissipated along OA is defined as:

$$Total\ Energy\ Dissipation\ on\ OA = [Ppe * sin\delta + c_a * (\overline{OA})]V_{o-AO}$$

Equation 4-32

4.4 Percussion

4.4.1 Introduction

The majority of the research done for excavation reaction force reduction has dealt with vibratory excavation. Vibratory excavation causes the soil to fail both passively when the plow blade is being driven forward and actively when the plow blade is driven backward. Vibratory excavation is defined as a carriage moving forward at a constant velocity with an excavator implement in the front being vibrated at a prescribed frequency and amplitude. Because the amplitude is fixed the power requirements for very stiff soils increase dramatically. However, having fixed amplitude enables the displacement, velocity, and acceleration to always be kinematically derived.

Percussive excavation, on the other hand, is defined as a carriage moving forward at a constant velocity with an excavator implement in the front being periodically hit with a prescribed amount of energy at a prescribed frequency. Because the displacement amplitude of the excavator implement is unknown a straight forward kinematic analysis cannot be used to determine acceleration. Instead, a material and energy analysis is performed based on the applied mechanical energy and soil stiffness.

4.4.2 Percussive System

The idea behind a percussive system is relatively simple; a periodic impact is applied to a control volume of soil and the impact energy causes a dynamic response altering the soil properties. The dynamic response is dependent on the soil stiffness, the amount of soil being displaced, and the damping properties of the soil. The theoretical model proposed in this work is only concerned with the peak acceleration of the soil, and consequently the damping properties within the soil are not considered.

To obtain the peak acceleration the displacement of the soil must be calculated. This is accomplished by knowing the input energy and the soil stiffness. The input energy is regulated by a mechanical spring used in the percussor.

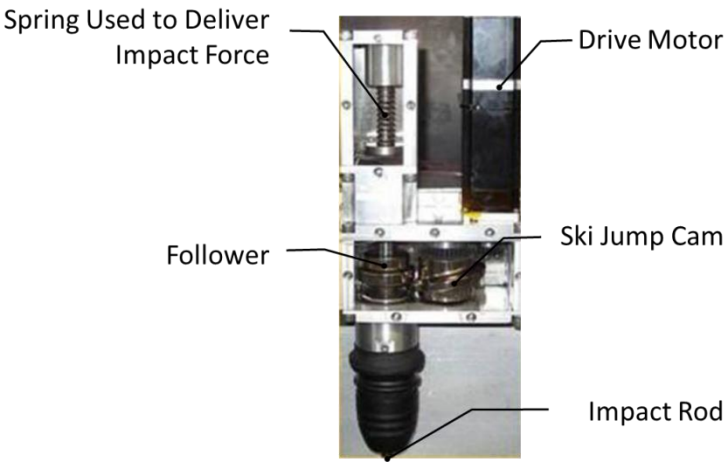

Figure 4-18: Percussion mechanical mechanism.

The motor-driven percussor works by using a gear train to spin a ski jump cam that engages a follower whose vertical displacement compresses a mechanical spring. The skip jump cam is designed to move the follower vertically until it reaches the height of the cam where a discontinuity in the cam's profile allows the follower to disengage. At this point the mechanical spring, which was compressed by the follower, is no longer constrained and can transfer its potential energy into kinetic energy through an attached impact rod. The impact rod is driven down and delivers an impact to the top of the excavation implement. After the spring has released its energy the follower is at its lowest position. At this point the follower engages the ski jump cam again to repeat the process.

The frequency of the applied impact is controlled by the user through the drive motor current and the impact energy is controlled by the mechanical spring stiffness. The mechanical spring displacement is geometrically constrained.

4.4.3 Soil Displacement and Acceleration

The fact that applied impact energy is regulated allows for the conservation of energy principle to be applied.

$$Spring\ Energy = \frac{1}{2} * k_{spring} * {x_{spring}}^2$$

$$Work\ Done\ to\ Soil = \int Force\ dx$$

$$Force = \sigma * A$$

$$Force = G * \varepsilon * A$$

$$Force = \frac{G * x * A}{l_o}$$

$$Work\ Done\ to\ Soil = \frac{Gx^2A}{2l_o}$$

$$Soil\ Displacement\ Due\ to\ Spring\ Energy = \sqrt{\frac{2l_o Spring\_Energy}{GA}}$$

Equation 4-33

By looking at the assumed slip line network of the soil failure volume the area and initial length of the displaced soil can be determined.

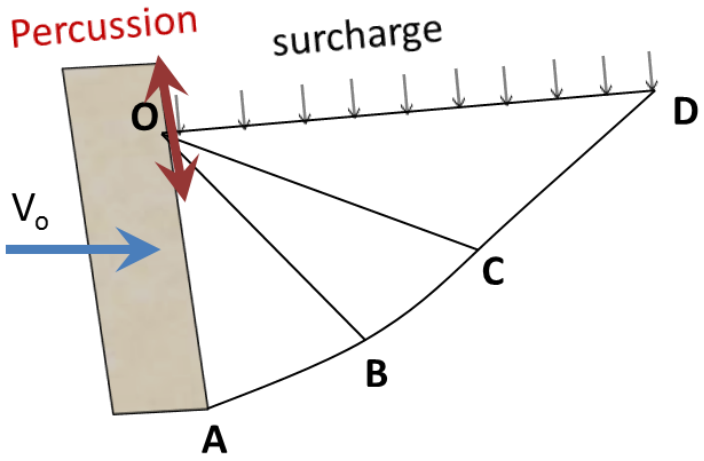

Figure 4-19: The application of percussion to the control volume.

It is assumed, for simplicity purposes, that the area is $\overline{OD} * width$ and the initial length of the displaced soil is the depth of the scoop, or $\overline{OA}$. Inputting these values into Equation 4-33 gives

$$Soil\ Displacement = \sqrt{\frac{2 * \overline{OA} * Spring\_Energy}{G * width * \overline{OD}}}$$

Equation 4-34

$$Soil\ Velocity = 2\pi * applied\ frequency * \sqrt{\frac{2 * \overline{OA} * Spring\_Energy}{G * width * \overline{OD}}}$$

Equation 4-35

$$Soil\ Acceleration = (2\pi * applied\ frequency)^2 * \sqrt{\frac{2 * \overline{OA} * Spring\_Energy}{G * width * \overline{OD}}}$$

Equation 4-36

4.4.4 Soil Stiffness

A soil's shear stiffness is not a constant. It depends on the state of compaction of the soil as well as the level of strain applied to the soil. [Seed 1970][Seed 1984][Hardin 1972] all show that all as the strain on dry sand increases there is degradation to the shear modulus. Discussed in the next section are the adjustments that were made to the soil-mechanical properties on account of percussive effects. It will be shown that in order to account for the dynamic changes to the soil-mechanical properties both the internal friction angle and cohesion are given as functions of percussive parameters. Because the soil-mechanical properties are being adjusted to account for dynamic effects, the shear stiffness is given as a function of the internal friction angle and not the applied strain.

Analytic work done to determine the effects of seismic excitations on ground settlements ubiquitously use hysteresis loops to produce a simplified definition of the shear modulus [Seed 1970][Silver 1969][Seed 1984][Hardin 1972a][Hardin 1972b][Assimaki 2000]. By taking the slope between the two extreme points, A-A', defined by the loop the modulus is approximated.

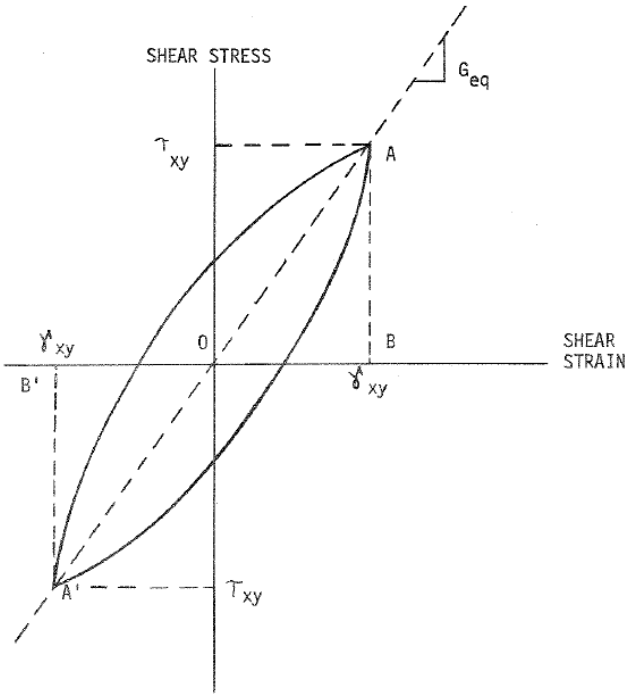

Figure 4-20: Shear modulus based on hysteretic stress-strain properties [Seed 1969].

[Seed 1984] provides a relationship defining the magnitude of the shear modulus for dry cohesionless sands as a function of the void ratio and the mean effective stress. Equation 4-37 has also been validated for both undisturbed cohesive soils, as well as sands [Seed 1970]. It is noted that this equation is based off of work done in [Hardin 1972a] and [Hardin 1972b].

$$G_{max} = 14760 * \frac{(2.973 - e)^2}{1 + e} (OCR)^a (\sigma_m)^{1/2}$$

Equation 4-37

e = void ratio
OCR = overconsolidation ratio
a = a parameter that depends on the plasticity index of the soil
σ_m = mean principal effective stress in psf. Defined as

$$\sigma_m = \frac{\sigma_v + 2\sigma_h}{3}$$

Equation 4-38

σ_v = vertical stress
σ_h = lateral stress

The void ratio is the volume of fluid space (air) divided by the volume of the soil (soil particles). It is directly related to the relative density through the following equation:

$$e = \frac{Relative\ Density * (e_{min} - e_{max})}{e_{max}}$$

Equation 4-39

The values for e_{max} and e_{min} for JSC 1a are found in [Alshibi 2009].

4.4.4.1.1 Power Relationship of Confining Stress

A great deal of data has been published that shows that G_{max} varies with the square root of the mean confining stress [Drnevich 1970][Hardin 1965][Hardin 1966][Hardin 1968][Lawrence 1965]. This, of course, is what is represented in Equation 4-37. However both [Hardin 1972b] and [Silver1969] recognized that at large strain amplitudes the modulus begins to vary with a higher exponential growth factor. Results presented in [Silver 1969] demonstrate this characteristic. On account of the cited variability of the exponent, the empirical results found in [Alshibi 2009] were used to determine if a more appropriate exponent should be used with Equation 4-37 to represent JSC 1a. It was concluded that .65 is a better fit.

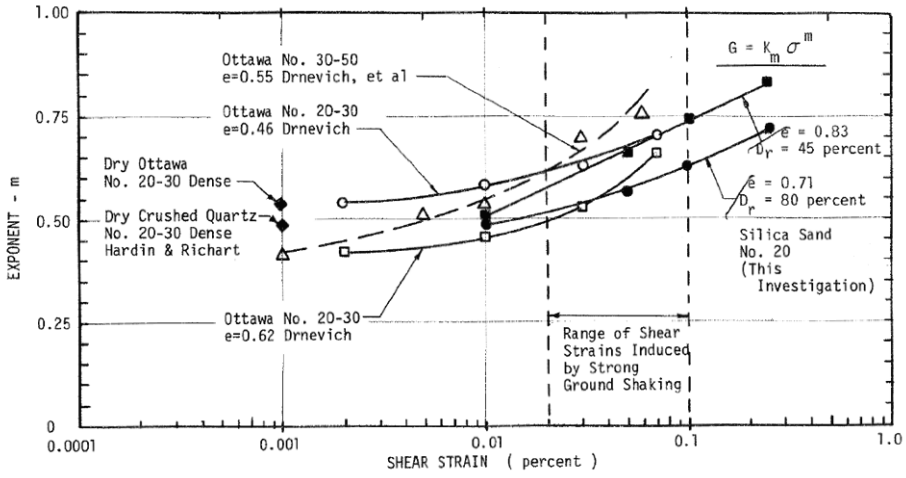

Figure 4-21: Effect of shear strain amplitude on measured exponent (m) [Silver 1969].

4.5 Vibration effects on Mechanical Soil Properties

4.5.1 Introduction

Most soil failure problems that deal with earthquake engineering and retaining wall geometry are resolved using a static failure analysis. At times, if the excitation is significant, the inertial effects are taken into account. The approach most commonly used is the Mononobe Okabe equation [Seed 1970 Design][Zheng 2007][Kramer 1996]. The inhibiting factor of the Mononobe Okabe equation is that it is only useful as long as the soil-mechanical properties remain constant. The cut-off point at which this no longer holds is often cited as acceleration magnitudes greater than .3-.5g [Seed 1970 Design][Chen 1990][Kramer 1996].

As already shown in Chapter 3, percussive excavation does indeed alter the mechanical-soil properties. The simplistic Mononobe Okabe approach was not a viable option for this work and consequently was not considered for examining the effects of percussion. Still, the upper limit analysis approach is only meant to deal with static failure. In order to utilize its procedural method a relationship was created between the percussive parameters and the defining soil-mechanical properties.

4.5.2 Barkan's Work on Internal Friction Angle

Unpredicted and undesired eccentric forces can plague any type of machinery. The ramification of such forces is unsolicited vibration. Vibrations can cause fatigue to a system, excess wear, or simply undesired noise. However, when looking at a sandy foundation, vibrations can also cause reduction in soil integrity. It was this initial reason that early work was done to investigate the effects of vibration on sand.

G.I. Pokrovsky and associates were some of the first to experimentally investigate the influence of vibrations on a soil's internal friction. A little of their work is presented in Figure 4-22. Their conclusion was that the coefficient of internal friction depends on the kinetic energy of vibrations. As the energy increases, the coefficient decreases and approaches a value 25 to 30 percent smaller than before vibrations [Barkan 1962] [Pokrovskiy 1934].

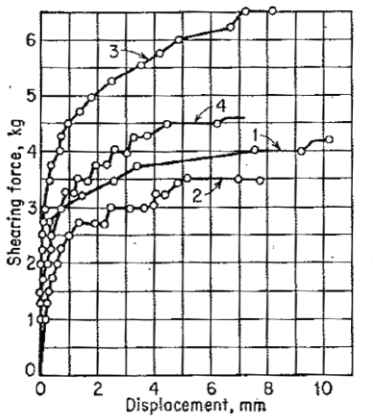

Figure 4-22: Effect of shearing force on displacement, with and without vibrations (data from [Pokrovskiy 1934]). Figure from [Barkan 1962].

In Figure 4-22 Test 1 was conducted on freshly filled sand without vibrations. Test 2 involved vibrations with an amplitude of .5 mm and a frequency of 140 Hz. Test 3 was conducted after the vibrations ceased. Test 4 involved vibrations of the same frequency as in test 2 but with amplitude of only 0.15mm [Barkan 1962].

Although Pokrovsky's work was insightful, it did not lend itself well to a functional relationship between soil-mechanical properties and vibration. D.D. Barkan used Pokrovsky's work as a stepping stone into his own soil vibration research. Barkan created and used an experimental shearing device and subjected it to vibrations, Figure 4-23. The influence of vibrations on the coefficient of internal friction was evaluated by comparing the value determined in the absence of vibrations with the value obtained during soil vibrations, all other conditions remaining equal [Barkan 1962].

Based on the results of his experiments, Figure 4-24 shows the relationship between the tangent of the internal friction angle, tan ϕ, and the amplitude of vibrations for dry medium-grained sand with frequency being held constant. Figure 4-25 shows the dependence of tan ϕ for the same sand, but now with the angular frequency varying and the amplitude of vibration remaining constant.

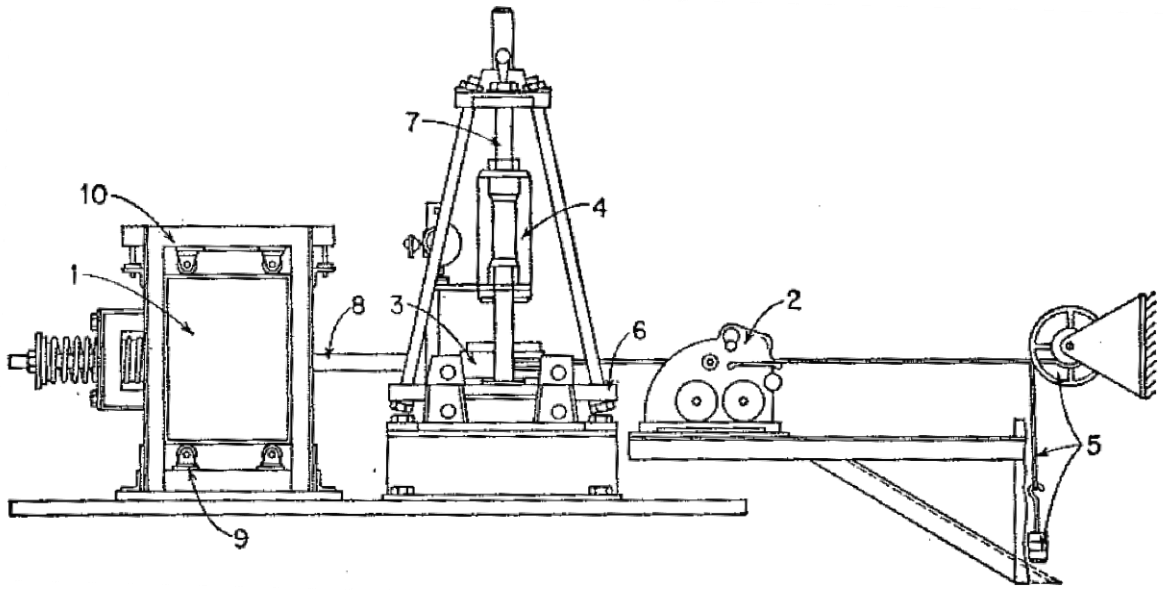

Figure 4-23: Barkan's experimental test stand: 1. motor driven vibrator; 2. recording instrument; 3. soil box; 4. spring jack; 5. application of shearing stresses; 6. vibrating platform; 7. jack supports; 8. trunbuckle; 9. rollers; 10. guide frame [Barkan 1962].

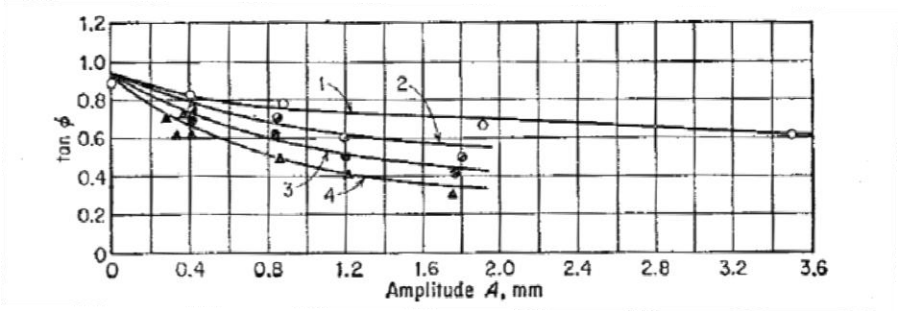

Figure 4-24: Relationship between the coefficient of internal friction of dry medium-grained sand and the amplitude of vibrations: (1) ω= 25 hz; (2) ω=144 hz; (3) ω=177 hz; (4) ω=208 hz [Barkan 1962].

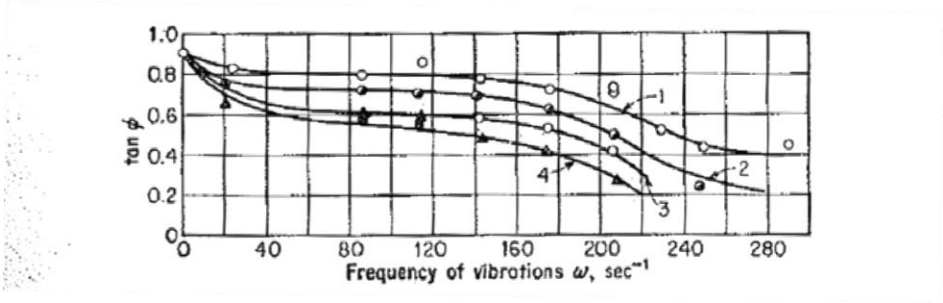

Figure 4-25: Relationship between the coefficient of internal friction of sand and the frequency of vibrations: (1) A=.35 mm; (2) A=.85 mm; (3) A=1.2 mm; (4) A=1.6 mm [Barkan 1962].

From these figures it was concluded by Barkan that tan ϕ depends on both the amplitude as well as the frequency of vibrations [Barkan 1962]. To demonstrate this fact Barkan created a non-dimensional variable called the relative acceleration magnitude and plotted it against tanϕ, Figure 4-26. This variable is defined as the magnitude of soil acceleration divided by the gravitational constant.

$$\eta = \frac{A\omega^2}{g}$$

Equation 4-40

Where:

A = the amplitude of displacement

ω = the frequency of vibration

g = the gravitational constant

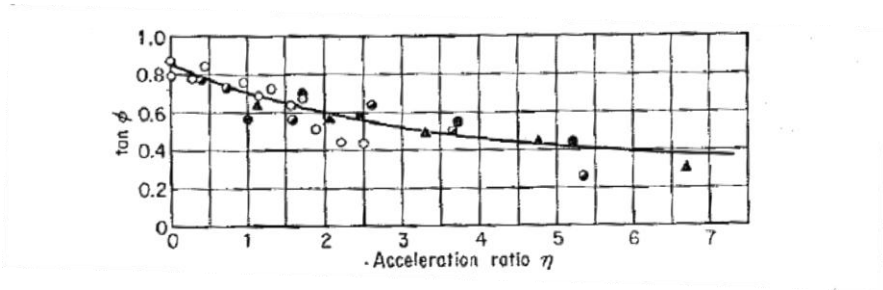

Figure 4-26: Relationship between the coefficient of internal friction of sand and the relative acceleration of vibration [Barkan 1962].

Starting with these findings, other scientists, [Ermolaev 1968][Balyshkin 1966],refined some of the original conclusions made by Barkan. Ermolaev and Senin determined that the exponential decrease in the internal friction angle doesn't actually occur on the onset of vibration, but rather at a threshold value. This coincides more with the general consensus in earthquake engineering regarding the applicability of the Mononobe Okabe approach. The threshold of invalidity generally being accepted as accelerations greater than .3g [Seed 1970 Design][Chen 1990][Kramer 1996].

Ermolaev and Senin deduced that there are roughly 3 distinct and separate stages that shear strength goes through during its degradation. In stage one the soil roughly maintains its static mechanical properties. In stage two the soil's mechanical properties begin to be compromised, but the reduction in the shear integrity of the soil is still relatively minor. At stage 3 the mechanical properties are dramatically and severely altered and the shear strength exponentially decays. Ermolaev and Senin go on to say that the difference between stage 1 and 2 is minimal and of lesser importance that the transition from stage 2 to 3. Consequently they characterize the soil transition as simply being before and after 'trans-threshold', the transition value between stage 2 and stage 3 [Ermolaev 1968]. Important observations made, in regards to the trans-threshold behavior, were: the decay doesn't actually reach zero but asymptotically approaches a minimum shear strength value, τ_{min}; the acceleration magnitude at which the trans-threshold takes place varies depending on the soil type, as well as the static surcharge [Ermolaev 1968].

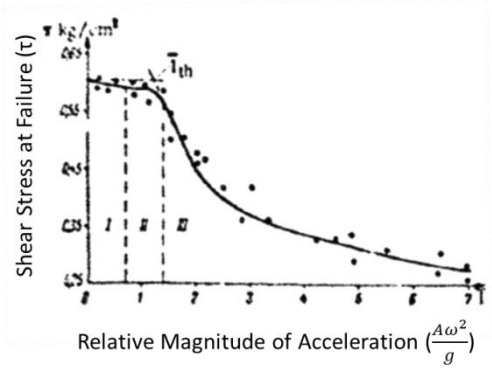

Figure 4-27: Dependence of shear stress on the relative acceleration magnitude. Regions I,II, and III are shown to demonstrate the different stages of degradation of sandy loam due to vibrations [Ermolaev 1968].

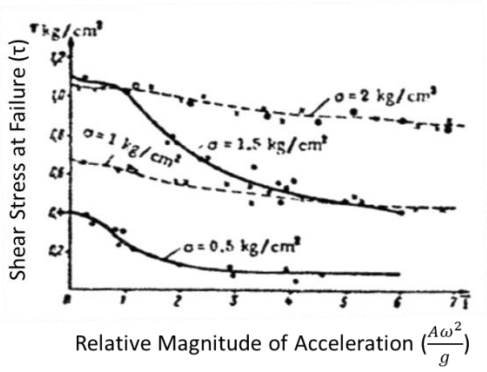

Figure 4-28: Change of shear strength of cohesive (broken line) and cohesionless (solid curve) soil under different surcharges [Ermolaev 1968].

The findings presented by both Barkan and Ermoloav are in agreement with the empirical test data presented in Chapter 3. The noted asymptotic value referenced by Ermoloav is the effect of the residual surface-to-surface internal fiction. The effects of dilatancy are removed as the agitation energy reaches a sufficient magnitude to disengage the particles along the shear plane boundary layer.

Barkan [1962], Ermoloav [1968] and Balyshkin [1966] each present a characteristic relationship between the internal friction angle and the relative acceleration magnitude. Although their nomenclature is different the proposed equation in each is nearly the same. For Ermoloav the equation only pertains to the relationship at soil accelerations above the trans-threshold value. The equation, as defined in [Barkan 1962], is:

$$tan\phi_{dynamic} = (tan\phi_{static} - tan\phi_{min})e^{-\beta\eta} + tan\phi_{min}$$

Equation 4-41

Where:

$tan\phi_{static}$= value of coefficient of internal friction without vibrations

$tan\phi_{min}$= limit value of coefficient of internal friction

η=ratio of accerlationof vibrations to acceleration of gravity ($\frac{A\omega^2}{g}$)

β=coefficient for determining the effect of vibrations for soil type

Given the kinematic relation between percussion and vibration are different, this work uses Equation 4-36 divided by g to define η.

4.5.3 Interrelationship between Mechanical Properties of Basaltic Simulant

After the success of NASA's Apollo program all the recoded data pertaining to the moon were gathered and compiled into a resource book in 1991 called Lunar Sourcebook. In Chapter 9 of that book the physical properties of the lunar surface are discussed along with the in situ testing performed by the astronauts. It is noted that due to the very limited access of lunar soil samples for the geotechnical engineers on Earth extensive experimental work was difficult. To not be constricted to small amounts of test data, a simulant was created which was meant to mimic specific mechanical properties of lunar regolith. The simulant created was a basaltic simulant. Work from [Mitchell 1972] and [Mitchell 1974], presented in the Lunar Sourcebook, show how the basaltic simulant compares with lunar regolith.

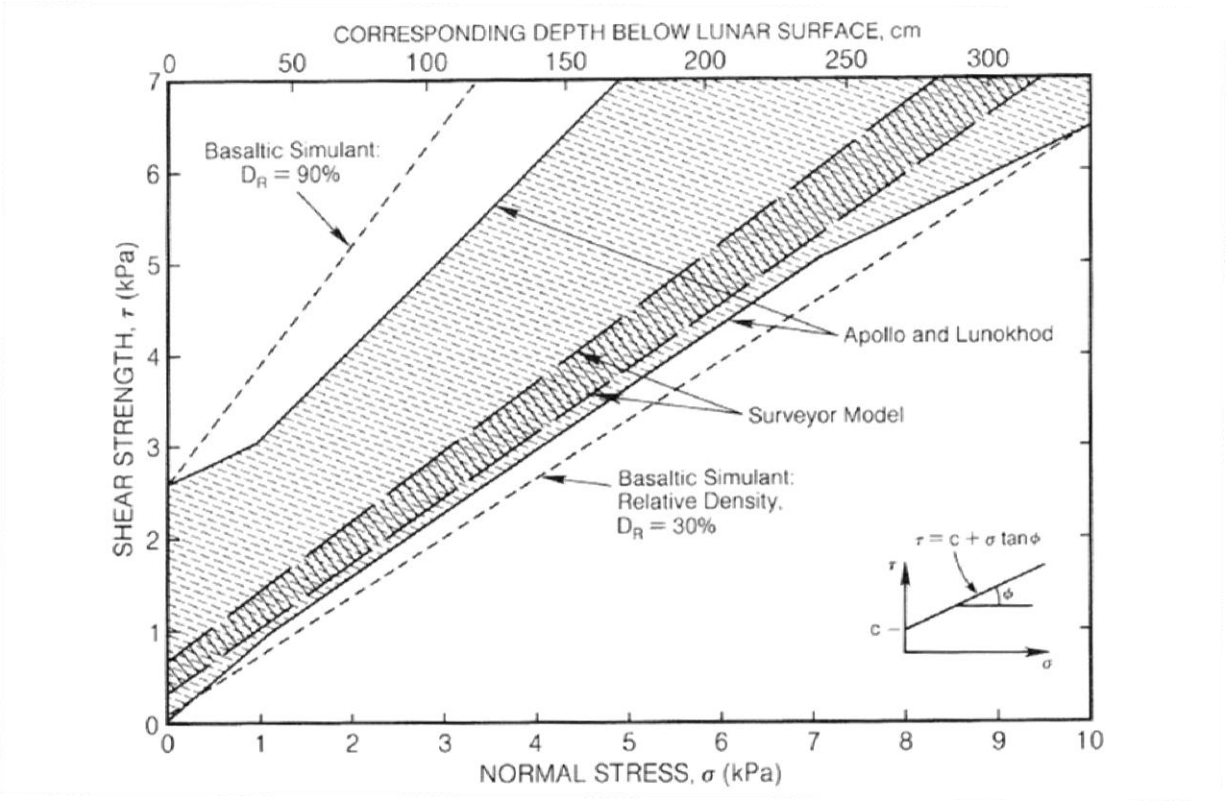

Figure 4-29: Calculated in situ shear strengths of lunar soil, plotted as a function of normal stress and corresponding depth below the lunar surface (data from[Mitchell 1972][Mitchell 1974]). Envelopes of shear strength are shown for basaltic simulant at relative densities of 30% and 90% [Carrier 1991].

Figure 4-29 shows that the mechanical properties of lunar regolith, as tested during the Apollo missions, fall within a range of tested mechanical properties given by the basaltic simulant. The upper and lower limits of this range are defined by the relative density of the simulant. Based on the similarity between the mechanical properties of the simulant and lunar regolith, the interrelationship between the mechanical properties of one should be quite similar to the interrelationship between the mechanical properties of the other. Thus, the relationships established for the basaltic simulant in the Lunar Sourcebook are hypothesized to be the same as those that exist for lunar regolith, as well as the basaltic simulant which was used for testing in this research, JSC-1a [Carrier 2010].

Figure 4-30 presents the interrelationship of the mechanical properties: relative density, internal friction angle, and cohesion for the tested basaltic simulant.

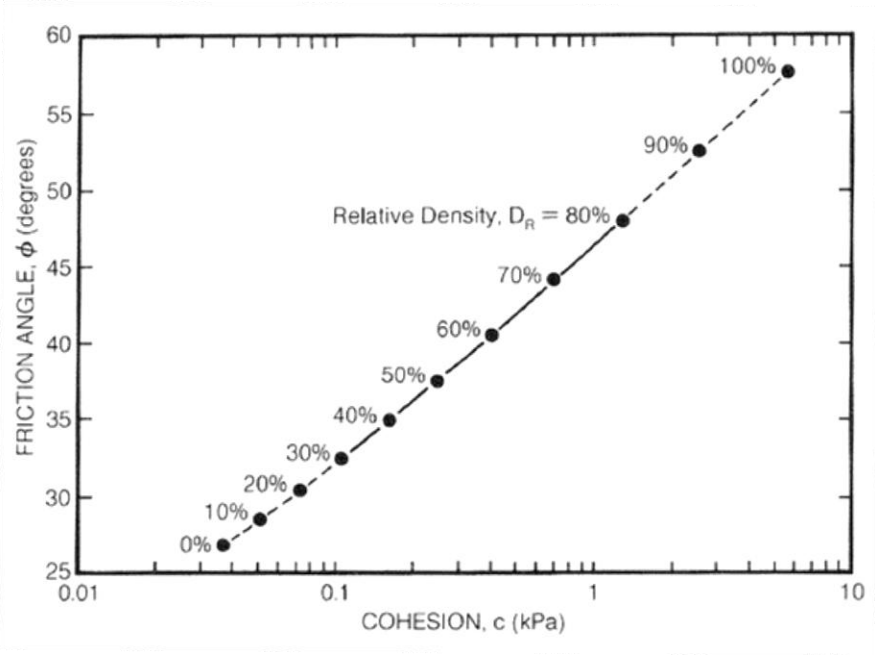

Figure 4-30: Relationship between internal friction angle, cohesion, and relative density basalt simulant (data from Mitchell 1972][Mitchell 1974]) [Carrier 1991].

To better understand this data a brief description of relative density is provided. Following this description, a relationship between the internal friction angle and cohesion, as well as a relationship between the internal friction angle and density are presented.

4.5.3.1 Relative Density

The bulk density of a given soil can vary over a wide range, depending on how the particles are assembled. For example, a soil consisting of uniform spheres could be arranged in a face-

centered cubic configuration or a hexagonal close packing configuration. The face-centered cubic configuration is the loosest possible stable arrangement while the hexagonal close packing arrangement is the densest. The difference in these arrangements is a 30% reduction in volume without deforming or breaking any of the particles. Hence, an ideal soil that only contains uniform spheres would lie somewhere between these two extremes. In real materials, however, these limits vary from soil to soil, depending on the particle size distribution, shape, texture, orientation, and specific gravity [Carrier 1991]. The relative density of a soil is the percent of compaction between the soils loosest state to its densest state. This idea is explained in equation form as follows:

$$D_R = \frac{\rho_{max}}{\rho} * \frac{\rho - \rho_{min}}{\rho_{max} - \rho_{min}} * 100\%$$

Equation 4-42

ρ = in situ density of soil

ρ_{max} =maximum possible density

ρ_{min} = minimum possible density

Based on Method A of ASTM-D4253 standard the maximum index density for JSC-1a is 2.016 g/cm^3, and based on ASTM-D4254 standard the minimum index density for JSC-1a is 1.556 g/cm^3 [Alshibli 2009]. Carrier [1991] states that no direct relative density measurements have been made of returned lunar core samples, instead an average specific gravity is assumed of 3.1 and the respective minimum and maximum density are approximated as 1.15 g/cm^3 and 1.82 g/cm^3[Carrier 1991][Mitchell 1974][Houston 1974].

4.5.3.2 Dynamic Equations for Cohesion and Density

Using Figure 4-30, characteristic equations defining the cohesion and relative density in terms of the internal friction angle for basaltic simulant can be generated [Carrier 2010]. The equation relating soil cohesion to the internal friction angle used in this work was based off of Figure 4-30 but slightly modified to better fit experimental results. The specific value for the soil density can be obtained by using Equation 4-42.

$$Cohesion(kPa) = .0017e^{.118\phi}$$

Equation 4-43

$$Relative\ Density(\%) = -.0007\phi^2 + .0929\phi - 1.9468$$

Equation 4-44

Since density and cohesion are defined in terms of the internal friction angle, a dynamic relationship for each, based on the relative acceleration of the soil, can be presented by using Equation 4-41 to represent the dynamic internal friction angle.

$$cohesion_{dynamic}(kPa) = .0017e^{.118*tan^{-1}\{(tan\phi_{static} - tan\phi_{min})e^{-\beta\eta} + tan\phi_{min}\}}$$

Equation 4-45

$$\begin{aligned} &Relative\ Density(\%) \\ &\quad = -.0007\left(tan^{-1}\left\{(tan\phi_{static} - tan\phi_{min})e^{-\beta\eta} + tan\phi_{min}\right\}\right)^2 \\ &\quad + .0929\left(tan^{-1}\left\{(tan\phi_{static} - tan\phi_{min})e^{-\beta\eta} + tan\phi_{min}\right\}\right) - 1.9468 \end{aligned}$$

Equation 4-46

It is recognized by the author that this substitution does not provide an exact relationship between cohesion and vibration, nor relative density and vibration. Alternatively, these equations represent a first approximation which can be used in the upper limit analysis approach when the control volume is undergoing excessive (greater than .3g) seismic accelerations.

These relationships make physical sense. The soil integrity of a control volume under percussive excitation is compromised. This means not only a change to the internal friction angle, but also a change to the relative density and cohesion along the shear plane boundary layer. The effects of percussion decrease the confining pressure of individual particles along the shear plane. This decrease in confining pressure disrupts the stress history which, in turn, results in a reduction to the cohesion effect.

4.6 Upper limit Percussive Excavation Equation

4.6.1 Introduction

The upper limit analysis discussed in Section 4.3.4 is meant to predict the applied traction load for soil failure in the case of static excavation. This section discusses the modifications that were made to the original model so that it could serve as a predictive tool for percussive excavation. In addition, this section presents the numeric equations, defined by the soil failure geometry and the applied velocity, to solve for the unknown traction force.

First it is necessary to revisit the conditions that must be satisfied to use the upper limit analysis approach:

1. Changes in the geometry of the soil mass at the instant of collapse are small, and thus, the virtual work equation is applicable.

2. The material is perfectly plastic and obeys the Mohr-Coulomb yield criterion.

3. The axes of principle plastic strain increments coincide with the principle stress axes during plastic flow and the resultant plastic strain increment vector is normal to the yield surface [Chen 1975][Chen 1991].

The geometry used to define the soil mass and slip-line network is show in Figure 4-9, which is copied below. Since ϱ and ψ are determined through an optimization routine the problem-defining geometric variables are the internal friction angle, the angle of attack from the plow blade, and the surface angle relative to horizontal. If percussion is applied to this system the attack angle and surface angle will not change. The internal friction angle, however, will change. The geometric effect of reducing the internal friction angle through the removal of dilatancy is shown in Figure 4-31.

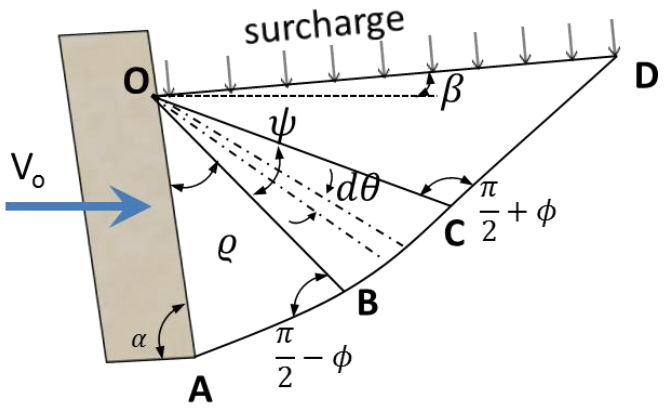

Figure 4-9: Geometric variable definitions of soil failure volume.

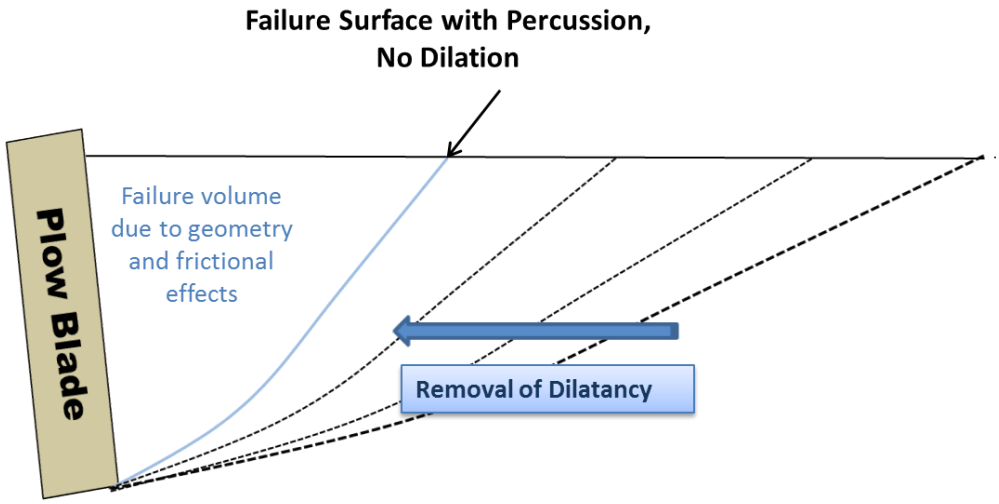

Figure 4-31: Formation of failure geometry dependent on dilatancy in terms of the internal friction angle.

A failure volume geometry dramatically changes on account of percussion being applied to the system. However, in this work it was assumed that those changes were made to the defining characteristic variables of the soil, and not through deformation of the control volume. In other words, the effects of percussion were assigned to the geometry of the problem in the same manner as if the soil was statically failing but with a smaller failure volume and a lower internal friction angle. Consequently condition number one was still satisfied.

Condition 2 and 3 go hand-in-hand and essentially require that the strain rate be derived through the flow rule. The consequence of making this assumption is that the dissipation energy, per unit volume, along the boundary layer is equal to the velocity discontinuity at the boundary layer multiplied by $\cos\phi$ and the soil cohesion. Because the effects of percussion in this research were taken into account through the defining problem geometry, as well as the magnitude of the soil cohesion, no additional modifications needed be made to the dissipation energy term. The soil was still assumed to be perfectly plastic, and obey the flow rule.

Given the fulfillment of the stated critical conditions, the upper limit analysis was used as an approximate solution procedure for percussive excavation.

The upper limit analysis approach presented in Section 4.3.4 was given in its most basic form. The approach will now be given again, but will incorporate the effects of percussion. The underlying derivation will be the same but now those terms which are a function of percussion will be subscripted with the term “dynamic”. This means that when considering percussive excavation these terms will no longer be constant but will depend on the dynamic relationships discussed in sections 4.4 and 4.5.

As a consequence of creating dynamic terms dependent on percussive parameters, the defining soil properties become dependent on one another. Given the interdependency between the

variables an iterative scheme must be employed. The formation of this iteration scheme is discussed at the conclusion of this chapter.

4.6.2 Percussive limit analysis

The derivation of the percussive upper limit analysis is the same as that in the static case. The difference comes from the defining geometry and soil properties. The derivation begins, once more, with the virtual work equation:

$$\int_A T_i \dot{u}_i dA + \int_V F_i \dot{u}_i V = \int_V \sigma_{ij} \dot{\varepsilon}_{ij} dV$$

Equation 4-13

T_i and F_i are traction and body forces. They are in equilibrium with the stress state defined as σ_{ij}. $\dot{\varepsilon}_{ij}$ represents any set of strains or deformation compatible with the real or imagined displacement rate $\dot{u}_i$ at the points of application for the forces T_i and F_i.

2 free body diagrams are given of the failure volume. The first shows all the applied traction, body, and dissipative forces; while the second shows all the velocities which will be used in the virtual work equation to describe the displacements caused by those forces. The specific magnitude and direction of the velocities given in Figure 4-33 are also provided.

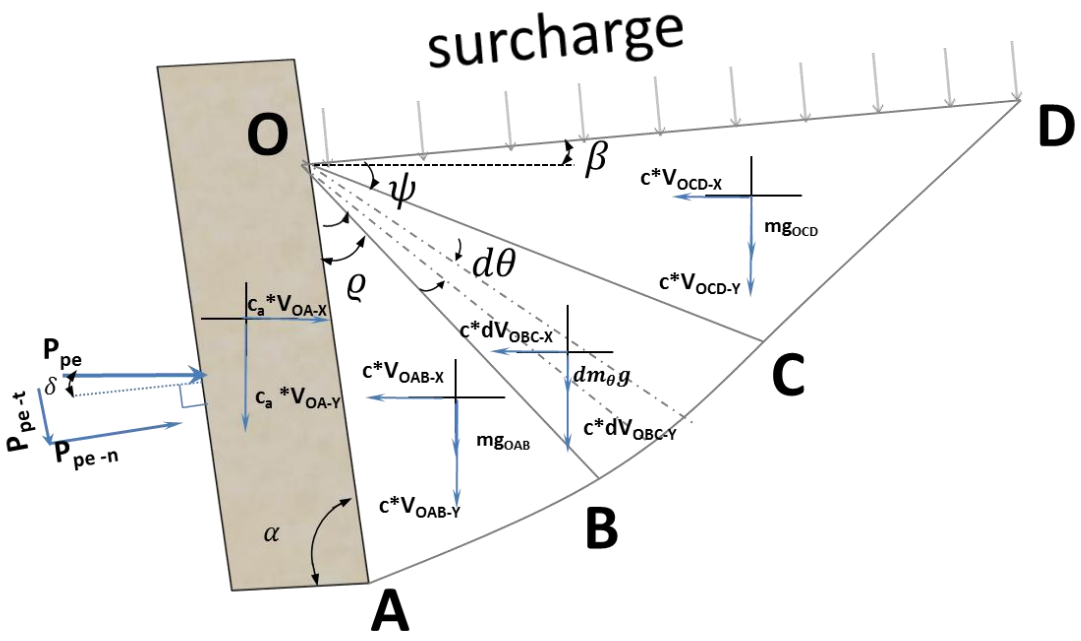

Figure 4-32: All force vectors, dynamic as well as static, characterizing the soil failure control volume.

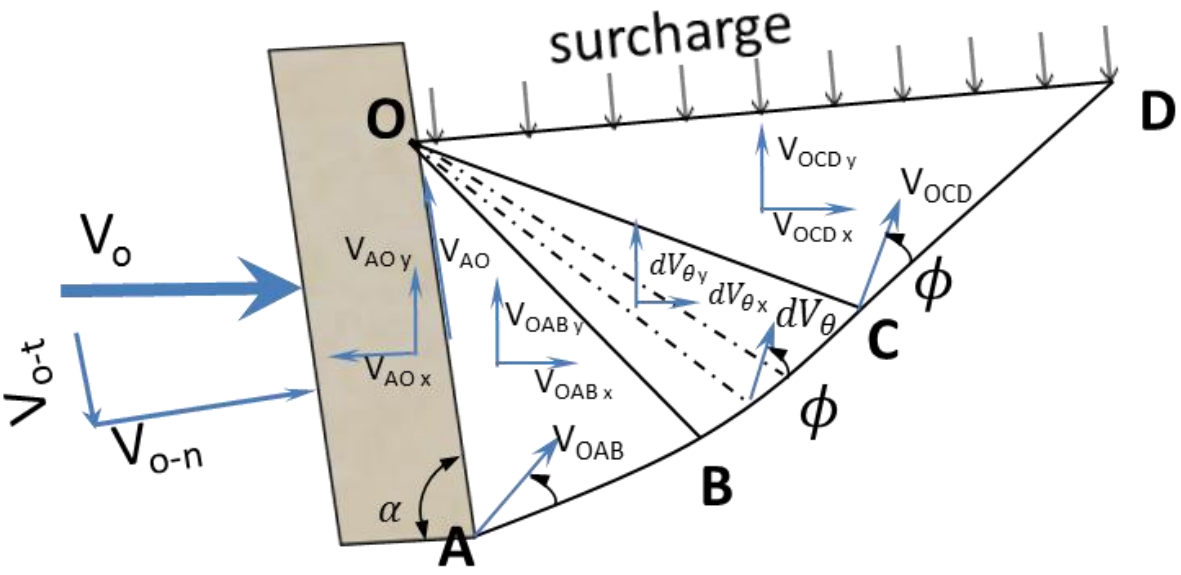

Figure 4-33: The projected velocity vector components for the forces given in Figure 4-32

$$\vec{V}_{AO} = \bar{V}_o \left(\frac{\sin(\alpha)}{\cos(\varrho)} \right) e^{2\pi - \alpha}$$

Equation 4-47

$$\vec{V}_{OAB} = \bar{V}_o \left(\frac{\sin(\alpha)}{\cos(\varrho)} \right) e^{\frac{\pi}{2} - (\alpha - \varrho)}$$

Equation 4-48

$$\vec{V}_{OBC} = \bar{V}_o \left(\frac{\sin(\alpha)}{\cos(\varrho)} \right) e^{\theta \tan(\phi) + \frac{\pi}{2} - (\alpha - \varrho)}$$

Equation 4-49

$$\vec{V}_{OCD} = \bar{V}_o \left(\frac{\sin(\alpha)}{\cos(\varrho)} \right) e^{\psi \tan(\phi) + \frac{\pi}{2} - (\alpha - \varrho)}$$

Equation 4-50

To accommodate problem robustness, a directional term, gamma, is introduced to describe the angle of the surcharge force. This angle is most commonly set to $\frac{\pi}{2}$.

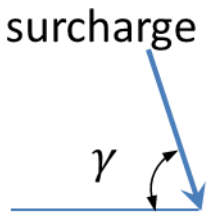

Figure 4-34: Definition of the angle defining the direction of surcharge force.

The virtual work equations, per unit of width, which describe the energy inputs and outputs to the control volume, are given below. Those terms describing the energy being done on the system by the traction and body forces are titled the work terms. Those which describe the energy losses due to the shear stress and strain of the material, using the flow rule, are labeled dissipation terms. These 2 sets of terms are initially presented in their most basic terminology

and then derived in terms of the defining geometric parameters and the applied velocity. It is the second set of equations which will include the subscript “dynamic” for those terms which are functions of the percussive variables.

$$Work_{OAB} = -m_{OAB} g V_{OAB_y}$$

Equation 4-51

$$Work_{OBC} = -\int_{A} (\rho g \, V_{\theta_y}) dA$$

Equation 4-52

$$Work_{OCD} = -m_{OCD} g V_{OCD_y} - q_y \overline{OD} V_{OCD_y} + q_x \overline{OD} V_{OCD_x}$$

Equation 4-53

$$Work_{Ppe} = Ppe V_o sin(\alpha + \delta)$$

Equation 4-54

$$Dissipation\ on\ AB = c\overline{AB} V_{OAB} cos\phi$$

Equation 4-55

$$Dissipation\ on\ BC = \int_{Arc\ Length\ of\ BC} (cV_{\theta'} cos\phi) dL$$

Equation 4-56

$$Dissipation\ on\ CD = c\overline{CD} V_{OCD} cos\phi$$

Equation 4-57

$$Dissipation\ within\ OBC = \int_{Arc\ Length\ of\ BC} (cV_{\theta'} cos\phi) dL$$

Equation 4-58

$$Adhesion\ and\ interface\ Dissipation\ on\ OA = (Ppesin\delta + c_a\overline{OA})V_{o-AO}$$

Equation 4-59

By using the geometry that is presented in Figure 4-9, Equation 4-51 through Equation 4-59 are broken down in terms of only V_o. The distinguishing subscript "dynamic" is also used.

$$Work_{OAB} = -\frac{\rho g H^2}{2} \frac{\cos(\varrho - \phi_{dynamic}) \cos(\alpha - \varrho)\, sin\alpha tan\varrho}{cos\phi_{dynamic}} * V_o$$

Equation 4-60

$$Work_{OBC} = \frac{-H^2 V_o \rho g \cos^2(\phi_{dynamic} - \varrho) \sin\alpha cot\phi_{dynamic}}{10 \cos^2(\phi) \cos\varrho} \{\sin(\alpha - \varrho) - 2\cos(\alpha - \varrho) - e^{2\psi tan\phi_{dynamic}} [\sin(\alpha - \varrho - \psi tan\phi_{dynamic}) - 2\cos(\varrho - \alpha + \psi tan\phi_{dynamic})]\}$$

Equation 4-61

$$Work_{OCD} = \frac{V_o}{cos(\phi_{dynamic})\cos(\alpha + \beta + \phi_{dynamic} - \varrho - \psi)\cos(\varrho)} \left[\left[Hqe^{2\psi tan\phi_{dynamic}} \cos(\phi_{dynamic} - \varrho)\, sin\alpha \cos(\phi_{dynamic}) \sin(\alpha - \varrho - \psi - \gamma) - \frac{H^2 \rho g sin(\alpha + \beta - \varrho - \psi) \cos(\alpha - \varrho - \psi)\, e^{3\psi tan\phi_{dynamic}} cos^2(\phi_{dynamic} - \varrho) \sin(\alpha)}{2} \right]\right]$$

Equation 4-62

$$Work_{Ppe} = PpeV_o sin(\alpha + \delta)$$

Equation 4-63

$$Dissipation\ on\ AB = c_{dynamic} H sin\alpha tan\varrho V_o$$

Equation 4-64

$$Dissipation\ on\ BC = \frac{1}{2}\frac{c_{dynamic} H sin\alpha cos(\varrho - \phi_{dynamic})(e^{2\psi tan\phi_{dynamic}} - 1)}{sin\phi_{dynamic} cos\varrho} V_o$$

Equation 4-65

$$Dissipation\ on\ CD = \frac{c_{dynamic} H sin\alpha cos\left(\varrho - \phi_{dynamic}\right)\sin(\alpha + \beta - \varrho - \psi) e^{2\psi tan\phi_{dynamic}}}{cos\varrho\cos(\alpha + \beta + \phi_{dynamic} - \varrho - \psi)} V_o$$

Equation 4-66

$$Dissipation\ within\ OBC = \frac{1}{2}\frac{c_{dynamic} H cos(\varrho - \phi_{dynamic})(e^{2\psi tan\phi_{dynamic}} - 1)}{sin\phi cos\varrho} V_o$$

Equation 4-67

$$Adhesion\ and\ interface\ Dissipation\ on\ OA = \left[Ppesin\delta + c_{a_{dynamic}} H\right]\frac{\cos(\alpha - \varrho)}{cos\varrho} V_o$$

Equation 4-68

The unknown traction force P_{pe} is solved for my equating the work terms to the dissipation terms, Equation 4-69, and then isolating P_{pe}. After P_{pe} is isolated it is solved for through an optimization routine in which ρ and ψ are adjusted until the minimum possible P_{pe} value is found. The optimization routine used in this work was performed through the MATLAB function fmincon.

$$W_{OAB} + W_{OBC} + W_{OCD} + W_{Ppe} = D_{OA} + D_{AB} + D_{BC} + D_{OBC} + D_{CD}$$

Equation 4-69

4.6.2.1 Inclusion of Dynamic Effects

The point of applying percussion to an excavation system is to alter the soil-mechanical properties and reduce the shear strength. This is accomplished by nullifying the force effects of

dilatancy along the shear plane, degrading the shear modulus of the soil by increasing the void ratio along the shear plane, removing the stress history and subsequently decreasing the effect of particle cohesion along the shear plane, and reconstructing the failure volume geometry. In order to account for all these different effects, adjustments must be made to some of the variables used in the upper limit analysis derivation. Those variables have been given the subscript "dynamic". It is important to note that although the angles ρ and ψ were not given a dynamic subscript their values will change with percussion. Since their values are found through an optimization routine they do not need to be given explicit adjustments. Those variables which do need modification are given below.

$$Soil\ Acceleration = (2\pi * applied\ frequency)^2 * \sqrt{\frac{2 * \overline{OA}_{dynamic} * Spring\_Energy}{G_{dynamic} * width * \overline{OD}_{dynamic}}}$$

Equation 4-36

$$G_{dynamic} = 14760 * \frac{\left(2.973 - e_{dynamic}\right)^2}{1 + e_{dynamic}} (OCR)^a (\sigma_m)^{.65}$$

Equation 4-37

$$e_{dynamic} = \frac{Relative\ Density_{dynamic} * (e_{min} - e_{max})}{e_{max}}$$

Equation 4-39

$$\phi_{dynamic} = tan^{-1}\{(tan\phi_{static} - tan\phi_{min})e^{-\beta\eta} + tan\phi_{min}\}$$

Equation 4-41

$$cohesion_{dynamic}(kPa) = .0017e^{.118 * tan^{-1}\{(tan\phi_{static} - tan\phi_{min})e^{-\beta\eta} + tan\phi_{min}\}}$$

Equation 4-45

$$Relative\ Density_{dynamic}(\%) = -.0007\left(tan^{-1}\left\{(tan\phi_{static} - tan\phi_{min})e^{-\beta\eta} + tan\phi_{min}\right\}\right)^2 + .0929\left(tan^{-1}\left\{(tan\phi_{static} - tan\phi_{min})e^{-\beta\eta} + tan\phi_{min}\right\}\right) - 1.9468$$

Equation 4-46

By including these adjustments the defining soil failure geometry and resultant traction force, P_{pe}, will be representative of percussive excavation.

4.7 The Iterative Scheme

4.7.1 Structure of Iteration

Unfortunately the solution process for the percussive upper limit analysis is not perfectly straight forward. Several variables depend on one another to be properly defined. For example, the soil geometry dictates the mass of the failure volume as well as the magnitude of percussive impact soil displacement. The mass and displacement values are necessary to determine the normalized acceleration constant which determines the exponential decay of the internal friction angle. The internal friction angle, however, is necessary to calculate the failure volume geometry.

On account of this inter-dependence amongst the dynamic soil properties, an iterative scheme must be employed to arrive at a solution. This iterative scheme is solved in conjunction with the optimization of angles ρ and ψ, and the traction force P_{pe}.

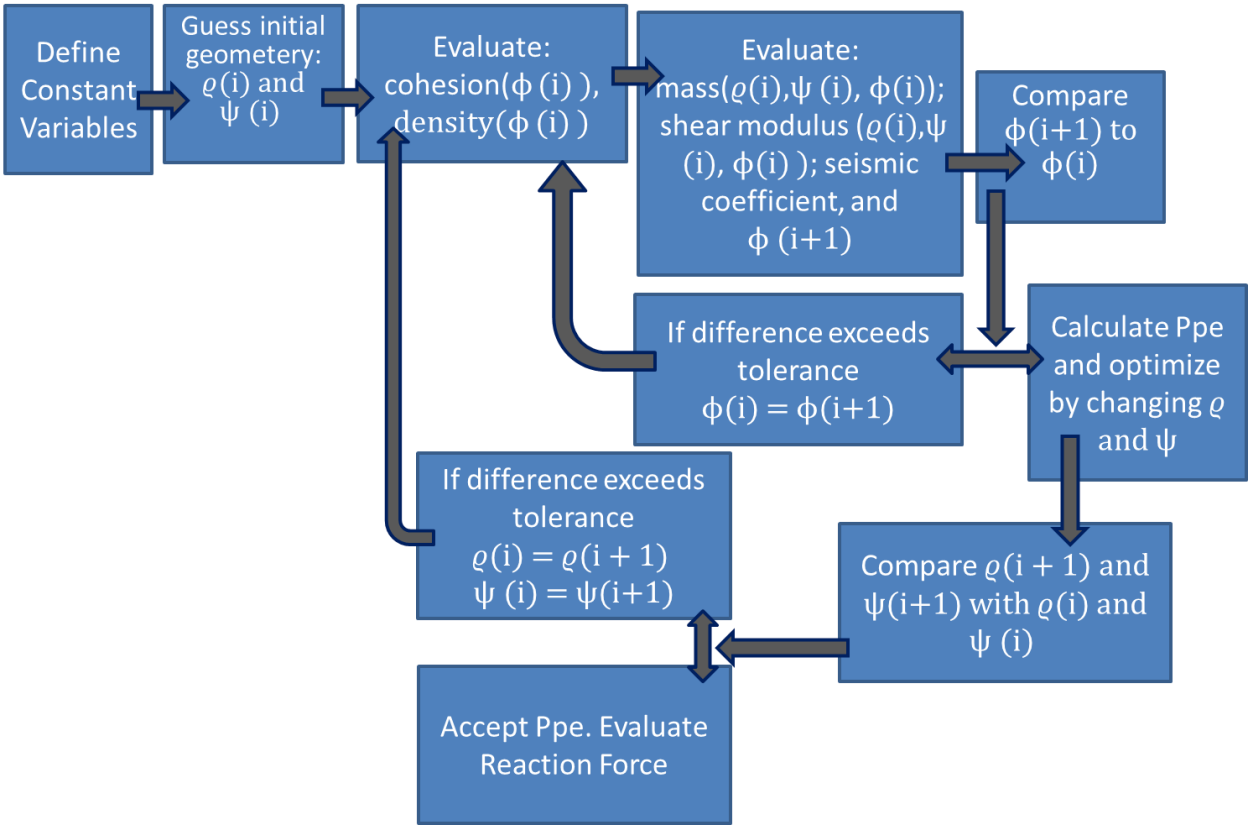

Figure 4-35: Flow diagram representing the iteration process for solving for the critical passive pressure term, $P_{pe.}$.

5 Numeric Model Predictions

5.1 Refining Adjustments to Numeric Model:

5.1.1 Omission of Strain Hardening and Shear Plane Formations

The upper limit analysis for percussive excavation provides a framework through which an approximate solution can be obtained for the reaction force of a soil failure problem with a prescribed velocity-controlled excavation motion. It is important to remember that this force is the baseline draft force for a perfectly plastic material, with no strain hardening, and with zero boundary displacement. The formation of the sudden and dramatic force spikes discussed in Chapter 3 is not taken into account with this numeric predictive tool. The idealization used for the material behavior inhibits the prediction of force spike aberrations during excavation. However, when high percussive effects are applied, those forces spikes are removed and their formation becomes immaterial to the problem.

5.1.2 Width

Another factor which must be considered when comparing the analytical failure results to those found empirically is the effect of scoop width. The upper limit analysis approach assumes plane strain which allows for the predicted force to be scaled linearly according to width. Unfortunately, because the experimental testing was only performed with one scoop the force variation due to scoop width is unknown. A linear scaling factor is assumed at present until future testing can take place and provide more specific insight.

5.1.3 Effects of Velocity

As discussed in Chapter 3, the magnitude of the velocity and the applied impact frequency determine the travel of the scoop between successive percussive impacts. If the scoop is expected to transverse a large distance it will have to combat adverse effects of dilatancy. It is only after the velocity and impact frequency reach an appropriate ratio that the advantageous effects of percussion are manifested. A non-dimensionalized velocity ratio parameter is used to determine the appropriate ratio for a given soil state.

$$Velocity\ Ratio = \frac{2\pi * applied\ frequency * \sqrt{\frac{2 * \overline{OA} * Spring\_Energy}{G * width * \overline{OD}}}}{V_o}$$

Equation 5-1

The idea of assigning a threshold to the velocity ratio term coincides well with the observations reported by Ermolaev and Senin in Section 4.5.2. Their findings describe a 2-phase effect in dry sand, the first being a slight drop off in the in situ shear strength, and the second being a dramatic exponential decrease.

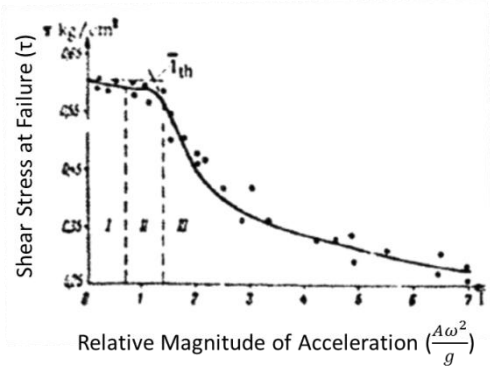

Figure 5-1: Dependence of shear strength on the relative acceleration magnitude. Regions I,II, and III are shown to demonstrate the different stages of degradation of sandy loam due to vibrations [Ermolaev 1968]. The trans-threshold value occurs between stage II and III.

The threshold value of the velocity ratio is dependent on the initial state of soil compaction. A relationship is provided which determines the threshold velocity ratio based on the in situ internal friction angle. This relationship is purely based on the experimental results found in this study. This relationship makes intuitive sense given that the effect of velocity on percussion cannot only be dependent on how far the blade travels between successive impacts, but must also depend on the amount of soil particles it displaces.

Based on empirical data, a simple quadratic function was created. This function gives the 'trans-threshold' value that must be achieved to instigate exponential decay of the internal friction angle. The in situ internal friction angle is given in units of degrees.

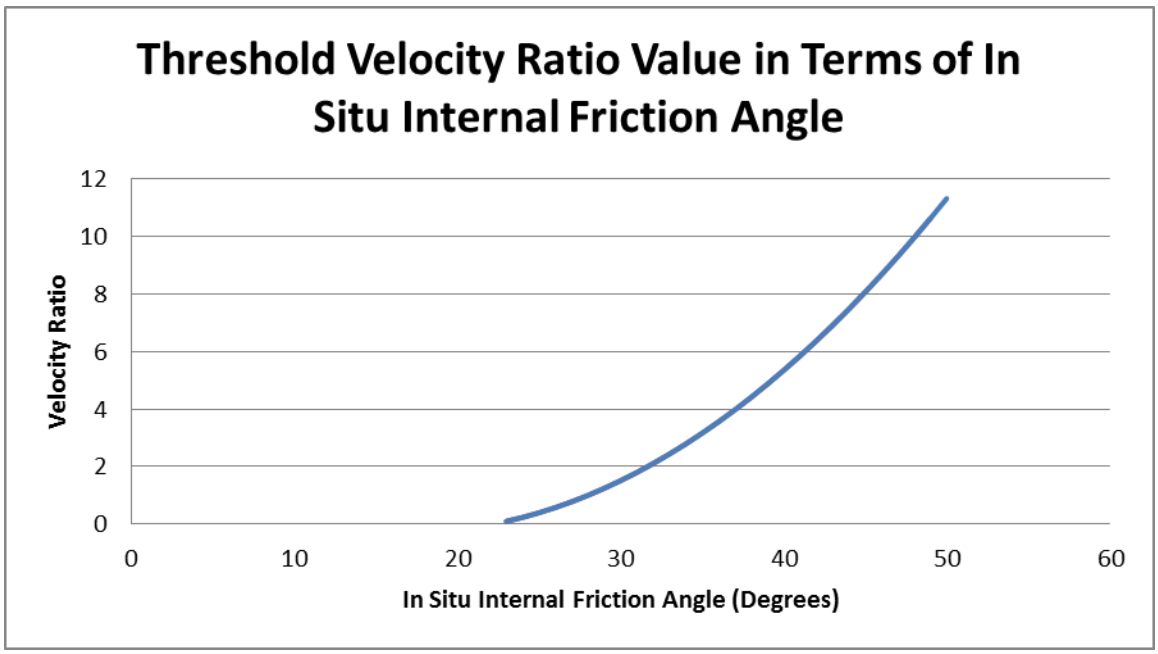

Figure 5-2: The required velocity ratio of the soil to reach the threshold value for shear strength exponential decay. The value of the velocity ratio is dependent on the in situ internal friction angle.

$$Velocity\ Ratio\ Theshold\ Value = .0107{\phi_o}^2 - .365\phi_o + 2.86$$

Equation 5-2

5.1.4 Scaling Factor for the Internal Friction Angle

The perfect plasticity assumption is necessary to validate the utilization of the upper limit analysis approach. However this assumption is not an exact representation of real soil behavior. During the calibration of the numeric code there was good agreement between experimental and theoretical values within the medium relative density range but that agreement progressively got worse as the relative density changed to either higher or lower states. The high density solutions increased in margin-of-error by over predicting the expectant value. The low density solutions, however, increased in margin-of-error by under predicting the expectant value. In order to accommodate the discrepancy between the idealized soil and the real behavior of JSC-1a a simple scaling factor was applied about the median.

$$scaled\ \phi = \frac{\phi}{2} + 17.5^o$$

Equation 5-3

The internal friction angle is given in degrees. This allows the median value of the internal friction angle, 35^{o}, to remain the same for computation while scaling the upper and lower limit values appropriately.

5.1.5 The Asymptotic Limit of the Internal Friction Angle

According to the empirical results, as well as the work done by Barkan [1962] and Ermolaev [1968], the internal friction angle exponentially decays as the soil acceleration increases. This relationship was given in Equation 4-41 as:

$$tan\phi_{dynamic} = (tan\phi_{static} - tan\phi_{min})e^{-\beta\eta} + tan\phi_{min}$$

Ermolaev and Senin, in their work, discuss that as the surcharge is increased the asymptotic limit of the internal friction angle, ϕ_{min}, also increases. In this work the effects of different surcharge forces were not explored outside of the accumulation of displaced soil. It was observed, however, that the minimum internal friction angle was dependent on the initial relative density of the soil and the excavation velocity. This isn't to say that the effects of dilatancy weren't removed through percussion, rather that the density of particle-to-particle surface friction interaction was higher for more compact soils than for loose soils. This higher friction density resulted in a higher asymptotic internal friction angle value.

Velocity affects a minimum internal friction angle because of its relevance to the magnitude of frictional effects which must be overcome during a specific time period. Based on experimental data, the minimum possible internal friction value had a quadratic relationship with the in situ internal friction angle and a linear relationship with the excavation velocity.

In addition to velocity and relative density, the orientation of the scoop has an effect on the asymptotic value of the internal friction angle. This effect is accommodated by taking the sine of the angle between the plow blade and the direction of travel, the attack angle.

$$\emptyset_{min} = 9 * \left(.0011 * {\emptyset_o}^2 - .0366 * \emptyset_o + 1.28\right) * (V_o * 20 + 1) * \sin(\alpha)$$

Equation 5-4

Velocity is given in m/s. The in situ internal friction angle is in degrees. 9 is a scaling coefficient. $\emptyset_{min}$ is in degrees.

5.2 Shape Definition for Exponential Effect of Percussion

5.2.1 Effect of Relative Density

During experimental testing the relative density term was assigned one of three defining states: High DR, Medium DR, or Low DR. The process to determine a soil's relative density was dependent on where it's measured pressure index fell on a calibration curve. The calibration curve, along with the table outlining the relative density levels are provided below. A more detailed description of the complete testing procedure can be found in Chapter 2.

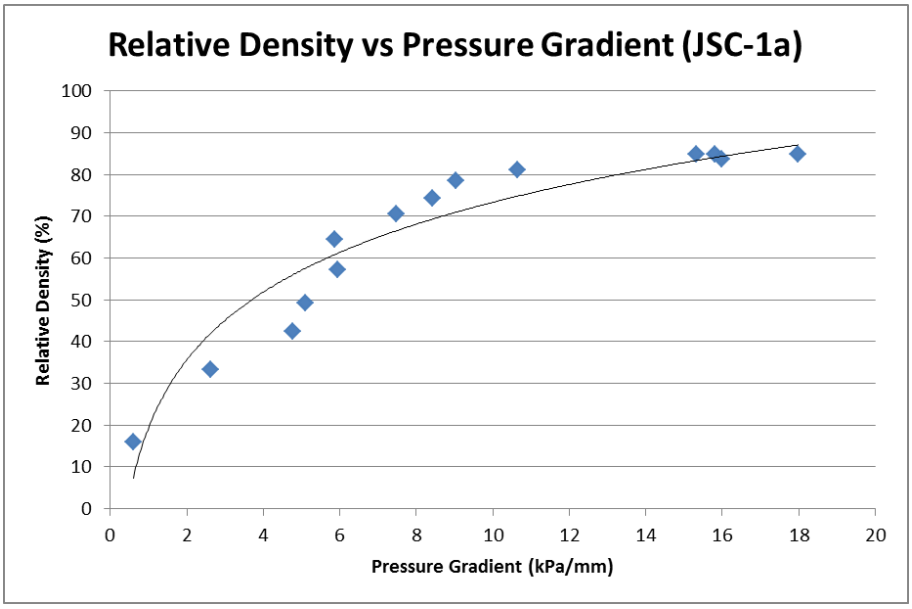

Figure 2-22: Relative Density verses Pressure Gradient for JSC-1a.

Relative Density (%)	Description
5-20%	Low DR
45-60%	Medium DR
85-99%	High DR

Figure 2-24: Description of soil states tested in this research based on relative density

The numeric code is sensitive to a soil's in situ compaction level. Consequently a soil which has a 45% relative density will produce a different answer than will a soil with a 60% relative density even though they are both classified as having a medium relative density. Given that there is a difference in the numeric solution it is difficult to show how the numeric results

match with the empiric results if the exact measured state of relative density is not known. Further, it is difficult to show trends between the experimental and numeric solutions if every soil tested was at a different soil state. Hence, the comparisons between the numeric and empirical results will include the numeric solution for the lower bound of a described soil state as well as the upper bound. In other words the numerically-predicted behavior of a soil with 5% relative density and 20% relative density is plotted for low relative density soils, 45% and 60% for medium density soils, and 85% and 99% for high density soils. Figure 5-3 gives a graphic representation of the expected soil behavior for the upper and lower bounds for Low, Medium, and High DR soils.

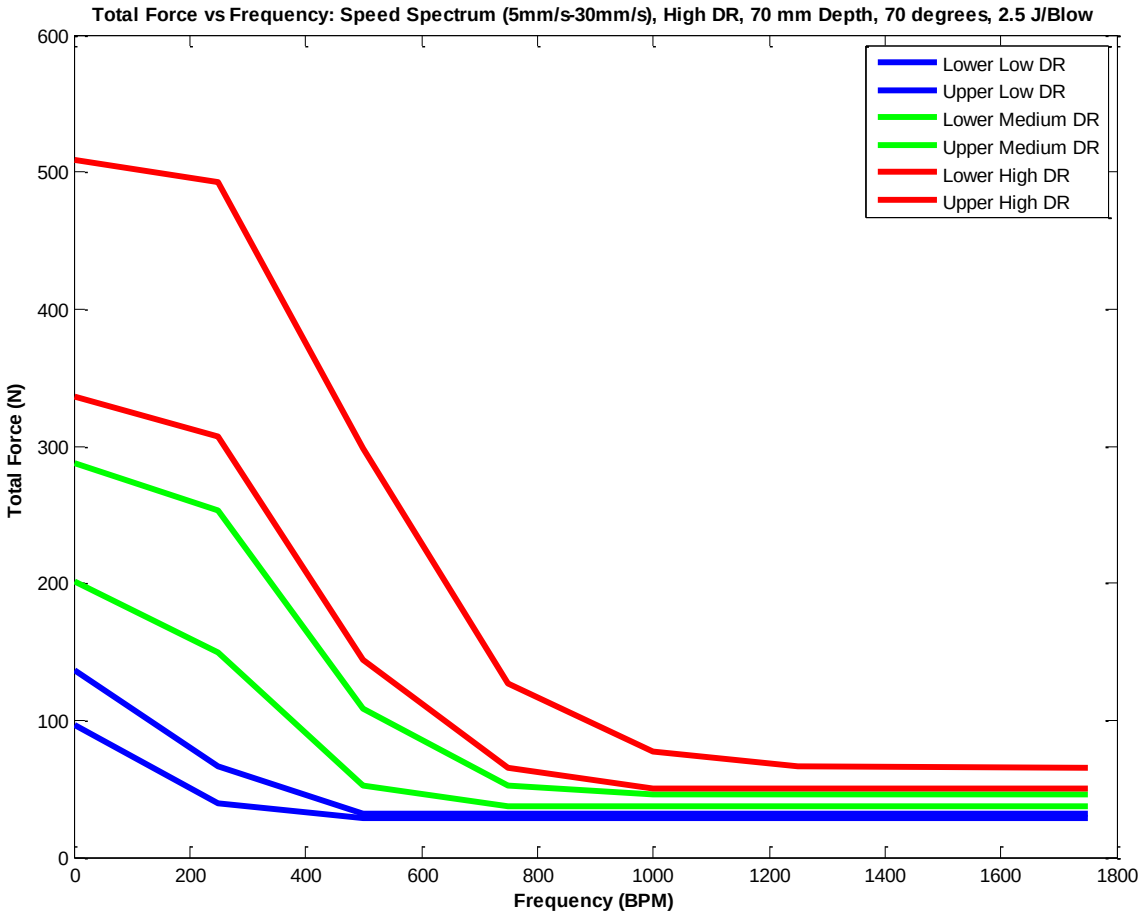

Figure 5-3: The upper and lower bounds for Low, Medium, and High DR classified soils. Numeric solution is for 70 mm Depth, 5 mm/s, 70 degree attack angle, and 2.5 J/blow percussion.

5.2.2 Degradation Curve as a Function of Velocity and Soil Compaction

Much like the asymptotic value of the internal friction angle, the degradation curve is also dependent on the state of in situ soil compaction and excavation velocity. To account for the effects of both, the exponential decay coefficient given in Equation 4-41 as β is defined as:

$$\beta = \frac{velocity\_ratio}{.134 * {\phi_o}^2 - 6.61 * \phi_o + 84.6}$$

Equation 5-5

Where ϕ_o represents the in situ internal friction angle.

The manner in which the exponential coefficient affects the degradation curve is presented below. Curves representing the degradation of the theoretical upper and lower limits of Low, Medium, and High DR are presented. The red curves represent the upper limit, while the blue curves the lower limit. A series of different curves are provided, each representing the degradation for a different speed from 5 mm/s to 30 mm/s, in increments of 5 mm/s. Although the curvature of the degradation curve is smooth it is graphically given in incremental values of 250 BPM because experimental tests were done in increments of 250 BPM. These figures also show how the asymptotic value changes as a function of speed and in situ internal friction.

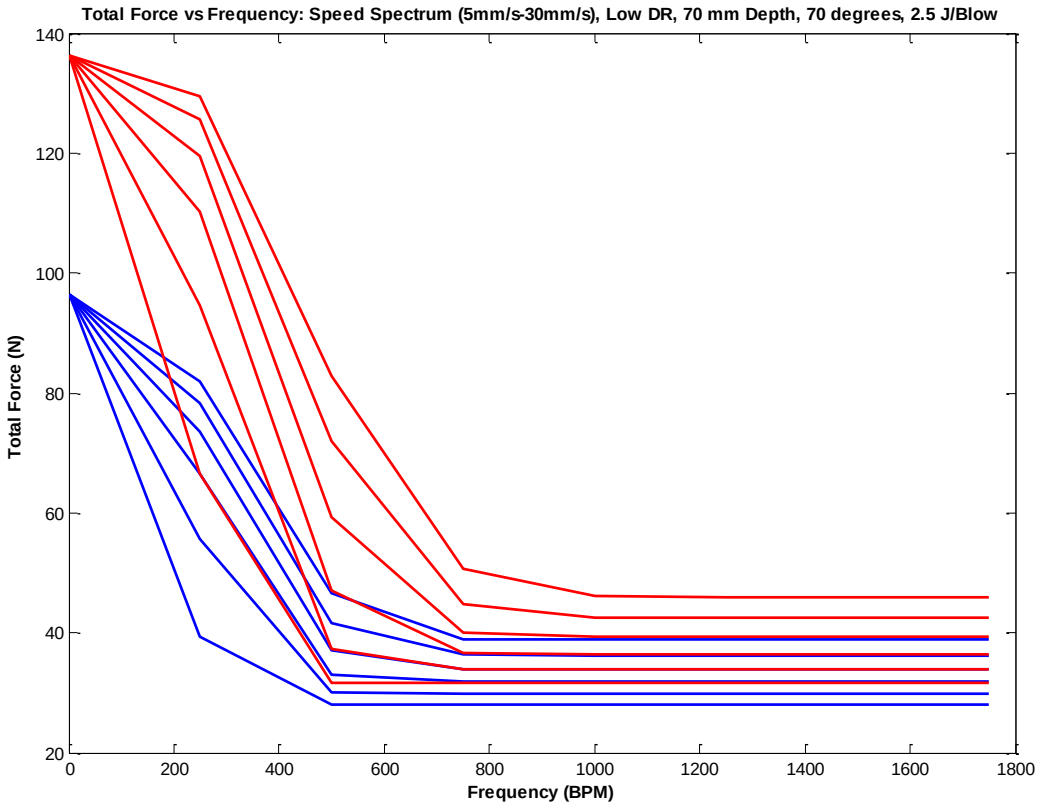

Figure 5-4: Shape of exponential degradation curve based Low RD and speeds of 5 mm/s through 30 mm/s. Constants are: Depth, 70 mm; Angle, 70 degrees; and Percussive Energy, 2.5 J/blow.

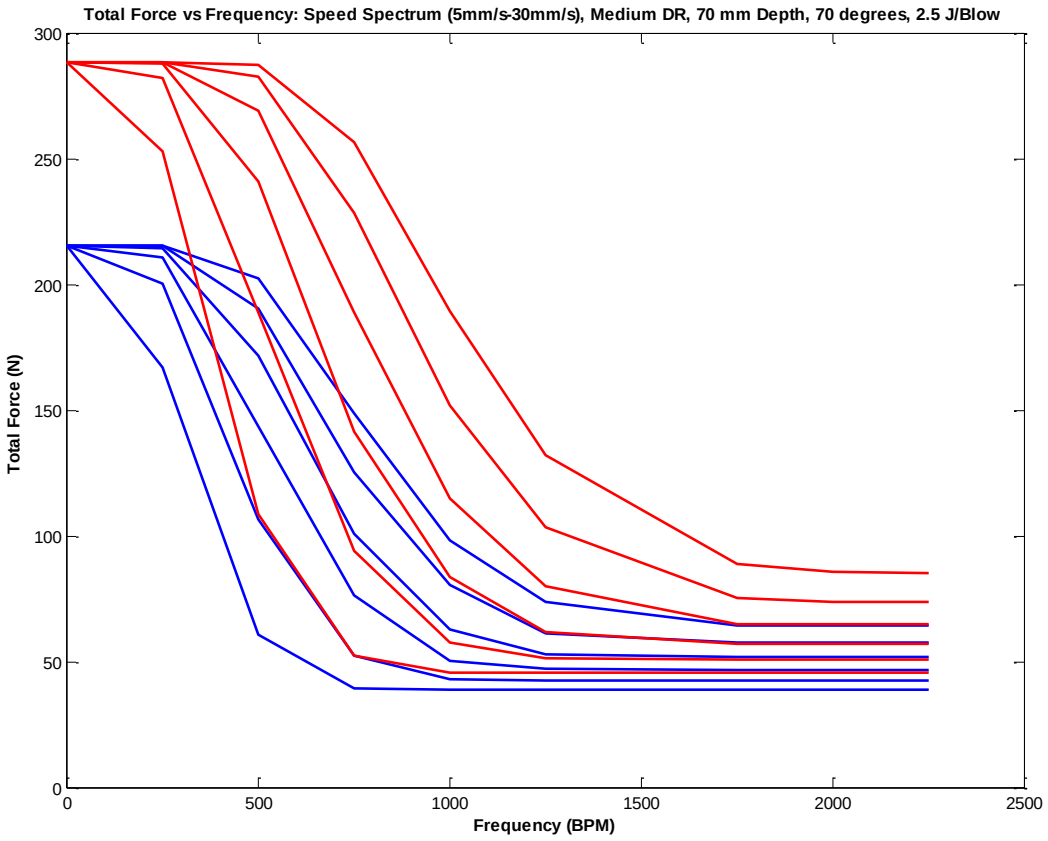

Figure 5-5: Shape of exponential degradation curve based Medium RD and speeds of 5 mm/s through 30 mm/s. Constants are: Depth, 70 mm; Angle, 70 degrees; and Percussive Energy, 2.5 J/blow.

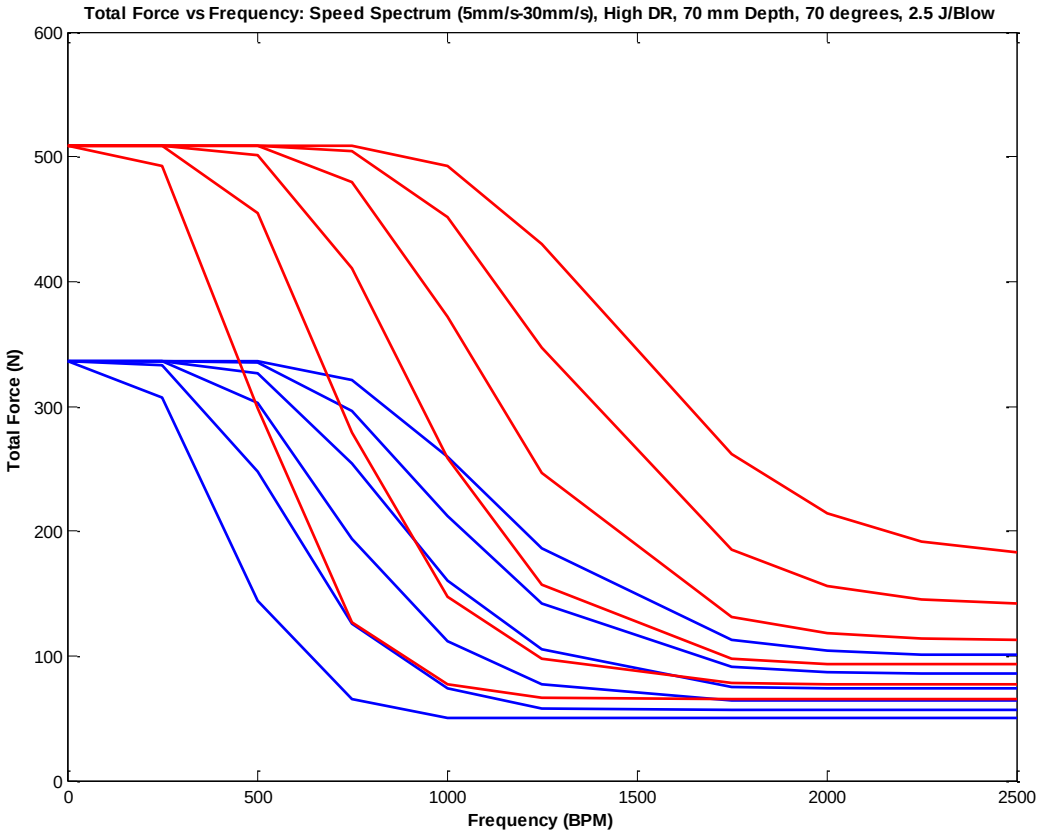

Figure 5-6: Shape of exponential degradation curve based High DR and speeds of 5 mm/s through 30 mm/s. Constants are: Depth, 70 mm; Angle, 70 degrees; and Percussive Energy, 2.5 J/blow.

5.3 Comparing Theoretical and Empirical Results

5.3.1 Frequency for the Independent Variable

The effectiveness of percussion most heavily relies on the impact frequency variable. It is also the variable which was tested across the widest spectrum of values. Consequently, the best way to observe a trend between theoretical and experimental results is to compare the two using frequency as the independent variable. The other defining parameters of percussive excavation will be examined, but in the context of the defining soil characteristic describing a figure and not the independent variable. In order to more appropriately show how the theoretical model matches up with the experimental data only those frequencies tested experimentally are reproduced with the theoretical model. However, it should be noted that the theoretical model can be used to predict any frequency and is not limited to those presented.

5.3.2 Different Relative Densities, Full Frequency Spectrum, 70 mm Depth, 5 mm/s Velocity, 70º Scoop Angle, 2.5 Joules/Blow

It is well known that the relative density of a soil varies dramatically across the lunar surface within a depth of only 30 cm [Heiken 1991]. Consequently it is imperative that the theoretical model have the capability to approximate reaction forces across a span of different soil densities. The following three figures represent the theoretical and experimental results for Low, Medium, and High DR soils. The other excavation variables were held constant while the frequency was varied from 0-1750 BPM. The remaining variable values were set to 70 mm depth, 5 mm/s velocity, 70 degree attack angle and 2.5 Joules/impact.

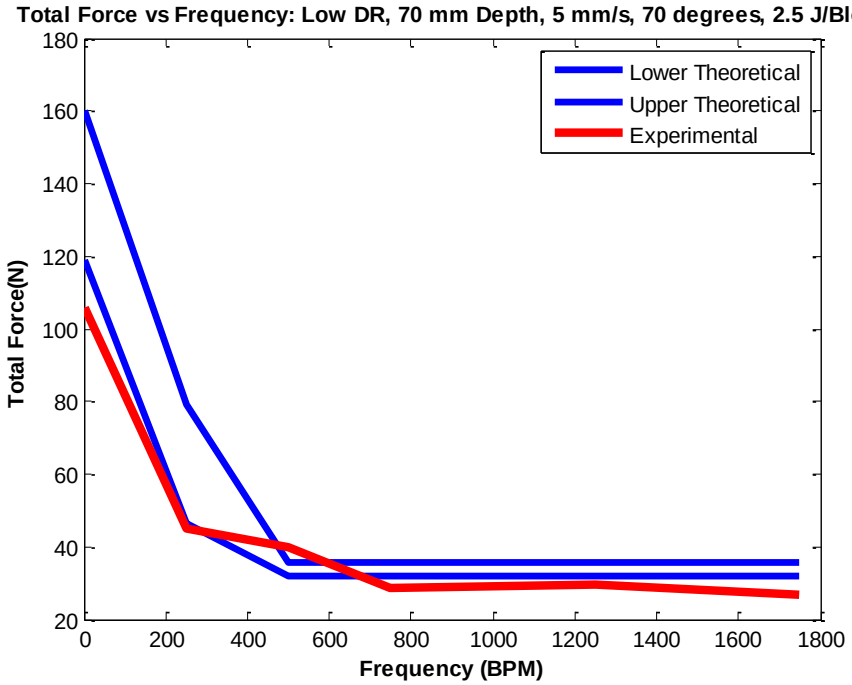

Figure 5-7: Comparison of theoretical and empirical results for a Low DR soil across the frequency spectrum. Tests conducted at 70 mm Depth, 5 mm/s, 70 degrees, and 2.5 J/blow.

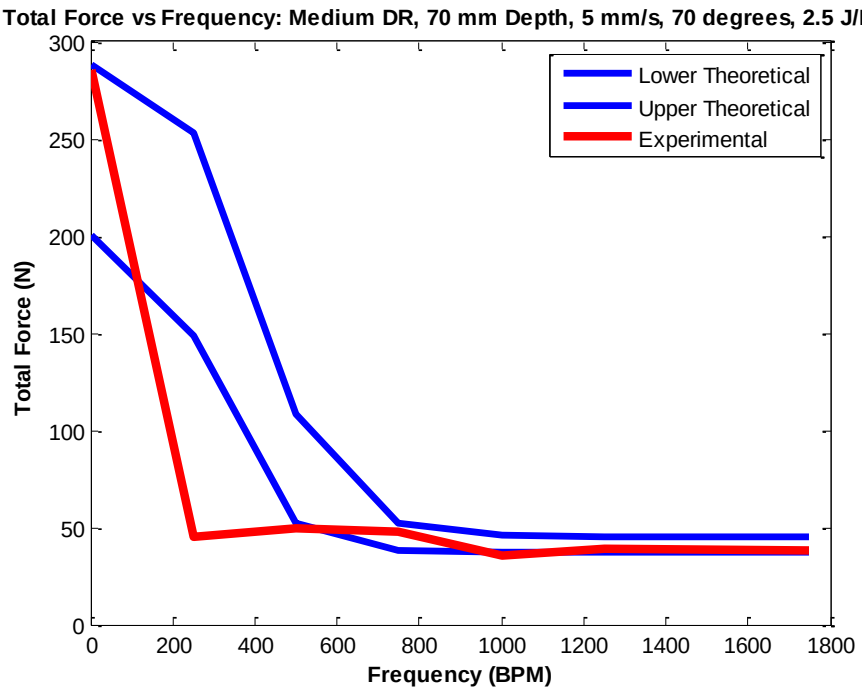

Figure 5-8: Comparison of theoretical and empirical results for a Medium DR soil across the frequency spectrum. Tests conducted at 70 mm Depth, 5 mm/s, 70 degrees, and 2.5 J/blow.

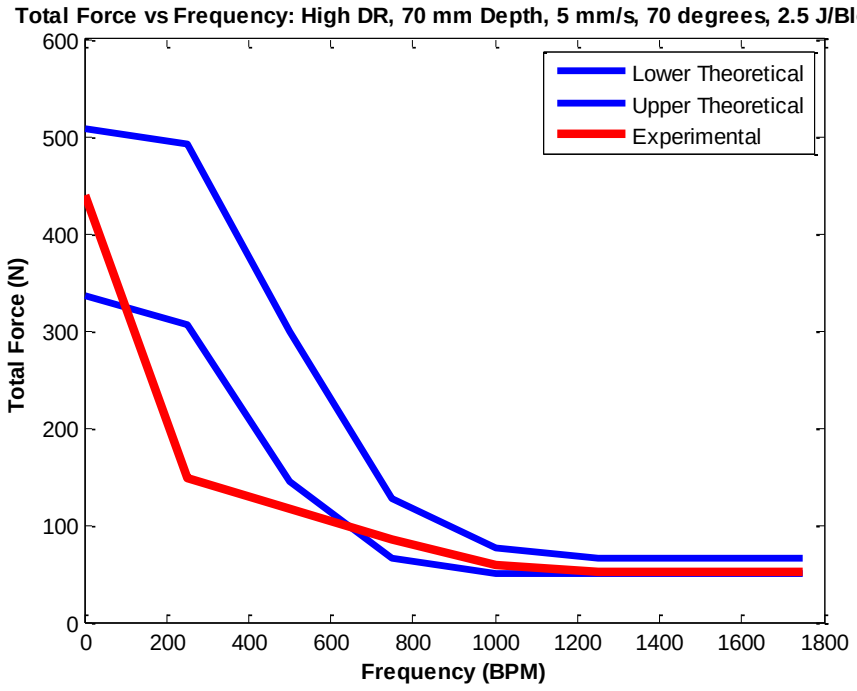

Figure 5-9: Comparison of theoretical and empirical results for a High DR soil across the frequency spectrum. Tests conducted at 70 mm Depth, 5 mm/s, 70 degrees, and 2.5 J/blow.

5.3.3 Different Relative Densities, Full Frequency Spectrum, 70 mm Depth, 20 mm/s Velocity, 70^0 Scoop Angle, 2.5 Joules/Blow

In addition to sensitivity toward the soil's relative density, the numeric code must also be able to predict the effects of velocity change. The following 3 figures represent the numeric and empirical results for all the same parameters as before, but now with 4x the previous velocity, 20 mm/s instead of 5 mm/s. Due to saturation limitations of the load cell the high relative density soil was not able to be tested at 20 mm/s statically, or at low frequencies. Figure 5-12 does however show agreement between the proposed numeric model and the recorded empirical testing done at 1250 BPM and 1750 BPM.

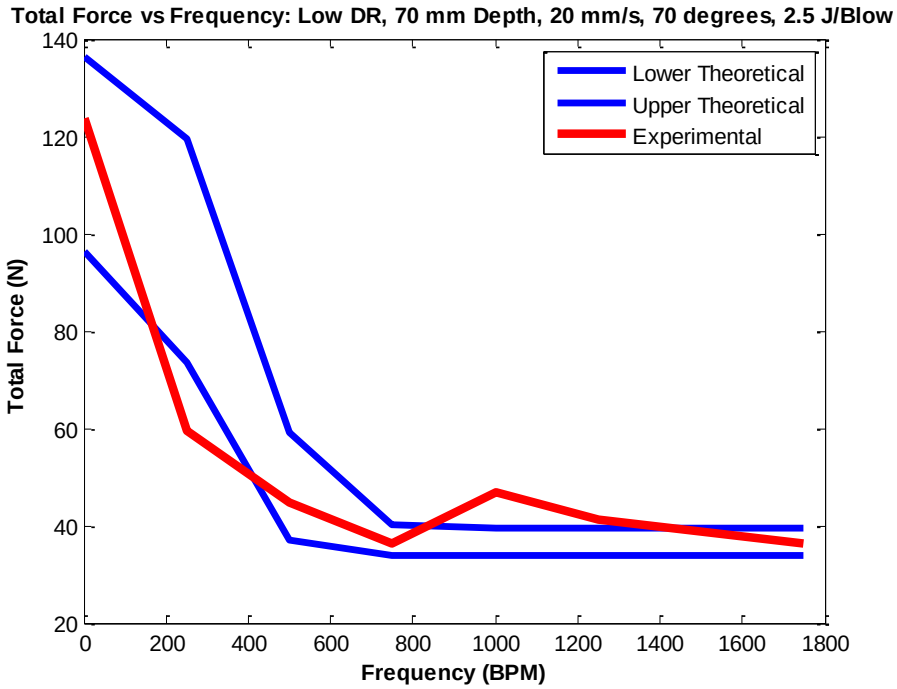

Figure 5-10: Comparison of theoretical and empirical results for a Low DR soil across the frequency spectrum. Tests conducted at 70 mm Depth, 20 mm/s, 70 degrees, and 2.5 J/blow.

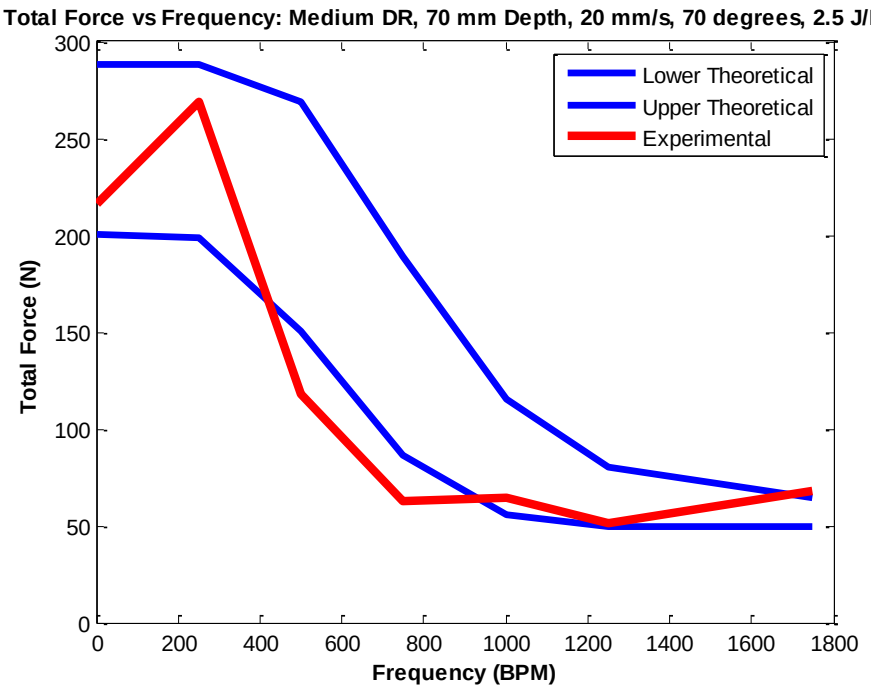

Figure 5-11: Comparison of theoretical and empirical results for a Medium DR soil across the frequency spectrum. Tests conducted at 70 mm Depth, 20 mm/s, 70 degrees, and 2.5 J/blow.

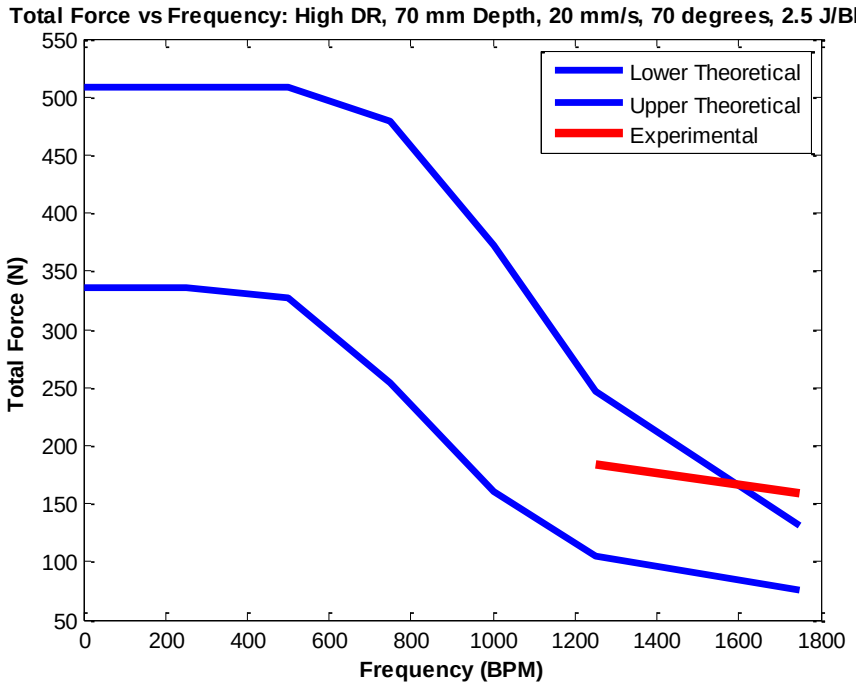

Figure 5-12: Comparison of theoretical and empirical results for a High DR soil across the frequency spectrum. Tests conducted at 70 mm Depth, 20 mm/s, 70 degrees, and 2.5 J/blow.

5.3.4 Different Relative Densities, Full Frequency Spectrum, 30 mm Depth, Different Speeds, 70^0 Scoop Angle, 2.5 Joules/Blow

The depth of an excavation instrument will vary depending on its application. The following figures show how the numeric model agrees with the empirical model at 30 mm depth, as opposed to the 70 mm depth used in the preceding figures. Different speeds were run at different densities to further show agreement between the numeric model and theoretical model in terms of speed at lower depths. In Figure 5-14 different sets of data are shown. The entire spectrum of data points collected was not at 20 mm/s or 5 mm/s; rather the lower frequencies were tested at 5 mm/s and the higher ones at 20 mm/s.

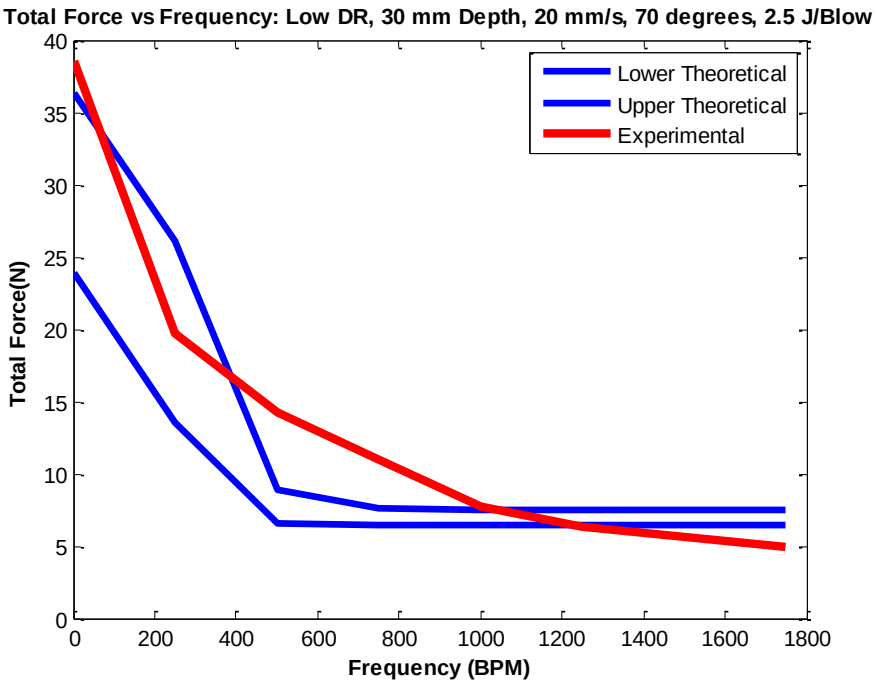

Figure 5-13: Comparison of theoretical and empirical results for a Low DR soil across the frequency spectrum. Tests conducted at 30 mm Depth, 20 mm/s, 70 degrees, and 2.5 J/blow.

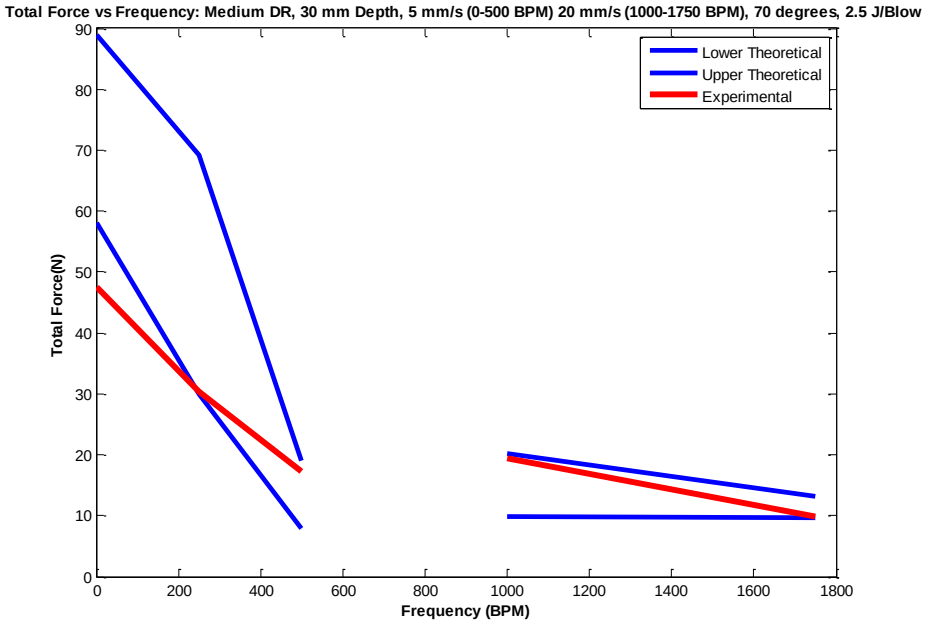

Figure 5-14: Comparison of theoretical and empirical results for a Medium DR soil across the frequency spectrum. Tests conducted at 30 mm Depth, 5 mm/s and 20 mm/s, 70 degrees, and 2.5 J/blow.

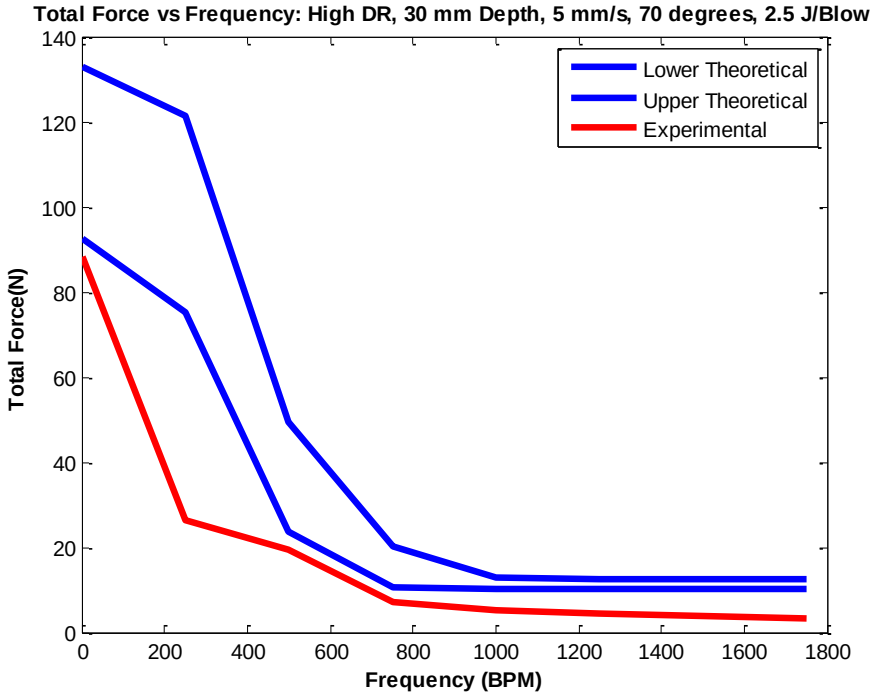

Figure 5-15: Comparison of theoretical and empirical results for a High DR soil across the frequency spectrum. Tests conducted at 30 mm Depth, 5 mm/s, 70 degrees, and 2.5 J/blow.

5.3.5 Different Relative Densities, 500, 1250, and 1750 BPM, 70 mm Depth, 5 mm/s, 70^0 Scoop Angle, Different Impact Energies (2.25, 2.5, 4.5) Joules/Blow

Although the results from Chapter 3 show little effect with a change in impact energy, it is still important to see how the theoretical model reacts to changes in the impact energy magnitude. To this end, the experimental test data that is available is contrasted against the theoretical model. Only frequencies of 500, 1250, and 1750 BPM were tested at different impact energies. The impact energies tested were 2.25 Joules/impact and 4.5 Joules/impact.

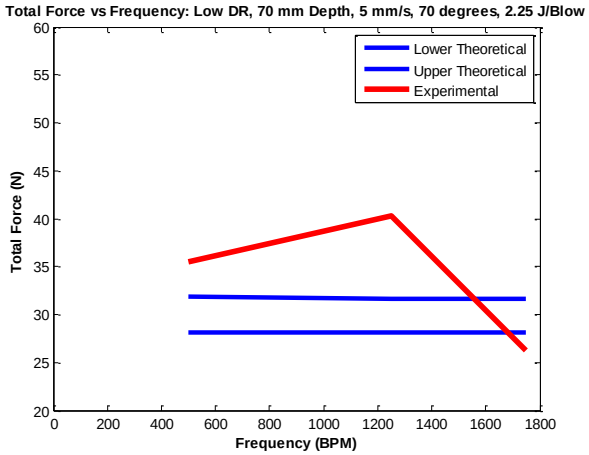

Figure 5-16: Comparison of theoretical and empirical results for a Low DR soil for frequencies of 500, 1250, and 1750 BPM using impact energy of 2.25 Joules. Tests conducted at 70 mm Depth, 5 mm/s, 70 degrees.

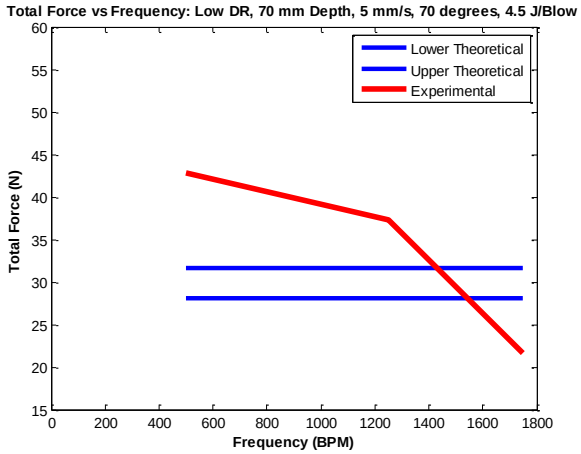

Figure 5-17: Comparison of theoretical and empirical results for a Low DR soil for frequencies of 500, 1250, and 1750 BPM using impact energy of 4.5 Joules. Tests conducted at 70 mm Depth, 5 mm/s, 70 degrees.

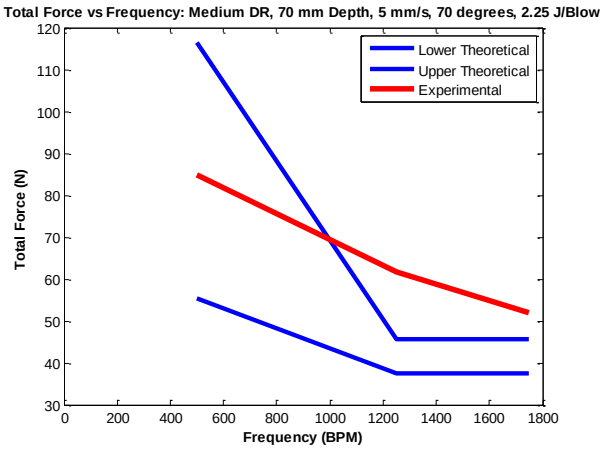

Figure 5-18: Comparison of theoretical and empirical results for a Medium DR soil for frequencies of 500, 1250, and 1750 BPM using impact energy of 2.25 Joules. Tests conducted at 70 mm Depth, 5 mm/s, 70 degrees.

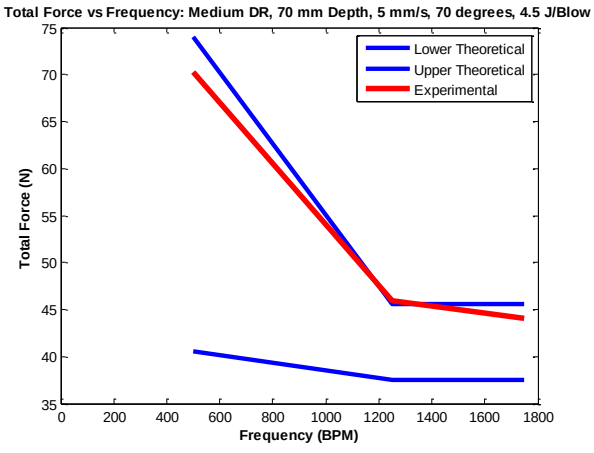

Figure 5-19: Comparison of theoretical and empirical results for a Medium DR soil for frequencies of 500, 1250, and 1750 BPM using impact energy of 4.5 Joules. Tests conducted at 70 mm Depth, 5 mm/s, 70 degrees.

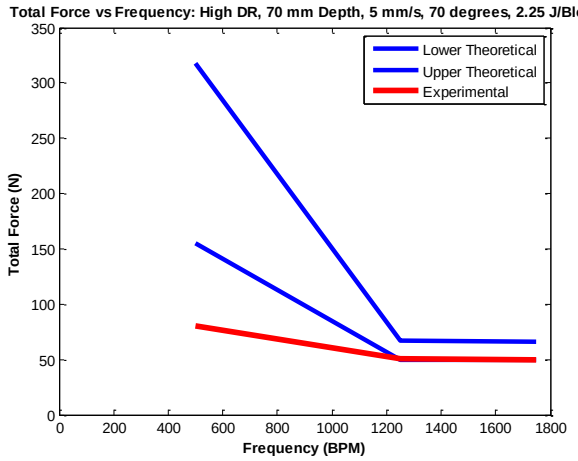

Figure 5-20: Comparison of theoretical and empirical results for a High DR soil for frequencies of 500, 1250, and 1750 BPM using impact energy of 2.25 Joules. Tests conducted at 70 mm Depth, 5 mm/s, 70 degrees.

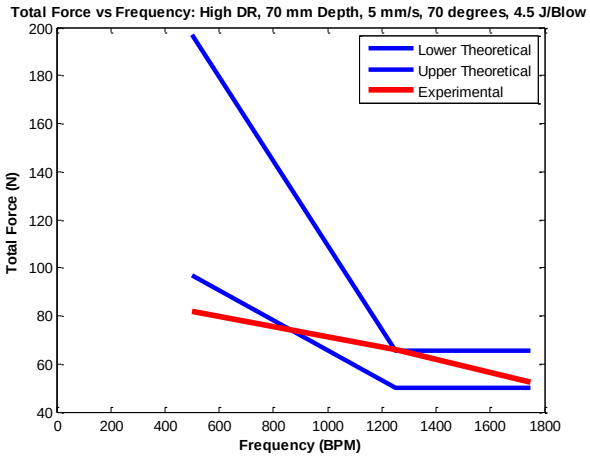

Figure 5-21: Comparison of theoretical and empirical results for a High DR soil for frequencies of 500, 1250, and 1750 BPM using impact energy of 4.5 Joules. Tests conducted at 70 mm Depth, 5 mm/s, 70 degrees.

5.3.6 Different Relative Densities, 0,500, and 1750 BPM, 70 mm Depth, 5 mm/s, 90^0 Scoop Angle, 2.5 Joules/Blow

The ability to predict changes to the attack angle was investigated. Due to hardware constraints, and limitations on the number of tests performed, only attack angles of 70 degrees and 90 degrees were tested. The majority of the testing was done at 70 degrees but a small set of 90 degree tests were collected for frequencies of 0, 500, and 1750 BPM at low and medium relative density soils and 500, 1250, and 1750 BPM at higher relative density soil. The reason for this testing variation is due to saturation limitations of the load cell. A static test could not be performed at 90 degrees in high relative density soil.

As shown in the figures below, at 1750 BPM the experimental results show an increase in excavation force over 500 BPM, or 1250 BPM in the case of high density. The cause of this increase is unknown. It is hypothesized that the cause is based on the dynamic response of the soil being farther away from the resonant frequency of excitation. This effect is only made manifest in the case of the 90 degree orientation because the directional component of percussion acting along the boundary layer is reduced when compared to the 70 degree orientation. Because this effect is not clearly understood the theoretical model does not take into account this phenomenon. It is suggested that future research be undertaken to further investigate this effect.

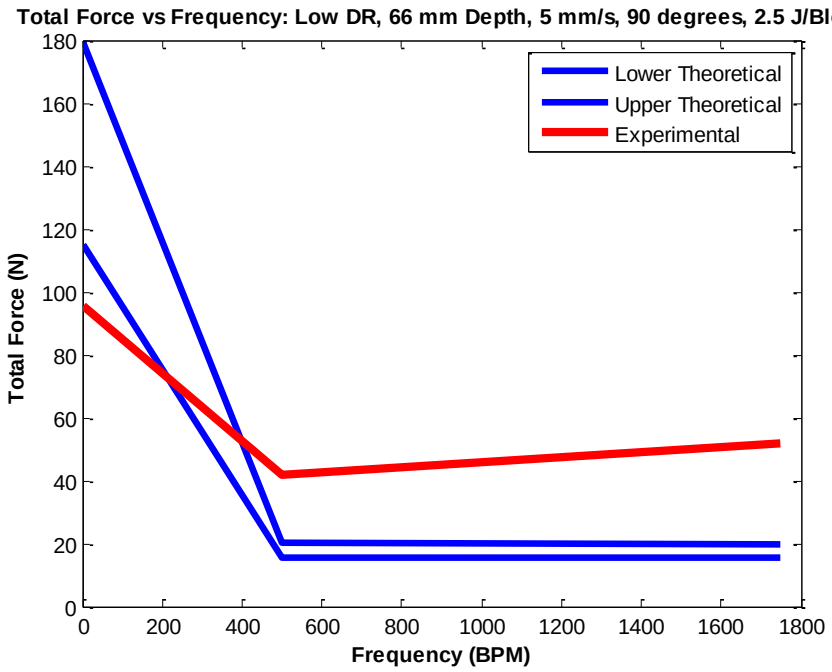

Figure 5-22: Comparison of theoretical and empirical results for a Low DR soil for frequencies of 0, 500, and 1750 BPM at an attack angle of 90 degrees. Tests conducted at 70 mm Depth, 5 mm/s, 2.5 J/blow.

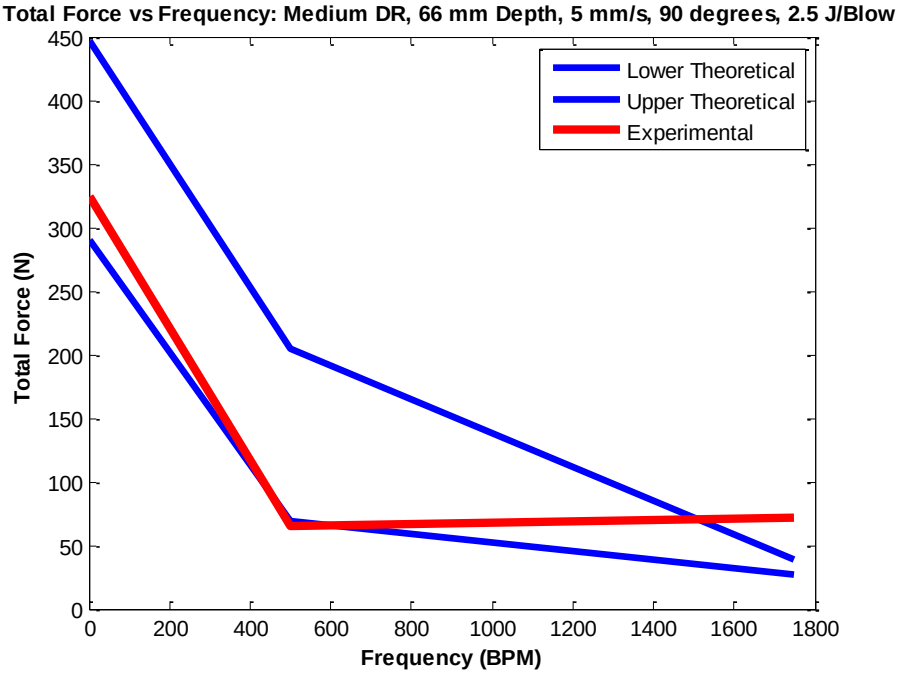

Figure 5-23: Comparison of theoretical and empirical results for a Medium DR soil for frequencies of 0, 500, and 1750 BPM at an attack angle of 90 degrees. Tests conducted at 70 mm Depth, 5 mm/s, 2.5 J/blow.

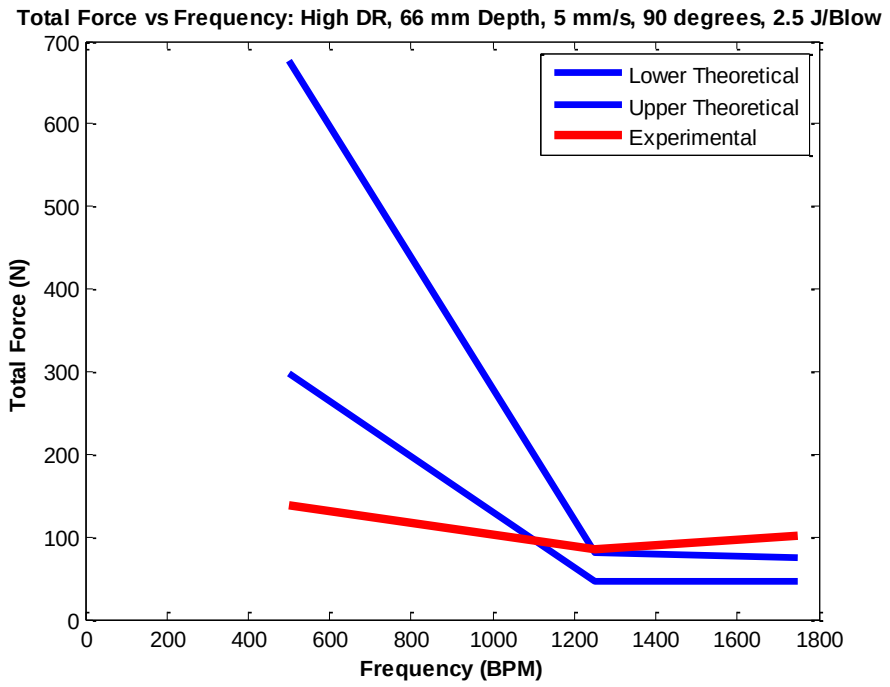

Figure 5-24: Comparison of theoretical and empirical results for a High DR soil for frequencies of 500, 1250, and 1750 BPM at an attack angle of 90 degrees. Tests conducted at 70 mm Depth, 5 mm/s, 2.5 J/blow.

5.4 Comparison of Empirical and Theoretical Failure Volume Geometry

The numeric model does a good job of predicting the excavation reaction force across a wide variety of input variable values. The theoretical excavation force is approximated through energy balance and virtual work by means of a perfectly plastic mechanical-soil behavior assumption. In order to incorporate the effects of percussion into this idealistic numeric model a change is made to the shape of the failure geometry based on the magnitude of percussive soil acceleration. As demonstrated in Section 5.3 this approach is able to replicate the exponential decrease to the reaction force. It is further shown in this section that this approach also lends itself well to a prediction of the true failure control volume geometry.

5.4.1 The Shape of the Failure Volume as a Function of Relative Density and Percussive Frequency

The manner in which the failure volume changes in a perfectly plastic soil as dilatancy force effects are removed is given in Figure 5-25.

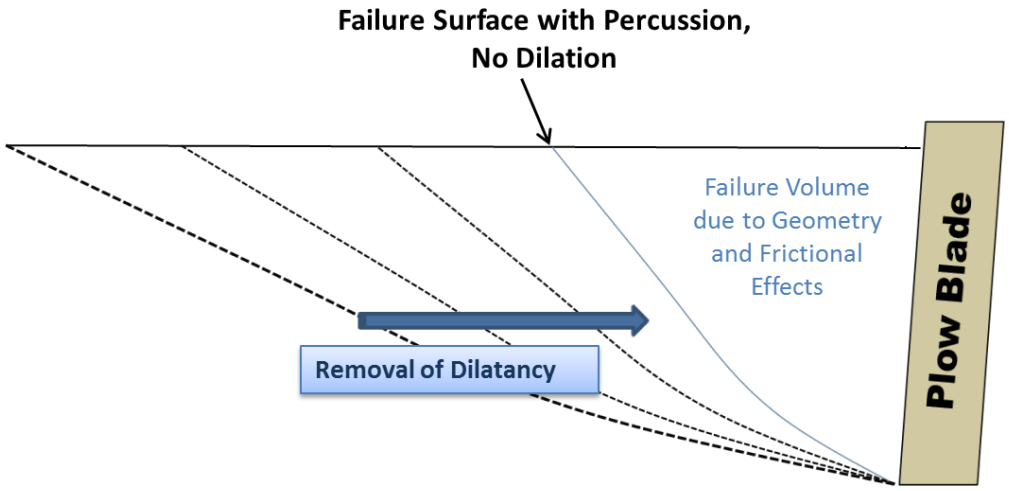

Figure 5-25: Boundary layer geometry during excavation dependent on dilatancy.

A profile view of the scoop inserted into the soil is not possible. However Figure 5-26 provides a still shot of the scoop in different soil states under the effect of different impact frequencies. From these still shots a rough approximation can be made to the protruded length of the displaced soil in front of the scoop. Although this length changes as surcharge accumulates, specifically in the case of static excavation or low-impact-frequency excavation, it is still a means by which a change in geometry of the failure volume can be approximated in contrast to different excavation variables.

This change is demonstrated in the numeric model. Figure 5-27 to Figure 5-29 show how the numeric model predicts the protruded length of the failure volume. Because the numeric model is an idealization of a perfectly plastic soil the length will be a little bit longer than that observed experimentally with real soil. The units of measurement shown in the experimental figures are in centimeters. Likewise, the units given in the theoretical results are in centimeters.

Figure 5-26: Graphic of physical change in shape of failure boundary geometry during excavation.

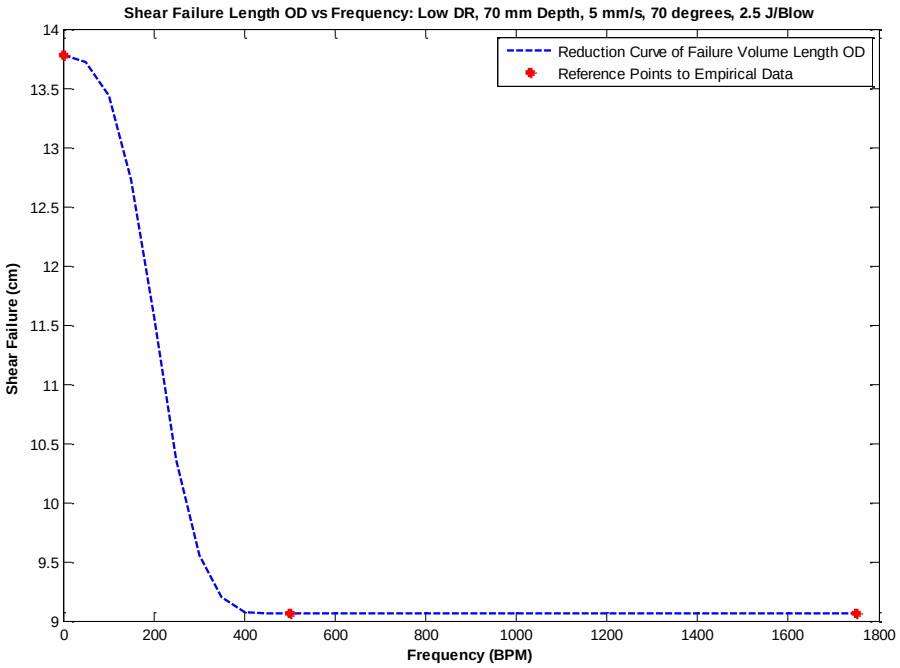

Figure 5-27: Theoretical representation of the change in the protruded length of the failure volume for a Low DR soil as a function of applied impact frequency. Tests performed at 70 mm Depth, 5 mm/s, 70 degrees, and 2.5 J/Blow.

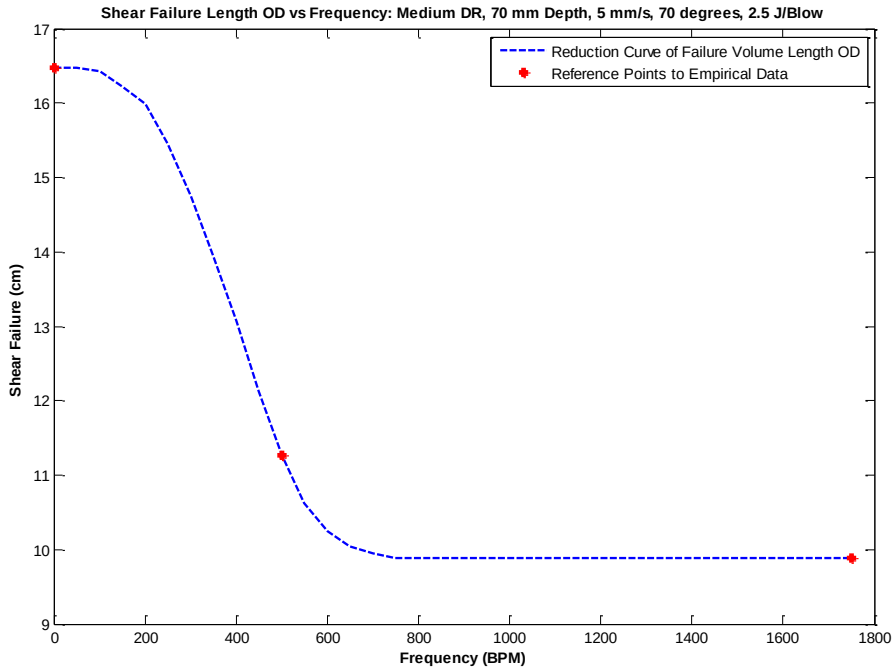

Figure 5-28: Theoretical representation of the change in the protruded length of the failure volume for a Medium DR soil as a function of applied impact frequency. Tests performed at 70 mm Depth, 5 mm/s, 70 degrees, and 2.5 J/Blow.

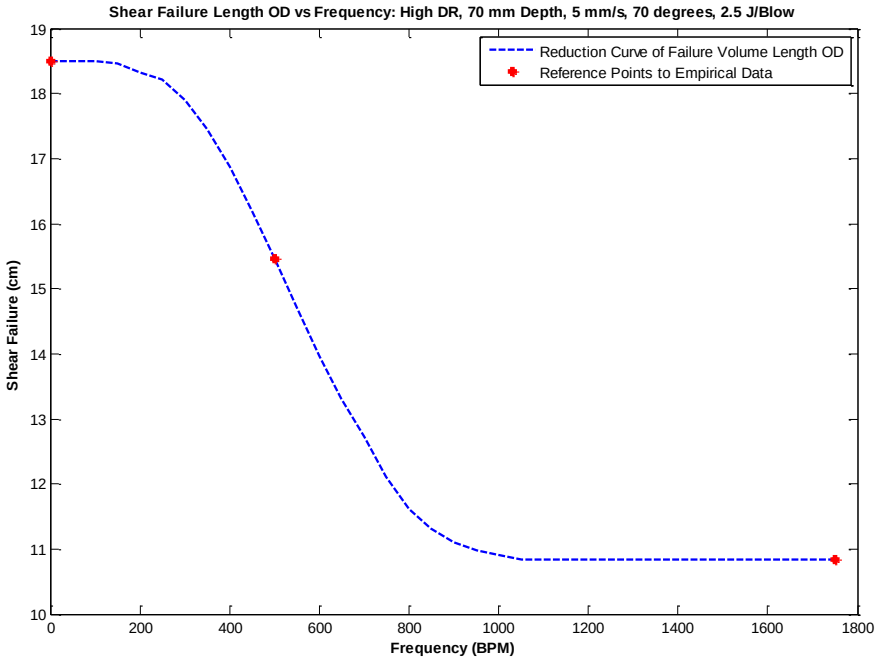

Figure 5-29: Theoretical representation of the change in the protruded length of the failure volume for a High DR soil as a function of applied impact frequency. Tests performed at 70 mm Depth, 5 mm/s, 70 degrees, and 2.5 J/Blow.

5.4.2 The Shape of the Failure Volume as a Function of Speed and Depth

In addition to relative density and applied impact frequency, the theoretical model is able to show an appropriate change in failure volume protrusion length on account of scoop excavation speed and depth.

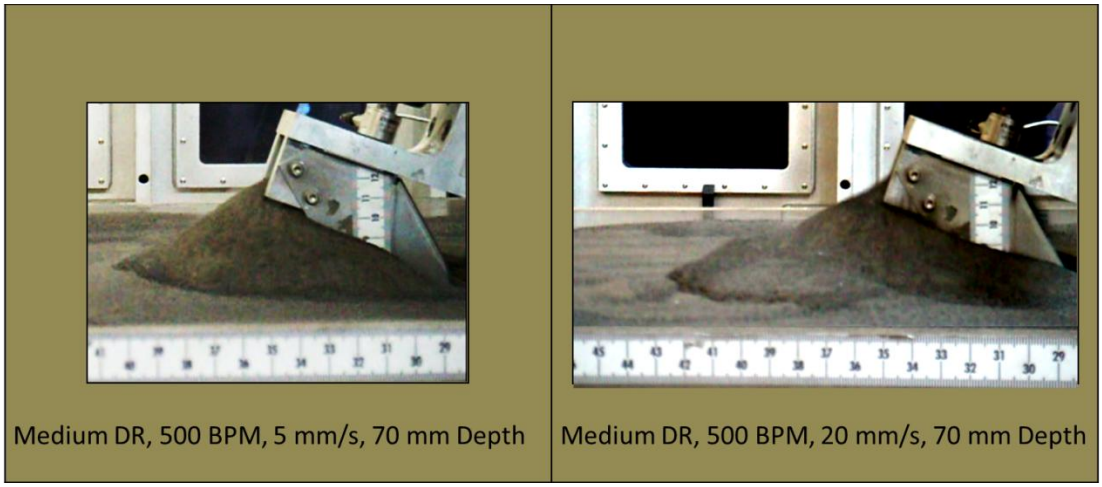

Figure 5-30: Graphic of physical change in shape of failure boundary geometry during excavation based on speed.

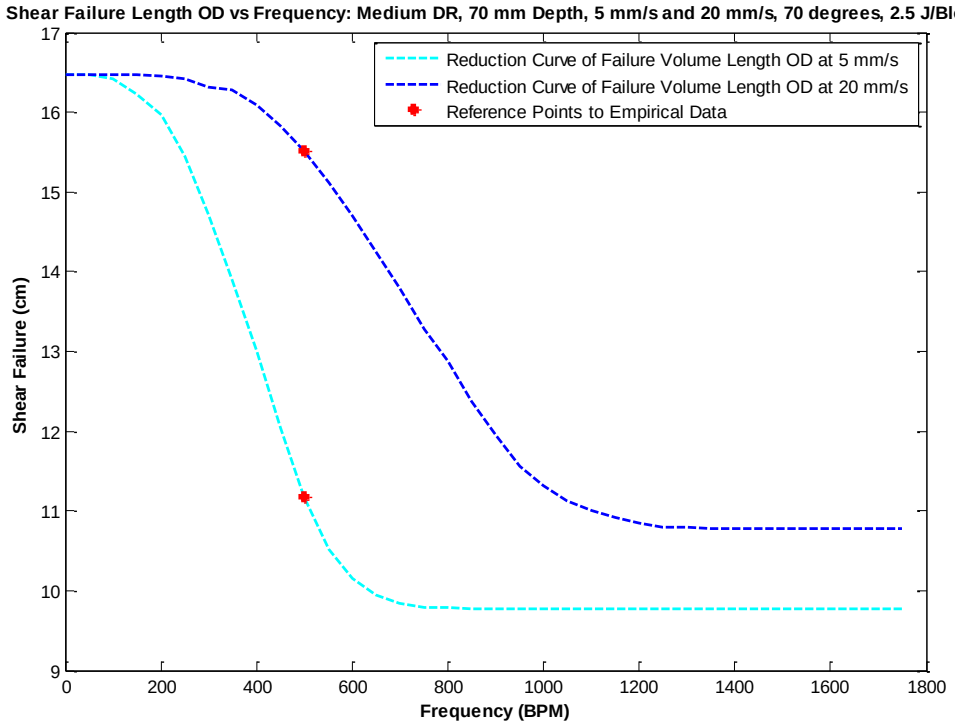

Figure 5-31: Theoretical representation of the change in the protruded length of the failure volume for a Medium DR soil at 5 mm/s and 20 mm/s. The shear failure length is given as a function of applied impact frequency. Markers represent the frequency at which the experimental still shots were taken, 500 BPM. Tests performed at 70 mm Depth, 70 Degrees, and 2.5 J/Blow.

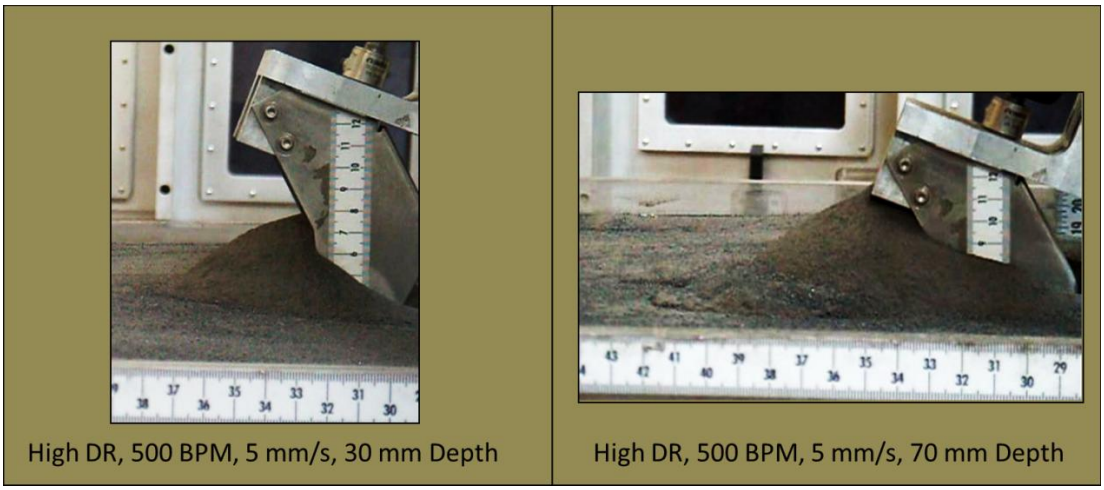

Figure 5-32: Graphic of physical change in shape of failure boundary geometry during excavation based on depth.

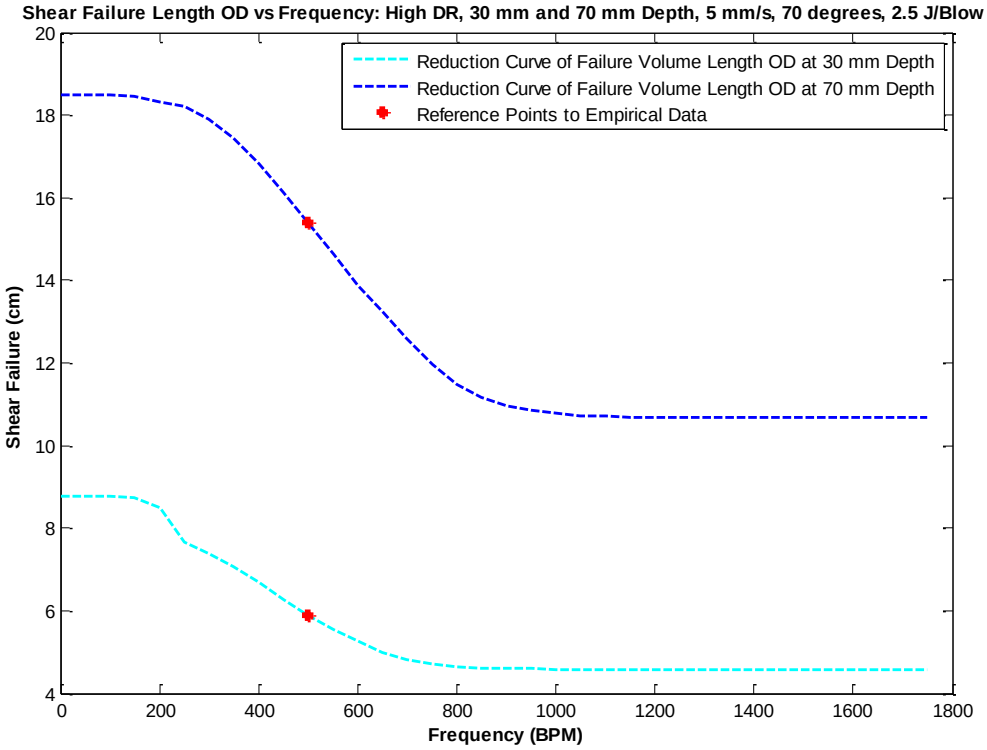

Figure 5-33: Theoretical representation of the change in the protruded length of the failure volume for a High DR soil at 30 mm and 70 mm Depth. The shear failure length is given as a function of applied impact frequency. Markers represent the frequency at which the experimental still shots were taken, 500 BPM. Tests performed at 5 mm/s, 70 degrees, and 2.5 J/Blow.

5.5 Gravity Scaling Capability

5.5.1 Limitations of Theoretical Prediction for Gravity Scaling

One of the underlying assumptions that the theoretical model is based on is perfectly plastic soil which obeys the flow rule. Given this assumption, the model is heavily dependent on cohesion. As noted in Chapter 4 Section 4.3.4.5 the dissipation energy, per unit volume, of a perfectly plastic soil obeying the flow rule is equal to the velocity difference along the boundary layer multiplied by the soil's cohesion. The kinematically admissible velocity field is prescribed by the user in the problem definition. Consequently the magnitude of all the dissipated energy in the virtual work model is dependent on the cohesion term.

Unfortunately in soil mechanics, the magnitude of the cohesion term is determined by forcing a straight line to fit through measured values of shear and normal stress even though the data

actually falls on a curve. The end result being that the cohesion value is often times a little ambiguous and is found to have a wide range of accepted values depending on compaction and surcharge. The cohesion term used in this theoretical model is based off a relationship with the internal friction angle of a basalt simulant. This relationship is taken from Figure 4-30 in Chapter 4 and is derived from work done in [Mitchell 1972d] and [Mitchell 1974]. In addition to this figure, the Lunar Sourcebook also provides a table of collected data from different measured, estimated, and calculated internal friction angle and cohesion values. Simply by looking through the table it is readily apparent that there is not a consistent relationship between the two. The consequence of this ambiguity is that an exact cohesion term for the perfectly plastic assumption is not available simply based on the value of the internal friction angle.

Source	Cohesion, c (kPa)	Friction Angle, ϕ (degrees)	References
EARLY INFERRED: REMOTE SENSING			
	24–240	0	*Halajian* (1964)
	>0.007	>28	*Jaffe* (1964)
	>0	>25	*Jaffe* (1965)
INFERRED: BOULDER TRACKS			
	0.35	33	*Nordmeyer* (1967)
	0.1	10–30	*Moore* (1970)
	0.5*	21–55 (39†)	*Hovland and Mitchell* (1971)
Apollo 17 - North, East and South Massifs	1*	26–50 (37†)	*Mitchell et al.* (1973a)
SURVEYOR: EARLY ESTIMATES			
1: TV and Landing Data	10	0	*Halajian* (1966)
TV and Landing Data	0.15–15	55	*Jaffe* (1967)
TV and Landing Data	0.4–0.13	30–40	*Christensen et al.* (1967)
3: Soil Mechanics Surface Sampler, TV, and Landing Data		>35	*Scott and Roberson* (1968a)
	0 for	45–60	*Christensen et al.* (1968a)
	10 for	0	
6: Vernier Engine	>0.07 for	35	*Christensen et al.* (1968b)
Attitude Jets	0.05–1.7		*Christensen et al.* (1968b)
3 and 7: Soil Mechanics Surface Sampler	0.35–0.70	35–37	*Scott and Roberson* (1969)
SURVEYOR MODEL: BEST ESTIMATE			
	0.35–0.70	35–37	*Scott and Roberson* (1969)
APOLLO 11			
LM Landing, Bootprints, Crater Slope Stability	Consistent with Surveyor Model		*Costes et al.* (1969)
Core Tube, Flag Pole, SWC Shaft Penetration	0.75–2.1	37–45	*Costes et al.* (1971)
APOLLO 12			
LM Landing, Bootprints, Crater Slope Stability	Consistent with Surveyor Model		*Scott et al.* (1970)
Core Tube, SWC Shaft Penetration	0.56–0.75	38–44	*Costes et al.* (1971)
LUNOKHOD I			
Vane Shear	3.9–4.9	N/A	*Leonovich et al.* (1971, 1972)
- Lowest	0.26–1.1	50–25	*Mitchell et al.* (1972d)
- Highest	1.2–4.8	50–25	
- Mode	0.64–2.6	50–25	
Cone Penetrometer			*Mitchell et al.* (1972d)
- Crater Wall (inner)	0.17–1.0	45–25	
- Crater Slope (outer)	0.52–2.7	45–25	
- Horizontal Ground	0.34–1.8	45–25	
APOLLO 14			
Soil Mechanics Trench	<0.03–0.1	35–45	*Mitchell et al.* (1971)
Apollo Simple Penetrometer	Equal to or greater than Surveyor Model		*Mitchell et al.* (1971)
MET Tracks		37–47	*Mitchell et al.* (1971)

Source	Cohesion, c (kPa)	Friction Angle, ϕ (degrees)	References
APOLLO 15			
SRP Data and Simulation Studies		47.5–51.5	*Mitchell et al.* (1972a)
SRP Data and Soil Mechanics Trench	1.0	50	*Mitchell et al.* (1972a)
APOLLO 16			
SRP: Station 4 (10–20 cm depth)	0.6	46.5	*Mitchell et al.* (1972b)
SRP: Station 10	0.37	49.5	*Mitchell et al.* (1972b)
SRP: Station 10	0.25–0.60	50–47	*Mitchell et al.* (1972b)
Drill Core Open Hole	1.3	46.5*	*Mitchell et al.* (1972b)
APOLLO 17			
Drill Core Open Hole (Neutron Flux Probe)	1.1–1.8	50–30	*Mitchell et al.* (1973a)
LRV	0.17	35	*Mitchell et al.* (1973a)
APOLLO MODEL: BEST ESTIMATE			
	0.1–1.0	30–50	*Mitchell et al.* (1972d, 1974)
LUNOKHOD 1 AND 2 (AVE.)	0.4§	40§	*Leonovich et al.* (1974a, 1975)
RETURNED LUNAR SAMPLES			
Apollo 11: Penetrometer	0.25–0.85	42–38	*Costes et al.* (1969, 1970a,b); *Costes and Mitchell* (1970)
Apollo 12: Penetrometer (Surveyor 3)		N/A	*Jaffe* (1971a)
Apollo 12: Vacuum Direct Shear	0–0.7	28–35	*Carrier et al.* (1972b, 1973c)
Apollo 12: Direct Shear (Surveyor 3)	0.1–3.1	13–56	*Jaffe* (1973)
Apollo 12: Triaxial Shear (Surveyor 3)	0–1	51–59	*Scott* (1987; personal communication, 1988)
Luna 16 and 20: Direct Shear and Coulomb Device	3.9–5.9	20–25	*Leonovich et al.* (1974a, 1975); *Gromov et al.* (1972)

* Assumed.
† Mean of 69 values.
† Mean of 25 values.
§ Estimated.

Figure 5-34: Estimated values of lunar soil cohesion and friction angle [Carrier 1991].

The cohesion relationship used in Equation 4-43 has shown to be effective in predicting the expected forces for the experimental parameters tested, Section 5.3. However, based on the lack of consistency shown in Figure 5-34, the accuracy of extrapolating this model is put into question and should be validated through further testing. That said, the purpose of this work is to create a first generation numeric model to be used for approximating percussive excavation reaction forces in low gravity environments and so the following sections entail comparison graphs of percussive excavation for earth gravity, g, and for lunar gravity, 1/6g.

It is suggested that future validation work pertaining to this proposed model include experiments done in a low gravity environment. Such experiments are common for critical low gravity technology.

5.5.2 Theoretical Comparisons of Reaction Forces in Earth's Gravity verses Lunar Gravity

In order to represent a variety of different design prototype scenarios 9 different comparison figures have been generated with alternations in soil relative density, excavation speed, and scoop dimensions. There are three figures of each soil compaction type: low, medium, and high. The first 6 figures show comparisons with respect to a variation in relative density and in speed. The implement dimensions are maintained as those given for the Surveyor Scoop, 70 mm depth and 50 mm width. The last 3 figures represent a more practically sized scoop for excavation purposes, 125 mm depth and 500 mm width, for all three relative densities, at a speed of 5 mm/s.

5.5.2.1 Change in Relative Density at 70 mm Depth, 5 mm/s, 70° Scoop Angle

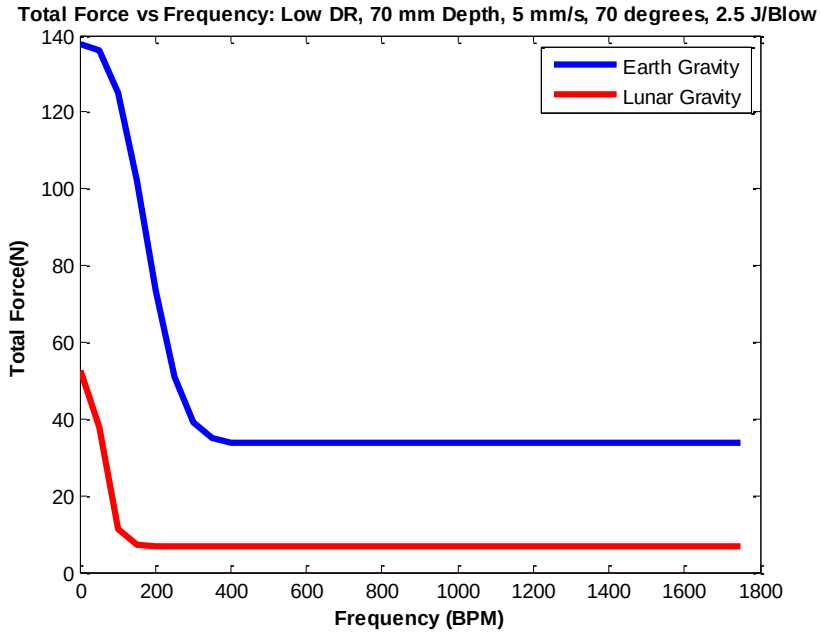

Figure 5-35: Comparison of theoretical reaction force for earth gravity and lunar gravity. Tests conducted in low relative density (internal friction angle of 26), 70 mm Depth, 5 mm/s, 2.5 J/blow.

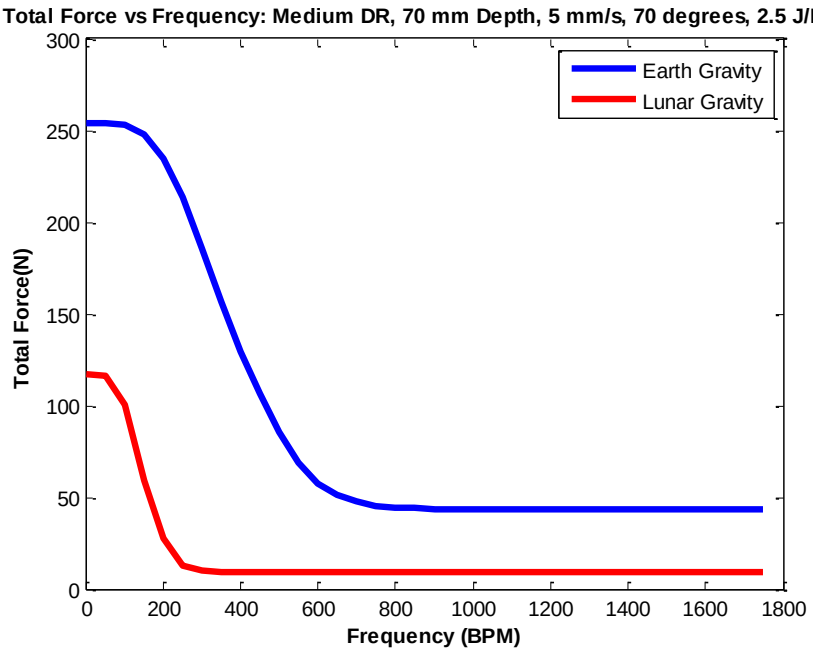

Figure 5-36: Comparison of theoretical reaction force for earth gravity and lunar gravity. Tests conducted in medium relative density (internal friction angle of 37.5), 70 mm Depth, 5 mm/s, 2.5 J/blow.

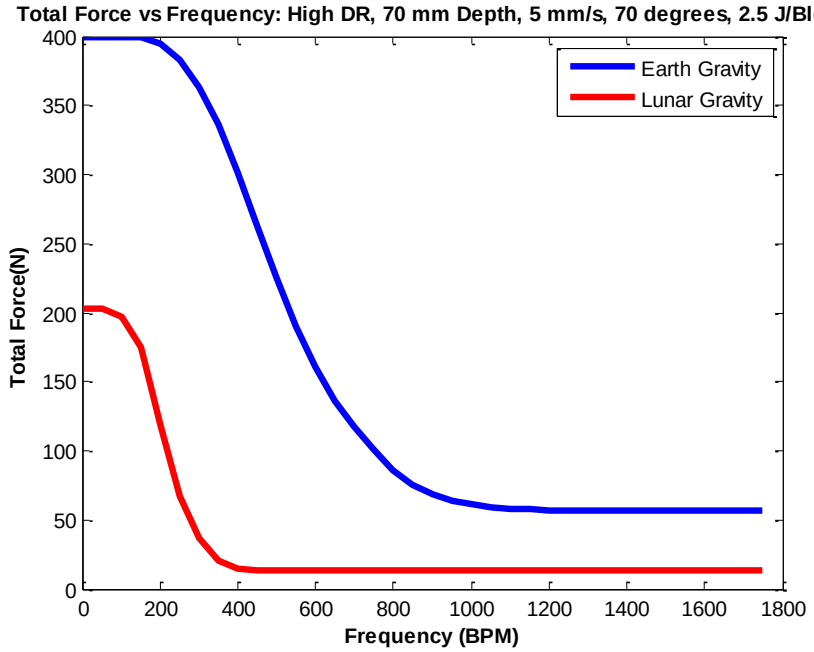

Figure 5-37: Comparison of theoretical reaction force for earth gravity and lunar gravity. Tests conducted in high relative density (internal friction angle of 45), 70 mm Depth, 5 mm/s, 2.5 J/blow.

5.5.2.2 Increase in Excavation Speed, 20 mm/s

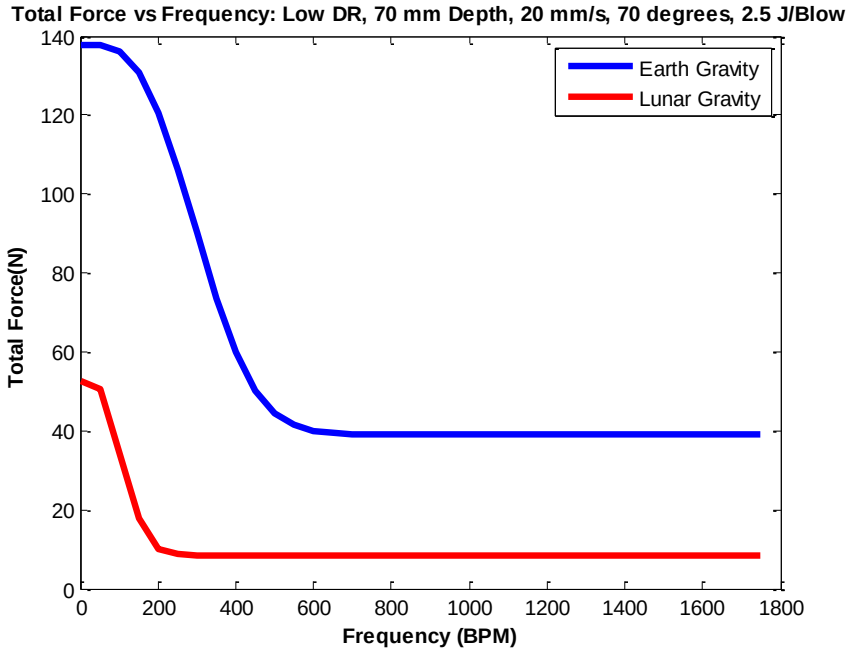

Figure 5-38: Comparison of theoretical reaction force for earth gravity and lunar gravity. Tests conducted in low relative density (internal friction angle of 26), 70 mm Depth, 20 mm/s, 2.5 J/blow.

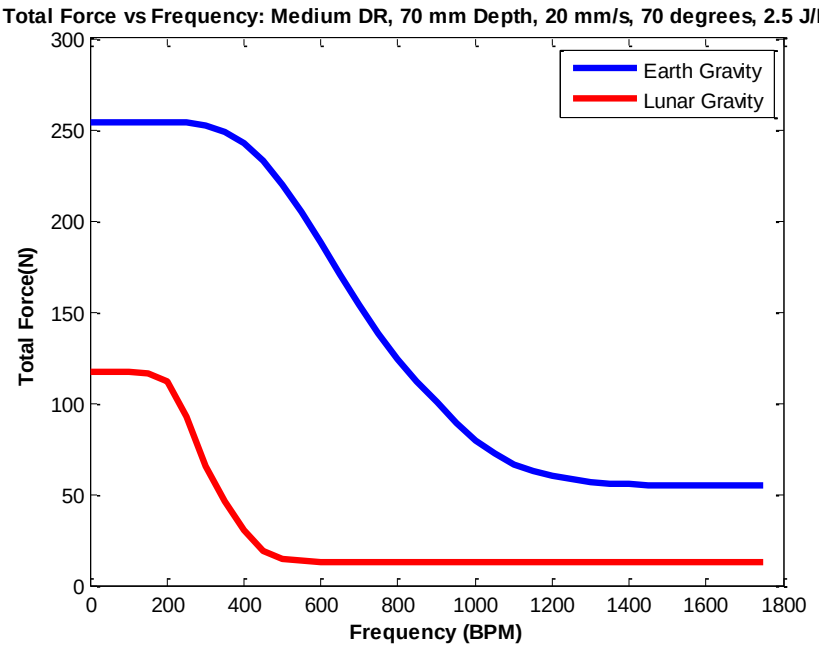

Figure 5-39: Comparison of theoretical reaction force for earth gravity and lunar gravity. Tests conducted in medium relative density (internal friction angle of 37.5), 70 mm Depth, 20 mm/s, 2.5 J/blow.

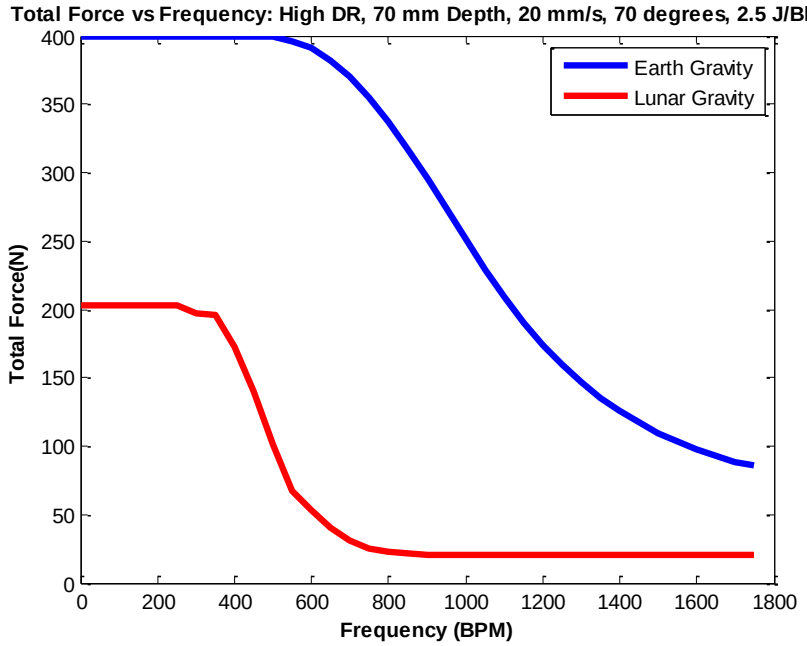

Figure 5-40: Comparison of theoretical reaction force for earth gravity and lunar gravity. Tests conducted in high relative density (internal friction angle of 45), 70 mm Depth, 20 mm/s, 2.5 J/blow.

5.5.2.3 Increase in Excavation Scoop Dimensions, 125 mm Depth and 500 mm Width

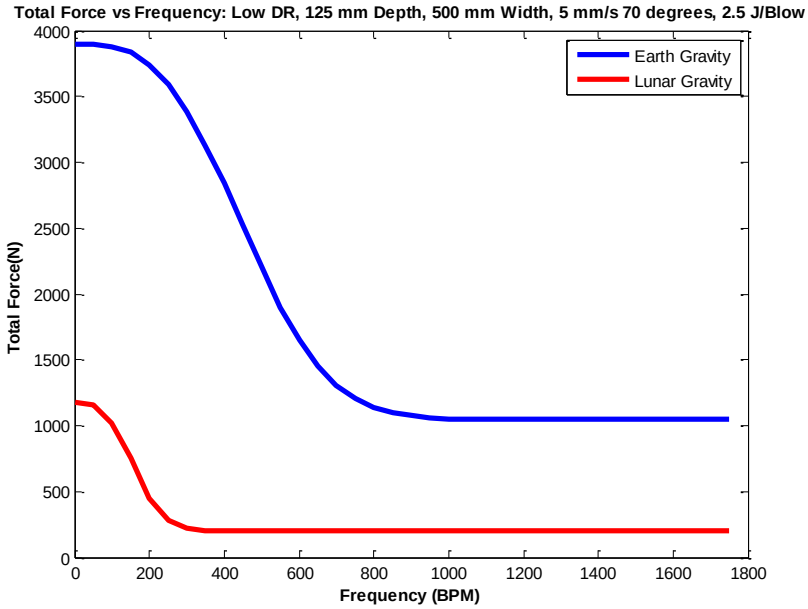

Figure 5-41: Comparison of theoretical reaction force for earth gravity and lunar gravity. Tests conducted in low relative density (internal friction angle of 26), 70 mm Depth 500 mm Wide, 5 mm/s, 2.5 J/blow.

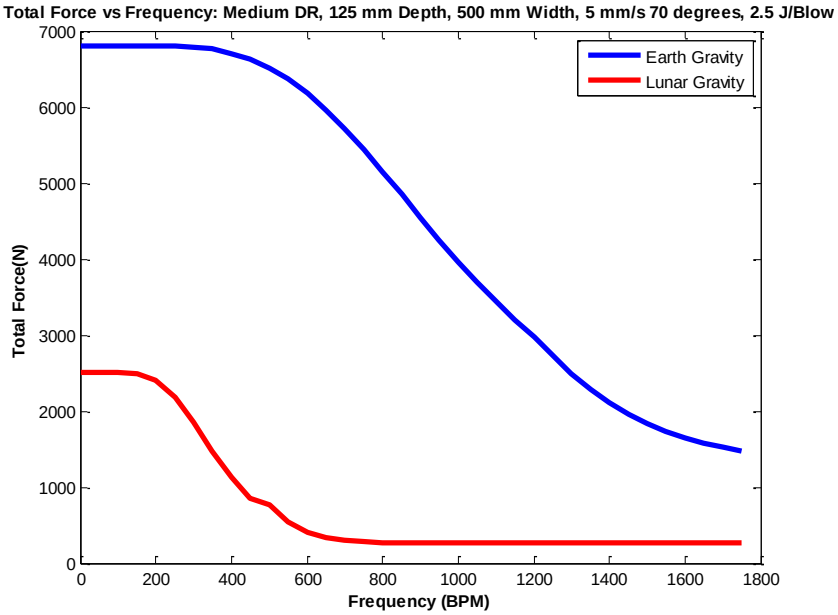

Figure 5-42: Comparison of theoretical reaction force for earth gravity and lunar gravity. Tests conducted in medium relative density (internal friction angle of 37.5), 70 mm Depth 500 mm Wide, 5 mm/s, 2.5 J/blow.

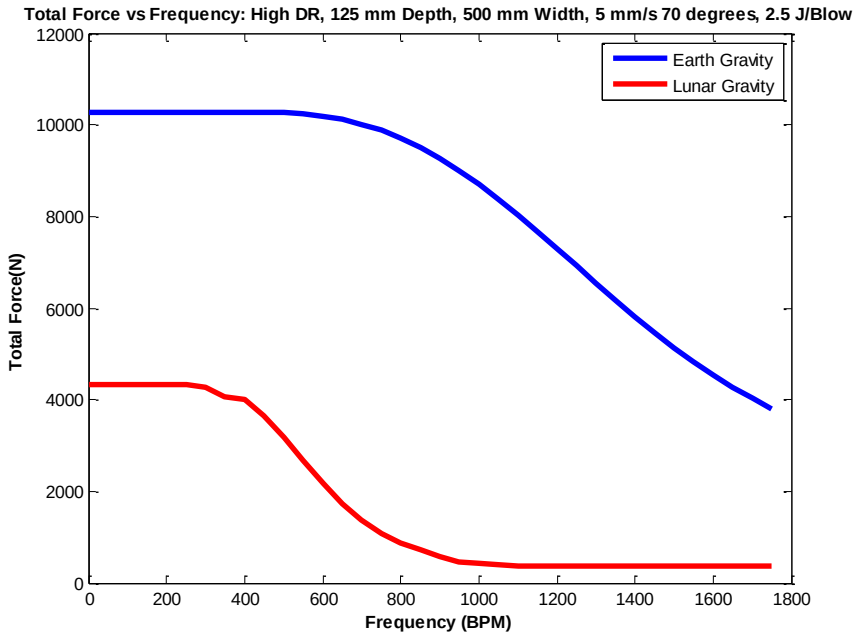

Figure 5-43: Comparison of theoretical reaction force for earth gravity and lunar gravity. Tests conducted in high relative density (internal friction angle of 45), 70 mm Depth 500 mm Wide, 5 mm/s, 2.5 J/blow.

5.5.3 Observations Regarding Lunar Gravity Scaling

Based on Figure 5-35 through Figure 5-43, the percent reduction in exaction force between earth and moon gravity is not a constant; rather it's dependent on excavation and soil parameters. In addition, the degradation curve for lunar gravity has a lower threshold value and a higher exponential decay curve at lower frequencies. This means that there are lower frequency and power requirements in lunar gravity than in earth gravity to reach the reaction force asymptotic limit.

With respect to using this theoretical model as a prediction tool, it is important to note that very small scoop dimensions at high internal friction angles will yield an unbounded solution. This is on account of the virtual work equation breaking down when very low body forces are applied to the failure volume while requiring relatively high soil cohesion effects. Until further refinement is made to the theoretical model it is suggested that either larger scoop dimensions or smaller internal friction angles be tested and that those results be extrapolated for dimensions which lead to unbounded solutions.

6 Conclusions and Future Work

6.1 Summation of Work and Findings

6.1.1 Background

Sustainable exploration has become a prominent topic of research for NASA as plans are made for future human exploration missions into deeper space [Wilson 2011]. Constrained by the amount of mass that can be launched from Earth, project engineers are focusing on the ability to extract necessary resources from the surfaces of neighboring moons, planets and/or asteroids. This field of study, focusing on sustainable exploration, is called In Situ Resource Utilization, ISRU.

Given that Earth's moon is only 3 days journey away and contains resources for the production of oxygen and water, it is an attractive test bed for development of ISRU hardware. As part of the design process of ISRU hardware a persistent obstacle presents itself: how to overcome reaction forces partnered to excavation in a low-gravity environment. Terrestrial earth-moving machines rely on high body forces to break up and excavate soil. The simple and consistent solution whenever combating high reaction forces is to build bigger and heavier excavators with stronger hydraulics. However this one-dimensional approach is not feasible when considering excavation in low gravity space environments. The prohibitive nature of increasing excavator weight is twofold: first, any increase in weight will need to be scaled appropriately for reduced gravity force; and second, any increase in weight is coupled with a dramatic increase in launch cost.

The solution comes by not increasing the excavator's body forces, rather by decreasing the soil's reaction forces. This is accomplished by degrading the shear strength of the soil with percussion. Percussion, in its most basic definition is the periodic application of impact energy. With every impact, the percussive energy delivers shock to the system which propagates energy along the failure volume's boundary layer, disrupting and altering the soil-mechanical properties which determine its shear strength.

6.1.2 Objective

The objective of this work was to understand how percussion effects the soil-mechanical properties of lunar regolith simulant JSC 1a, and to create a first-generation theoretical model which will be able to approximate the magnitude of the reaction force for an excavation implement given specific soil, excavation, and percussion parameters. In order to facilitate the needs of NASA design engineers, the requirements for this numeric model are: simple to use,

has a fast calculation time, and the underlying theory not be too esoteric to allow for future enhancement and refinement.

6.1.3 Research Approach

To understand and analyze the effects of percussion on soil-mechanical properties a test stand apparatus was built to measure and record reaction forces during static and percussive excavation. Tests were done using JSC 1a. 125 different and unique tests were performed, each one with a different permutation of percussive excavation variables. The variables considered were: soil relative density, percussive frequency, percussive impact energy, excavation speed, excavation depth, and attack angle of excavation implement. The implement used for testing was a replica of the Surveyor Soil Surface Sampler. The results of those empirical tests were broken down and analyzed.

6.1.4 Experimental Findings

Based on the experimental data it was concluded that, by means of percussion, the boundary layer describing the failure volume is degraded and the force effects of soil dilatancy are attenuated. This observation was made manifest through the ability to continuously create shear failure planes during the excavation process. It was determined that the continuous creation of shear planes, through percussion, was dependent on the relative density of the soil, the excavation speed, and the geometry of the excavation implement in terms of depth and angle.

In addition to the creation of shear planes, the application of percussion also reduced the baseline draft force. Through an analysis of variance of formatted test data, a relationship between the total baseline excavation force and each test variable was established. Furthermore the inter-variable effects on the total baseline force were presented. It was found that: a linear increase in percussive frequency yields an exponential decrease to the baseline reaction force; the effect of relative soil density is almost nullified once percussion has caused the reaction force to reach its asymptotic value; the tested impact energy values were all above a requisite energy threshold value and each produced similar reaction force reduction; that the speed of excavation and the frequency of percussion are inter-related, speed having a more significant effect on percussive excavation than it does on static excavation; the force effects of changing scoop depth are dramatically decreased with percussion; there are little to no variable dependencies on attack angle between 70 and 90 degrees but the overall reaction force is less for 70 degrees than it is for 90 degrees.

6.1.5 Theoretical Model Development

The numeric model was based off of the upper limit analysis approach which uses the virtual work equation to solve for unknown traction forces. To facilitate the upper limit analysis

approach key assumptions were made regarding soil behavior. The soil was considered perfectly plastic at failure; to obey Drucker's Postulate and follow the flow rule. Given these constraints, and a kinematically admissible velocity field, the upper limit analysis approach was used to solve for unknown reaction forces.

To include the effects of percussion the same upper limit analysis approach was used but with a change in geometry as well as dissipation energy. The internal friction angle was made a function of percussion based on a relationship proposed by Barkan in his work in [Barkan 1962]. This relationship utilized an exponential term defined by percussion, in situ relative density, and excavation speed. The asymptotic value of this curve was determined based on the same variables: applied percussion, in situ relative density, and excavation speed.

6.1.6 Comparing the Predicted Theoretical Results with Empirical Results

The theoretical model provided a robust capability of predicting the reaction force across a wide array of input variables. In addition, the theoretical model was able to predict an appropriate change to the shape of the failure volume based on still photographs of excavation during testing.

Given the versatility of the theoretical code, it was used to predict excavation reaction forces for a low gravity environment. A sampling of different excavation scenarios was provided for lunar gravity. Those samples showed that the percentage reduction in reaction force due to gravity is not a constant but rather it depends on soil and excavation properties. Furthermore, it showed that the onset and magnitude of the shear strength exponential decay was formed at lower percussive frequencies and at less power for lunar gravity than for earth gravity.

A precautionary note was given that due to a high reliance on the value of cohesion, the predicted force given by the numeric model should be refined through a further tested and established relationship between cohesion and percussion.

6.1.7 Reflection on Objective

The driving motivation behind this research was to obtain an understanding of how percussion influences soil-mechanical behavior and to develop a predictive numeric model. That numeric model was given constraints consisting of: ease of use, quick calculation time, and be based in theory allowing for engineering intuition and future refinement. In considering the work which has been presented in this report, those goals have been met.

The effects of percussion were analyzed in Chapter 3 where it was concluded that through percussion the force effects of dilatancy are mitigated. Those effects are inclusive of shear failure plane development as well as draft force magnitude. In Chapter 4 it was further proposed that this decrease in dilatancy be characterized through an exponential decay curve relating internal friction angle to the applied percussion.

With respect to the development of a numeric code, the predicted results matched well with collected empirical data. The proposed code had the versatility to have a wide array of different parameters varied by the design engineer to determine the resultant effects.

The nature of the code and its iterative scheme converge. The code delivered results on the order of tenths of a second.

The code not only provided good approximations in a timely manner, but it also provided an intuitive feel. Being based on the simple principle of virtual work allows an engineer to understand how energy is being supplied and dissipated by the system. The formation of the code also left room for further refinement as future empirical test data is collected.

In addition, the methodology of the upper limit analysis approach, with its incorporation of percussion, can be used to develop schemes for other excavation implement geometry. By knowing and providing a kinematically admissible velocity field and slip-line network geometry, the same relationships used in this work can be used for new problem types.

6.2 Recommendations for Future Work

This research has produced a wealth of knowledge concerning percussion and its interactions with soil-mechanical properties. However, with new insight come new questions. After analyzing the experimental results and constructing a numeric model to approximate those results several different ideas came to my mind about what other information would be helpful to further develop this work. The following are recommendations for future work which will enhance the research presented in this paper.

6.2.1 Scoop Dimensions and the Effect of Implement Geometry

All tests conducted in this work were done with a replica of the Surveyor Soil Surface Sampler. This scoop measures approximately 50 mm across, has a flat back plate and very thin side walls. Although different depths were tested using the scoop, a variable width was not possible. The upper limit analysis approach assumes plain strain, but it is recommended that future tests be run with different widths to corroborate this assumption and to determine what kind of scaling factor should be applied to the code, if necessary.

A variable width could also provide insight into how the threshold value for the impact energy depends on scoop dimensions. All impact energies tested in this work exceeded the necessary threshold to excite soil-mechanical degradation. It is assumed that if the width of the scoop were to become larger the effects of the impact energy would decrease and reach a critical point at which percussion would no longer alter any soil-mechanical properties.

6.2.2 Relationship between Impact Energy and Velocity Ratio

It is also recommended that lower impact energies be tested to develop a relationship between the threshold impact energy and the velocity ratio; as well as the threshold energy and the in situ relative density. The attenuation of dilatancy along the boundary layer is dependent on the percussion energy density and its ability to disrupt particle interlocking. Shown in this work was how the asymptotic value and shape of the soil degradation curve is dependent on both the in situ relative density and the velocity ratio. Intuitively, there should be a similar relationship between threshold impact energy and in situ relative density; as well as threshold impact energy and velocity ratio.

6.2.3 Orientation of Percussion and Attack Angles

The design of the percussive mechanism in this research was such that the direction of percussion was always in line with the attack angle. It's suggested that a different design be constructed which will allow the angle of applied percussion to be independent of the attack angle. It is hypothesized that if percussion were to be placed more in-line with the direction of travel it would facilitate a more efficient design. It might also be the case that the effectiveness of the angle of percussion be more contingent on the attack angle of the excavation implement.

Only attack angles of 70^{o} and 90^{o} were tested. In comparing these results, the 70^{o} angle produced a lower excavation force regardless of different permutations of other test variables. It recommended that more shallow angels be tested to see if this trend continues and what the optimum attack angle might be.

The results from the 90^{o} attack angle testing presented an interesting relationship between impact frequency and the excavation reaction force. As the frequency was increased from 500 BPM to 1750 BPM, or 1250 BPM to 1750 BPM the reaction force increased. This observation goes against intuition and the theoretical model. It could be the vibrational effects have passed an optimum resonant zone for the soil failure zone. This effect should be explored further by using a wider spectrum of frequencies and attack angles.

6.2.4 Influence of Water Content on the Effectiveness of Percussion

Recently ice has been discovered on the polar ice caps on Moon and Mars. All tests in this research were done in dry JSC-1a and subsequently all conclusions are only justified for dry JSC 1a. Given that future exploration missions will want to excavate these pockets of saturated soil, it is suggested that future work involve research into how water content influences the effectiveness of percussion.

6.2.5 Influence of Vacuum on the Effectiveness of Percussion

In addition to the gravitational force, other planets, moons, and asteroids have a different atmosphere. To properly extrapolate the results found in this work to the development of hardware for other planets, moons, and asteroids the effects of vacuum on percussion must also be investigated. Early work has suggested that in low vacuum, 1-5 Torr, there is further reduction to reaction forces. However, once high vacuum is reached, $1x10^{-5}$ Torr, there is an increase to reaction forces. Given that these findings are preliminary and unsubstantiated it is recommended that more work be undertaken to develop a relationship between vacuum and percussion.

6.2.6 Experimental Test Data for Low Gravity

For most hardware designs pertinent to the moon, it is critical to understand how each performs in a low gravity environment. To this end NASA and collaborating companies run experiments in a fixed-wing aircraft affectionately named “vomit comet”. The aircraft flies along an elliptical path relative to the center of the earth in order to replicate the sensation of reduced gravity for momentary periods of time. The influence of gravity is critical to the prediction of excavation reaction forces. It is therefore recommended that a series of tests be conducted on the “vomit comet”, in a low gravity environment, to substantiate or disprove the validity of the proposed theoretical model for space environments with a different gravitational force.

6.2.7 Refining the Relationship between Cohesion and Percussion

In the proposed theoretical model the value of cohesion used to calculate energy dissipation is based on a fixed exponential relationship with the internal friction angle. It is recommended that work be done to further corroborate the proposed relationship, or to provide a direct relationship between cohesion and applied percussion.

6.2.8 Field Tests to Determine Usability of Code for Design

The result of this research is a preliminary theoretical code which can predict an expected excavation reaction force given geometry, soil characteristics, and percussion parameters. In order to determine how easy the code is to use, as well as its effectiveness in the design processes, it is suggested that a field test be conducted in which only specific soil characteristics are given to design engineers along with hardware requirements and they are asked to develop a percussive excavation device using the proposed theoretical model. Through this process, feedback can be given regarding what adjustments and improvements should be made to deliver more effective results and provide easier user compatibility.

7 Work Cited

Alshibli, Khalid A. and Hasan Alsidqi (2009). "Strength properties of JSC-1A lunar regolith simulant". Journal of Geotechnical and Geoenvironmental Engineering, Vol. 135, No. 5, May 1, p 673-679.

Assimaki, Dominic; Kausel, Eduardo; Whittle, Andrew. (2000) "Model for Dynamic Shear Modulus and damping for Granular Soils" Journal of Geotechnical and Geoenvironmental Engineering. October

Balyshkin, P. G. (1966)"The effect of Vibration on Internal Friction in Sand" Journal of Mining Science Volume 2, Number 2, 206-209

Barkan, D.D. (1962) Dynamics of Bases and Foundations. McGraw-Hill Book Company, Inc.

Carrier D. W. III. (2010)Telephone Interview. 1 March 2010

Carrier, W. D. III, Olhoeft, G. R., and Mendell, W. (1991). "Physical properties of the lunar surface." Chap. 9, *Lunar Sourcebook*, Heiken, G. H., Vaniman, D. T., and French, B. M., eds., Cambridge University Press, Cambridge, UK.

Chang, Kenneth. (2009)"Water Found on Moon, Researchers Say" New York Times. November 14, 2009

Chen, W.F. and Rosenfarb, J.L. (1973) Limit analysis solutions of earth and pressure problems. Soils Found., 13(4): 45-60.

Chen, W.F., Giger, M.W. and Fang, H.Y., (1969). On the limit analysis of stability of slopes. Soil Foundations 9(4): 23-32

Chen, Wai-Fah. (1975) Limit Analysis and Soil Plasticity Elsevier Publishing Company Amsterdam.

Chen, W.F.; Liu, X.L.; (1990) Limit Analysis in Soil Mechanics Elsevier Science Publishers B.V.

Craft, J., J. Wilson, P. Chu, K. Zacny, and K. Davis, (2009) Percussive digging systems for robotic exploration and excavation of planetary and lunar regolith, IEEE Aerospace conference, 7-14 March 2009, Big Sky, Montana.

Das, Braja M. Das (1983) Advanced Soil Mechanics Hemisphere Publishing Corporation. McGraw-Hill Book Company.

Drnevich, V.P.; Hall, J.R., Jr.; Richart,F.E., Jr. (1966) "Large Amplitude Vibration Effects on the Shear Modulus of Sand," University of Michigan Report to Waterways Experiment Station, Corps of Engineers, U.S., Army Contract DA-22+079-eng-340 Oct.

Drnevich, V.P.; Richart, F.E., Jr. (1970)“Dynamic Prestraining of Dry Soil”, Journal of the Soil Mechanics and Foundations Division, ASCE, Vol 96, No. SM2, March 453-529

Drucker. D.C. (1953) “Coulomb Friction, Plasticity and Limit Loads” Journal of Applied Mechanics A.S.M.E. paper No. 53-A-57

Ermolaev, N.N.; Senin, N. V. (1968) Shear strength of soil in the presence of vibrations. *Soil Mech. Found. Engn*~1.

Hardin, B.O. (1965) “Dynamic Verses Static Shear Modulus for Dry Sand”, Materials Research and Standards, American Society for Testing and Materials, Vol. 5, No. 5 May 232-235

Hardin, B.O. (1965) “The Nature of Damping in Sands.” Journal of the Soil Mechanics and Foundations Division, ASCE, Vol. 91, No. SM1, Jan. pp 63-67

Hardin B.O.; Black, W.L. (1966) “Sand Stiffness Under Various Triaxial Stresses”, Journal of the Soil mechanics and Foundations Division, ASCE Vol. 92, No. SM2, March 27-42

Hardin, B. O.; Black, W.L. (1968) “Vibration Modulus of Normally Consolidated Clay.” Journal of the Soil Mechanics Foundations Division, ASCE, Vol. 94, No. SM2 Mach 353-369

Hardin, B. O.; Drnevich, V. P. (1972a) “Shear Modulus and Damping in Soils: Design Equations and Curves.” Journal of Soil Mechanics & Foundations Div. Vol. 98. Issue SM7. pp 667-92

Hardin, B. O.; Drnevich, V. P. (1972b). “Shear Modulus and Damping in Soils: Measurements and Parameter Effects,” J. Geotech. Engng Div., Am. Soc. Civ. Engrs,102, No. GT9, 975±987.

Heiken, G., D. T. Vaniman, and B. M. French (editors), (1991) Lunar Sourcebook: A User's Guide to the Moon, Cambridge. University Press.

Hettiaratchi, R.P.; Reece, A.R. (1975) Boundary Wedges in two-dimensional Passive Soil Failure. Geotechnique, 25(2); 197-220

Hong, W. J. (2001) “Modeling, estimation, and control of robot–soil interactions,” Ph.D. dissertation, Dept. Mechanical Eng., Massachusetts Inst. Technol., Cambridge.

Houston W. N., Mitchell J.K., and Carrier W. D. III (1974) Lunar soil density and porosity. *Proc. Lunar Sci. Conf. 5th*, pp. 2361-2364

Johnson, W.; Mellor, P.B. (1983) Engineering Plasticity Ellis Horwood Ltd. Publishers

Kobayahi, T.,H. Ochiai, N. Yasukuku, K. Omine (2005) ”Prediction of Soil Collapse by Lunar Surface Operations in Reduced Gravity Environment” Proceedings of the 15th International Conference of the ISTVS Hayama, Japan, September 25 to 29, 2005

Klosky, J.L.; Sture, S.; Ko, H.; Barnes, F. (1996) Vibratory Excavation and Anchoring Tools for the Lunar Surface, pp. 903-911, Engineering, Construcion and Operations in SPACE V, Proceedings of the Fifth International Conference on Space '96 vol 2, ASCE

Kramer, Steven L. (1996) Geotechnical Earthquake Engineering Prentice Hall Pub.

Lawrence, F. V., Jr. (1965) “Ultrasonic Shear Wave Velocities in Sand and Clay”, Report 23, Response of Soils to Dynamic Loadings, directed by R.V. Whitman, Mssachusetts Institute of Technology, Cambridge, Mass. Jan

Lubliner, Jacob. (1990) Plasticity Theory. Macmillan Publishing Company.

McLemore, Carole. (2011) “WELCOME to In Situ Resource Utilization (ISRU)” In Situ Resource Utilization (ISRU) Element <http://isru.msfc.nasa.gov/> (August 15, 2011)

Mitchell J.K., Houston W.N., Carrier W. D. III, and Costes N.C. (1974) *Apollo Soil Mechanics Experiment S-200*. Final report, NASA Contract NAS 9-11266, Space Sciences Laboratory Series 15, Issue 7, University of California, Berkeley

Mitchell J. K., Houston W.N., Scott R. F., Costes N.C., Carrier W. D. III, and Bromwell L.G. (1972) Mechanical Properties of Lunar Soil: Density, Porosity, Cohesion, and Angle of Friction, *Proc.Lunar Sci. Conf. 3rd*, pp.3235-3253

Pokrovskiy, G.I. (1934) “New Methods of Investigation of the Compressibility and Internal Friction of Soils” Journal of Military Engineering Academy, No.6

Richart, F. E., Jr., Hall, J.R., Jr. and Lysmer, J. (1962). “Study of the Propagation and Dissipation of ‘Elastic ‘ Wave Energy in Granular Soils,” University of Florida Report to Waterways Experiment Station, U.S. Army, Contract DA-22-070-eng-314

Seed, H. B.; Whitman, R. V. (1970) Design of earth retaining structures for dynamic loads. *ASCE Specialty Conf.: Lateral Stresses in the Ground and Design of Earth Retaining Structures,* pp. 103-147.

Seed, H. Bolton; Idriss, I. M. (1970) Soil moduli and damping factors for dynamic response analyses Report No. UCB/EERC-70/10, Earthquake Engineering Research Center, University of California, Berkeley

Seed, H. Bolton; Wong, Robert T.; Idriss, I. M.; Tokimatsu, K. (1984) Moduli and Damping Factors for Dynamic Analyses of Cohesionless Soils Report No. UCB/EERC-84/14, Earthquake Engineering Research Center, University of California, Berkeley

Silver, Marshall L.; Seed, H. Bolton (1969) The Behavior of Sands under seismic loading conditions Report No. UCB/EERC-69/16, Earthquake Engineering Research Center, University of California, Berkeley

Sulatisky, M. T.; Ukrainetz, P.R. (1972) “ Draft Reduction by Vibratory Soil Cutting” Transactions of the Canadian Society for Mechanical Engineering. Vol. 1 Issue 4.

Szabo, B.; Barnes, F.; Sture, S.; Ko; H. Y. (1998) “ Effectiveness of Vibrating Bulldozer and Plow Blades on Draft Force Reduction” Transactions of the ASABE. VOL. 41(2):283-290

Trapp, A.D.; Abrahams, M.; Reece, A.R. (1974) “The Performance of Longitudinally Vibrating Earth Cutters” Journal of Agricultural Engineering Research. 19, 371-390

Wilson, Jim. (2011) “What’s Next for NASA?” http://www.nasa.gov/about/whats_next.html, Accessed on August 15, 2011.

Zacny, K.; Mueller, R.; Galloway, G.; Craft, J.; Hedlund, M.; Mungas, G.; Wilson, J. (2009a) Percussive and Pneumatic Approaches to Lunar Excavation and Mining, Planetary and Terrestrial Mining Science Symposium, Toronto, 7-10 June.

Zacny, K.; Mueller, R.; Galloway, G.; Craft, J.; Mungas, G.; Hedlund, M.; Fink, P. (2009b) Novel Approaches to Drilling and Excavation on the Moon, AIAA-2009-6431, Earth and Space

Zheng, X., Burnoski, L., Agui, J., Wilkinson, A. (2007). *Calculation of Excavation Force for ISRU on Lunar Surface.* Paper presented at the 45th AIAA Aerospace Sciences Meeting and Exhibit.

Zhu, Jian-xin; Yang, Cheng-yun; Hu, Huo-yan; Zou, Xiang-fu (2008)“Reducing-resistance mechanism of vibratory excavation of hydraulic excavator” Journal of Central South University of Technology Volume 15, Number 4, 535-539

8 Bibliography

Bucek, Micheal; Agui, Juan; Zeng, Xiangwu; Wilkinson, R. Allen (2008) " Experimental Measurments of Excavation Forces in Lunar Soil Test Beds" Conference Proceedings. Earth and Space 2008.

Dobry, R., Ladd, R. S., Yokel, F. Y., Chung, R. M., and Powell, D. (1982).''Prediction of pore water pressure buildup and liquefaction of sands during earthquakes using the cyclic strain method.'' *NBS Build. Sci. Ser. 138*, National Bureau of Standards, Gaithersburg, Md.

Donovan, N.C. (1969) Research Brief, Soil Dynamics Specialty Session, 7th International Conference on Soil Mechanics and Foundation Engineering, Mexico City

Iwasaki, T., Tatsuoka, F., and Takagi, Y. (1978). ''Shear moduli of sands under cyclic torsional shear loading.'' *Soils and Found.*, Tokyo, 18(1), 39–56.

King, R.H.; Van Susante, P.J.; Mueller ,R.P. (2010) "Comparison of Lance Blade Data and Analytical Force Models" . Space Resources Roundtable XI /Planetary & Terrestrial Mining Sciences Symposium. June

Kishida, H.; Takano, A. (1970), "The Damping in Dry Sand." Proceedings of the 3rd Japan Earthquake Engineering Symposium, Tokyo, Japan

Matsushita, K.; Kishida, H.; Kyo, K. (1967). "Experiments on Damping of Sands." Transactions of the Architectural Institute of Japan, Summaries of Technical Papers, Annual Meeting of AIJ, p. 166

Seed, H. B., Wong, R. T., Idriss, I. M., and Tokimatsu, K. (1986). ''Moduli and damping factors for dynamic analyses of cohesionless soils.'' *J. Geotech. Engineering*, ASCE, 112(11), 1016–1032.

Tatsuoka, F., Iwasaki, T., Fukushima, S., and Sudo, H. (1979). ''Stress conditions and stress histories affecting shear modulus and damping of sand under cyclic loading.'' *Soils and Found.*, Tokyo, 19(2), 29–43.

Tongue, B.H.(2002) Principles of Virbations. Oxford University Press

Weissman, G.F.;Hart, R.R. (1961) "The damping Capacity of Some Granular Soils." Symposium on Soil Dynamics. ASTM Special Technical Publication No. 305, June pp. 45-54

Wilkinson, A.; DeGennaro, A. (2007) "Digging and Pushing Lunar Regolith: Classical Soil Mechanics and the Forces Needed for Excavation and Traction" Journal of Terramechanics, 44(2)

Zacny, K.A.; Cooper, G.A. (2007) "Friction of drill bits under Martian pressure" Journal of Geophysical Research. Vol. 112. E03003. 2007

Zacny, K.; Mueller, R.P.; Craft, J.; Wilson, J.; Hedlund, M.; Cohen, J. (2010)“Five-Step Parametic Prediction and Optimization Tool for Lunar Surface Systems Excavation Tasks” Earth and Space

9 Appendix

9.1 Chapter 2 Appendix

9.1.1 Motor and Transmission Specifications

	Bearing Test & Penetrometer Axis	Excavation Axis	
Inputs	**Value**	**Value**	**Units**
Torque at Drivetrain	5.94	3.76	Nm
Speed at Drivetrain	123.8	218.2	RPM
Drive Speed of Ball Screw	1.0	1.8	cm/s
Torque at Gearhead	4.954	5.573	Nm
Speed at Gearhead	165.04	163.62	RPM
Torque at Motor	0.1600	0.1800	Nm
Speed at Motor	7096.6	7035.7	RPM
Motor Current	2.722	3.054	A
Motor Power Draw	127.52	143.45	W
No Load Speed at Voltage	7584.0	7584.0	RPM
Motor			
Part Number	148877 re 40	148877 re 40	
Nominal Voltage	48	48	V
Stall Torque	2500	2500	mNm
Max Continuous Current	3120	3120	mA
Max. Continuous Torque	184	184	mNm
Max Efficiency	91.8	91.8	%
Applied Torque	160	180	mNm
Applied Voltage	48	48	V
Gearhead			
Part Number	203120 GP 42 C	203120 GP 42 C	
Diameter	42	42	mm
Reduction	43	43	
Max. Interminnent Torque	22	22	Nm
Max. ContinuousTorque	15	15	Nm
Max. Efficiency	72	72	%
Drivetrain			
Reduction	1.333333333	0.75	
Efficiency	90	90	%
Ball Screw			
Lead	5.00	5.00	mm
Lead	0.20	0.20	inch
Screw Efficiency	85.00	85.00	%
Max Load	**350.00**	**225.00**	**lb**
Max Load	**1556.88**	**1000.85**	**N**
Drive Torque	12.90	8.29	lb-in
Drive Torque	1.46	0.94	N-m
Ideal DriveTorque	10.97	7.05	lb-in

9.1.2 Original Proposed Graphical User Interface (GUI)

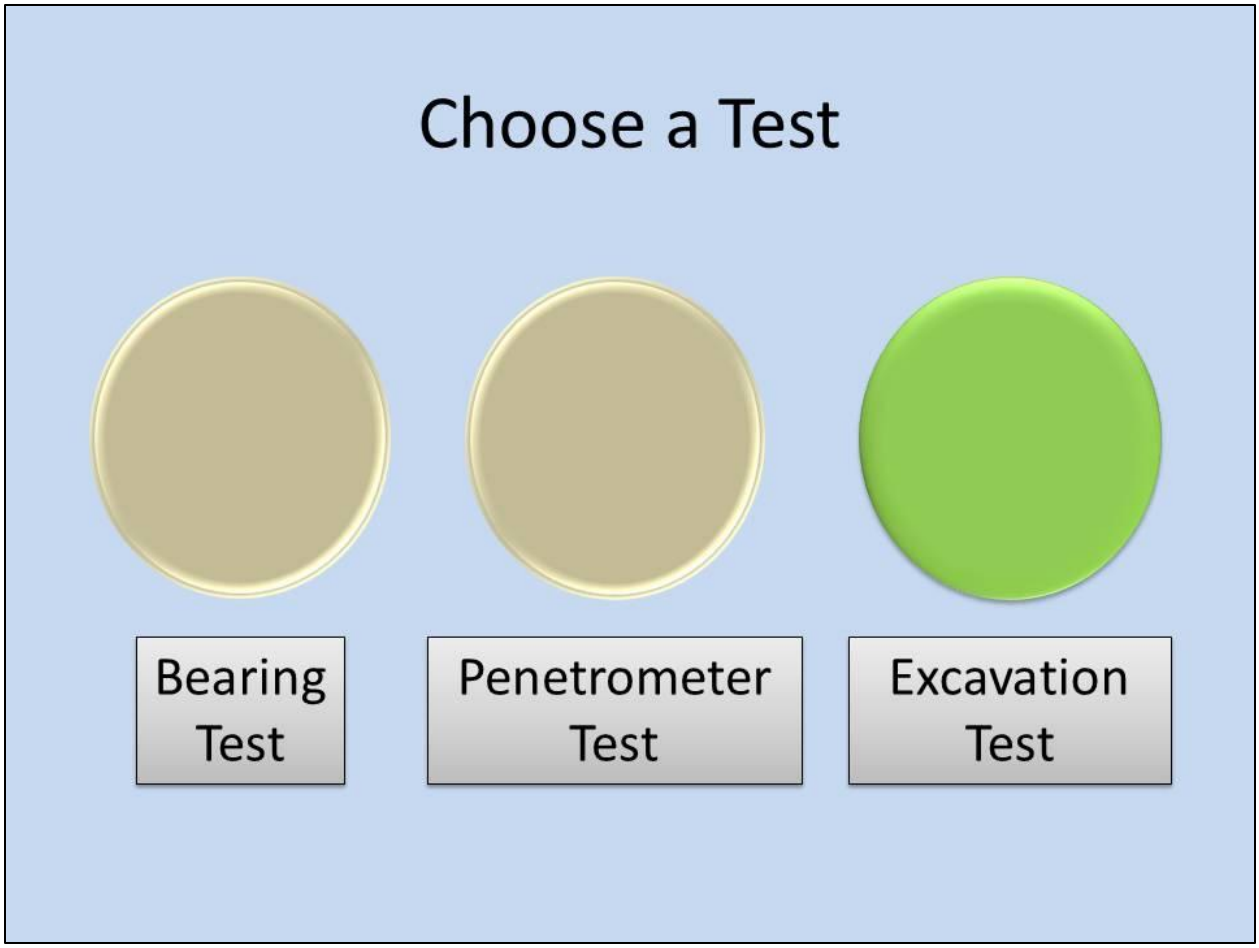
Choose a Test
Bearing Test
Penetrometer Test
Excavation Test

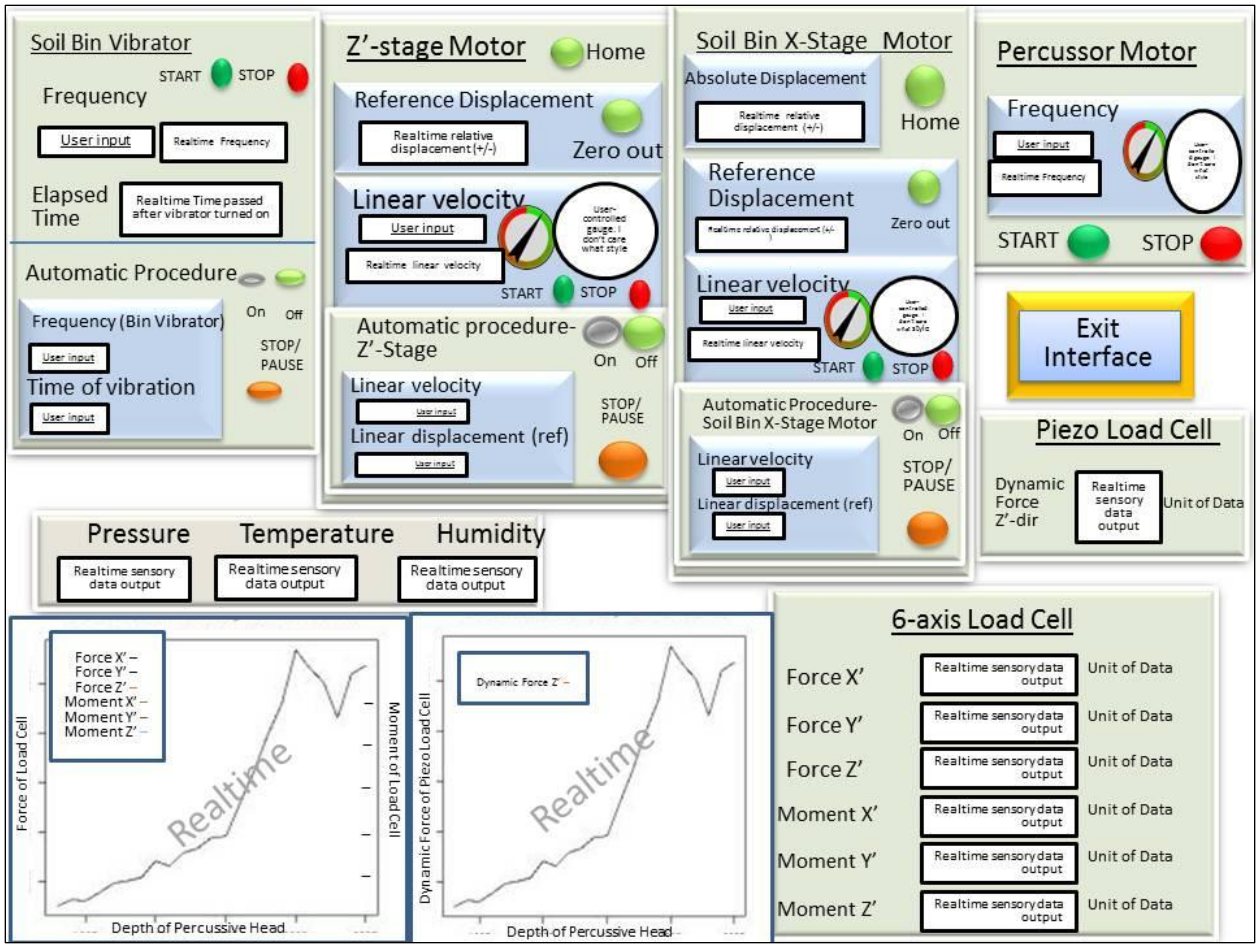
Soil Bin Vibrator
START
STOP
Frequency
User input
Realtime Frequency
Elapsed Time
Realtime Time passed after vibrator turned on
Automatic Procedure
On
Off
Frequency (Bin Vibrator)
User input
STOP/ PAUSE
Time of vibration
User input
Z'-stage Motor
Home
Reference Displacement
Realtime relative displacement (+/-)
Zero out
Linear velocity
User input
Realtime linear velocity
START
STOP
Automatic procedure- Z'-Stage
On
Off
Linear velocity
User input
Linear displacement (ref)
User input
STOP/ PAUSE
Soil Bin X-Stage Motor
Absolute Displacement
Realtime relative displacement (+/-)
Home
Reference Displacement
Zero out
Linear velocity
User input
Realtime linear velocity
START
STOP
Automatic Procedure- Soil Bin X-Stage Motor
On
Off
Linear velocity
User input
Linear displacement (ref)
User input
STOP/ PAUSE
Percussor Motor
Frequency
User input
Realtime Frequency
START
STOP
Exit Interface
Piezo Load Cell
Dynamic Force Z'-dir
Realtime sensory data output
Unit of Data
Pressure
Realtime sensory data output
Temperature
Realtime sensory data output
Humidity
Realtime sensory data output
Force X' –
Force Y' –
Force Z' –
Moment X' –
Moment Y' –
Moment Z' –
Force of Load Cell
Moment of Load Cell
Realtime
Depth of Percussive Head
Dynamic Force Z' –
Dynamic Force of Piezo Load Cell
Realtime
Depth of Percussive Head
6-axis Load Cell
Force X'
Realtime sensory data output
Unit of Data
Force Y'
Realtime sensory data output
Unit of Data
Force Z'
Realtime sensory data output
Unit of Data
Moment X'
Realtime sensory data output
Unit of Data
Moment Y'
Realtime sensory data output
Unit of Data
Moment Z'
Realtime sensory data output
Unit of Data

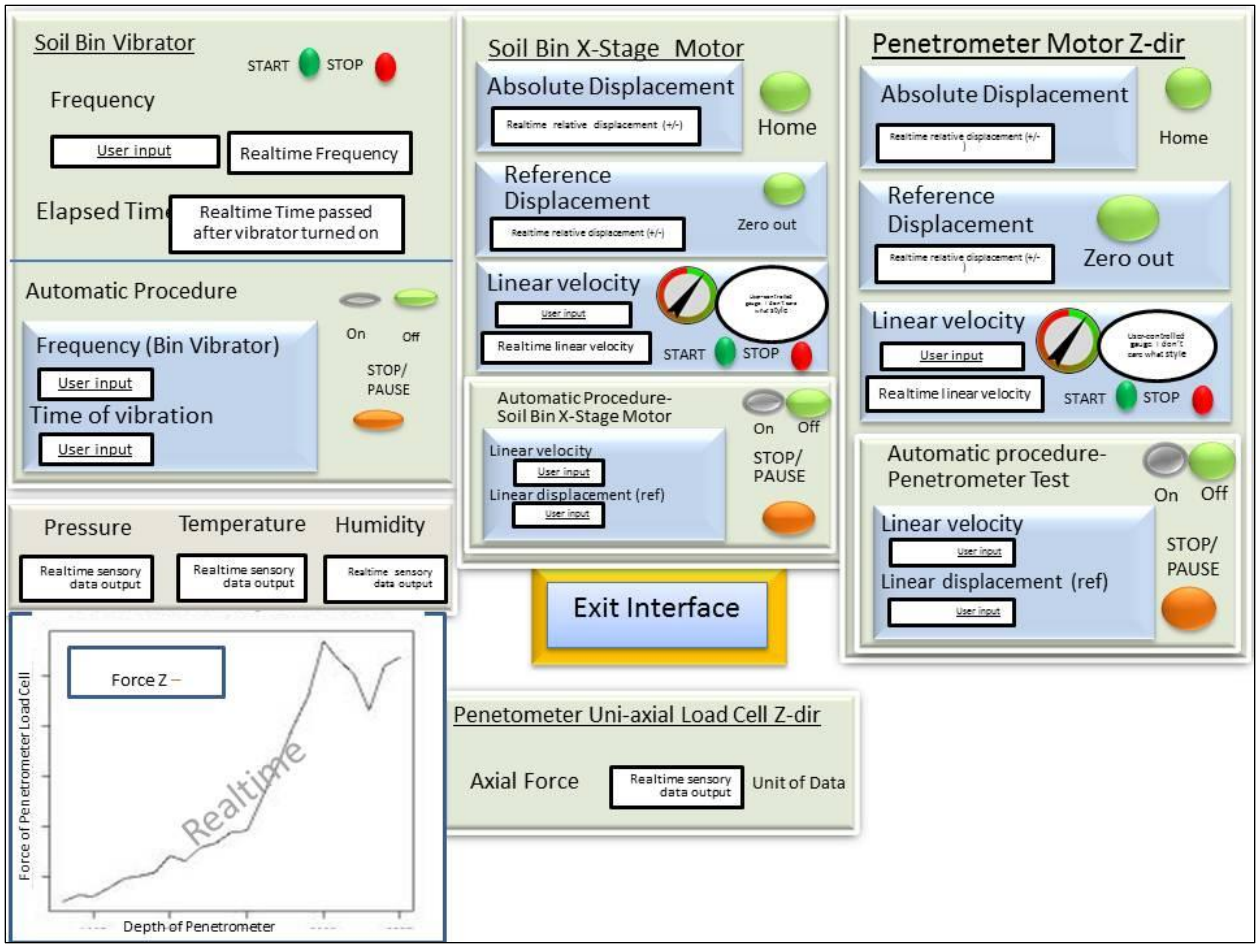
Soil Bin Vibrator
START
STOP
Frequency
User input
Realtime Frequency
Elapsed Time
Realtime Time passed after vibrator turned on
Automatic Procedure
On
Off
Frequency (Bin Vibrator)
User input
Time of vibration
User input
STOP/ PAUSE
Pressure
Temperature
Humidity
Realtime sensory data output
Realtime sensory data output
Realtime sensory data output
Force Z –
Realtime
Force of Penetrometer Load Cell
Depth of Penetrometer
Soil Bin X-Stage Motor
Absolute Displacement
Realtime relative displacement (+/-)
Home
Reference Displacement
Realtime relative displacement (+/-)
Zero out
Linear velocity
User input
Realtime linear velocity
START
STOP
Automatic Procedure- Soil Bin X-Stage Motor
On
Off
Linear velocity
User input
Linear displacement (ref)
User input
STOP/ PAUSE
Exit Interface
Penetrometer Motor Z-dir
Absolute Displacement
Realtime relative displacement (+/-)
Home
Reference Displacement
Realtime relative displacement (+/-)
Zero out
Linear velocity
User input
Realtime linear velocity
START
STOP
Automatic procedure- Penetrometer Test
On
Off
Linear velocity
User input
Linear displacement (ref)
User input
STOP/ PAUSE
Penetometer Uni-axial Load Cell Z-dir
Axial Force
Realtime sensory data output
Unit of Data

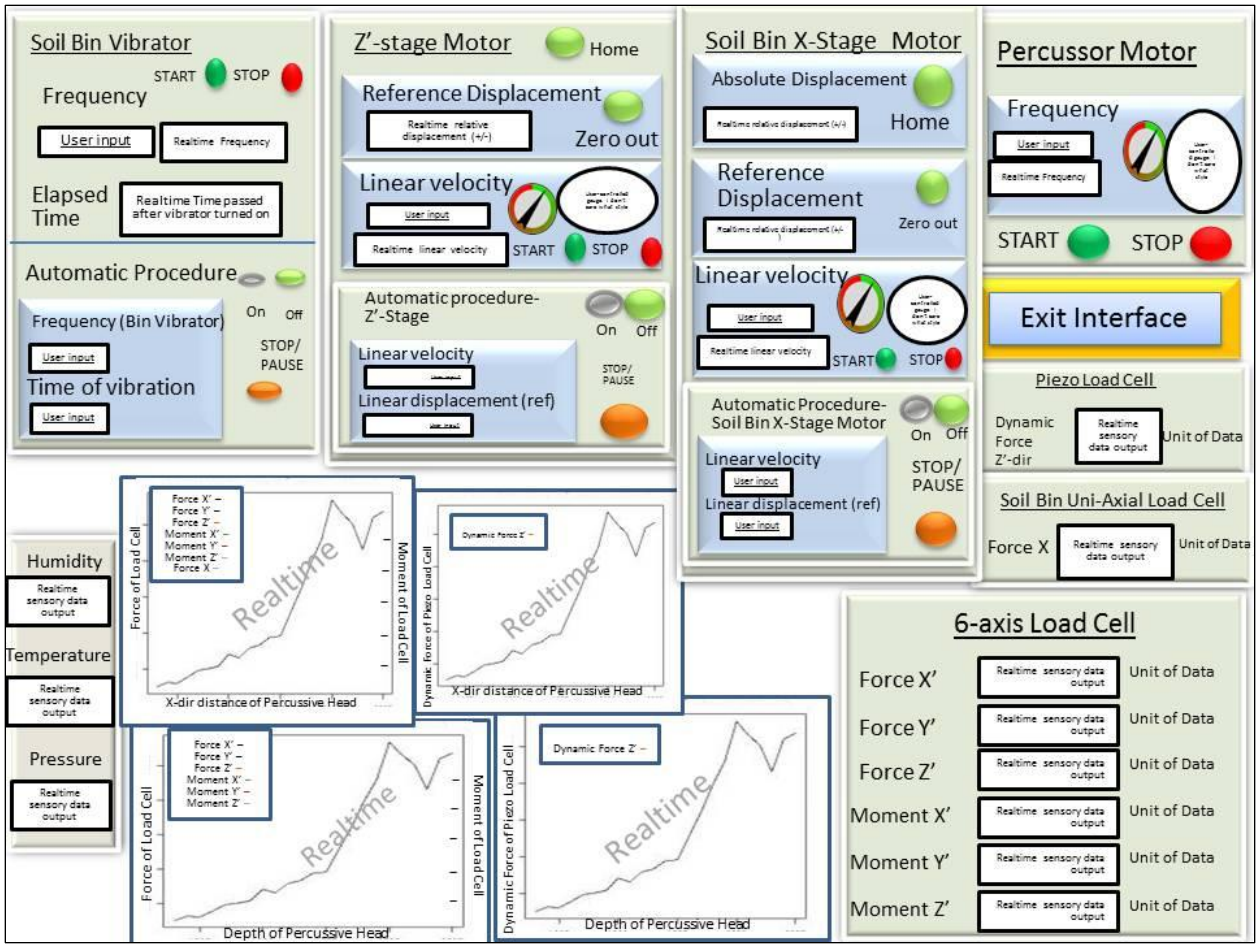
Soil Bin Vibrator
START
STOP
Frequency
User input
Realtime Frequency
Elapsed Time
Realtime Time passed after vibrator turned on
Automatic Procedure
Frequency (Bin Vibrator)
User input
Time of vibration
User input
On
Off
STOP/ PAUSE
Z'-stage Motor
Home
Reference Displacement
Realtime relative displacement (+/-)
Zero out
Linear velocity
User input
Realtime linear velocity
START
STOP
Automatic procedure- Z'-Stage
On
Off
Linear velocity
Linear displacement (ref)
STOP/ PAUSE
Soil Bin X-Stage Motor
Absolute Displacement
Realtime relative displacement (+/-)
Home
Reference Displacement
Realtime relative displacement (+/-)
Zero out
Linear velocity
User input
Realtime linear velocity
START
STOP
Automatic Procedure- Soil Bin X-Stage Motor
On
Off
Linear velocity
User input
Linear displacement (ref)
User input
STOP/ PAUSE
Percussor Motor
Frequency
User input
Realtime Frequency
START
STOP
Exit Interface
Piezo Load Cell
Dynamic Force Z'-dir
Realtime sensory data output
Unit of Data
Soil Bin Uni-Axial Load Cell
Force X
Realtime sensory data output
Unit of Data
Humidity
Realtime sensory data output
Temperature
Realtime sensory data output
Pressure
Realtime sensory data output
Force X' –
Force Y' –
Force Z' –
Moment X' –
Moment Y' –
Moment Z' –
Force X –
Force of Load Cell
Moment of Load Cell
Realtime
X-dir distance of Percussive Head
Dynamic force Z' –
Dynamic force of Piezo Load Cell
Realtime
X-dir distance of Percussive Head
Force X' –
Force Y' –
Force Z' –
Moment X' –
Moment Y' –
Moment Z' –
Force of Load Cell
Moment of Load Cell
Realtime
Depth of Percussive Head
Dynamic Force Z' –
Dynamic Force of Piezo Load Cell
Realtime
Depth of Percussive Head
6-axis Load Cell
Force X'
Realtime sensory data output
Unit of Data
Force Y'
Realtime sensory data output
Unit of Data
Force Z'
Realtime sensory data output
Unit of Data
Moment X'
Realtime sensory data output
Unit of Data
Moment Y'
Realtime sensory data output
Unit of Data
Moment Z'
Realtime sensory data output
Unit of Data

9.1.3 Original Proposed Testing Procedure

GUI

The user is presented with the main GUI interface page. The user will select which test he wants to run:

Bearing Test

Penetrometer Test

Excavation Test

Upon selection, the user is taken to a separate interface page which pertains to the test selected. On this interface page the user has access to a variety of commands which will enable him to perform functions specific to that test. When he wants to exit out of that interface and return to the main interface page he will simply have to click on the "Exit Interface" button.

Figures used in the design of the interface pages:

The GUIs pictures presented were made in PowerPoint. The different figures are used to represent different functions. The shapes and designs do not correlate exactly with the final interface, but the functionality does translate to the final product.

Text boxes in PowerPoint call out what is supposed to be presented. It will either be a realtime read-out from a sensor, or a command window where the user inputs a desired value.

The home button is to be pressed as the beginning of every procedure to set the motor, to which the button pertains, to an absolute location. This will provide a standard procedure for all experimental runs. The user should be able to have to ability to adjust where "home" is located.

The start and stop buttons are assigned to each motor control. Once the user has input his desired velocity he must hit the start button to actuate the motor. The stop button will stop the motor if pressed. If the user desires to adjust the motor velocity while it's moving he can input the new desired value into the text box or adjust the value with the gauge.

On and Off switches are meant to toggle back and forth. They are to be used for automatic procedure functions. Once the button is pressed "on" the procedure will run until either the user presses the "STOP/PAUSE" button, the "Off" button, or the procedure has reached its desired final location. Upon reaching its final location the procedure with automatically turn off and read "Off".

The “STOP/PAUSE” button is meant to pause the procedure while maintaining all the current values set by the user. When pressed again the procedure will resume at the same spot where it was paused.

The “Off” button kills power to the motor(s) and the procedure is dead at that point.

Completion of procedure: For all the automatic procedures there is a desired time or displacement that is to be reached. Once the set amount of time/displacement is obtained the procedure is set to the “Off” position.

There are a couple of user-controlled “gauges” on different interfaces. These are a separate means of adjusting the velocity to which they pertain. They give the user the ability to adjust the velocity in realtime without having to start or stop the motor.

The graphs show that a realtime graphical representation is provided. Some of the graphs will have several variables being displayed on the same graph while others just have one. The graphs representing the information given from the 6-axis load cell contain both the forces as well as the moments. Consequently they will have the units of the forces on one “y-axis” and the units of the moments on the other.

Frames of Reference

In order to try and describe the directions of travel for different motors and the forces being measured by different load cells 2 different reference frames are used. Both are oriented with respect to the right hand rule.

The first is the global reference frame. Here the Z is vertical, the X is along the length of the test stand, and the Y is along the width of the test stand.

The second is a local reference frame. It belongs to the 6 axis load cell. Normal to the face of the load cell is the Z’ axis. The direction with a strong vertical component is the X’ axis. And the Y’ axis is in line with the global Y axis.

Bearing Test Procedure

Non Vacuum

1. Manually add a prescribed amount of soil to the bin
2. Vibrate bin for a set amount of time at a specified frequency (automatic procedure or manual)
3. Set the percussor head to its home position by pressing the “home” button for the Z’-stage motor
4. Move the soil bin to its home position by pressing the “home” button for the X-stage motor
5. Adjust the soil bin to the desired location by actuating the X-stage motor with either an automatic routine or manually.

I. For an automatic routine
    i. set the reference location to zero
    ii. input desired velocity and displacement
    iii. hit the “on” button
    iv. when the bin has traveled the desired distance the routine will automatically stop

II. For manual routine
    i. Set the reference location to zero
    ii. Manually input the desired velocity
    iii. Hit the “start” button
        1. or use the dial to increase/decrease the velocity in realtime
    iv. When the realtime referenced displacement has reached the desired location hit the “Stop” button

6. Move the percussive head till it barely touches the soil using the X’-stage motor
    I. Manually move the percussor head by changing the desired velocity and starting the motor
    II. Force in X’ direction will register on 6-axis load cell when contact is made
    III. Hit the “stop” button
7. Set reference displacement to zero
8. Run bearing test

A. For user-controlled bearing test
    1. Set desired velocity of motor
    2. Hit the “start” button for the X’ stage motor
    3. Run bearing plate into soil until desired displacement is reached
    4. Hit the “stop” button on the X’ stage motor

a. For user-controlled bearing test with frequency

    1. Set desired frequency
    2. Hit the “start” button for the percussor
    3. Repeat steps 8.A.1, 8.A.2, and 8.A.3
    4. Hit the “stop” button on both the percussor motor and the X’-stage motor

B. For automatic bearing test
    1. Set desired velocity
    2. Set desired displacement
    3. Set the X’ stage automatic procedure to “On”

b. For automatic bearing test with frequency
    1. Set desired velocity
    2. Set desired displacement
    3. Set desired frequency
    4. Hit the “start” button for the percussor
    5. Set the X’ stage automatic procedure to “On”

6. When the automatic procedure has stopped hit the “stop” button for the percussor

For Vacuum

1. Manually add the full amount of soil to the bin (dry soil)
2. Bring chamber down to vacuum pressure
3. Vibrate bin for a set amount of time at a specified frequency (automatic procedure or manual)
4. Set the percussor head to its home position by pressing the “home” button for the X’-stage motor
5. Move the soil bin to its home position by pressing the “home” button on the X-stage motor.
6. Adjust the soil bin to the desired location by actuating the X-stage motor with either an automatic routine or manually.
    I. For an automatic routine
        i. set the reference location to zero
        ii. input desired velocity and displacement
        iii. hit the “on” button
        iv. when the bin has traveled the desired distant the routine will automatically stop
    II. For manual routine
        i. Set the reference location to zero
        ii. Manually input the desired velocity
        iii. Hit the “start” button
            1. use the dial to increase/decrease the velocity in realtime
        iv. When the realtime referenced displacement has reached the desired location hit the “Stop” button
7. Move the percussive head till it barely touches the soil
    I. Manually move the percussor head by changing the desired velocity and starting the X’-stage motor
    II. Force in X’ direction will register on 6-axis load cell when contact is made
    III. Hit the “stop” button
8. Set reference displacement to zero
9. Run bearing test
    A. For user-controlled bearing test
        1. Set desired velocity of X’-stage motor
        2. Run bearing plate into soil until desired displacement is reached
        3. Hit the “stop” button

    a. For user-controlled bearing test with frequency

        1. Set desired frequency

2. Hit the “start” button for the percussor
3. Repeat steps 8.A.1, 8.A.2 and 8.A.3
4. Hit the “stop” button for both the percussor and the X’-stage motor

B. For automatic bearing test
   1. Set desired velocity
   2. Set desired displacement
   3. Set the automatic procedure for the X’ stage motor to “On”

b. For automatic bearing test with frequency

   1. Set desired velocity
   2. Set desired displacement
   3. Set desired frequency
   4. Hit the “start” button for the percussor
   5. Set the automatic procedure for the X’ stage motor to “On”
   6. When the automatic procedure has stopped hit the “stop” button for the percussor

Penetrometer Test Procedure

Non Vacuum

1. Manually add a prescribed amount of soil to the bin
2. Vibrate bin for a set amount of time at a specified frequency (automatic procedure or manual)
3. Hit the “home” button on the penetrometer Z-stage motor
4. Hit the “home” button on the X-stage soil bin motor
5. Set the reference displacement to zero for the soil bin motor
6. Move the X-stage motor to desired location
   I. Adjust the desired linear velocity
   II. Hit the “start” button
   III. Once desired reference location has been reached hit the “stop” button
7. Move the penetrometer head till it barely touches the soil
   I. Manually move the penetrometer head by changing the desired velocity
   II. Hit the “start” button
   III. Force in Z direction will register on uni-axial load cell when contact is made
   IV. Hit the “stop” button
8. Set reference displacement on penetrometer motor to zero
   A. For user-controlled penetrometer test
      1. Set desired velocity of motor
      2. Hit the “start” button
      3. Run penetrometer cone into soil until desired displacement is reached
      4. Hit the “stop” button

B. For automatic penetrometer test
    1. Set desired velocity
    2. Set desired displacement
    3. Set to the automatic procedure to “On”

For Vacuum

1. Manually add the full amount of soil to the bin (dry soil)
2. Bring chamber down to vacuum pressure
3. Vibrate bin for a set amount of time at a specified frequency (automatic procedure or manual.)
4. Hit the “home” button on the penetrometer Z-stage motor
5. Hit the “home” button on the X-stage soil bin motor
6. Set the reference displacement to zero for the soil bin motor
7. Move the X-stage motor to desired location
    I. Adjust the desired linear velocity
    II. Hit the “start” button
    III. Once desired reference location has been reached hit the “stop” button
8. Move the penetrometer head till it barely touches the soil
    I. Manually move the penetrometer head by changing the desired velocity
    II. Hit the “start” button
    III. Force in Z direction will register on uni-axial load cell when contact is made
    IV. Hit the “stop” button
9. Set reference displacement on penetrometer motor to zero
    A. For user-controlled penetrometer test
        1. Set desired velocity of motor
        2. Hit the “start” button
        3. Run bearing plate into soil until desired displacement is reached
        4. Hit the “stop” button

    B. For automatic penetrometer test
        1. Set desired velocity
        2. Set desired displacement
        3. Set to “On”

Excavation Test Procedure

Non Vacuum

1. Manually add a prescribed amount of soil to the bin
2. Vibrate bin for a set amount of time at a specified frequency (automatic procedure or manual)
3. Hit the “home” button for the X’-stage motor
4. Hit the “home” button for the X-stage soil bin motor
5. Move the percussive head till it barely touches the soil

I. Manually move the head by changing the desired velocity and starting the Z'-stage motor
II. Force in Z' direction will register on the 6 axis load cell when contact is made
III. Hit the "stop" button

6. Set reference displacement of X'-stage motor to zero
   A. For user-controlled scoop insertion
      1. Set desired velocity of X'-stage motor
      2. Hit the "start" button
      3. Run scoop into soil until desired displacement is reached
         I. Most tests will be run at a scoop depth of 80 mm
      4. Hit the "stop button"

   a. For user-controlled scoop insertion with frequency

      1. Set desired frequency on the percussor motor
      2. Hit the "start' button on the percussor
      3. Repeat steps 6.A.1-6.A.4
      4. Hit the "stop" button on the percussor

   B. For automatic scoop insertion
      1. Set desired velocity of X'-stage motor
      2. Set desired displacement with respect to reference
         I. Most tests will be run at a scoop depth of 70 mm
      3. Set the automatic routine for the X'-stage motor to "On"
      4. When the automatic routine is finished hit the "Stop" button on the percussor

   b. For automatic scoop insertion with frequency

      1. Set desired velocity of X'-stage motor
      2. Set desired displacement with respect to reference
         I. Most tests will be run at a scoop depth of 80 mm
      3. Set desired frequency of percussor motor
      4. Hit the "start" button for the percussor
      5. Set the automatic routine for the X'-stage motor to "On"
      6. When the automatic routine is finished hit the "Stop" button on the percussor
7. Set reference displacement of X-stage motor to zero
8. Run excavation test
   A. For user-controlled scoop excavation
      1. Set desired velocity of X-stage motor
      2. Hit the "start" button
      3. Run scoop through soil until desired reference displacement is reached
      4. Hit the "stop" button

a. For user-controlled scoop excavation with frequency

1. Set desired frequency of the percussor motor
2. Hit the “start” button for the percussor
3. Repeat steps 8.A.1- 8.A.4
4. Hit the stop button for the “percussor”

B. For automatic scoop excavation
1. Set desired X-stage velocity
2. Set desired X-stage displacement
3. Set the automatic procedure for the X-stage motor to “On”

b. For automatic scoop excavation with frequency

1. Set desired X-stage velocity
2. Set desired X-stage displacement
3. Set desired frequency
4. Set the automatic procedure for the X-stage motor to “On”
5. Once the automatic procedure has finished hit the “stop” button for the percussor

For Vacuum

1. Manually add the full amount of soil to the bin (dry soil)
2. Bring chamber down to vacuum pressure
3. Vibrate bin for a set amount of time at a specified frequency (automatic procedure or manual.)
4. Hit the “home” button for the X’-stage motor
5. Hit the “home” button for the X-stage soil bin motor
6. Move the percussive head till it barely touches the soil
   I. Manually move the head by changing the desired velocity and starting the X’-stage motor
   II. Force in X’ direction will register on the 6 axis load cell when contact is made
   III. Hit the “stop” button
7. Set reference displacement of X’-stage motor to zero
   A. For user-controlled scoop insertion
      1. Set desired velocity of X’-stage motor
      2. Hit the “start” button
      3. Run scoop into soil until desired displacement is reached
         I. Most tests will be run at a scoop depth of 80 mm
      4. Hit the “stop button”

   a. For user-controlled scoop insertion with frequency

1. Set desired frequency on the percussor motor
2. Hit the “start’ button on the percussor
3. Repeat steps 7.A.1-7.A.4
4. Hit the “stop” button on the percussor

B. For automatic scoop insertion
   1. Set desired velocity of X’-stage motor
   2. Set desired displacement with respect to reference
      I. Most tests will be run at a scoop depth of 80 mm
   3. Set the automatic routine for the X’-stage motor to “On”
   4. When the automatic routine is finished hit the “Stop” button on the percussor

b. For automatic scoop insertion with frequency

   1. Set desired velocity of X’-stage motor
   2. Set desired displacement with respect to reference
      I. Most tests will be run at a scoop depth of 80 mm
   3. Set desired frequency of percussor motor
   4. Hit the “start” button for the percussor
   5. Set the automatic routine for the X’-stage motor to “On”
   6. When the automatic routine is finished hit the “Stop” button on the percussor

8. Set reference displacement of X-stage motor to zero
9. Run excavation test
   A. For user-controlled scoop excavation
      1. Set desired velocity of X-stage motor
      2. Hit the “start” button
      3. Run scoop through soil until desired reference displacement is reached
      4. Hit the “stop” button

   a. For user-controlled scoop excavation with frequency

      5. Set desired frequency of the percussor motor
      6. Hit the “start” button for the percussor
      7. Repeat steps 9.A.1- 9.A.4
      8. Hit the stop button for the “percussor”

   B. For automatic scoop excavation
      1. Set desired X-stage velocity
      2. Set desired X-stage displacement
      3. Set the automatic procedure for the X-stage motor to “On”

   b. For automatic scoop excavation with frequency

1. Set desired X-stage velocity
2. Set desired X-stage displacement
3. Set desired frequency
4. Set the automatic procedure for the X-stage motor to “On”
5. Once the automatic procedure has finished hit the “stop” button for the percussor

9.2 Chapter 3 Appendix

9.2.1 Permutations Used for Frequency Test Data

Frequency (BPM)	Density (DR)	Spring (J/blow)	Depth (mm)	Speed (mm/s)	Response Force (N)
0	Low	0	70	20	123.6862614
250	Low	2.5	70	20	59.31077425
500	Low	2.5	70	20	44.88827153
750	Low	2.5	70	20	36.47841836
1000	Low	2.5	70	20	46.86463924
1250	Low	2.5	70	20	41.38875465
1750	Low	2.5	70	20	36.17118129
0	Low	0	70	5	105.7404865
250	Low	2.5	70	5	45.18079631
500	Low	2.5	70	5	39.73567654
750	Low	2.5	70	5	28.61453414
1000	Low	2.5	70	5	29.04667738
1250	Low	2.5	70	5	29.47882063
1750	Low	2.5	70	5	26.99043569
0	Medium	0	70	20	216.5962284
250	Medium	2.5	70	20	268.5915086
500	Medium	2.5	70	20	117.6130031
750	Medium	2.5	70	20	62.37855337
1000	Medium	2.5	70	20	64.5586428
1250	Medium	2.5	70	20	51.65614141
1750	Medium	2.5	70	20	67.86833527
0	Medium	0	70	5	285.1002148
250	Medium	2.5	70	5	45.41619015
500	Medium	2.5	70	5	49.73238051
750	Medium	2.5	70	5	47.43492725
1000	Medium	2.5	70	5	35.10932825
1250	Medium	2.5	70	5	38.89228544
1750	Medium	2.5	70	5	37.99585209
0	High	0	70	5	438.954499
250	High	2.5	70	5	147.648134
500	High	2.5	70	5	116.7815867
750	High	2.5	70	5	85.9147054
1000	High	2.5	70	5	59.08185677
1250	High	2.5	70	5	52.02021427
1750	High	2.5	70	5	52.34134257
0	High	0	30	5	82.09479547
250	High	2.5	30	5	26.3473479
500	High	2.5	30	5	19.39053116
750	High	2.5	30	5	7.127638229
1000	High	2.5	30	5	5.361066093
1250	High	2.5	30	5	4.332215332
1750	High	2.5	30	5	3.37926494
0	Low	0	30	20	38.49287016
250	Low	2.5	30	20	19.67285205
500	Low	2.5	30	20	14.30125627
750	Low	2.5	30	20	10.98828426
1000	Low	2.5	30	20	7.675312247
1250	Low	2.5	30	20	6.287904461
1750	Low	2.5	30	20	4.900496676
0	Medium	0	30	5	47.47853681
250	Medium	2.5	30	5	30.29990715
500	Medium	2.5	30	5	17.25622058
750	Medium	2.5	30	5	14.98445
1000	Medium	2.5	30	5	12.71267941
1250	Medium	2.5	30	5	9.607360964
1750	Medium	2	30	5	6.502042514

9.2.2 Permutations Used for Spring Test Data

Spring (J/blow)	Density (DR)	Frequency (BPM)	Response Force (N)
2.25	Low	500	35.46092924
2.25	Low	1250	40.34077655
2.25	Low	1750	26.19949573
4.5	Low	500	42.83651178
4.5	Low	1250	37.28496886
4.5	Low	1750	21.70518662
2.25	Medium	500	84.81643416
2.25	Medium	1250	61.80278068
2.25	Medium	1750	51.97744529
4.5	Medium	500	70.24879215
4.5	Medium	1250	45.88761219
4.5	Medium	1750	44.11900946
2.25	High	500	80.3244906
2.25	High	1250	50.71059932
2.25	High	1750	49.14541762
4.5	High	500	81.93102637
4.5	High	1250	66.0518666
4.5	High	1750	52.28681675
2.5	Low	500	39.73567654
2.5	Low	1250	29.47882063
2.5	Low	1750	26.99043569
2.5	Medium	500	49.73238051
2.5	Medium	1250	38.89228544
2.5	Medium	1750	37.99585209
2.5	High	500	116.7815867
2.5	High	1250	52.02021427
2.5	High	1750	52.34134257

9.2.3 Permutations Used for Speed Data

Speed (mm/s)	Density (DR)	Pressure	Spring (J/blow)	Frequency (BPM)	Depth (mm)	Response Force (N)
20	Low	Atmosphere	0	0	70	123.6862614
5	Low	Atmosphere	0	0	70	105.7404865
20	Low	Atmosphere	0	0	50	86.65208281
5	Low	Atmosphere	0	0	50	55.75274407
20	Low	Atmosphere	0	0	30	38.49287016
5	Low	Atmosphere	0	0	30	35.0350701
20	Low	Atmosphere	2.5	250	70	59.31077425
20	Low	Atmosphere	2.5	500	70	44.88827153
20	Low	Atmosphere	2.5	750	70	36.47841836
20	Low	Atmosphere	2.5	1000	70	46.86463924
20	Low	Atmosphere	2.5	1250	70	41.38875465
20	Low	Atmosphere	2.5	1750	70	36.17118129
5	Low	Atmosphere	2.5	250	70	45.18079631
5	Low	Atmosphere	2.5	500	70	39.73567654
5	Low	Atmosphere	2.5	750	70	28.61453414
5	Low	Atmosphere	2.5	1000	70	29.04667738
5	Low	Atmosphere	2.5	1250	70	29.47882063
5	Low	Atmosphere	2.5	1750	70	26.99043569
20	Low	Vacuum	2.5	1250	70	33.58397301
5	Low	Vacuum	2.5	1250	70	26.01918114
20	Medium	Atmosphere	0	0	70	216.5962284
5	Medium	Atmosphere	0	0	70	285.1002148
20	Medium	Atmosphere	0	0	50	155.7892556
5	Medium	Atmosphere	0	0	50	87.46147877
20	Medium	Atmosphere	0	0	30	63.52205487
5	Medium	Atmosphere	0	0	30	47.47853681
20	Medium	Atmosphere	2.5	250	70	268.5915086
20	Medium	Atmosphere	2.5	500	70	117.6130031
20	Medium	Atmosphere	2.5	750	70	62.37855337
20	Medium	Atmosphere	2.5	1000	70	64.5586428
20	Medium	Atmosphere	2.5	1250	70	51.65614141
20	Medium	Atmosphere	2.5	1750	70	67.86833527
5	Medium	Atmosphere	2.5	250	70	45.41619015
5	Medium	Atmosphere	2.5	500	70	49.73238051
5	Medium	Atmosphere	2.5	750	70	47.43492725
5	Medium	Atmosphere	2.5	1000	70	35.10932825
5	Medium	Atmosphere	2.5	1250	70	38.89228544
5	Medium	Atmosphere	2.5	1750	70	37.99585209
20	Medium	Vacuum	0	0	50	65.52855347
5	Medium	Vacuum	0	0	50	74.7390937
20	Medium	Vacuum	2.5	500	70	73.64360308
20	Medium	Vacuum	2.5	1250	70	51.38695323
5	Medium	Vacuum	2.5	500	70	34.75664823
5	Medium	Vacuum	2.5	1250	70	26.31697704
5	High	Atmosphere	2.5	1250	70	52.02021427
5	High	Atmosphere	2.5	1750	70	52.34134257
20	High	Atmosphere	2.5	1250	70	183.1071201
20	High	Atmosphere	2.5	1750	70	158.6862569

9.2.4 Permutations Used for Angle Data

Angle (Degrees)	Denstiy (DR)	Spring (J/blow)	Frequency (BPM)	Response Force (N)
90	Low	0	0	95.32471813
90	Low	2.5	500	41.73708588
90	Low	2.5	1750	51.98911067
90	Medium	0	0	324.9630042
90	Medium	2.5	500	64.77947985
90	Medium	2.5	1750	71.57890353
90	High	2.5	500	138.086239
90	High	2.5	1250	84.50433378
90	High	2.5	1750	101.8091196
70	Low	0	0	105.7404865
70	Low	2.5	500	39.73567654
70	Low	2.5	1750	26.99043569
70	Medium	0	0	285.1002148
70	Medium	2.5	500	49.73238051
70	Medium	2.5	1750	37.99585209
70	High	2.5	500	116.7815867
70	High	2.5	1250	52.02021427
70	High	2.5	1750	52.34134257

9.2.5 Permutations Used for Depth Data

Depth (mm)	Density (DR)	Spring (J/blow)	Frequency (BPM)	Speed (mm/s)	Response Force (N)
70	Low	0	0	20	123.6862614
70	Low	0	0	5	105.7404865
30	Low	0	0	20	38.49287016
30	Low	0	0	5	35.0350701
70	Low	2.5	250	20	59.31077425
70	Low	2.5	500	20	44.88827153
70	Low	2.5	750	20	36.47841836
70	Low	2.5	1000	20	46.86463924
70	Low	2.5	1250	20	41.38875465
70	Low	2.5	1750	20	36.17118129
30	Low	2.5	250	20	19.67285205
30	Low	2.5	500	20	14.30125627
30	Low	2.5	750	20	10.98828426
30	Low	2.5	1000	20	7.675312247
30	Low	2.5	1250	20	6.287904461
30	Low	2.5	1750	20	4.900496676
70	Medium	0	0	20	216.5962284
70	Medium	0	0	5	285.1002148
30	Medium	0	0	20	63.52205487
30	Medium	0	0	5	47.47853681
30	Medium	2.5	250	5	30.29990715
30	Medium	2.5	500	5	17.25622058
30	Medium	2.5	750	5	14.98445
30	Medium	2.5	1000	5	12.71267941
30	Medium	2.5	1250	5	9.607360964
30	Medium	2.5	1750	5	6.502042514
70	Medium	2.5	250	5	45.41619015
70	Medium	2.5	500	5	49.73238051
70	Medium	2.5	750	5	47.43492725
70	Medium	2.5	1000	5	35.10932825
70	Medium	2.5	1250	5	38.89228544
70	Medium	2.5	1750	5	37.99585209
70	High	0	0	5	438.954499
30	High	0	0	5	82.09479547
70	High	2.5	250	5	147.648134
70	High	2.5	500	5	116.7815867
70	High	2.5	750	5	85.9147054
70	High	2.5	1000	5	59.08185677
70	High	2.5	1250	5	52.02021427
70	High	2.5	1750	5	52.34134257
30	High	2.5	250	5	26.3473479
30	High	2.5	500	5	19.39053116
30	High	2.5	750	5	7.127638229
30	High	2.5	1000	5	5.361066093
30	High	2.5	1250	5	4.332215332
30	High	2.5	1750	5	3.37926494

9.2.6 Permutations Used for Density Data

Density(DR)	Pressure	Spring (J/blow)	Frequency (BPM)	Depth (mm)	Speed (mm/s)	Response Force (N)
Low	Atmosphere	0	0	70	5	105.7404865
Low	Atmosphere	0	0	50	5	55.75274407
Low	Atmosphere	0	0	30	5	35.0350701
Low	Atmosphere	2.5	1250	70	20	41.38875465
Low	Atmosphere	2.5	1750	70	20	36.17118129
Low	Atmosphere	2.5	250	70	5	45.18079631
Low	Atmosphere	2.5	500	70	5	39.73567654
Low	Atmosphere	2.5	750	70	5	28.61453414
Low	Atmosphere	2.5	1000	70	5	29.04667738
Low	Atmosphere	2.5	1250	70	5	29.47882063
Low	Atmosphere	2.5	1750	70	5	26.99043569
Low	Atmosphere	2.5	750	50	5	30.5303479
Low	Atmosphere	2.5	1250	50	5	27.21439519
Low	Atmosphere	2.5	1750	50	5	22.28183748
Low	Atmosphere	2.5	250	30	5	19.67285205
Low	Atmosphere	2.5	500	30	5	14.30125627
Low	Atmosphere	2.5	750	30	5	10.98828426
Low	Atmosphere	2.5	1000	30	5	7.675312247
Low	Atmosphere	2.5	1250	30	5	6.287904461
Low	Atmosphere	2.5	1750	30	5	4.900496676
Low	Vacuum	2.5	500	70	5	24.94498362
Medium	Vacuum	2.5	500	70	5	34.75664823
High	Vacuum	2.5	500	70	5	100.0121665
Medium	Atmosphere	0	0	70	5	285.1002148
Medium	Atmosphere	0	0	50	5	87.46147877
Medium	Atmosphere	0	0	30	5	47.47853681
Medium	Atmosphere	2.5	1250	70	20	51.65614141
Medium	Atmosphere	2.5	1750	70	20	67.86833527
Medium	Atmosphere	2.5	250	70	5	45.41619015
Medium	Atmosphere	2.5	500	70	5	49.73238051
Medium	Atmosphere	2.5	750	70	5	47.43492725
Medium	Atmosphere	2.5	1000	70	5	35.10932825
Medium	Atmosphere	2.5	1250	70	5	38.89228544
Medium	Atmosphere	2.5	1750	70	5	37.99585209
Medium	Atmosphere	2.5	750	50	5	43.22837986
Medium	Atmosphere	2.5	1250	50	5	39.98725936
Medium	Atmosphere	2.5	1750	50	5	30.03690681
Medium	Atmosphere	2.5	250	30	5	30.29990715
Medium	Atmosphere	2.5	500	30	5	17.25622058
Medium	Atmosphere	2.5	750	30	5	14.98445
Medium	Atmosphere	2.5	1000	30	5	12.71267941
Medium	Atmosphere	2.5	1250	30	5	9.607360964
Medium	Atmosphere	2.5	1750	30	5	6.502042514
High	Atmosphere	0	0	70	5	438.954499
High	Atmosphere	0	0	50	5	172.5836457
High	Atmosphere	0	0	30	5	82.09479547
High	Atmosphere	2.5	250	70	5	147.648134
High	Atmosphere	2.5	500	70	5	116.7815867
High	Atmosphere	2.5	750	70	5	85.9147054
High	Atmosphere	2.5	1000	70	5	59.08185677
High	Atmosphere	2.5	1250	70	5	52.02021427
High	Atmosphere	2.5	1750	70	5	52.34134257
High	Atmosphere	2.5	1250	70	20	183.1071201
High	Atmosphere	2.5	1750	70	20	158.6862569
High	Atmosphere	2.5	750	50	5	32.57088164
High	Atmosphere	2.5	1250	50	5	26.97018752
High	Atmosphere	2.5	1750	50	5	22.66915875
High	Atmosphere	2.5	250	30	5	26.3473479
High	Atmosphere	2.5	500	30	5	19.39053116
High	Atmosphere	2.5	750	30	5	7.127638229
High	Atmosphere	2.5	1000	30	5	5.361066093
High	Atmosphere	2.5	1250	30	5	4.332215332
High	Atmosphere	2.5	1750	30	5	3.37926494